

DISTRIBUTION STATEMENT A
Approved for Public Release
Distribution Unlimited

**LARGE EDDY SIMULATION OF BUBBLY
SHIP WAKES**

**Ismail B. Celik, Ibrahim Yavuz, and
Andrei Smirnov**

**Mechanical and Aerospace Engineering
Department
West Virginia University
Morgantown, WV**

Report No: MAE-IC05-TR04

**Final Report Submitted to
Office of Naval Research (ONR)
as Part of the Deliverables under
Grant No: N0014-01-1-0646**

August 2005

***Mechanical and Aerospace
Engineering Department***

College of Engineering and Mineral Resources
West Virginia University • Morgantown, WV 26506-6106

20050822073

LARGE EDDY SIMULATION OF BUBBLY SHIP WAKES

Ismail B. Celik, Ibrahim Yavuz, and Andrei Smirnov

Mechanical and Aerospace Engineering Department

West Virginia University

Morgantown, WV

Report No: MAE-IC05-TR04

**Final Report Submitted to Office of Naval Research (ONR)
as Part of the Deliverables under Grant No: N0014-01-1-0646**

August 2005

ABSTRACT

The presence of air bubbles in ship wakes and their dynamic interaction with the turbulent vortical flows create security problems by modifying the hydro-acoustic properties of ship navigation. This study concerns understanding and controlling the mechanisms, which may lead to selective concentration of bubbles to form clusters or clouds and to predict their size distribution and motion. Numerical simulations were conducted using the Large Eddy Simulation (LES) technique in conjunction with a Lagrangian particle tracking (LPT) technique appropriate for dispersed two-phase turbulent flows.

In order to cut down on the execution time of LES, the simulation for the flow around the ship model are not considered, instead the simulations started just after the ship where the inlet conditions are prescribed with the help of a newly developed Random Flow Generation (RFG) procedure, and to compute bubble distributions. Moreover, to improve turn-around time of the computations and allow LES of the developing wake in a larger domain, parallel simulation tools are developed and adopted in this study.

The turbulence characteristics of ship wakes on a straight tract and a circular tract are investigated using the above mentioned techniques, and processes (e.g. free surface effects, anisotropy, etc.) contributing to turbulence generation are identified, and appropriate sub-grid scale (SGS) models are developed and applied. For the first time, a relatively long developing near wake of three ship lengths was simulated using LES on parallel computers with more than six million nodes.

ACKNOWLEDGEMENTS

I wish to express my sincere thanks to Dr. Edwin Rood and Dr. Patrick Putell who have presided as program monitors for this grant. Without their encouragement and help this research would not have been possible.

Major contributors to research presented in this report are graduate students: Dr. S. Shi, Dr. Z. Cehreli and Mr. G. Hu.

I wish to acknowledge many valuable discussions and guidance by Dr. Mark Hyman of U.S. Navy Coastal System Station, Panama City, FL.

TABLE OF CONTENTS

1	INTRODUCTION	1
1.1	Background.....	1
1.2	Current Status of Turbulent Two-phase Flow Modeling.....	2
1.3	Objective and Present Contribution.....	7
2	METHODOLOGY	8
2.1	Governing Equations and Navier Stokes solver	9
2.2	Numerical Method	14
2.3	Sub-grid Scale Models.....	17
3	THE RFG METHOD.....	19
3.1	Formulation	22
3.2	Validation of RFG Procedure	26
3.3	Application of RFG procedure	30
3.3.1	Boundary Conditions for LES/RANS	30
3.3.2	Particle Dynamics Modeling	31
3.3.3	Large-Eddy Simulations (LES)	32
3.4	Discussions	34
4	SHIP WAKE SIMULATIONS	50
4.1	Experiments on Turbulent Ship Wake Flows.....	50
4.2	Computations of Turbulent Ship Wake Flows	51
4.3	Ship Wake Simulations on a Straight Track.....	54
4.3.1	Boundary Conditions.....	55
4.3.2	Results and Discussion	55

4.4	Ship Wake Simulations on a Circular Track	70
4.4.1	Conditions and Grids	71
4.4.2	Boundary Conditions	72
4.4.3	Results and Discussions	74
4.4.4	Properties of Turbulent Ship Wakes	82
5	BUBBLE DYNAMICS	90
5.1	Formulation	91
5.2	Implementation	94
5.3	Validation on a Turbulent Mixing Layer	96
5.4	Ship-wake Simulations	98
5.4.1	LES Results	98
5.4.2	Bubble Clustering Effects	100
5.5	Discussions	106
6	PARALLELIZATION OF THE LES CODE FOR SHIP WAKES	119
6.1	Methodology	119
6.2	Applications	121
6.2.1	One Way Communication Simulations	121
6.2.2	Two Way Communication Simulations	121
6.2.3	Parallel LES Simulations of a Ship Wake on a Straight Track	125
6.3	Discussions	132
7	CONCLUSION	134
8	REFERENCES	136
9	APPENDIX A	148

LIST OF FIGURES

Figure 3.1: Simulated flow-field using RFG	36
Figure 3.2: Instantaneous velocity vs time step at different locations, $y^* = y/\delta$	37
Figure 3.3: Vorticity contours in the boundary layer	38
Figure 3.4: Convergence of velocity correlations	39
Figure 3.5: Comparison with experimental data	40
Figure 3.6: Normalized divergence of an anisotropic velocity field	41
Figure 3.7: The schematic of the flat plate wake.....	41
Figure 3.8: Turbulence intensities at the inflow boundary.....	42
Figure 3.9: Energy spectrum at different x locations	43
Figure 3.10. Comparison between simulation and measured turbulence intensity (u_{rms}).	44
Figure 3.11. Comparison between simulation and measured turbulence intensity (v_{rms}). ..	45
Figure 3.12: Comparison between simulation and measured turbulence intensity (w_{rms}).	45
Figure 3.13: Comparison between simulation and measured shear stresses	45
Figure 3.14: Kinetic energy profile along the center line in the wake of a flat plate	46
Figure 3.15: Unsteady inlet velocity components: inlet conditions for LES of a ship- wake.....	47
Figure 3.16: Turbulent velocity around a ship hull computed with the RFG algorithm. (View from below.)	48
Figure 3.17: Bubbles in a ship-wake. (Background shading is according to the turbulent kinetic energy.)	48

Figure 3.18: LES of a ship-wake flow.....	49
Figure 4.1: a) Hydrodynamic wake schematic showing major large-scale contributors to the wake (Reed et al. 1990), b) The schematic of the ship-wake	56
Figure 4.2: a) Geometry of DTMD 5415, b) Grid of the computational domain: 162x50x66.	56
Figure 4.3: Typical instantaneous streamwise vorticity (ω_x)contours on different y-z planes in the wake of the ship model 5512.....	59
Figure 4.4: Typical instantaneous vorticity contours(ω_x) on a x-z plane parallel to free surface at $y/L = -0.01$ in the wake of the ship model 5512	59
Figure 4.5: Typical instantaneous streamwise velocity contours on a x-z plane parallel to free surface at $y/L = -0.01$ in the wake of the ship model 5512	60
Figure 4.6: Axial velocity contours: $X/L = 0.61$	60
Figure 4.7: Velocity vectors: $X/L = 0.61$	61
Figure 4.8: Streamwise mean velocity profiles in axial and vertical directions.....	61
Figure 4.9: Turbulent kinetic energy variation in axial and vertical directions.	61
Figure 4.10: Axial mean velocity contours in the wake of the ship model 5512.	62
Figure 4.11: Turbulent kinetic energy contours in the wake of the ship model 5512	63
Figure 4.12: Comparison of resolved turbulence kinetic energy for different simulated cases; the wake of a ship model 5512.....	64
Figure 4.13: RANS solution at $x/L = 0.0$	65
Figure 4.14: RANS+RFG solution at $x/L = 0.0$	65
Figure 4.15: Typical instantaneous velocity vectors on y-z plane at $x/L = 0.2$ in the wake of the ship model 5512	66
Figure 4.16: Typical instantaneous velocity vectors on y-z plane at $x/L = 0.6$ in the wake of the ship model 5512	66
Figure 4.17: Typical instantaneous velocity vectors on y-z plane at $x/L = 1.0$ in the wake of the ship model 5512	67
Figure 4.18: (a) Typical instantaneous velocity vectors on y-z plane at $x/L = 1.2$ in the wake of the ship model 5512 (b) The enlarged view of area A in Fig. 4.18(a).....	67
Figure 4.19: Typical instantaneous velocity vectors on y-z plane at $x/L = 1.4$ in the wake of the ship model 5512	68

Figure 4.20: Typical instantaneous vorticity contours (ω_x) on y-z plane at $x/L = 0.2$ in the wake of the ship model 5512	68
Figure 4.21: Typical instantaneous vorticity contours (ω_x) on y-z plane at $x/L = 0.6$ in the wake of the ship model 5512	69
Figure 4.22: Typical instantaneous vorticity contours (ω_x) on y-z plane at $x/L = 1.2$ in the wake of the ship model 5512	69
Figure 4.23. Arleigh-Burke class destroyer (DDG51)	72
Figure 4.24. Turning ship wake: a) The geometry b) velocity profile specified at the IDP (top view) c) The coordinate space system and numerical grid (Only the core region is shown, distances are non-dimensionalized with ship length, L)	73
Figure 4.25. Typical instantaneous vertical velocity contours with Coriolis force on different y-z plane in the turning ship wake (coarse grid).....	75
Figure 4.26. Radial velocity profiles on different y-z planes in the turning ship wake (fine grid)	75
Figure 4.27. Temporal history of streamwise velocity components at 10° with the z axis, and $x=1.02$, $y=-0.002$ (coarse grid), a) w Coriolis force b) w/o Coriolis force.....	76
Figure 4.28. Temporal history of streamwise velocity components at 10° with the z axis, and $x=1.02$, $y=-0.002$ (medium grid), $C_s=0.042$	76
Figure 4.29. Temporal history of streamwise velocity components at 10° with the z axis, and $x=1.02$, $y=-0.002$ (medium grid), $C_s=0.065$	76
Figure 4.30. The velocity vectors on a vertical plane at an angle of 5° with the z-axis with Coriolis force (coarse grid).....	77
Figure 4.31. The velocity vectors on a vertical plane at an angle of 5° with the z-axis without Coriolis force (coarse grid).....	77
Figure 4.32. The velocity vectors on a vertical plane at an angle of 5° with the z-axis (medium grid) a) $C_s=0.042$ b) $C_s=0.065$	77
Figure 4.33. The velocity vectors on a vertical plane at an angle of 25° with the z-axis with Coriolis force (coarse grid).....	79
Figure 4.34. The velocity vectors on a vertical plane at an angle of 25° with the z-axis without Coriolis force (coarse grid).....	79

Figure 4.35. The velocity vectors on a vertical plane at an angle of 25° with the z-axis (medium grid) a) $C_s=0.042$ b) $C_s=0.065$	79
Figure 4.36. The comparison of the resolved turbulence kinetic energy for ship cruising on a circular track	80
Figure 4.37. Velocity vectors at $x/L=0.2$: a) Non-turning ship (Shi et al. 2001) (fine grid) b) Turning ship (fine grid).....	80
Figure 4.38. Velocity vectors at $x/L=0.65$ a) Non-turning ship (Shi et al. 2001) (finest grid) b) Turning ship (finest grid).....	81
Figure 4.39. Velocity vectors at $x/L=0.65$ for turning ship wake a) Case-1; $Re=1.5 \times 10^9$: DDG51 (finest grid) b) Case-2; $Re=1.0 \times 10^7$: DTMB 5415 (finest grid).....	81
Figure 4.40. Temporal history of streamwise velocity components at 10° ($x=1.02$, $y=-0.001$ and $z=-3.18$) (finest grid) and $C_s=0.052$ a) Case-1 b) Case-2.....	83
Figure 4.41 a) The mean axial velocity contour at the inlet data plane (IDP) for non-turning ship (Shi et al. 2001) (finest grid) b) The mean axial velocity contours at the IDP for turning ship wake (finest grid) c) The mean axial velocity contours after subtracting solid body rotation contribution at the IDP for turning ship wake (finest grid)	84
Figure 4.42. a) The axial flow field provided by RFG at the inlet plane (IDP) for turning ship wake b) Enlarged view of A (finest grid)	85
Figure 4.43. a) Axial velocity contour at $x/L=0.65$ for non-turning ship (Shi et al. 2001) (finest grid) b) Axial velocity contours after subtracting solid body rotation contribution at $x'/L=0.65$ for turning ship.....	85
Figure 4.44. a) Predicted velocity contours at $x/L=1.20$ for non-turning ship-(Shi et al. 2001) (finest grid) b) Macro wake measurements at $x/L=1.20$ by Hoekstra & Ligtelijn (1991) for ship model No. 5452 ($Re \sim 1 \times 10^7$)	87
Figure 4.45. Velocity vectors for turning ship using standard Smagorinsky model (finest grid) on a vertical plane at an angle of a) 5° ($x'/L=0.8$) b) 10° ($x'/L=1.02$) c) 20° ($x'/L=1.55$) d) 30° ($x'/L=1.75$).....	88
Figure 4.46. Energy spectra of the velocity fluctuations a) Non-turning ship (Shi et al. 2001) (finest grid) b) Turning ship (finest grid)	89

Figure 4.47. Predicted vertical vorticity (ω_y) for a) Non-turning ship (Shi et al. 2001) (finest grid), b) Turning ship wake (finest grid) (Case 2)	89
Figure 5.1 Dynamic memory allocation of particle storage	96
Figure 5.2 Mixing layer experimental setup.....	97
Figure 5.3 Instantaneous bubble distribution	108
Figure 5.4. Normalized histogram of probability density function of bubble distributions.	109
Figure 5.5 Mixing layer thickness.	109
Figure 5.6 Bubble concentrations ($\lambda=0.079365$ m).....	110
Figure 5.7 Near and far ship wake regions.	111
Figure 5.8 Turbulent kinetic energy in the computational inlet plane (m^2/s^2).	111
Figure 5.9 Bubbles in a ship-wake. Rear bottom view. The upper surface of the box represents the free surface. The middle rectangle represents the inlet plane. More detailed cross-sectional distributions are shown in Figure 11.....	112
Figure 5.10 Velocity vectors and bubble distribution at $X/L = 0.2$	113
Figure 5.11 Bubble distributions at different cross-sections	114
Figure 5.12 Bubble probability density functions at different cross-sections	115
Figure 5.13 Bubble depletion in the wake (LES).	116
Figure 5.14 Velocity in a vortex.....	116
Figure 5.15 Trajectory of a bubble in a turbulent vortex ($R=700\mu\text{m}$).....	117
Figure 5.16 Convergent bubbles (Bubble motion shown is relative to an observer moving with the axial velocity of the vortex.).....	118
Figure 6.1 Domain decomposition strategy.....	120
Figure 6.2: Laminar channel flow. Results of 8-processor run. Axes dimensions are given in meters.	122
Figure 6.3 Comparison of numerical meshes used in single and 3-processor simulation (black lines indicate inter-processor boundaries.)	122
Figure 6.4 Comparison of predicted streamwise velocity contour in single and 3-processor simulations (black lines indicate inter-processor boundaries.)	123
Figure 6.5 Comparison of predicted streamwise velocity at one point in single and 3-processor simulations	123

Figure 6.6: Comparison of wake simulations on different number of processors.....	124
Figure 6.7: Large-scale 8-processor simulation (250K nodes on each processor).....	125
Figure 6.8. Temporal history of streamwise velocity components at $x = 0.6$, $y = -0.012$, $z = -0.06$	127
Figure 6.9. The root mean square velocity profiles at 3 spanwise locations at a) $x'/L=0.09$, b) $x'/L=1.60$, c) $x'/L=2.80$ (parallel).....	128
Figure 6.10. The root mean square velocity profiles at 3 spanwise locations at a) $x'/L=0.09$, b) $x'/L=1.60$, c) $x'/L=2.80$ (parallel).....	129
Figure 6.11 Contours on vertical x-planes of time averaged a) streamwise velocity b) turbulent kinetic energy (parallel simulations, $108 \times 50 \times 66$ nodes per processor) ...	130
Figure 6.12 Contours on horizontal y-planes of time averaged a) streamwise velocity b) turbulent kinetic energy (parallel simulations, $108 \times 50 \times 66$ nodes per processor) ...	130
Figure 6.13 a) Vorticity magnitude contours obtained for the wake behind a ship on a straight track using parallel computations with 3 Million grid nodes, b) Preliminary vorticity magnitude contours obtained for the wake behind a ship on a straight track using parallel computations with 6 Million grid nodes (black lines show processor boundaries, overlap/communication regions).....	131
Figure 6.14 Resolved turbulence kinetic energy of the wake simulation of a ship cruising on a straight and circular track normalized w.r.t. its inlet value (single node computation).....	131
Figure 6.15 Resolved turbulence kinetic energy of the wake simulation of a ship cruising on a straight track normalized w.r.t. its inlet value along a line of center $z = 0.055$, $y=-0.012$ (Parallel computations)	132

LIST OF TABLES

Table 4.1. Comparison of the maximum values of the root mean square fluctuations for some locations in units of (m/s) for non-turning ship	87
Table 5.1 Cumulative bubble distributions in different planes	100

1 INTRODUCTION

1.1 Background

The problem of bubble dynamics in ship wakes is important in naval hydrodynamics because of ship security as some bubbles somehow form clusters within the turbulent eddies (vortical structures) and some are able to persist for miles leaving a field signature. Bubbles can be generated by various mechanisms, e.g. cavitation, wave breaking, ship nose hydrodynamics, and propeller ventilation. The acoustic properties such as the resonance frequency of the media are a function of local bubble size and population as well as the random motion and pressure fluctuations of the surrounding liquid. The detailed microscale dynamics of turbulent bubbly flows leading to acoustic radiation needs to be studied in order to understand and eventually to control hydro-acoustics properties. Unless the vortical structures at the lower end of the integral length scale of turbulence are resolved in relation to bubble size and cluster size the bubble dynamics can not be understood. Most researchers use classical turbulence models called Reynolds Averaged Navier-Stokes (RANS) models. The classical turbulence models need extensive empirical input and their success is quite limited. The direct numerical simulations can provide very detailed information, but application to practical problems such as that of the wake of a ship is impossible due to excessive amount of computer time and storage requirements. Large-eddy simulation (LES) on the other hand resolves only the large eddies to the extent it is necessary, hence optimizing details, accuracy, and computational requirements. Not many researchers utilize large eddy simulations for this problem in spite of the successful predictions seen in other areas such as atmospheric turbulence, flow past bluff bodies, boundary and shear layers (see Galperin and Orszag, 1993; Lesieur and Metais, 1996; Reynolds, 1989). The interaction of two-phases from the perspective of turbulence enhancement or damping in the near wake of ships seems to play an active role in determining bubble size and population. This, in turn, determines the phenomenon in the far wake which can be predicted using non-conventional techniques such as large eddy simulations. This is the focus area of the present study.

1.2 Current Status of Turbulent Two-phase Flow Modeling

We shall consider only the non-reacting, isothermal two-phase flows with a dispersed phase within a continuous phase. The local instantaneous formulation for such flows is fairly well established (Anderson and Jackson, 1967; Ishii, 1975; Drew, 1992; Joseph and Lundgren, 1990). The continuum equations are identical to the Navier-Stokes Equations for a variable property fluid except for the phase interaction terms. The constitutive equations for the interaction terms are not as well understood, and there is still much research and debate underway for the advancement of these equations. The equation of motion for a single particle is the well known BBO (Basset-Boussinesq-Osseen) equation which has been extended to the case of unsteady, spatially non-uniform ambient flow (Maxey and Riley, 1983; Maxey, 1987). Simplified versions and many variants of this equation are used in applications to specific problems. For example, when the fluid to particle density ratio is small, many terms in the particle equation can be neglected leading to a fairly simple equation involving only the drag and lift forces.

Numerical solution of the turbulent single phase flow equations can be categorized into three major groups, (1) Reynolds averaged Navier-Stokes (RANS) approach, (2) large-eddy simulation (LES) technique, and (3) direct numerical simulation (DNS) approach. The same approaches have been extended to two-phase flows but with much more controversy and empiricism primarily due to the complex nature of the interaction terms. Before we briefly explain the merits of these three approaches another classification of two-phase flow simulations needs to be mentioned, these are: the Eulerian-Lagrangian (EL), Eulerian-Eulerian, (EE) and Mixed Eulerian-Lagrangian (MEL) formulations.

In the EL approach, the “Monte-Carlo Method” is used almost exclusively (see e.g. Chen and Crowe, 1984; Mostafa and Mongia, 1987, 1989; Ounis and Ahmadi, 1990; Gouesbet, 1992). The equation of motion for the particle is solved directly using a randomly generated fluid velocity fluctuation added to the calculated mean velocity field. The fluctuating components of the fluid velocity are calculated using a probability density distribution function (PDF) which is usually assumed to be Gaussian. Its mean is equal to the time averaged fluid velocity, and the variance is the root mean square of the fluid velocity functions, $\text{rms } u_g = (2k/3)^{1/2}$, where k is the turbulent kinetic energy. This relation is only valid for locally isotropic turbulence. The time variation of the fluid velocity fluctuations are calculated by random sampling of the PDF at

certain time intervals. This time interval is called the particle fluid interaction time, t_{int} . It is taken as the minimum of a characteristic eddy life time, t_e , and a particle transit time, t_r , defined as the time it takes a particle to traverse across an eddy of size, l_e , which is usually related to ε , the dissipation rate of k .

In the EE approach the motion of the particulate phase is resolved by solving continuum transport equations (continuity and momentum) similar to those for the fluid phase in an Eulerian frame of reference (Durst et al., 1984; Mostafa and Mongia, 1987; Chen and Pereira, 1995). Here the major problem is the modeling of turbulence augmentation by the presence of the dispersed phase in addition to the modeling of interfacial momentum exchange between the two phases.

A review and comparison of the Lagrangian and Eulerian Approaches is presented by Durst et al. (1984), Mostafa and Mongia (1987), and Gouesbet (1992). Durst et al. concludes that for the Lagrangian approach the computer storage requirement does not increase with the number of particle size groups. In order to obtain more complete information in an Eulerian approach, the equation of motion for each representative particle size group must be solved. This would be very time consuming. Mostafa and Mongia concludes that the Monte-Carlo technique is more expensive than the multi-size Eulerian treatment. Elgobashi (1996) points out that in Lagrangian handling of the particle equation of motion about 90% time is spent in particle tracking. However, this situation can be improved considerably if the Lagrangian particle equations are solved in parallel using efficient parallelization techniques. A further advantage of the Lagrangian approach is that droplet or bubble coalescence and/or breakup (disintegration) can be modeled with relative ease.

In the MEL approach, the equations of mass, momentum, and energy along with the trajectory equations for a range of particle sizes or injection locations and properties, are solved in Lagrangian frame of reference to determine the history of each particle. The mean fluid velocity is used in the particle equation of motion. The influence of fluid turbulence is accounted for separately either by adding a turbulent diffusion force, f_{td} into the particle equation, or by correcting the particle velocity obtained from the single particle equation by adding a turbulent diffusion velocity, U_{pd} (Celik, 1988; Dukowicz, 1980; Berlemont et al., 1993; Hallmann et al., 1995). The calculation of U_{pd} usually involves solving an Eulerian transport equation for the particulate phase. The transport equation involves a transport coefficient called particle diffusivity, which must be prescribed empirically. Many empirical equations are suggested in the

literature (e.g. Mostafa and Mongia, 1989) for calculating this parameter. The Eulerian gas-phase equations contain source (or sink) terms to account for the influence of particulate phase on the fluid and vice versa. This input can also be computed from a probability distribution function (PDF) using a Monte Carlo method. The PDF is usually of Gaussian type with the mean and the variance being a function of k and ϵ or other turbulence parameters. Typically tens of thousands of particle trajectories must be calculated to obtain reasonable statistics for the particles. Particle-particle interaction is also taken into account to a certain extent using semi-empirical relations, and by allowing fragmentation, coagulation (or agglomeration).

RANS Models

The RANS models are derived by time-smoothing and/or averaging of the local instantaneous equations which are already volume averaged (see e.g. Dasgupta et al., 1994, Drew, 1992; and Morel and Bestion, 1997). Most researchers use some version of the so called k - ϵ model or algebraic stress models with marginal success (see for example Saif and Bertodano, 1996; Shimizu and Yokomine, 1993; Sato et al., 1996; Celik and Gel, 1997; Paterson et al., 1996). The central assumptions in the k - ϵ model are the same as in single phase models, i.e. the isotropic eddy viscosity concept and the gradient diffusion model, in addition to the assumption of local equilibrium which is valid with limitations only at very high Reynolds numbers. As reviewed by Sato et al. and Shimizu and Yokomine the turbulent kinetic energy and epsilon equations are most problematic for two-phase flow applications. It has been shown in the literature (e.g. Shimizu et al., 1993; Balzer et al., 1997; Celik and Gel, 1997) that these equations must be modified to include the turbulence modification due to the presence of dispersed phase. The void fraction fluctuations can not be neglected in the continuous phase equations. It is particularly difficult to incorporate higher order correlation terms which arise from the particle-fluid interaction terms, which may account in certain cases (particle Reynolds number $Re_p < 100$) for the suppression of turbulence and in certain cases ($Re_p > 400$) for enhancement of the turbulence of the main stream. As demonstrated by Celik and Gel (1997) the cross-stream distribution of bubble concentration in shear layers is primarily determined by the kinetic energy of the continuous phase. The more advanced Reynolds stress models (see e.g. Bertodano et al., 1990; Simonin et al., 1995) have not proven to be any more successful than the k - ϵ model. These

models involve many more additional equations and ad-hoc assumptions in the presence of the second phase.

LES and DNS Approach

Much of the uncertainties in turbulence modeling can be eliminated if the recently developed Large-eddy simulation (LES) technique (Galperin and Orszag, 1993; Lesieur and Metais, 1996; Karniadakis et al., 1990; Reynolds, 1989; Piomelli et al., 1988) can be extended to two-phase flow with appropriate modifications. LES is a numerical technique in which large-scale energy containing eddies (those responsible for the primary transport) are resolved explicitly and only the small-scale sub-grid motions are modeled. This is not the same as the Direct Numerical Simulations (DNS) which solves the full conservation equations without parameterization and resolves all scales down to the Kolmogorov scales. Consequently it is limited to much lower Reynolds numbers (typically Reynolds numbers less than 10^4) and simple geometries (see e.g. Elgobashi, 1996). For most engineering problems the turbulence Reynolds number is in the order great than 10^4 (easily reaching 10^8 in geophysical flows) which require computations involving more than 10^{12} grid nodes. This is beyond the practical limits of present computer technology. More over it is also extremely difficult to extend the highly accurate schemes such as spectral methods which are necessary for DNS to more complicated geometries. LES technique, on the other hand, solves the unsteady three-dimensional Navier-Stokes equations with an appropriate filtering procedure. The filtered equations involve Reynolds stress type of terms (contributions from the sub-grid scales) which are modeled by relating them to strain rates with an eddy viscosity as the proportionality coefficient. This is referred to as SGS closure model. The eddy viscosity is usually calculated as a function of the mesh size. Hence, the finer the numerical mesh size, the less important is the effect of the smaller scales that are filtered out. The three-dimensional time-dependent details of the largest scales of motion (those responsible for the primary transport) are computed. The size of the scales that need to be resolved determine the numerical mesh size to be used. LES makes extensive use of computational accuracy and computer power rather than solving a large number of empirically modeled equations as is the case for RANS models. In this regard it also requires the use of accurate numerical schemes. In the DNS of dispersed two-phase flows (see e.g. Elgobashi, 1996:

Part 1 & 2; McLaughlin, 1994; Chen and Pereira, 1995; Rouson and Eaton, 1994; Pedinotti et al., 1993), in addition to the Navier-Stokes equations, the instantaneous particle equation is solved in a Lagrangian frame of reference as explained above for the EL approach. Two-way coupling is achieved by adding the momentum source terms in each computational cell as the calculations proceed in time. DNS is the most sophisticated approach to represent the details of two-phase dispersed flows at all scales. However, because of the restrictions cited above the most viable technique for predicting two-phase flow turbulence is probably the LES.

LES has also been applied (Wang and Squires, 1995; Lavieville et al., 1995; Ebert and Dehning, 1992) to two-phase flow turbulence, but in most studies only the continuous phase turbulence is resolved using LES, and almost exclusively the applications are in the area of gas solid flows with the exception of Lapin and Lubbert (1994). The later authors have reported successful results for gas-slurry column reactors. Their approach might be classified as LES but they do not refer to the LES literature. In gas-solid flow applications the particles are treated usually as passive agents (one-way coupling) and their motion is calculated using the BBO equation in which the filtered continuous phase velocity components are used directly. The particle equation of motion is not filtered which is inconsistent with the formulation of the LES equations. If the filtered values are used in the particle equation, the contribution from sub-grid turbulence must be included. The prediction of turbulence augmentation by the presence of dispersed phase (two-way coupling) is not trivial and there remain many issues to be resolved.

Inflow Boundary Conditions

Although advantageous to RANS based turbulence models there are still some unresolved issues in LES applications to turbulent flow simulations. One of the most critical problems is that large eddy simulations of spatially inhomogeneous flows require unsteady turbulent inflow boundary conditions. Especially if high Reynolds number flows exist, the inflow turbulence cannot be ignored and its effects has to be accounted for via methods of generating turbulence with prescribed turbulence intensity at the inflow boundary. Two main groups of approaches in large eddy simulation studies are usually adopted to generate inflow turbulence. The first one is to conduct the auxiliary simulations of turbulent flow fields using the LES approach (e.g. Lund et al., 1998 and Spalart, 1988) and to store the time series of fluctuating

velocity components, which in turn will be reintroduced as inflow boundary conditions of the main simulations. The main disadvantage of this approach is the computational cost which has to be invested. The second group artificially generates time series of random velocity fluctuations by performing an inverse Fourier transform for prescribed spectral densities. The main disadvantage of this method is that the generated velocity field may lack both turbulent structure and non-linear energy transfer. This may be remedied by Celik et al.'s (1999) approach, which suggest a relatively simple random flow generation (RFG) algorithm, which can be used to prescribe inlet conditions for spatially developing inhomogeneous anisotropic turbulent flows.

1.3 Objective and Present Contribution

The objective of this study is to develop theoretical and numerical capabilities and use these to study the physics of bubble dynamics and mixing in three dimensional, turbulent flows encountered in the near wake ($\sim 1-3$ ship lengths) of ships using LES. Our focus will be on prediction of bubble size and concentration variations, modeling of cluster formation mechanisms in vortical structures, including their influence on the turbulence of the carrier liquid. In the first phase of this study the surface waves will be imposed at most as boundary conditions a priori. The phenomenon related to wave breakup, and air entrainment at the free surface by waves will not be considered. The conditions at the inlet data plane will be obtained from other researchers who already have grants from ONR to study ship hydrodynamics. Our theoretical effort will be supplemented by laboratory experiments which will be used for model validation. We shall develop parallel algorithms for high performance computers to be able to compute realistic particle statistics with the goal of at least 10^5 particle trajectories. Our contribution will be in advancement of the LES technique and its application to dispersed two-phase turbulent flows with two-way coupling. This work will be unique in bringing a new formulation regarding the subgrid-scale turbulence which will be based on a one-equation model involving the kinetic energy of small scales. This equation will be modified to account for the suppression and/or enhancement of turbulence by the dispersed phase. A new sub-grid length scale parameterization will also be developed. As such this study will be the first (to the best of our knowledge) attempt to apply the LES technique to bubbly ship wakes.

2 METHODOLOGY

We performed this study utilizing a readily available computer code obtained from Stanford University, with appropriate modifications to make the code suitable for gas-liquid two phase flows. The computer code is based on an essentially non-staggered grid, finite volume method using a fractional time step approach. Non-orthogonal curvilinear coordinates are applied with an overall second order accuracy in both space and time. The Crank-Nicolson discretization scheme has been applied for diagonal viscous and diffusion terms and an explicit Adams-Bashforth scheme is employed for other terms. The central differencing (CD) scheme (with special care due to numerical instabilities) is applied to discretize the convective terms. Detailed information can be found in Shi (2001). It has been modified by our group to run in LES mode with particles on parallel machines (see Yavuz et al., 2004; Shi et al., 2006; Smirnov et al., 2005).

The current solution method is 2nd order accurate both in space and time. Theoretically the higher the order of the numerical scheme, the better the resolution should be under the same grid spacing (Shi, 2001). However, Rai and Moin (1991) have shown that higher order of accuracy combined with coarse grid spacing does not necessarily give better results. Jordan (1999) showed that the results could be improved by improving the grid spacing. The power law scheme is inaccurate under some limitations, in that when convection is dominant; it reduces to 1st order upwind scheme (Patankar, 1980). On the other hand, higher order CD schemes have in addition the problem of artificial high frequency oscillations that may contaminate the turbulence field (Rai and Moin, 1991). In LES, explicit schemes are preferable, but if stability is an issue, some implicitness can be introduced, i.e. Crank-Nicolson time splitting. For information on the LES code, i.e. equations, time advancement and spatial discretization schemes, the fractional step method, poisson solver, etc., the reader is referred to Cehreli (2004) and Shi (2001).

Subgrid-scale closure for two phase bubbly turbulent flows have been considered at various levels, starting from the simplest zero-equation Smagorinsky closure, and extending to 1-equation, hybrid Smagorinsky-turbulent kinetic energy (TKE) closure, and, if necessary, to dynamic SGS eddy viscosity model (for a review see Ferziger, (1993)). The basic Smagorinsky

model and its variants need empirical modifications for wall damping and low turbulence Reynolds numbers (see Reynolds (1989)). The RNG (Yakhot and Orszag, (1989)) method produces a modified form of the Smagorinsky model by an analytical scale elimination method, and it leads to an automatic correction for low turbulence Reynolds numbers. The need for wall damping was satisfied using a van Driest damping function. We conducted a comparative study of various subgrid-scale models and made improvements to better model the dispersed, gas-liquid two phase flows relevant to ship wakes.

2.1 Governing Equations and Navier Stokes solver

The LES code used was originally developed by Zang et al. (1994). The equations for an incompressible, viscous fluid flow in Cartesian (physical) space can be presented in terms of the Cartesian velocities u_j as

$$\frac{\partial u_j}{\partial x_j} = 0 \quad (2.1)$$

$$\frac{\partial u_i}{\partial t} + \frac{\partial(u_i u_j)}{\partial x_j} = -\frac{1}{\rho} \frac{\partial P}{\partial x_i} + \nu \frac{\partial^2 u_i}{\partial x_j^2} + 2\Omega_s \left(u_1 \frac{\partial x_3}{\partial x_i} - u_3 \frac{\partial x_1}{\partial x_i} \right) + \Omega_s^2 x_i (1 - \delta_{i3}) \quad (2.2)$$

An additional equation that represents the conservation of a scalar, such as kinetic energy, temperature, etc. is,

$$\frac{\partial \phi}{\partial t} + \frac{\partial(\phi u_j)}{\partial x_j} = \alpha \frac{\partial^2 \phi}{\partial x_j^2} + S_i(\phi) \quad (2.3)$$

where α is a material coefficient that could be thermal diffusivity, conductivity or viscosity, depending on which scalar equation is solved. $S_i(\phi)$ is a sink/source term. In the above equations, u_j is the Cartesian velocity vector, P is the total pressure, and i, j, k , are the notations that represent the directions; x_1 is the axial coordinate, x_2 is the vertical coordinate, and x_3 is the transverse coordinate in the Cartesian coordinate system. Ω_s is the angular velocity of the system rotation due to the turning of the ship, ν is the kinematic viscosity and δ_{ij} is the Kronecker delta symbol. In Eqn. 2.2, third term in the right hand side (RHS) represents the Coriolis force and the fourth term represents the Centrifugal force due to the turning of the ship.

It should be noted that Einstein summation rule applies to repeated indices except for the term, $\Omega_s^2 x_i (1 - \delta_{i3})$.

The Navier Stokes equations have been developed for a general purpose model of fluid flow from basic principles of conservation of mass and momentum for a Newtonian fluid. Moreover, the numerical models, such as finite volume method (Ferziger and Peric, 1997) also incorporate the law of conservation of mass and momentum for space integration.

The filtering process plays an important role in distinguishing small scales and large scales in LES. A flow variable, f can be decomposed into a large scale of the flow field component that is resolved, \bar{f} and a small scale component that is filtered out, f' , as,

$$f = \bar{f} + f' \quad (2.4)$$

Then the resolved scale field is obtained by applying spatial filtering that can be generally expressed by the convolution integral (Leonard, 1974) for the calculation domain, D , as,

$$\bar{f}(x_1 x_2 x_3) = \int_D \prod_{j=1}^3 G_j(x_j, x'_j : \bar{\Delta}) f(x'_1 x'_2 x'_3) dx'_1 dx'_2 dx'_3 \quad (2.5)$$

where G is the filter function and $\bar{\Delta}$ is the filter width, i.e. the wavelength of the smallest scale retained by the filtering function. The most commonly used filter functions are the box filter, the sharp Fourier cutoff filter and Gaussian filter (best defined in wave space), and the top hat filter (in real space) (Piomelli, 1999). In the present finite volume formulation, a volume average box filter used by Deardoff (1970), is used, in which $G_j=1$ (Zang et al., 1993).

Applying the filtering operator to the governing equations and following the formulation of Zang et al. (1993) in a conservative manner, the spatially filtered flow conservation equations can be written as,

$$\frac{\partial \bar{u}_j}{\partial x_j} = 0 \quad (2.6)$$

$$\frac{\partial \bar{u}_i}{\partial t} + \frac{\partial \bar{F}_{ij}}{\partial x_j} = \bar{S}_i \quad (2.7)$$

$$\frac{\partial \bar{\phi}}{\partial t} + \frac{\partial \bar{R}_j}{\partial x_j} = \bar{S}_i(\phi) \quad (2.8)$$

where

$$\bar{F}_{ij} = \bar{u}_i \bar{u}_j + \bar{p} \delta_{ij} - \nu \frac{\partial \bar{u}_i}{\partial x_j} + \tau_{ij} \quad (2.9)$$

$$\bar{S}_i = 2\Omega_s \left(\bar{u}_1 \frac{\partial x_3}{\partial x_i} - \bar{u}_3 \frac{\partial x_1}{\partial x_i} \right) \quad (2.10)$$

$$\bar{R}_j = \bar{u}_j \bar{\phi} - \alpha \frac{\partial \bar{\phi}}{\partial x_j} + \chi_j \quad (2.11)$$

Here, both, the SGS stress, τ_{ij} and the SGS flux, χ_j represent the effect of the SGS motion. They arise due to the filtering of the nonlinear advective terms. The formulations are,

$$\tau_{ij} = \overline{u_i u_j} - \bar{u}_i \bar{u}_j \quad (2.12)$$

$$\chi_j = \overline{u_j \phi} - \bar{u}_j \bar{\phi} \quad (2.13)$$

Hence, the SGS stress and the SGS flux both contain the interaction of subgrid scales with themselves and with the resolved scales. In the above equations, \bar{u}_j is the filtered velocity vector and p is the reduced dynamic pressure in which the total pressure, P , is calculated as;

$$P = \rho_o p + \frac{1}{2} \rho_o \Omega_s^2 r^2 \quad (2.14)$$

where r^2 is the square of the distance to the rotation axis, in terms of both the axial and the transverse directions, i.e. $r^2 (= x_1^2 + x_3^2)$ and ρ_o is the reference density. It should be noted that the non-inertial effects are split with Coriolis terms appearing as a source term in Equation 2.7 and since the centrifugal force term is independent of the fluid motion, the effect of centrifugal force is included in the total pressure term, i.e. Equation 2.14.

Since the discrete solution represents the resolved field which is topped by an overbar computed, thus the stress and the flux terms should be modeled using the resolved quantities. Most SGS models for τ_{ij} and χ_j are eddy viscosity models of the form:

$$\tau_{ij} - \frac{\delta_{ij}}{3} \tau_{kk} = -2\nu_t \bar{S}_{ij} + C_r \left(L_{ij}^m - \frac{\delta_{ij}}{3} L_{kk}^m \right) \quad (2.15)$$

$$\chi_j = -\alpha_t \frac{\partial \bar{\phi}}{\partial x_j} + C_r P_j \quad (2.16)$$

where ν_t is the turbulent eddy viscosity, it represents the effects of sub grid turbulence; in our case, α_t is the turbulence diffusivity and \bar{S}_{ij} is the large scale (resolved) strain rate tensor, defined as,

$$\bar{S}_{ij} = \frac{1}{2} \left(\frac{\partial \bar{u}_i}{\partial x_j} + \frac{\partial \bar{u}_j}{\partial x_i} \right) \quad (2.17)$$

Eq. 2.15 and 2.16 introduces two sets of additional terms to the filtered governing equations: C_r and L_{ij}^m ; C_r and P_j . L_{ij}^m , the modified Leonard term and P_j are defined by,

$$L_{ij}^m = \overline{\bar{u}_i \bar{u}_j} - \overline{\bar{u}_i} \overline{\bar{u}_j} \quad (2.18)$$

$$P_j = \overline{\bar{u}_i \bar{\phi}} - \overline{\bar{u}_i} \overline{\bar{\phi}} \quad (2.19)$$

The modified Leonard term or P_j represent the interactions between resolved scales that result in sub-grid scale contributions and can be computed directly from the resolved flow field (Piomelli, 1999). The value of the scale similarity coefficient, C_r in Eqn. 2.15 is either 0 or 1 or may be determined dynamically depending on the type of sub-grid scale (SGS) model being used. When $C_r = 0$, Eqn. 2.15 represents the Smagorinsky model. When $C_r = 1$, it represents the dynamic mixed model of Zang et al. (1993).

To tackle problems of complex geometries, the above mentioned equations are transformed from the physical to computational space and formulated for a generalized curvilinear coordinate system. The solution of numerical problems in complex domains using boundary-fitted curvilinear coordinates is now a typical technique. The physical space is denoted

by coordinates (x_1, x_2, x_3) and the computational space by (ξ_1, ξ_2, ξ_3) . The chain rule of derivatives has been applied.

$$\frac{\partial}{\partial x_j} = \frac{\partial \xi_z}{\partial x_j} \frac{\partial}{\partial \xi_z} \quad (2.20)$$

In order to use the finite volume discretization, it is desirable to cast the equations in the “Strong-Conservation-Law Form” as explained briefly in Zang et al. (1994).

Substituting Eqn. 2.15 into Eqn. 2.7, and applying coordinate transformation and combining terms accordingly, Eqs. 2.6, 2.7 and 2.8 in time-dependent boundary-fitted curvilinear coordinates are,

$$\frac{\partial \bar{U}_m}{\partial \xi_m} = 0 \quad (2.21)$$

$$\frac{\partial (J^{-1} \bar{u}_i)}{\partial t} + \frac{\partial \bar{F}_{im}}{\partial \xi_m} = \bar{S}_i \quad (2.22)$$

$$\frac{\partial (J^{-1} \bar{\phi})}{\partial t} + \frac{\partial \bar{R}_m}{\partial \xi_m} = \bar{S}_{Ti}(\phi) \quad (2.23)$$

where

$$\bar{F}_{im} = \bar{U}_m \bar{u}_i + J^{-1} \frac{\partial \xi_m}{\partial x_i} \bar{p} - (\nu + \nu_T) G^{mn} \frac{\partial \bar{u}_i}{\partial \xi_n} \quad (2.24)$$

$$\begin{aligned} \bar{S}_i = & 2J^{-1} \Omega_s \frac{\partial \xi_m}{\partial x_i} \left(\bar{u}_1 \frac{\partial x_3}{\partial \xi_m} - \bar{u}_3 \frac{\partial x_1}{\partial \xi_m} \right) + \\ & J^{-1} \frac{\partial \xi_m}{\partial x_j} \frac{\partial \xi_n}{\partial x_i} \frac{\partial \nu_T}{\partial \xi_m} \frac{\partial \bar{u}_j}{\partial \xi_n} - C_r \frac{\partial}{\partial \xi_m} \left(J^{-1} \frac{\partial \xi_m}{\partial x_j} L_{ij}^m \right) \end{aligned} \quad (2.25)$$

$$\bar{R}_m = \bar{U}_m \bar{\phi} - (\alpha + \alpha_T) G^{mn} \frac{\partial \bar{\phi}}{\partial \xi_n} \quad (2.26)$$

$$\bar{S}_{Ti}(\phi) = \bar{S}'_i(\phi) - C_r \frac{\partial}{\partial \xi_m} \left(J^{-1} \frac{\partial \xi_m}{\partial x_j} P_j \right) \quad (2.27)$$

where for the curvilinear space variables; the inverse Jacobian, defined as $J^{-1} = \det \left| \frac{\partial x_i}{\partial \xi_m} \right|$; the contravariant velocity, $\bar{U}_m = J^{-1} \frac{\partial \xi_m}{\partial x_j} \bar{u}_j$; the contravariant volume metrics, G^{mn} , that measures the skewness of a grid cell, is defined as $G^{mn} = J^{-1} \frac{\partial \xi_m}{\partial x_j} \frac{\partial \xi_n}{\partial x_j}$. $\bar{S}'_i(\phi)$, the transformation of $\bar{S}_i(\phi)$ to the computational domain, must be changed accordingly, depending on which scalar equation is solved.

If the flux terms $\partial \bar{F}_{im} / \partial \xi_m$ and $\partial \bar{R}_m / \partial \xi_m$ are split like in Zang (1993) as,

$$\frac{\partial \bar{F}_{im}}{\partial \xi_m} = -[C_i + B_i(p) + D_E(u_i) + D_I(u_i)] \quad (2.28)$$

$$\frac{\partial \bar{R}_m}{\partial \xi_m} = -[E_\rho + F_E(\rho) + F_I(\rho)] \quad (2.29)$$

where C_i and E_ρ represent the convective terms, B_i is the discrete operator for the pressure gradient term, D_E and D_I (F_E and F_I) are discrete operators for the explicitly treated off diagonal terms and the implicitly treated diagonal viscous (diffusive) terms.

2.2 Numerical Method

The computer code is based on an essentially non-staggered grid, finite volume method using a fractional time step approach. A staggered grid method in curvilinear coordinates requires a large amount of computer memory for the metrics (Zang et al., 1993), hence the non-staggered method originally developed by Rhie and Chow (1983) has been used to avoid these kind of difficulties. Cartesian variables such as velocity and pressure are stored at cell centers whereas the contravariant volume fluxes are defined at cell faces in a manner analogous to the staggered-mesh system. The volume fluxes are not solution variables, but rather are determined through interpolation of the cell-centered velocity values plus a projection operation that guarantees exact conservation of mass. A traditional non staggered method does not enforce

mass conservation in the cell and causes the pressure field to decouple (it produces spurious oscillations in the pressure field, i.e. “checkerboard” pattern) (Zang et al. 1994), whereas the method of Rhie and Chow (1983) prevents the decoupling in its structure by defining the volume flux on its corresponding face of the cell in addition to the Cartesian velocity components at the cell center, therefore the momentum and continuity are both enforced in the same control volume and the solutions are free from spurious pressure oscillations. It is directly applicable to curved domains, as the accuracy of the method is not affected by grid orientations because of the non-staggered grid layout. However, this process eliminates odd-even decoupling at the cost of introducing implicit 4th order dissipation, which in turn may affect mass conservation (Paterson, 2003).

Non-orthogonal curvilinear coordinates are applied with an overall second order accuracy in both space and time. The Crank-Nicolson discretization scheme has been applied for diagonal viscous (D_I) and diffusion (F_I) terms in order to remove the viscous instability (Zang et al., 1994) while an explicit Adams-Bashforth scheme is employed for all the other terms. The off diagonal viscous terms (D_E) are treated explicitly in order to simplify the LHS matrix of the momentum equation. The result, Zang (1993), is

$$\frac{\delta \bar{U}_m}{\delta \xi_m} = 0 \quad (2.30)$$

$$\begin{aligned} J^{-1} \frac{(\bar{u}_i^{n+1} - \bar{u}_i^n)}{\Delta t} = & \frac{3}{2} \left[C_i^n + D_E(\bar{u}_i^n) + \bar{S}_i^n \right] - \frac{1}{2} \left[C_i^{n-1} + D_E(\bar{u}_i^{n-1}) + \bar{S}_i^{n-1} \right] \\ & + B_i(\bar{p}^{n+1}) + \frac{1}{2} \left[D_I(\bar{u}_i^{n+1} + \bar{u}_i^n) \right] \end{aligned} \quad (2.31)$$

$$\begin{aligned} J^{-1} \frac{(\bar{\rho}_i^{n+1} - \bar{\rho}_i^n)}{\Delta t} = & \frac{3}{2} \left[E_\rho^n + F_E(\bar{\rho}^n) + \bar{S}_\rho^n \right] - \frac{1}{2} \left[E_\rho^{n-1} + F_E(\bar{\rho}^{n-1}) + \bar{S}_\rho^{n-1} \right] \\ & + \frac{1}{2} \left[F_I(\bar{\rho}_i^{n+1} + \bar{\rho}_i^n) \right] \end{aligned} \quad (2.32)$$

where $\delta/\delta \xi_m$ represents discrete finite difference operators in the computational space, superscripts represent the time step, C_i represents the convective terms, B_i represents the discrete operator for the pressure gradient terms.

The central differencing (CD) scheme (with special care due to numerical instabilities) or Quadratic Upstream Interpolation for Convective Kinematics (QUICK) that calculates the face value from the nodal values using a quadratic upwind interpolation is applied to discretize the convective terms (C_i). The accuracy of QUICK has been compared to CD, the 1st order upwind scheme, a hybrid scheme, with the result obtained that QUICK produced good results (Zang, Hayasa, 1999). The spatial derivatives are computed by 2nd order central differences in the momentum equations. Only the convective term in the scalar equation (E_p) is discretized using the SHARP scheme (Leonard, 1988) since it is computationally more expensive than QUICK.

Because there is no explicit equation to solve for the pressure in time, the fractional step method is applied to solve the incompressible Navier-Stokes equation. The fractional step approach (Kim and Moin, 1985) or projection method, basically a three step predictor corrector method, splits the numerical operators and achieves velocity–pressure decoupling. The intermediate velocities are interpolated onto the faces of the control volume to form the source terms of the pressure Poisson equation. The pressure field is obtained by solving the pressure Poisson equation iteratively with a multigrid method (Brandt, 1977). The true velocity field is then obtained by correcting the predicted velocity with pressure. The steps are summarized from Zang (1993) as,

1. Predictor step:

$$(I - \frac{\Delta t}{2J^{-1}} D_I)(u_i^* - \bar{u}_i^n) = \frac{\Delta t}{J^{-1}} \left\{ \frac{3}{2} [C_i^n + D_E(\bar{u}_i^n) + \bar{S}_i^n] - \frac{1}{2} [C_i^{n-1} + D_E(\bar{u}_i^{n-1}) + \bar{S}_i^{n-1}] + D_I(\bar{u}_i^n) \right\} \quad (2.33)$$

2. Computing the pressure field, i.e. finding ϕ ;

If the corrector step of the fractional step method (Equation 2.37) to the Cartesian velocity components defined on a certain face of the control volume,

$$\bar{u}_i^{n+1} = u_i^* - \Delta t \left(\frac{\delta \xi_m}{\delta x_i} \frac{\delta \phi^{n+1}}{\delta \xi_m} \right) \quad (2.34)$$

Combining $\bar{U}_m = J^{-1} \frac{\partial \xi_m}{\partial x_j} \bar{u}_j$ with Equation 2.34, the equations for \bar{U}_m^{n+1} ,

$$\bar{U}_m^{n+1} = U_m^* - \Delta t \left(G^{mn} \frac{\delta \phi^{n+1}}{\delta \xi_m} \right) \quad (2.35)$$

where $U_m^* = J^{-1} \frac{\delta \xi_m}{\delta x_j} u_j^*$ is called the intermediate volume flux. Since the intermediate velocity

u_j^* is defined at the cell center, while the fluxes U_m^* and \bar{U}_m^{n+1} are defined on the cell faces, u_j^* has to be interpolated onto the cell faces in order to compute U_m^* .

By substituting Equation 2.35 into Equation 2.30, the pressure passion equation for ϕ^{n+1} is obtained as,

$$\frac{\delta}{\delta \xi_m} \left(G^{mn} \frac{\delta \phi^{n+1}}{\delta \xi_m} \right) = \frac{1}{\Delta t} \left(\frac{\delta U_m^*}{\delta \xi_m} \right) \quad (2.36)$$

3. Corrector step:

$$\bar{u}_i^{n+1} - u_i^* = \frac{\Delta t}{J^{-1}} \left[B_i(\phi^{n+1}) \right] \quad (2.37)$$

where I is the identity matrix, u_i^* is the intermediate velocity and the scalar ϕ is related to the pressure \bar{p} by

$$B_i(\bar{p}) = \left(J^{-1} - \frac{\Delta t}{2} D_i \right) \left(\frac{B_i(\phi)}{J^{-1}} \right) \quad (2.38)$$

Detailed information can be found in Zang (1993).

2.3 Sub-grid Scale Models

SGS stresses that are modeled (see Eqn. 2.15) represent the effects of the sub-grid scale motion on the resolved motion in that they dissipate the resolved energy or backscatter energy to

the resolved eddies. To predict the flow dynamics of the wake behind a turning ship, the standard Smagorinsky model (Smagorinsky, 1963), based on Boussinesq eddy viscosity hypothesis, has been used. This model is developed by assuming that the small scales are in equilibrium so that energy production and dissipation are in balance, moreover the small scales dissipate all the energy they receive from the resolved scales. This assumption is made to simplify the phenomena and the algebraic model for the eddy viscosity is,

$$\nu_t = C_s \Delta^2 (\bar{S}_{ij} \bar{S}_{ij})^{1/2} \quad (2.39)$$

where the filter length scale, Δ is the volume average box filter used by Deardoff (1970) usually calculated as the geometric average of mesh spacings in the Cartesian directions, defined as $\Delta = (\Delta x_1 \Delta x_2 \Delta x_3)^{1/3}$ in finite volume formulations (especially for anisotropic grids) and C_s is the Smagorinsky constant. This constant is determined from the isotropic turbulence decay. It is interesting to note that the filtering process that's applied through control volume approach may use a significantly different length scales in different directions due to grid stretching. To see the influence of grid aspect ratio on filtering process, a model equation is used and different filter lengths have been applied (Cehreli, 2004). The results showed that the grid size in each direction influences mostly the degree of filtering in that direction; the influence on the other direction is much lesser.

3 THE RFG METHOD

In a Reynolds Averaged Navier-Stokes (RANS) turbulence modeling approach information about turbulent fluctuations is contained in the time averaged Reynolds stresses of the form $\overline{u_i u_j}$. These are obtained as an outcome of a turbulence model that links Reynolds Stresses to mean flow quantities (e.g. k - ε model), or solves modeled transport equations for each Reynolds stress component (e.g. Reynolds Stress models). However, this is not the case when the large eddy simulation (LES) methodology is employed since the goal here is to explicitly resolve the turbulent fluctuations. In LES the inlet conditions can not be derived directly from experimental results, because of the unsteady and pseudo-random nature of the flow being resolved, unless, off course, the turbulent intensity is zero at the inlet, which is rarely the case. This problem becomes more important for spatially developing turbulent flows where for example the boundary or shear layer thickness changes rapidly. In such cases periodic boundary conditions can not be specified like in the case of a fully developed channel flow (Ravikanth and Pletcher, 2000; Akselvoll and Moin, 1995). A similar situation exists when prescribing the initial conditions over the whole calculation domain. This can be of importance when the turbulent flow is not steady in the mean (i.e. non-stationary turbulence) and the transients of the flow are to be resolved. Even for stationary turbulent flows, if realistic initial conditions are not prescribed, the establishment of a fully developed turbulence takes unreasonably long execution time. For these reasons it is necessary to initialize the flow-field with some form of perturbation to provide the initial turbulent conditions. It is important that the perturbation be spatially correlated, as is the case with the real flow. For external flow problems the turbulent flow field can be initiated simply by appropriately perturbing the inlet flow-field. In this case an accurate representation of temporal correlations of the flow-field can be important. The inlet perturbation propagates throughout the domain and helps trigger the turbulence that is to be captured. Many applications of LES begin with initializing the flow field to that of a previously obtained RANS solution. A higher resolution grid is then used with an appropriate sub-grid-scale model. The Reynolds stress terms provided by the RANS solution can be used to construct spatially and temporally correlated perturbed inlet and initial conditions. In principle it is possible to predict turbulence via LES technique by starting from a quiescent flow or with the

mean flow obtained from RANS. Unfortunately, it takes a very long time for a turbulent flow to develop spatially and temporally. This is especially true in the case of decaying turbulence in the absence of strong turbulence generating factors like walls. A reasonably accurate approach to this problem is used in modeling of boundary layer turbulence (Lund, 1998). It consists in applying a separate flow solver with periodic boundary conditions to construct the inlet conditions for the LES/DNS solver. It provides well-formed inflow conditions consistent with the solution of the Navier-Stokes equation, which makes it particularly suitable for DNS. However, its implementation may not be straightforward for the problems without well defined fully developed boundary/shear layers. For some engineering problems it may also be too expensive in the usage of computer resources and programming effort.

To remedy this problem the inlet and initial conditions are often viewed as consisting of a mean component and a randomly fluctuating component with the appropriate statistics. Most of the work done in this direction is based on simplified variants of a spectral method, in which Fourier harmonics are generated with the appropriate statistics and assembled into a random flow-field. Realistic turbulence spectra can be realized in this way. In the work of Lee et al. (1992) for example, a very good representation of turbulence spectra was achieved by using Fourier harmonics with a random phase shift. This is a rather efficient method to generate the inflow turbulence with pre-defined characteristics. However, it does not satisfy the continuity of the flow-field, which may be important in diminishing the non-physical transition region between the inlet flow-field and the solution provided by the Navier-Stokes solver inside the computational domain.

A considerable amount of work in random flow generation has been performed in the area of particle dispersion modeling using the RANS approach (Zhou and Leschziner, 1991; Zhou and Leschziner, 1996; Li et al., 1994). RANS modeling produces smooth flow fields, which do not accurately disperse particles that are embedded in the flow. To correct this turbulent Reynolds stresses are used to generate temporally and spatially correlated fluctuations, such that the resultant instantaneous velocity can be superimposed on the particles to induce a realistic dispersion. A number of approaches found in the literature (Li et al., 1994; Bechara et al., 1994; Fung et al., 1992) are based on a variant of spectral method of generating an isotropic continuous flow-field proposed earlier by Kraichnan (1970). However, this flow-field does not satisfy the requirement of spatial inhomogeneity and anisotropy of turbulent shear stresses,

which may be important in realistic flows. The method of Zhou and Leschziner (1991) complies with the latter requirement, but the resultant flow field does not satisfy the continuity condition and is spatially uncorrelated. For homogeneous isotropic turbulence, the initial conditions can also be constructed as described by Ferziger (1983). The approach is based on a vector curl operation and forward/backward Fourier transforms, which require a considerable computational effort. The extension of this method to anisotropic inhomogeneous flows is not trivial. At least one study presents a successful application of Kraichnan's method to anisotropic flows (Maxey, 1987). The technique is based on filtering and scaling operations applied to the generated isotropic flow-field to filter only the vectors with the prescribed correlations. Again, the filtering operation may be expensive computationally. The method presented in this paper is different in that it is based only on scaling and simple coordinate transformation operations, which are efficient and fast.

It is the objective of this study to formulate a relatively simple random flow generation (RFG) algorithm, which can be used to prescribe inlet conditions as well as initial conditions for spatially developing inhomogeneous, anisotropic turbulent flows. In principle the same procedure can also be used for initializing direct numerical simulations, but the focus of our study is on LES, and particle tracking applications. The method takes advantage of the previous studies in the area of particle dispersion (Li et al., 1994; Maxey, 1987). The RFG procedure is developed on the basis of the work of Kraichnan (1970), and can be used as an efficient random flow-field generator in LES and in particle tracking (Shi et al., 2000; Smirnov et al., 2000). The technique was validated on the cases of boundary-layer and flat-plate shear layer flows and is further illustrated on the example of bubbly ship-wake flow as one of the most challenging cases for LES and particle dynamics applications. Performing LES of ship wakes is particularly difficult given the fact that the whole ship must be modeled to capture a relatively thin 3D-boundary layer, preferably including the viscous sub-layer. The boundary layer is the source of the flow dynamics that sets the initial conditions for the wake. A simulation that includes the whole ship and the wake would require prohibitively large computational resources. The needed computational resources could be substantially reduced if the appropriate time-dependent inlet conditions could be constructed at the beginning of the wake, thus avoiding the need to model the entire ship.

3.1 Formulation

To generate a realistic flow field we propose a modified version of Kraichnan's technique (Kraichnan, 1970). The procedure we call RFG (Random Flow Generation) combines the advantages of the approaches mentioned above and is also computationally efficient. It involves scaling and orthogonal transformation operations applied to a continuous flow-field generated as a superposition of harmonic functions. The procedure consists of the following steps.

Given an anisotropic velocity correlation tensor

$$r_{ij} \equiv \overline{\tilde{u}_i \tilde{u}_j} \quad (3.1)$$

of a turbulent flow field $\{\tilde{u}_i(x_j, t)\}_{i,j=1..3}$, find an orthogonal transformation tensor a_{ij} that would diagonalize r_{ij}^{-1} .

$$a_{mi} a_{nj} r_{ij} = \delta_{mn} c_{(n)}^2 \quad (3.2)$$

$$a_{ik} a_{kj} = \delta_{ij} \quad (3.3)$$

As a result of this step both a_{ij} and c_n become known functions of space. Coefficients $c_n = \{c_1, c_2, c_3\}$ play the role of turbulent fluctuating velocities (u' , v' , w') in the new coordinate system produced by transformation tensor a_{ij} . The new algorithm is as follows:

Step (i): Generate a transient flow-field in a three-dimensional domain $\{v_i(x_j, t)\}_{i,j=1..3}$ using the modified method of Kraichnan (1970)

$$v_i(\vec{x}, t) = \sqrt{\frac{2}{N}} \sum_{n=1}^N [p_i^n \cos(\tilde{k}_j^n \tilde{x}_j + \omega_n \tilde{t}) + q_i^n \sin(\tilde{k}_j^n \tilde{x}_j + \omega_n \tilde{t})] \quad (3.4)$$

$$\tilde{x}_j = \frac{x_j}{l}, \quad \tilde{t} = \frac{t}{\tau}, \quad c = \frac{l}{\tau}, \quad \tilde{k}_j^n = k_j^n \frac{c}{c_{(j)}} \quad (3.5)$$

$$p_i^n = \varepsilon_{ijm} \zeta_j^n k_m^n, \quad q_i^n = \varepsilon_{ijm} \xi_j^n k_m^n \quad (3.6)$$

$$\zeta_i^n, \xi_i^n, \omega_n \in N(0, 1), \quad k_i^n \in N(0, 1/2)$$

where l, τ are the length and time-scales of turbulence, ε_{ijk} is the permutation tensor used in vector product operation (Spain, 1965), and $N(M, \sigma)$ is a normal distribution with mean M

¹ $f_{,i} \equiv \frac{\partial f}{\partial x_i}$. Repeated sub-indexes imply summation, parentheses around indexes preclude summation.

and standard deviation σ . Numbers k_j^n, ω_n represent a sample of n wave-number vectors and frequencies of the modeled turbulence spectrum

$$E(k) = 16\left(\frac{2}{\pi}\right)^{1/2} k^4 \exp(-2k^2) \quad (3.7)$$

Step (ii): Apply a scaling and orthogonal transformations to the flow-field v_i generated in the previous step to obtain a new flow-field u_i

$$w_i = c_{(i)} v_{(i)} \quad (3.8)$$

$$u_i = a_{ik} w_k \quad (3.9)$$

The procedure above takes as input the correlation tensor of the original flow-field r_{ij} and information on length- and time-scales of turbulence (l, τ) . These quantities can be obtained from a steady-state RANS computations or experimental data. The outcome of the procedure is a time-dependent flow-field $u_i(x_j, t)$ with correlation functions $\overline{u_i u_j}$ equal to r_{ij} and turbulent length/time scales equal to l, τ . As will be shown later this flow-field is also divergence free for a homogeneous turbulence and to a high-degree divergence-free for an inhomogeneous turbulence. By virtue of Eq. (3.4), spatial and temporal variations of u_i follow Gaussian distribution with characteristic length and time-scales of l, τ . Sampling for a different spectrum instead of Gaussian can also be used in different problems.

Equation (3.8), provides the scaling, and (3.9) - the orthogonal transformation. Scaling factors c_i obtained in step 2 represent the scales of turbulent fluctuations along each axis. They do not depend on time, whereas vectors v_i and w_i represent time-dependent velocity fluctuations. Both the scaling factors c_i and the transformation tensor a_{ij} are computed in step 2 using efficient matrix diagonalization routines that can be found in standard libraries or programmed specifically for a 3D case to boost the performance. By construction, the correlation tensor of the flow-field produced by Eq. (3.4) is diagonal

$$\overline{v_i v_j} = \delta_{ij} \quad (3.10)$$

The flow-field w_i produced after the scaling transformation (3.8) is divergence free for a homogeneous turbulence and nearly divergence free for an inhomogeneous turbulence, as is shown by the following estimate

$$\begin{aligned}
w_{i,j} &= c_{i,j} v_i + c_i v_{i,j} \approx c_i v_{i,j} = \\
&= \frac{c}{l} \sqrt{\frac{2}{N}} \sum_{n=1}^N [-p_i^n k_j^n \sin(\frac{c}{c_j} k_j^n \frac{x_j}{l} + \omega_n \frac{t}{\tau}) + q_i^n k_j^n \cos(\frac{c}{c_j} k_j^n \frac{x_j}{l} + \omega_n \frac{t}{\tau})] = 0 \quad (3.11)
\end{aligned}$$

$$\Rightarrow w_{i,j} \approx 0 \quad (3.12)$$

where we neglected all derivatives of c_i , which are slowly varying functions of \vec{x} , and used the relation of orthogonality between k_i^n and p_i^n, q_i^n

$$k_i^n p_i^n = k_i^n q_i^n = 0$$

which follows from the way vectors p_i^n, q_i^n are constructed in (3.6). For a homogeneous turbulence the approximate equality in (3.11) will become a strict equality, leading to a divergence free flow-field. In the case of inhomogeneous turbulence the justification for neglecting the derivatives of c_i comes from the fact that c_i are derived from the correlation tensor r_{ij} , which is produced by the time-averaging operation in (3.1). As a result of this averaging r_{ij} is independent of time and may be a slowly varying function of space as compared to the fluctuating velocity u_i

$$\|c_{i,j}\| \approx \|r_{ij,k}\|^{1/2} \ll \|u_{i,j}\| \quad (3.13)$$

where $\|\cdot\|$ denotes an appropriate function norm. Relation (3.13) justifies the first approximate equality in (3.11), leading to an approximate satisfaction of continuity.

The orthogonal transformation (9) preserves the solenoidal (divergence-free) property of the flow-field

$$u_{i,j} = a_{ij} a_{ki} w_{j,k} = \delta_{jk} w_{j,k} = w_{j,j} = 0 \quad (3.14)$$

where we used relation (3.12) and the rule of transformation of derivatives: $f'_{,i} = a_{ji} f_{,j}$.

Thus, the generated flow-field u_i is divergence-free within the accuracy determined by (3.13).

At the same time the new flow field satisfies the anisotropy of the original flow-field $\bar{u}(\vec{x}, t)$, i.e.

$$\begin{aligned}
\overline{u_i u_j} &= \overline{a_{im} w_m a_{jn} w_n} = \\
&= a_{im} a_{jn} \overline{w_m w_n} = a_{im} a_{jn} c_m c_n \overline{v_m v_n} = \\
&= a_{im} a_{jn} c_m c_n \delta_{mn} = a_{im} a_{jn} \delta_{mn} (c_n)^2 = r_{ij} \quad (3.15)
\end{aligned}$$

Where we used relations (3.3), (3.8) and the last equality was obtained by solving (3.2) for r_{ij} . Thus, the obtained flow-field $u_i(\bar{x}, t)$ is transient, divergence-free, inhomogeneous, and anisotropic with the pre-defined correlation coefficients.

Considering the flexibility and computational efficiency of the algorithm, we should note that the random spectrum sampling in Eq. (3.6) can be performed separately from the actual assembly of the vectors in Eq. (3.4). This leads to a higher computational efficiency, since the spectrum sampling can be done outside of the main time iteration loop of the flow solver with only the assembly of fluctuating velocity components left inside the time loop. This efficiency comes at a price of extra memory requirements for storing the random sample. The size of this sample is equal to $10 \cdot N$, where N is the number of harmonic functions representing the turbulent spectrum in (3.4), which is independent of the actual grid size. So, for $N = 1000$ and double precision arithmetics only 80 KB of computer memory will be needed to store the spectrum for any grid size. This offers a flexibility of shifting the priorities between the high-accuracy spectrum generation and speed.

The RFG procedure can be extended to include the anisotropy of turbulence length-scale. In this case instead of using a scalar value for l in (3.5) one can define a vector l_i . An appropriate re-scaling would be necessary to preserve the continuity of the flow-field. This can be done by introducing another scaling transformation, similar to (3.8), which will guarantee that the resultant flow-field is divergence-free.

It should be noted that the turbulent flow-field obtained by the RFG procedure does not represent the solution of a complete Navier-Stokes (NS) equation, but rather of a continuity equation only. This is not a severe limitation, since the procedure is used mainly in the context of unsteady 3D computations, like LES, to generate initial or inlet boundary conditions. These conditions are given on three-dimensional subsets of a four-dimensional computational domain: two space and one time dimension for the inlet flow-field and three space and zero time dimensions for the initial flow-field. As such these flow-fields do not have to satisfy the NS equation, since for an unsteady LES this equation is defined on a four-dimensional, 3-space \times 1-time domain. However, the boundary conditions should be reasonably continuous, so that the NS solver will gracefully adjust the solution to the boundary conditions within the computational domain. This is exactly what the RFG procedure is designed to do. In addition to this it provides

the desired statistical characteristics of turbulence at the boundaries, like anisotropy and inhomogeneity, which is of importance for LES and unsteady particle-dynamics computations.

Naturally, this approach to generate the inlet/initial boundary conditions is an approximation and should be used only when the statistical features of turbulence at the boundaries are of special concern while the solution of a full unsteady NS equation beyond the given boundaries is a practical impossibility.

3.2 Validation of RFG Procedure

The first test of the procedure was for a homogeneous isotropic flow field. The Fourier space was sampled with 1000 wave-numbers selected according to Eq. (3.4). Figures 3.1(a), 3.1(b) shows the snapshot of a homogeneous isotropic velocity field. Fig. 3.1(a) shows the vorticity field in a cross-section of the computational domain, and in Fig. 3.1(b) the velocity distribution is presented. Statistical post-processing of velocity correlations was applied to the generated flow-field in order to verify that the velocity field was isotropic. For this purpose a turbulent flow-field with the characteristic time scale of 10^{-3} s was generated from the Fourier spectral sample of 1000 wave-vectors (Eq. 3.4). The fluctuating velocities were sampled at the rate of 10^5 Hz. Correlations of the fluctuating velocity components were computed at one point in space by averaging over time. Fig. 3.4 shows the behavior of the velocity correlations as a function of the averaging time-interval. The figure indicates convergence to the values corresponding to Eq. (3.10).

The procedure was next applied to a homogeneous anisotropic flow field with c_i selected from typical boundary layer distributions. This type of anisotropy leads to higher amplitudes of the velocity vectors in one direction relative to the other (Fig. 3.1(c)). The procedure was also used to generate the flow-field with anisotropic length-scales (see comments in Sec. 3.1). In this case the length-scale of fluctuations was selected differently in different spatial directions. This produced a flow-field where the structure of the velocity fluctuations seemed stretched in one direction (Fig. 3.1(d)).

Next we applied the procedure to the case of a non-homogeneous anisotropic boundary layer. Figure 3.1(e) shows a snapshot of the velocity magnitude in the three-dimensional boundary layer. An additional empirical factor related to the boundary-layer thickness was

introduced in this case to better account for the intermittency effects. Figure 3.2 shows the random signal produced by the RFG procedure sampled at different locations above the boundary plane. As can be seen from that figure both anisotropy and inhomogeneity are evident in the fluctuating components. Experimental and direct numerical simulation (DNS) data do exist for this flow field, providing both mean and fluctuating velocity profiles, as well as turbulent correlations. The turbulent boundary layer is two-dimensional in the mean, though turbulent fluctuations exist in all three dimensions, i.e. $c_1 = u'$, $c_2 = v'$, and $c_3 = w'$ for the axial, vertical, and tangential directions, respectively. In addition, the correlation involving the axial and vertical velocity fluctuations is significant. The Reynolds stresses were obtained from (Hinze, 1975) where the classical experiments of Klebanoff (1954) are summarized.

A number of realizations N_r of the boundary layer was computed using the turbulence time scale of $t_{turb} = 10^{-3} s$, length-scale of $l_{turb} = 10^{-3}$, and a sample size of 1000 harmonic functions. The wave-vectors for these functions were taken from a normal distribution with the mean $\sim t_{turb}^{-1}$. The boundary layer thickness (δ) was allowed to grow according to the following empirical relation:

$$\delta = 0.16 \cdot x \cdot \left(\frac{U_0 x}{\nu} \right)^{-1/7} = 0.16 \cdot x \cdot Re_x^{-1/7} \quad (3.16)$$

where x is the axial distance and U_0 is the free-stream velocity, which was set equal to $1.0 m/s$. The cross correlation (\overline{uv}) was normalized with the friction velocity U_τ , which is itself a function of U_0 . The boundary layer thickness was randomly perturbed with a continuous function using the same spectral sampling technique as for the velocity fluctuations to emulate intermittency.

Fig. 3.3 shows the vorticity field of the generated boundary layer flow-field compared with LES data (Speziale, 1998). As can be seen from the figure, by choosing the turbulence length-scale correctly, one can achieve a good resemblance in the flow structure simulated with this semi-analytic approach and a LES flow-field.

In Fig. 3.4, the convergence of the random sampling process is illustrated. After about 500 samples the statistics converge to the prescribed stationary correlations.

To compare the simulation results with the experimental data the velocity profile along a vertical line in the center of the axial plane was stored for each simulated realization of the flow-field. The profiles of the thousand time realizations were then used to calculate the average fluctuating components in each direction, as well as the corresponding cross correlations. These are compared to the original experimental data in Figure 3.5. As can be seen, the experimental data is well reproduced.

The divergence-free property of the generated flow-field was tested by computing the divergence as a function of turbulence length-scale for three cases: isotropic velocity field, generated according to the original Kraichnan method (Kraichnan, 1970; Li et al., 1994), anisotropic velocity field, generated according to the modified Kraichnan method, using Eqs. (3.4)-(3.5) with $\tilde{k}_j^n \equiv k_j^n$, and anisotropic velocity field generated according to the RFG algorithm based on Eqs.(3.2)-(3.9). For this test case the anisotropy of different fluctuating velocity components was selected to be given by a ratio: 0.1:1.4:1 for c_1, c_2 , and c_3 respectively.

The divergence test was done on a cubic grid. For each grid-cell the divergence was computed as the sum of fluxes through cell faces. The Fourier space was sampled with 1000 wave-numbers selected according to Eq. 3.4. Fig. 3.6 depicts the computed divergence as a function of the ratio of turbulence length-scale to grid cell size. The result represents an average over 10,000 realizations of the flow-field. As can be seen from the figure in all three cases the continuity error decreases with the increase of the turbulence length-scale. This decrease is considerably slower for the anisotropic flow-field generated according to the original Kraichnan method compared with the the cases of isotropic flow field and anisotropic flow generated with RFG procedure. It should be noted that the theoretical continuity error in the isotropic case is zero. The discrepancy between this case and the anisotropic case computed with the Kraichnan method is due to the violation of continuity of that method in the presence of anisotropy. In contrast, the flow-field produced with the new RFG procedure has practically the same as for the isotropic case. This means that the anisotropic flow-field generated by the RFG procedure is essentially divergence free. At the same time this shows the importance of scaling transformation for k_j^n in (3.5) for the fulfillment of continuity. The upper divergence limit in the figure occurs when the grid cell-size is comparable or greater than turbulence length-scale l . It is due to the integration errors, which in this limiting case can be estimated from the relation $\|\overline{u_i u_j}\| \approx 1$.

Another validation of the method was done on a flat-plate wake flow, which is a well documented case in the literature (Ramaprian et al., 1981). In this case the simulation starts from a plane located behind the plate in the wake region (Fig. 3.7). The inflow boundary is generated using RFG with an input from the experimental data (Ramaprian et al., 1981), including mean velocity U_m , the turbulence intensities u_{rms} , v_{rms} , w_{rms} and the shear stresses \overline{uv} . In this way we can provide realistic inflow boundary conditions including the turbulence characteristics created by the plate, which is an important factor for LES. The length of the plate is $L = 1.829m$. The inflow boundary is located at $19.5mm$ ($x/L = 0.01$) measured from the rear edge of the plate. The computational domain size is $1.0m \times 0.2m \times 0.6m$ in x , y and z direction, respectively. The corresponding grid sizes are $82 \times 50 \times 50$. Non-uniform grid is used in both x and y directions with stretching not exceeding three percent². The size of the smallest cell is $0.6mm \times 0.2mm \times 1.2mm$ while that of the biggest cell is $50mm \times 8mm \times 1.2mm$ in x , y , z direction, respectively. Neumann boundary condition is applied at the outflow boundary. Symmetry boundaries are used in a vertical direction and periodic boundaries are used in the span-wise direction. Central difference numerical scheme and Smagorinsky model are applied in this study.

Fig. 3.8 presents the comparison of the turbulent characteristics between the simulation and the experimental results at the inlet plane. They agree very well except in the central region. The reason for the discrepancies is that the grid is relatively coarse in the center, which leads to the smoothing of very sharp gradients. The overall difference is under 1%. It should be noted that the agreement is so good because the comparison is given for the inlet plane where the RFG procedure was designed to reproduce the turbulence quantities exactly.

Fig. 3.9(a) shows the energy spectrum at the inflow boundary. A sharp cut exists at wave length 0.01, which matches the length scale we selected for RFG. Fig. 3.9(b) and Fig. 3.9(c) show the energy spectrum at $x = 0.16$ and $x = 0.53$ respectively, which were produced after the application of LES inside the domain. From these figures, one can see that a good portion of the inertial range is captured. With the grid becoming coarser in the wake, only large wave lengths can be resolved.

²In this study, x represents stream-wise, y - vertical and z - span-wise directions, respectively

Next we investigated the turbulence intensities downstream from the plate. From Fig. 3.10 to Fig. 3.13 the Reynolds stresses computed along y - direction at different x locations are compared with the experimental results. The agreement looks good although more quantitative studies would be appropriate. Near the very beginning of the wake most of the fluctuations can be captured. Later in the flow field, the percentage of the resolved turbulence is becoming small due to the coarser grids. It can be noted that both v' and uv at the second x -station are higher than those at the first one. This effect has been investigated and discussed by Nakayama and Liu (1990) where they attribute it to a near wake phenomenon. Figure 3.14 shows the decay of the turbulent kinetic energy along the center line of the wake. Most part of the turbulent kinetic energy has been captured. We anticipate that with finer grid sizes the turbulence resolution will be much better.

3.3 Application of RFG procedure

3.3.1 Boundary Conditions for LES/RANS

As an illustration of the technique we used it first in conjunction with the RANS and LES methods to simulate turbulent fluctuations in a ship wake. The high-Reynolds number character of ship wakes ($Re \sim 10^7 - 10^8$) makes it rather time-consuming to perform full-scale LES of these flows. In this situation a combination of a RANS and the RFG technique can offer an efficient way to restrict the LES runs to the wake region only.

Figure 3.15 shows a snapshot of an unsteady turbulent flow-field in the inflow-plane serving as inlet condition for LES of a ship wake. Initially a steady state RANS solution is obtained (Figs. 3.15(a), 3.15(c)), providing turbulent stresses r_{ij} and time-scales ω_i . Next the RFG procedure is used to generate continuous time-dependent inlet conditions with the given turbulence characteristics (r_{ij} , ω_i , Figs. 3.15(b), 3.15(d)).

In another application (Fig. 3.16), namely, turbulent flow around a ship-hull was produced as a superposition of the mean flow velocity, computed with a RANS method (k- ϵ) (Larreteguy, 1999) and the fluctuating velocity obtained with the RFG procedure. This flow-field can be used to initialize the unsteady LES and for particle tracking applications (see Sec. 3.3.2).

As noted earlier, the flow generated in both cases may not necessarily represent realistic instantaneous turbulence vortex dynamics at the respective boundaries, but statistically the flow-field will reproduce the turbulent shear stresses and time/length scales correctly. Furthermore, the statistics of turbulent fluctuations imposed at the space/time boundaries may not necessarily be preserved by the flow-solver inside the domain. That is, there may be a transition region between the boundary and the inside of the domain where the flow-solver will adjust to the boundary conditions. However, if the boundary conditions were generated using continuous functions and realistic turbulence quantities and spectra, this transition region will be small and the technique may still present a good alternative to solving the complete NS equation in a larger computational domain.

3.3.2 Particle Dynamics Modeling

Particle tracking in transient flows is usually a time-expensive computational procedure. In the situations when the turbulent flow is computed using RANS models it is possible to compute particle dynamics in a steady-state mean flow field and add a fluctuating component to particle velocities. When LES technique is used particles should follow a time-dependent flow-field and the fluctuating component should still be added to it at smaller turbulence scales. In both cases the fluctuating component is derived from the turbulence intensity and length-scales, provided by the turbulence model.

Bubble-dynamics in a turbulent flow is described in Chapter 5 in detail. Here, we briefly present an illustrative example of particle-tracking application in a ship wake.

Simulations of bubbles in ship wakes requires account of several processes, like drag, lift and buoyancy forces, bubble dissolution in water, bubble interaction with the free-surface (including bubble disappearance at the surface and bubble generation due to air entrainment). In some cases, because of uneven bubble distribution (e.g. local clustering), the coalescence and/or breakup of bubbles may be important. Because of this non-uniformity, sharp gradients in bubble concentration, and low volume fraction of the bubbles Lagrangian approach to model bubble dynamics is often preferred. Compared to the two-fluids method (Elghobashi et al., 1993, 1994, 1996; Crowe et al., 1998) the Lagrangian approach requires less empiricism and is more suitable for parallel implementation. We use a particle dynamics (PD) algorithm based on efficient

particle tracking, population dynamics and a novel particle interaction techniques (Smirnov et al., 2000, 2001).

To simulate bubbles in a ship-wake we use the combination of RFG and PD algorithms. Fluid velocity at the location of every bubble was approximated as a sum of the mean fluid velocity obtained from the RANS calculations and the fluctuating part computed with the RFG procedure. Since RANS solution is given only at the Eulerian grid-node locations and bubbles follow Lagrangian trajectories, an interpolation is required to approximate the mean velocity at bubble's current location. No such approximation is necessary for the fluctuating part, since the RFG procedure defines a flow-field at every point in space and time. In the simulation the bubbles were injected at a single point close to the ship hull where the turbulent kinetic energy was near its maximum (Fig. 3.17). Drag, buoyancy and added-mass terms were included (Crowe et al., 1998; Crowe, 1998). A total of 10000 bubbles of 100 microns in diameter were continuously injected into the domain. Two seconds of real-time were simulated for the ship-length of 6m traveling with the speed of 3m/s. The figure shows the tendency of particles to agglomerate in dense groups. The characteristic sizes of these groups are in many instances smaller than the grid-cell size. This reflects the very sub-grid nature of the RFG method, which enables to capture finer details of particle dynamics than can be resolved on an Eulerian grid.

3.3.3 Large-Eddy Simulations (LES)

In Large Eddy Simulations the RFG procedure can be used to generate random inflow-conditions or serve as a subgrid-scale model. There is an extensive literature regarding LES techniques (Piomelli, 1999). To reach a state of developed turbulence in LES simulations require a substantial computational time. Regarding this there are two important problems in LES of a high-Reynolds number turbulence that can be solved with the RFG procedure: (1) assigning initial flow-field distribution and (2) assigning turbulent inflow conditions. Conventionally, the first problem is dealt with by increasing the transition phase of the simulation and the second - by extending the size of the computational domain. Consequently, the remedy comes at a price of a longer execution time and higher memory requirements. By using a RFG procedure to generate the initial conditions one can cut down on the execution time considerably. For stationary turbulence the approximate nature of the initial velocity distribution with respect to the

solution of the NS-equation is of little significance, since these discrepancies are corrected in the first few iterations of the NS-solver.

The problem of inlet conditions could be even more important, since extending the computational domain will increase both execution time and memory requirements of the simulation. In this case RFG can provide reasonable inflow conditions with the pre-determined anisotropy properties. Here again we illustrate these advantages on the example of a ship wake. A complete LES simulation of the wake would normally require simulating the unsteady flow around the ship hull and in the wake region. Employing the RFG procedure for the inlet conditions, we can restrict LES run to the wake region only. In this case the information on turbulence levels and anisotropy at the inlet plane, required by RFG, can be obtained from relatively inexpensive RANS calculations.

After validating this approach on the case of a flat-plate (see Sec.3.2), we applied it to the wake of a model ship (Navy 5415 model (Carrica et al., 1998)). As in the flat-plate case the inflow boundary was constructed using the data from RANS calculations (Larretguy, 1999) (Fig. 3.15). The turbulent normal stresses are based on the kinetic energy. The time scale and length scale which are used in generation of the perturbation at the inlet plane are selected from the corresponding relation between the turbulent kinetic energy and its dissipation rate provided by the RANS calculations.

Figure 3.18 shows the instantaneous stream-wise velocity contours and vertical vorticity contours, respectively, in a plane parallel to the free surface, where some of the turbulence structures in the wake can be observed. Small-scale turbulent structures can be seen in both figures in the near wake region. These structures tend to increase in the far wake. This can be due to the following two factors: (1) In the very near wake, fine grids are applied so that smaller turbulence structures are captured. (2) Physically, larger turbulence structures include more energy so that they can last longer, while smaller turbulence structures have less energy and die quickly by dissipation. Another phenomenon is the increase of the width of the wake in the downstream direction. The mean velocity profile (not shown here) also supports this result. Capturing of these phenomena testifies to the validity of our approach of computing the inflow boundary.

3.4 Discussions

The analytical method of Kraichnan (1970) was modified to account for the effects of inhomogeneity and anisotropy of turbulent shear stresses. The technique was realized in an efficient random field generation (RFG) algorithm which was tested on the cases of isotropic turbulence, channel flow anisotropic flows, boundary layer inhomogeneous anisotropic turbulence (Celik et al., 1999) and flat-plate wake flow. The simulated flow fields are transient in nature and satisfy the conditions of continuity and anisotropy for homogeneous flows and to a good approximation satisfy these conditions for inhomogeneous flows.

The RFG procedure offers a relatively inexpensive way to generate random velocity fluctuations, representing a turbulent flow-field. Since the generated velocity field satisfies the relations of continuity and anisotropy it is a far more realistic representation of turbulence than can be obtained with a simple Gaussian velocity distribution using a random-number generator. Because the flow-field produced by RFG may not satisfy the momentum equations it is still an approximation. However, in some applications this approach may offer a simple and reasonably accurate way to model turbulence without solving the complete Navier-Stokes equation, which would require much more memory and execution time.

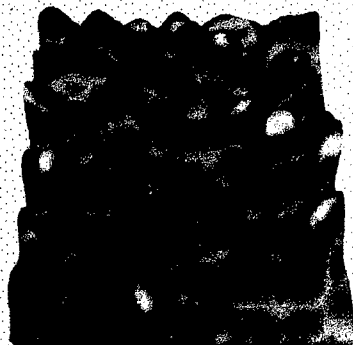
In practical applications the RFG procedure provides the flexibility of a trade-off between the accuracy of representing a turbulent spectrum and memory/time requirement. By increasing the spectral sample size N in Equation 3.4 one can increase the accuracy of reproducing the turbulent spectrum at the cost of longer execution time and higher memory utilization. In addition to that, since the velocity field is calculated by analytical functions it is given at any point in space and time, and not just at the grid nodes and at discrete time values. Because of this quality, the method has a potential as a subgrid-scale model for LES or RANS simulations and in modeling turbulent particle-laden flows, although its validity in this respect would require a separate study.

Advancing the realistic LES run to the stage of developed turbulence may require days of computation time³. Similarly, to obtain realistic turbulent inflow conditions may require the extension of the computational domain with the corresponding increase in computer time and memory requirements. The RFG technique can reduce the flow initialization time to several

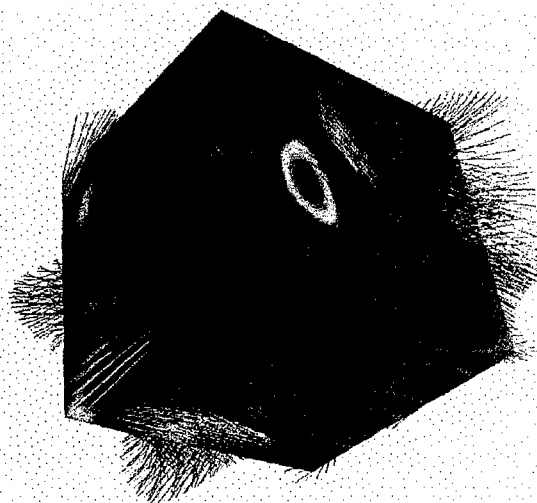
³Our benchmarking was performed on the 533 MHz DEC-Alpha processor

hours and can be used to continuously supply the turbulent inlet conditions close to the domain of interest, thereby reducing time and memory requirements of the LES simulations.

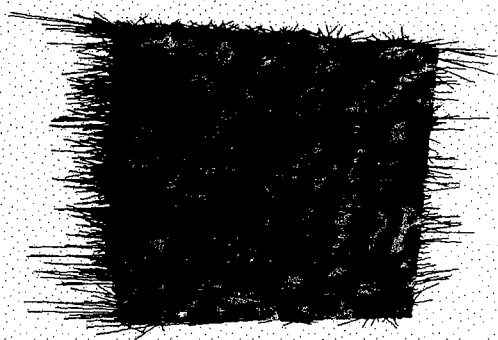
This study showed the feasibility of applying a hybrid LES technique in combination with RFG algorithm to high-Reynolds number flows, like those of ship wakes. It is also shown that the technique can be used effectively in conjunction with a Lagrangian particle dynamics approach, is appropriate for bubble tracking in the wake and can be easily incorporated into LES codes.



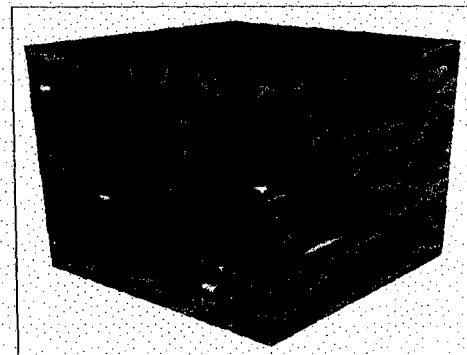
(a) Isotropic Vorticity



(b) Isotropic Velocity



(c) Anisotropic velocity

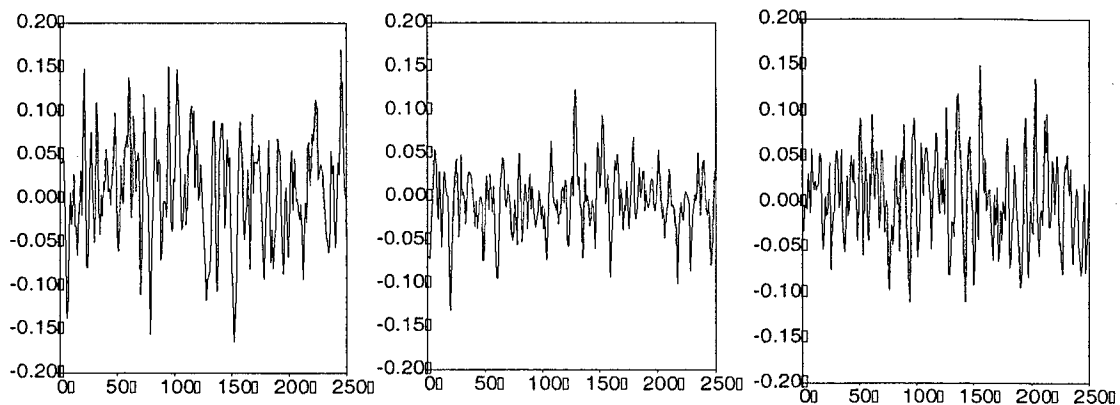


(d) Anisotropic length-scale



(e) Fluctuating velocity in the boundary layer

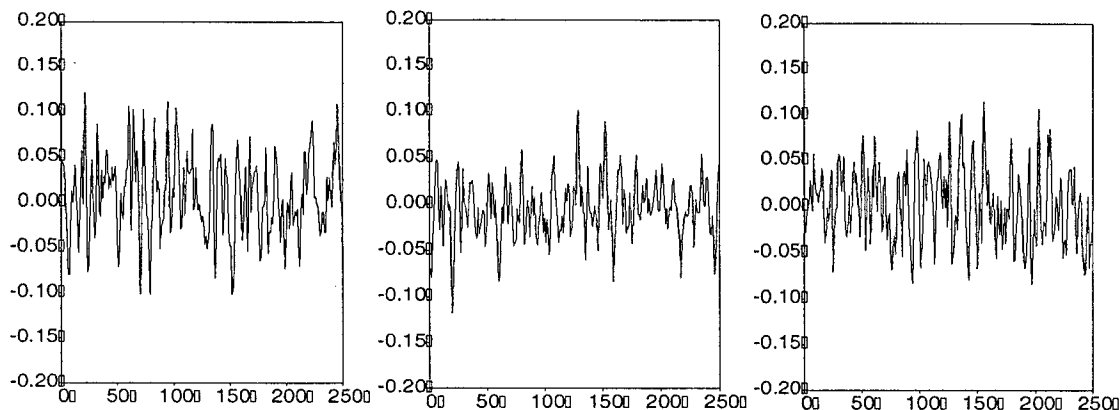
Figure 3.1: Simulated flow-field using RFG



(a) Axial, $y^* = 0.13$

(b) Vertical, $y^* = 0.13$

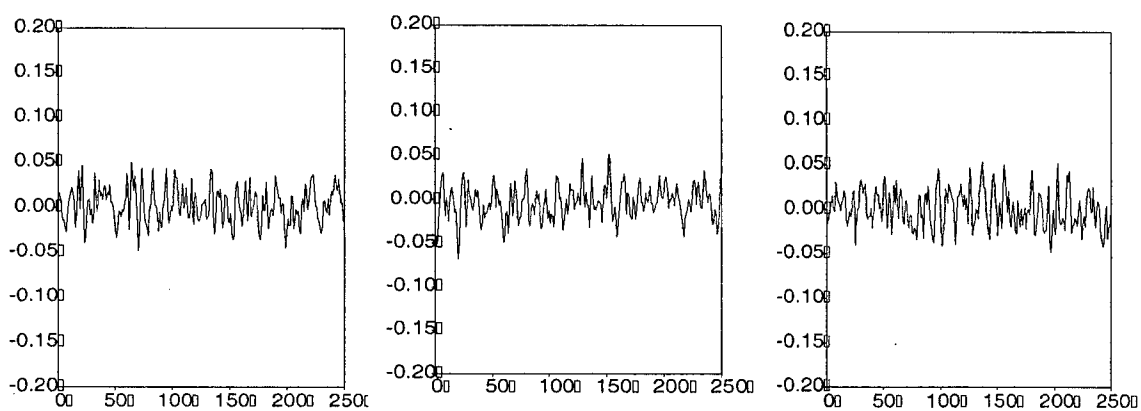
(c) Tangential, $y^* = 0.13$



(d) Axial, $y^* = 0.46$

(e) Vertical, $y^* = 0.46$

(f) Tangential, $y^* = 0.46$

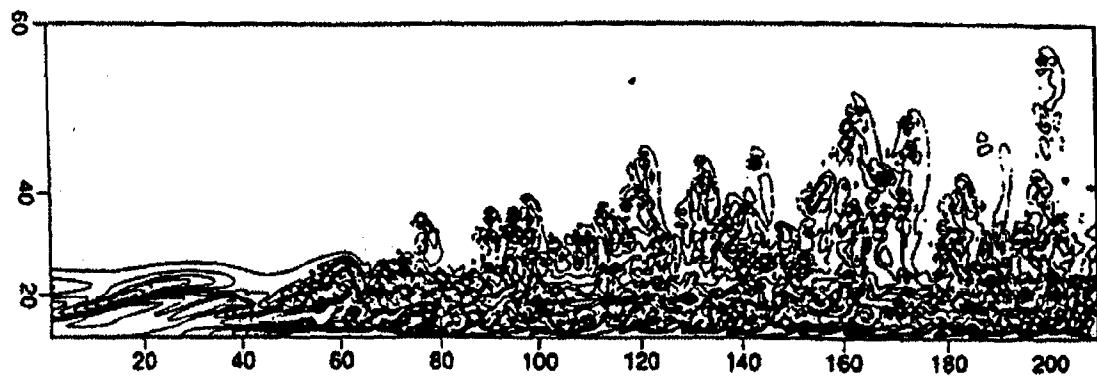


(g) Axial, $y^* = 0.76$

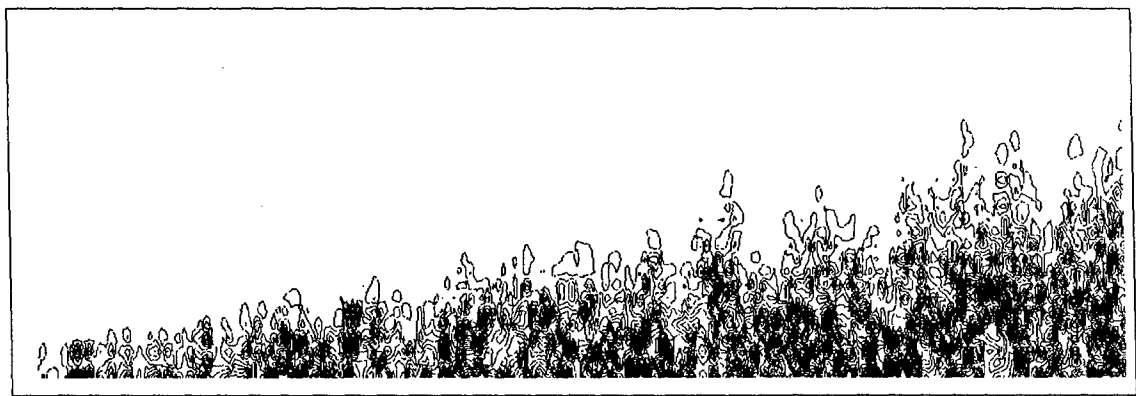
(h) Vertical, $y^* = 0.76$

(i) Tangential, $y^* = 0.76$

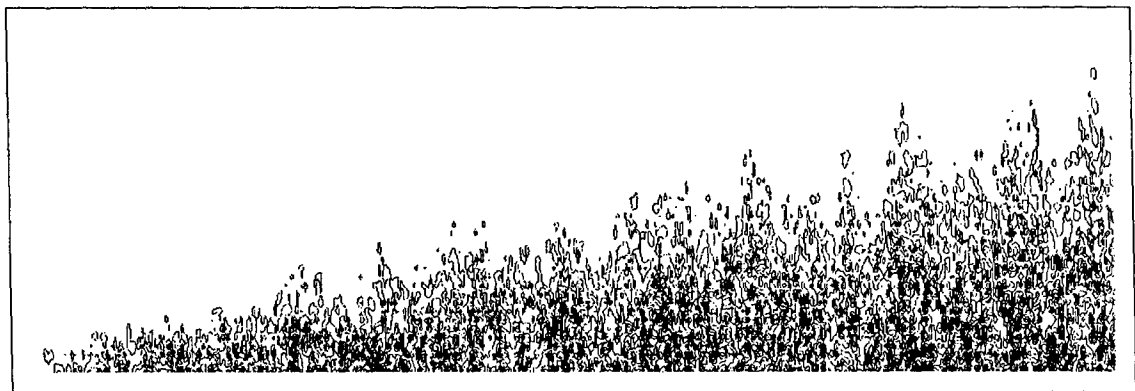
Figure 3.2: Instantaneous velocity vs time step at different locations, $y^* = y/\delta$



(a) LES (Speziale, 1998)

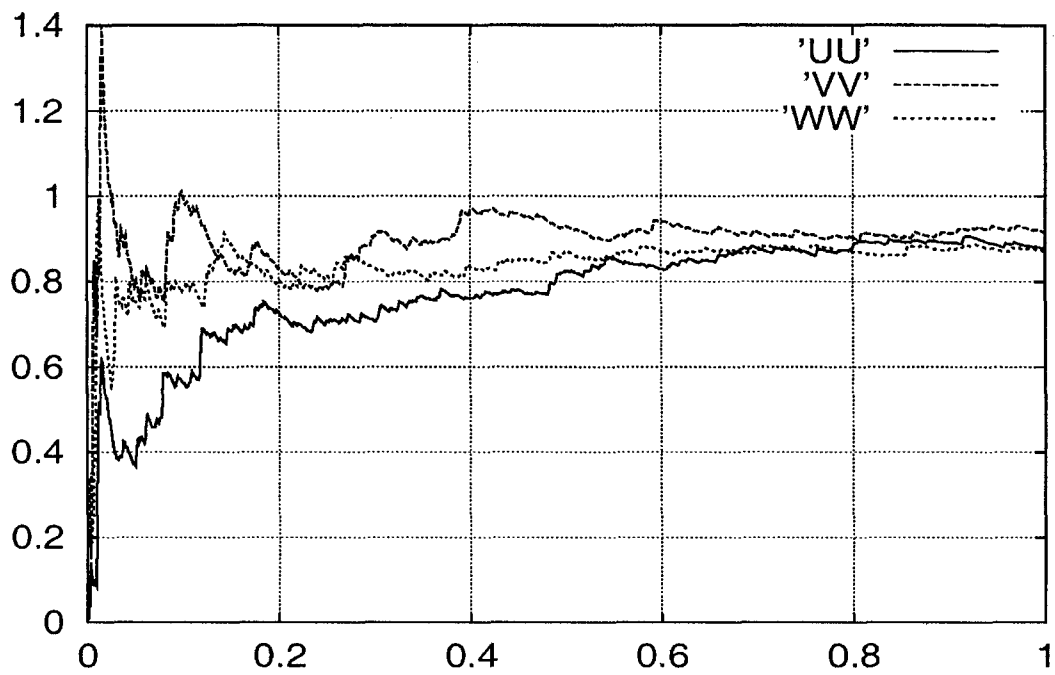


(b) RFG (large length-scale)

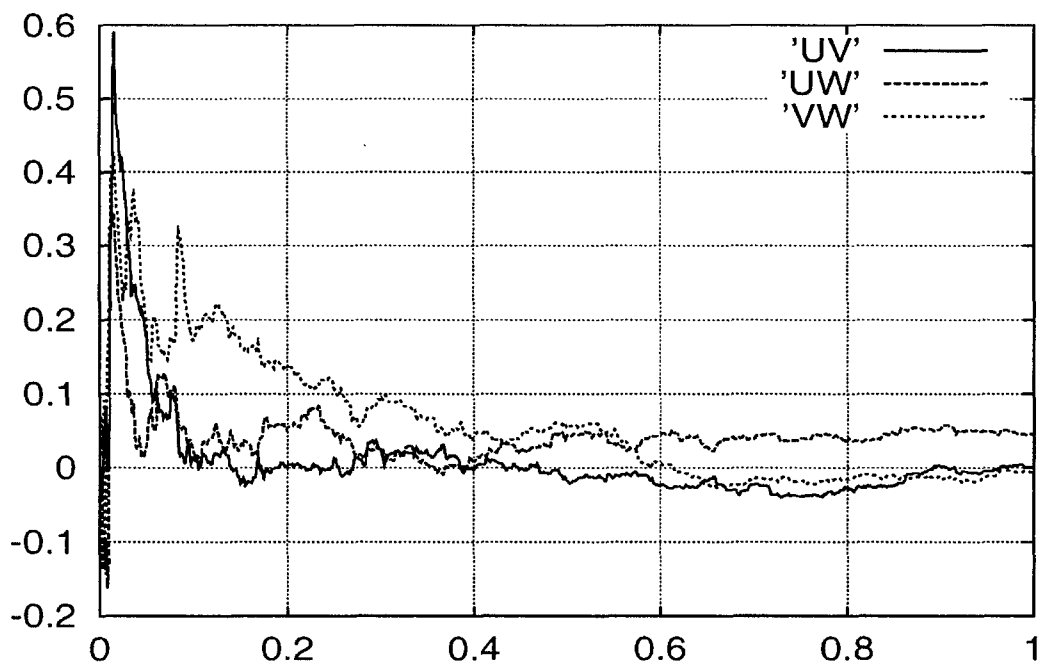


(c) RFG (small length-scale)

Figure 3.3: Vorticity contours in the boundary layer

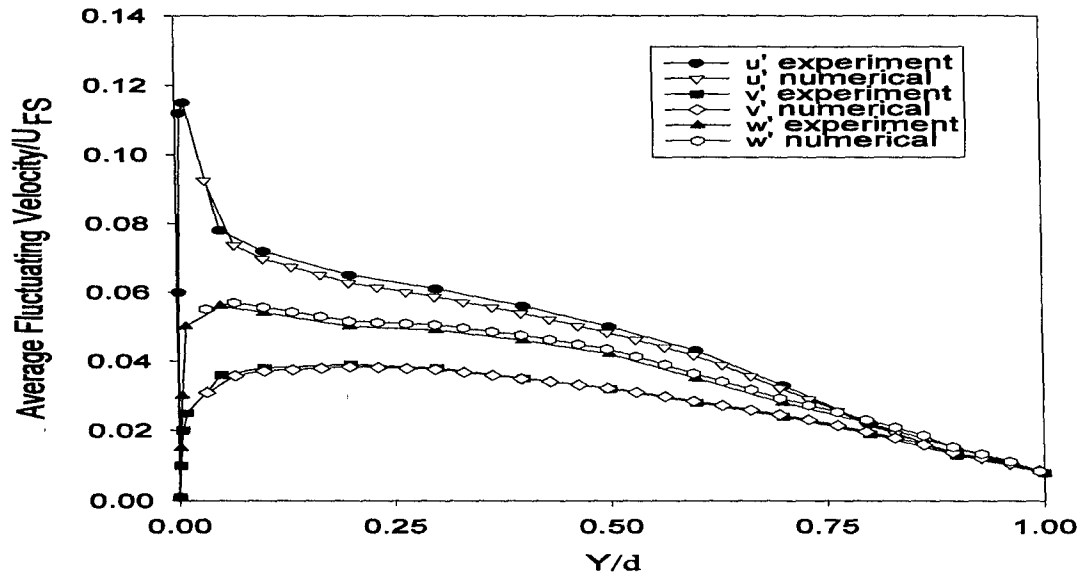


(a) Diagonal correlations

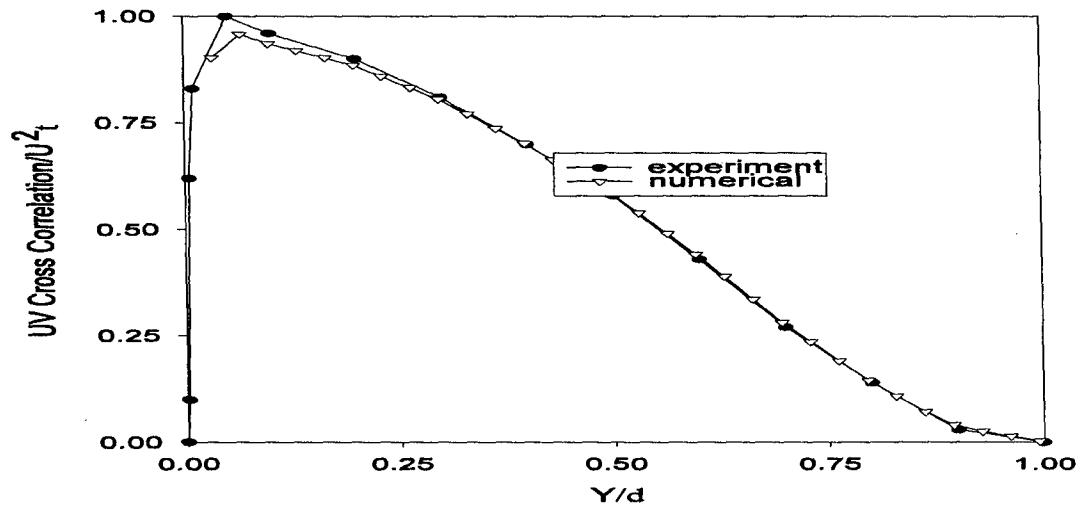


(b) Cross correlations

Figure 3.4: Convergence of velocity correlations



(a) Fluctuating velocities



(b) Axial/vertical cross correlations

Figure 3.5: Comparison with experimental data

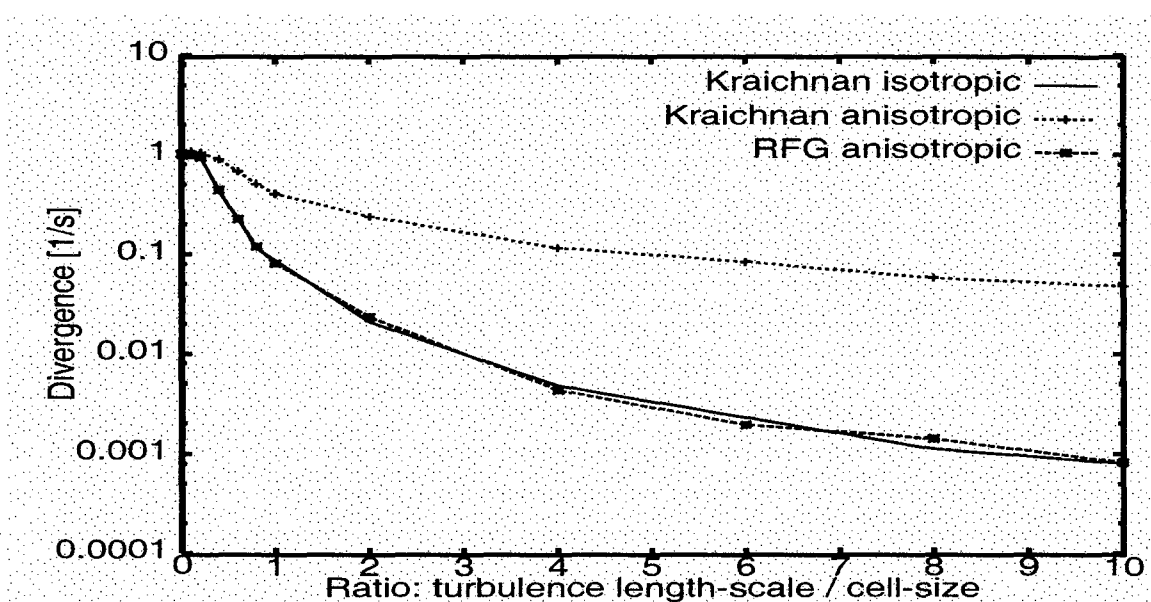


Figure 3.6: Normalized divergence of an anisotropic velocity field

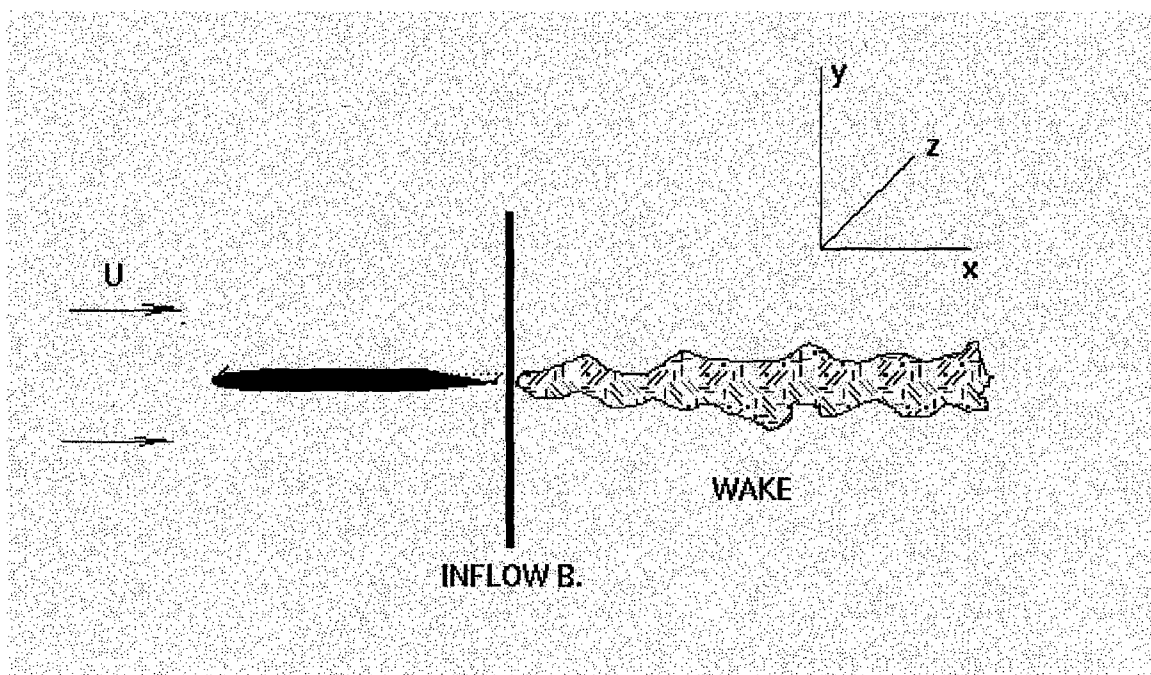
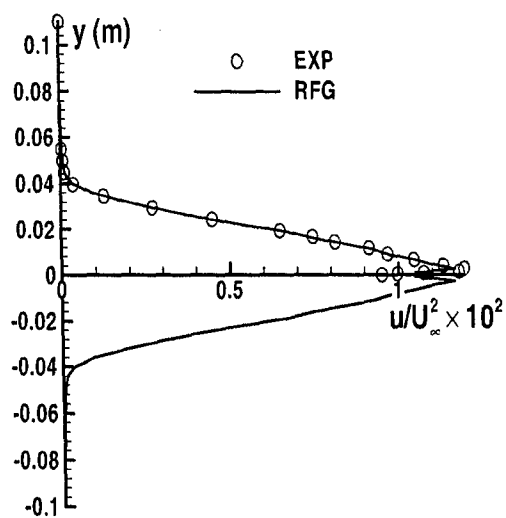
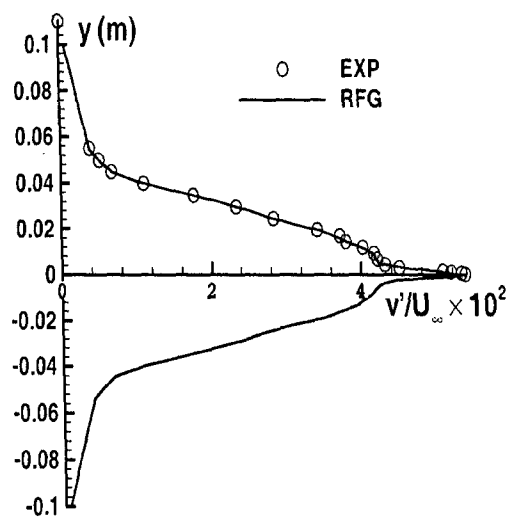


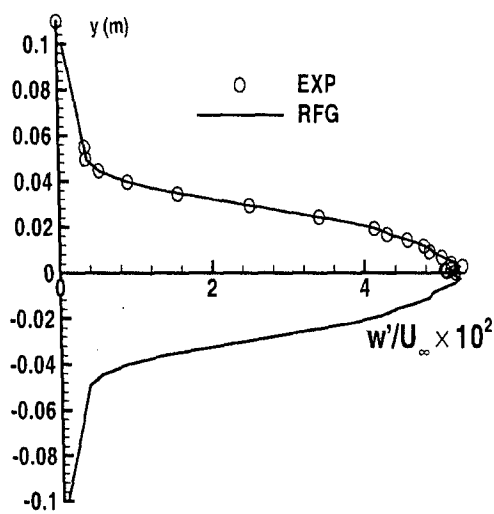
Figure 3.7: The schematic of the flat plate wake



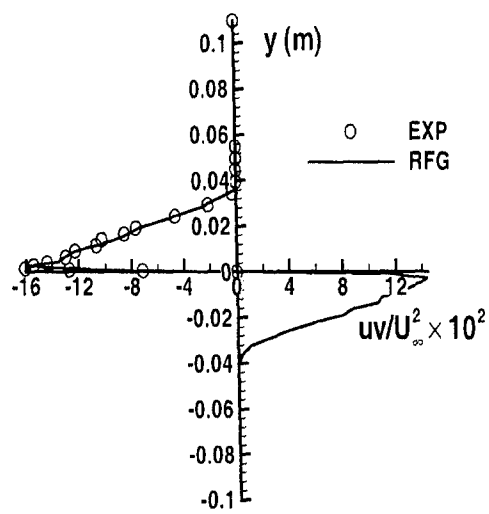
(a) Stream-wise, u_{rms}



(b) Span-wise, v_{rms}

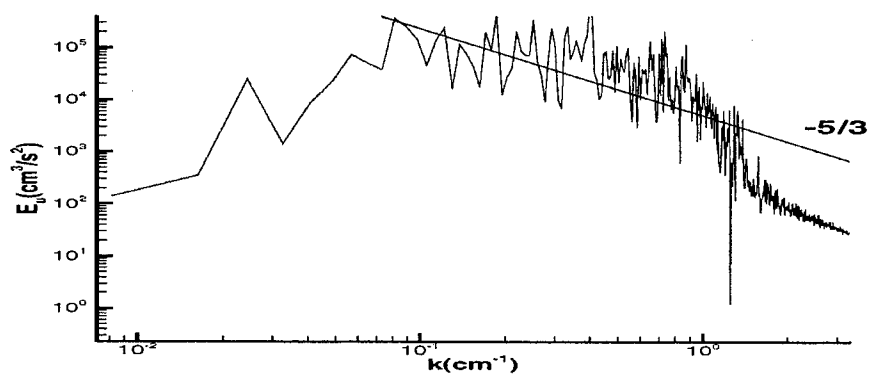


(c) Vertical, w_{rms}

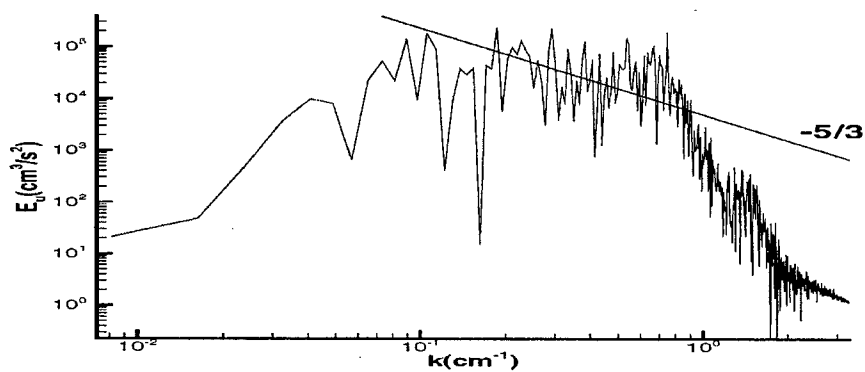


(d) Shear stress, uv_{rms}

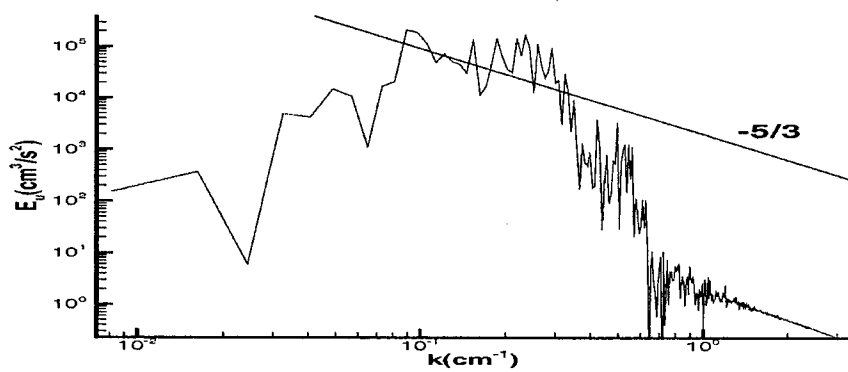
Figure 3.8: Turbulence intensities at the inflow boundary.



(a) Energy spectrum at the inflow boundary



(b) Energy spectrum at $x=0.16$



(c) Energy spectrum at $x=0.53$

Figure 3.9: Energy spectrum at different x locations

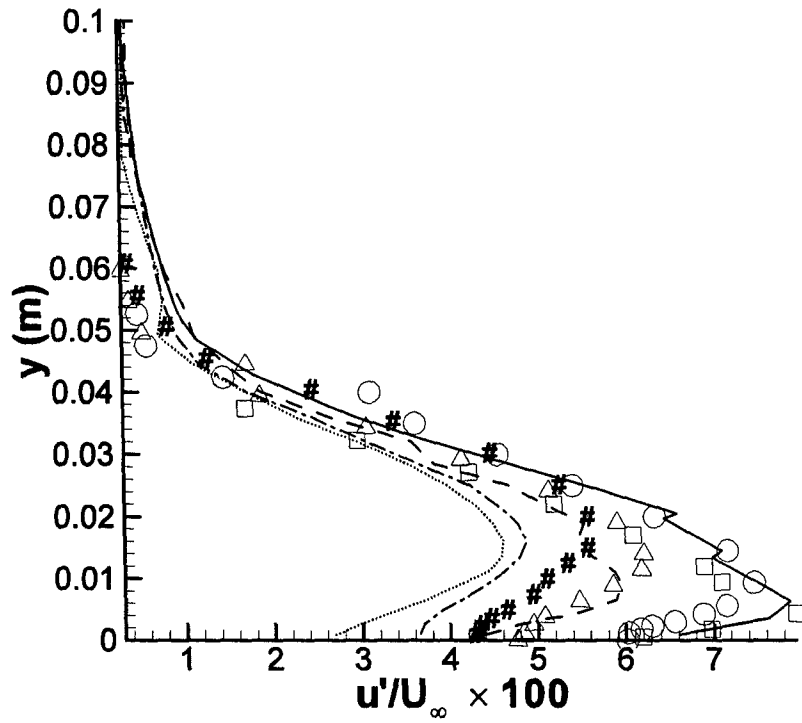


Figure 3.10. Comparison between simulation and measured turbulence intensity (u_{rms}).

- , present simulation results at $x = 31.75mm$;
- , present simulation results at $x = 158.75mm$;
- · - · -, present simulation results at $x = 361.95mm$;
- , present simulation results at $x = 590.55mm$;
- , Exp. results (Ramaprian, et al. 1981) at $x = 31.75mm$;
- , Exp. results (Ramaprian, et al. 1981) at $x = 158.75mm$;
- △, Exp. results (Ramaprian, et al. 1981) at $x = 361.95mm$;
- #, Exp. results (Ramaprian, et al. 1981) at $x = 590.55mm$;

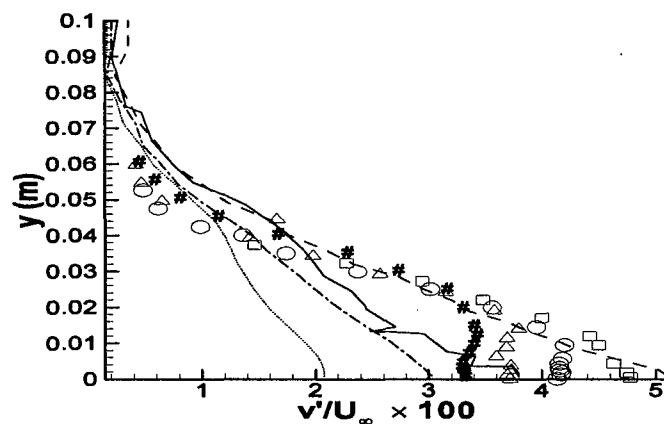


Figure 3.11. Comparison between simulation and measured turbulence intensity (v_{rms}).

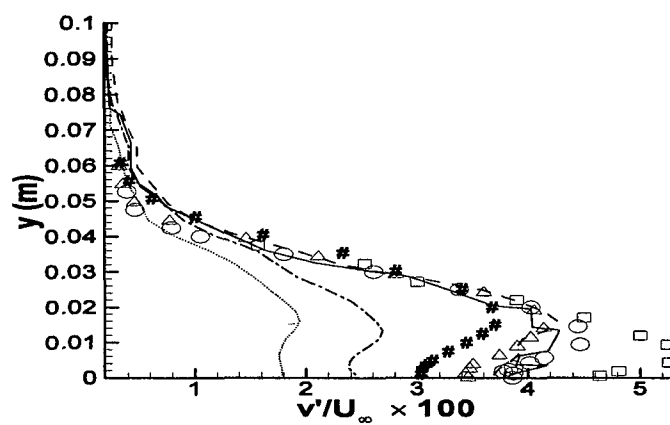


Figure 3.12: Comparison between simulation and measured turbulence intensity (w_{rms}).

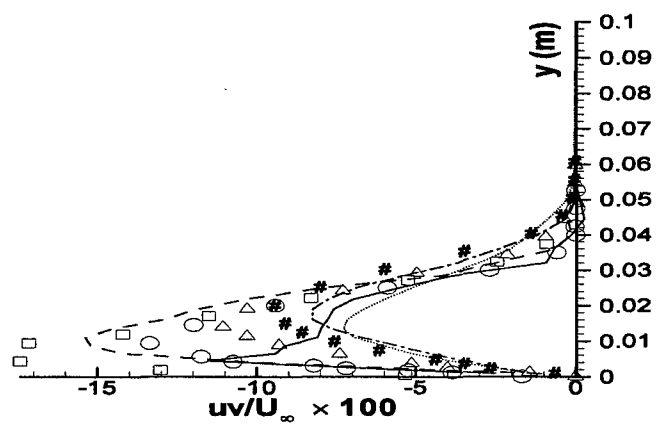


Figure 3.13: Comparison between simulation and measured shear stresses

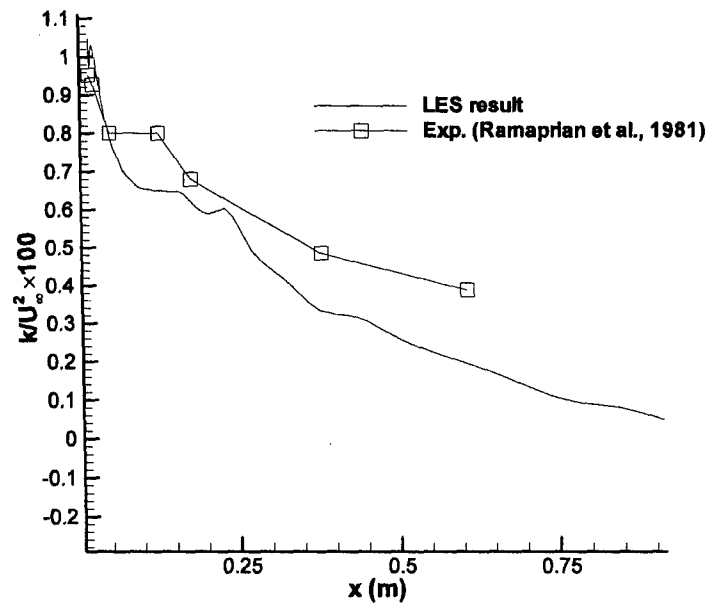
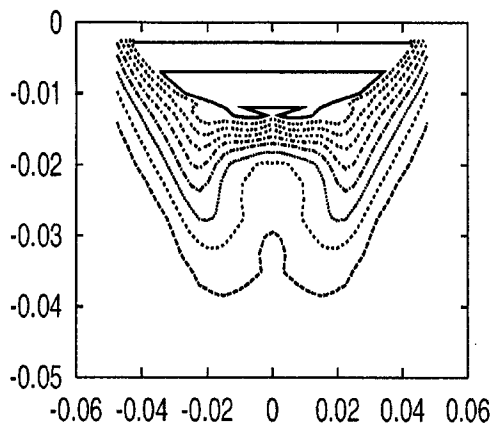
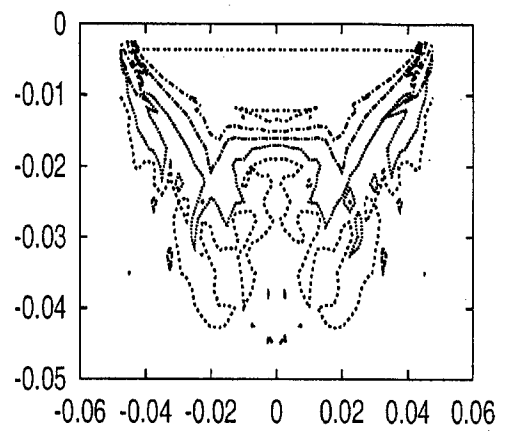


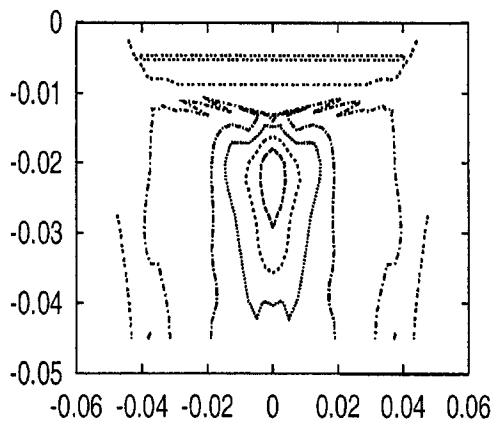
Figure 3.14: Kinetic energy profile along the center line in the wake of a flat plate



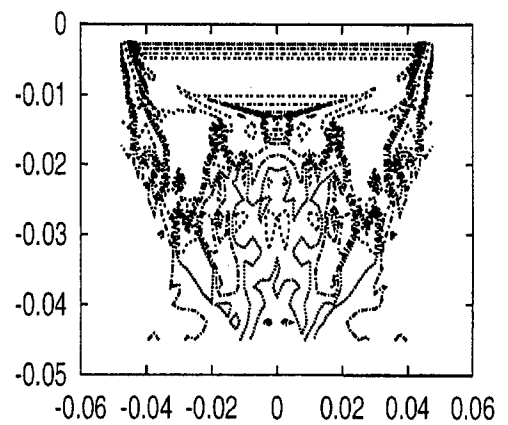
(a) Streamwise (RANS)



(b) Streamwise (RANS+RFG)



(c) Vertical (RANS)



(d) Vertical (RANS+RFG)

Figure 3.15: Unsteady inlet velocity components: inlet conditions for LES of a ship-wake.

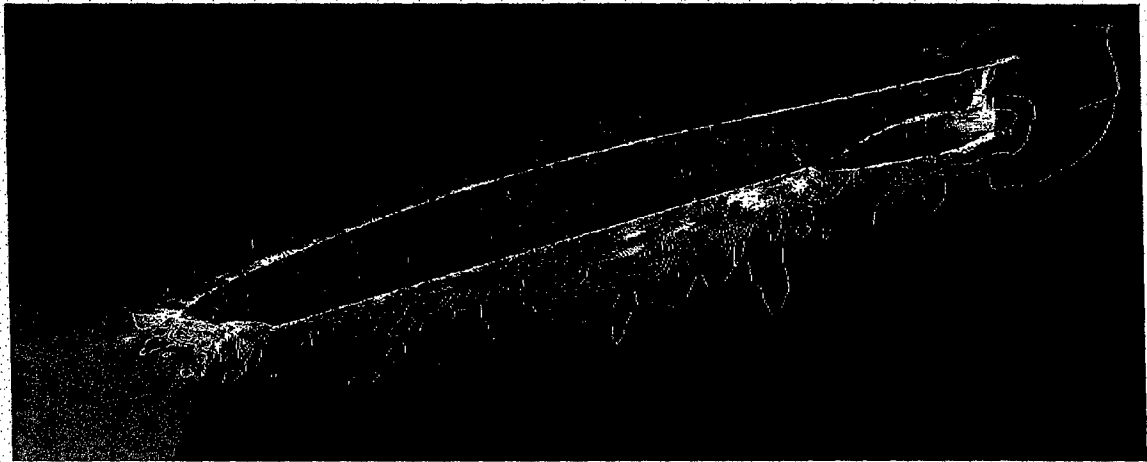
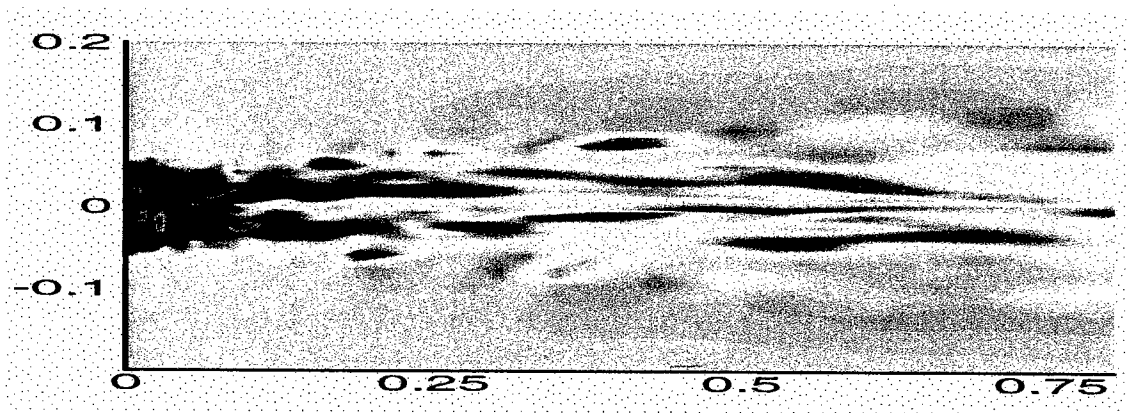


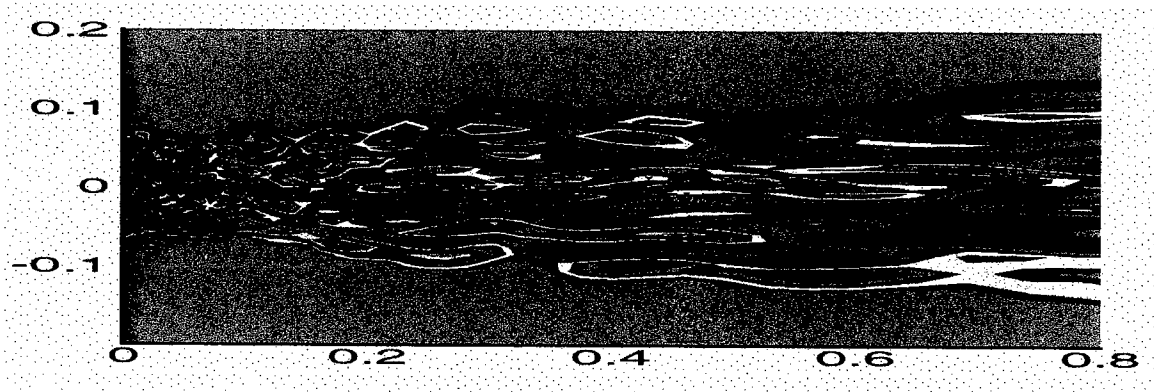
Figure 3.16: Turbulent velocity around a ship hull computed with the RFG algorithm. (View from below.)



Figure 3.17: Bubbles in a ship-wake. (Background shading is according to the turbulent kinetic energy.)



(a) Stream-wise velocity contours of the simulated wake flow



(b) Instantaneous vertical vorticity contours

Figure 3.18: LES of a ship-wake flow

4 SHIP WAKE SIMULATIONS

The subject of this Chapter is the application of the numerical schemes and SGS models described in previous chapters to the calculation of turbulent ship wake flows. Starting from the review of the current research status of ship wake hydrodynamics, this Chapter leads to the summary of the strategies described in previous chapters. Several cases have been simulated and results are analyzed and assessed.

Ship hydrodynamics has been the subject of numerous studies in the past. Both experimental and numerical achievements have been made. Since real ships can not be fitted into tow tanks, it is common practice to base the research on small-scale models of real ships. Experimentally, in the 60's or 70's of the last century, most of the experiments concerned the ship surface drag force, or propeller influence. Recently, experiments are more focused on the investigation of micro dynamics of flow around ships, such as wave dynamics, turbulence parameters, bubble dynamics, etc. Although experiments can provide useful results, there are many limitations encountered in practice. First, it takes a very long time to design, set, and perform the experiment. Secondly, it is very expensive. Thirdly, it can not provide very detailed information due to the limited space to arrange the measuring devices or detectors. Benefited from the rapidly developing capabilities of computers, the modern research in computational hydrodynamics has replaced the more elegant, but less general, analytical methods (Larsson et al., 1998). Since ship wake flows are the main subject of this study a separate but concise review is presented next.

4.1 Experiments on Turbulent Ship Wake Flows

In a earlier study of ship wake flows, Naudascher (1965) found that the wake width has a power law behavior. This was supported by Milgram et al. (1993). By carrying out field measurements for ship wakes, they found that the wake width has a power law behavior of the type $x^{1/5}$ where x is a distance from the ship stern. Reed et al. (1990) summarized the hydrodynamics research of ship wake flows both in experimental and numerical areas and pointed out the hydrodynamic wake schematic shown in Fig. 4.1. Benilov et al. (2000) found that

even in the far wake the ship wake turbulence is still well detectable and the Kolmogorov range can be identified. Hoekstra (1991) gave relatively comprehensive tests of turbulence parameters in which the wakes of different ship models were studied. The vortices generated by the ship body, named bilge vortices, were analyzed, and it was found that these vortices can be avoided by hull form adjustment but this was found to be impractical.

Stern et al. (2000) present some results for CFD validation, but the experiments providing turbulence intensities were still underway. For this study it was not possible to find the necessary experimental information to initialize an LES study, or to build the inflow boundary condition including the turbulence features induced by the ship hull. Thus the current simulation is based on RANS results.

4.2 Computations of Turbulent Ship Wake Flows

Most of the computational fluid dynamics efforts applied to flow past ships are based on Reynolds-Averaged Navier-Stokes (RANS) equations utilizing various turbulence models (Sotiropoulos and Patel, 1995; Paterson et al., 1996; Ratcliffe, 1998). The commonly used models include k - ϵ , k - ω and algebraic stress models. RANS is often quite adequate for mean flow predictions, but provides only limited information about turbulence characteristics and almost no details on large-scale unsteady structures of the flow field. The LES technique, on the other hand, was designed to capture the unsteady behavior of at least the large coherent turbulent eddies. There is hardly any study in the literature where LES has been applied to flow around ship-hulls including the wake. The main reason obviously lies in the fact that large computer resources are required. In LES, the energy containing eddies of the flow are computed explicitly, while only the more universal (isotropic) small eddies are modeled. Thus very fine grids have to be applied in order to resolve the boundary layer near the wall where the turbulence length scales tend to zero as the wall is approached.

However, in some applications, like bubble dynamics modeling, it is still necessary to resolve coherent flow structures - large turbulent vortices and eddies. In RANS simulations, especially those using two-equation models such as k - ϵ model, these unsteady flow features are usually smeared out.

Since it can be computationally prohibitive to include both the ship hull and the wake in LES, it would be desirable for the purposes of pure wake simulations to start the computations somewhere in the near wake excluding the ship hull. However, this technique, also known as the Initial Data Plane (IDP) approach (Hyman, 1998; Paterson et al., 1996; Dommermuth et al., 1996) can introduce considerable errors (Hyman, 1998) - not surprisingly though, since the body generating the wake is not included in the non-steady LES simulations.

In principle it is possible to predict turbulence via the LES technique by starting from a quiescent flow or with the mean flow obtained from RANS. Unfortunately, it takes a very long time for a turbulent flow to develop spatially and temporally without any initial perturbation.

This is especially true in the case of decaying turbulence in the absence of strong turbulence generating factors like walls. A reasonably accurate approach to this problem was used in modeling of boundary layer turbulence (Lund et al., 1998). It consisted of applying a separate flow solver with periodic boundary conditions to construct the inlet conditions for the LES/DNS solver. It provides fully turbulent inflow conditions consistent with the solution of the Navier-Stokes equation, which makes it particularly suitable for DNS. This method was used later by Wang and Moin (2000) to compute the inflow boundary for simulating a trailing-edge flow. However, its implementation may not be straightforward for the problems without well defined fully developed boundary/shear layers. For some engineering problems it may also be too expensive in terms of computer resources and programming effort.

Another numerical simulation with time dependent turbulent inflow boundaries was performed by Voke and Potamitis (1994) for a wake of a flat plate. In their simulation, the inflow boundary information was derived from a separate simulation, called the precursor simulation, in which a low Reynolds number turbulent boundary layer was simulated. At the inflow plane of the wake simulation the three velocity components were specified by reading one transverse plane of velocity data from the boundary layer simulations at each time step. The transverse plane was selected at a location where the flow was fully turbulent but with a safe distance from the outflow boundary of the precursor simulation. Two separate sets of velocity data of the boundary layer were needed to provide inflow conditions for the upper and lower halves of the wake simulation. To achieve this they used the data of the same precursor simulation of the boundary layer at well-separated times in its history. This method is costly and only applicable

to parabolic wake flows. In application to the ship wake flow it would require LES of the flow around the hull itself which is impractical.

To achieve a higher accuracy of ship-wake simulations and still remain within realistic constraints on computer resources, the whole problem of computing the flow past ships and their wakes is divided into two parts: steady-state RANS calculations around the ship hull, and non-steady LES of the wake. In this approach the LES starts from a plane in the near wake where the inflow conditions are retrieved from the RANS results. This is similar to the IDP approach used by Hyman (1995) and Dommermuth et al. (1993) where the data reflects the mean flow, mean turbulence quantities and the scalar field at this plane. In the present approach, a wider range of turbulent quantities at the inlet plane are allowed, which include length- and time-scales, and all nine components of the turbulent shear-stress tensor (only six components to be computed due to symmetry), thus providing anisotropic and inhomogeneous turbulent inlet conditions. The technique is based on a Random Flow Generation (RFG) algorithm (Celik et al., 1999; Smirnov et al., 2001b; Shi et al., 2000b), which is applied to generate the inflow turbulence on the basis of the information obtained from experiments or RANS calculations. The generated velocity fluctuations satisfy instantaneous continuity equation, and the turbulence statistics (Reynolds stresses) are prescribed a priori. Thus in some sense, although the LES starts at a plane behind the body, the influence of the body is implicitly included. The features of the generated flow-field such as continuity, anisotropy and inhomogeneity make the RFG method also well suited for setting the initial conditions for LES.

In the present simulations anisotropic, inhomogeneous, unsteady IDP conditions were applied. Thus the flow develops according to the dynamics prescribed by the Navier-Stokes equations without forcing and it is believed more reasonable in the near wake. This approach differs from that of Dommermuth et al. (1996) which is appropriate for the far wake field (Hyman, 2001).

To describe the dynamic behavior of the turbulence in the ship wake, in another study (Benilov et al., 2000) made the following assumptions:

The wake turbulent kinetic energy significantly exceeds the upper layer turbulence that reduces the turbulent wake problem to the turbulent region development in a non-turbulent liquid.

The main source of turbulence is a moving ship which means that all interactions between the wake turbulence and environment do not contribute in the wake dynamics and allow the problem to be reduced to the shear-free turbulence model.

Through all this study, those assumptions were taken to simplify the problem which is to perform LES on the wake flow of the ship model DTMB 5415 (5512).

4.3 Ship Wake Simulations on a Straight Track

The ship wake simulations in the present study are for the ship model DTMB 5512, a smaller ship model scaled from DTMB 5415 which are well known in the ship hydrodynamics community. Model 5415 is a towing tank model representing a modern naval combatant. It was constructed out of wood and measured 5.72 m (18.767 ft) between perpendiculars. Model 5512 measures 3.04 m (10.000 feet) between perpendiculars. It is an appended version of 5415, with shafts, struts, rudders and propellers. However in this study it has been simplified as a bare hull model. The geometry of this ship model is shown in Fig. 4.2. Note that this picture is not scaled, and it is only used to show the profile of the ship model.

The Reynolds number is 4.65×10^6 and the Froude number is 0.28. The length, L , of the ship model is 3.048m. The ship is located on the region of $x/L = 0$ to $x/L = 1.0$. The inflow boundary is located at $x/L = 1.05$, a small distance downstream of the rear end of the ship. The computational domain size is 1.5m x 0.3m x 0.6m in x , y and z direction, respectively, with the corresponding grid size of 162 x 50 x 66 (Fig. 4.2). For convenience, the streamwise direction (x) of the computational domain is marked from 0 to 1.5 ($x = 0$ corresponding to $x/L = 1.05$, where the inlet plane is located). Non-uniform grid is used in both x and y directions with stretching not exceeding one percent. The size of the smallest cell is $0.0015 \times 0.0028 \times 0.0068$ while that of the largest cell is $0.028 \times 0.007 \times 0.012$ in x , y , z direction, respectively.

We have also performed simulations with various other coarser grids. Results from those showed consistent trends in increased resolution of finer structures in the flow field and turbulent kinetic energy as the grid cell size decreased. Here we present the results from the finest grid resolution we were able to achieve on a single processor.

4.3.1 Boundary Conditions

The inflow boundary is generated using the RFG method in conjunction with the RANS calculations (Stern & Wilson 2000), providing the mean velocity U_m , the turbulence kinetic energy k and the specific dissipation ω . The time scale τ can be taken proportional to $1/\omega$. The length scale can be calculated from k and ω . In this study, the length scale and time scale used in RFG were selected as constant. The length scale was 0.02 of the ship length, and the time scale was 0.001, non-dimensionalized by free stream velocity and ship length. These numbers were selected so that the turbulence length scale is about 15% of the ship width. Neumann boundary condition was applied at the outflow boundary. Symmetry conditions are used in y direction and periodic boundary conditions are used in the spanwise (z) direction. At the free surface slip in x and z directions is allowed but the velocity component normal to the free surface is set to zero. As such the free surface is approximated as a moving flat plane.

The periodic boundary conditions in the span-wise direction were selected for the reason of preserving the possible lateral fluctuations caused by unsteady motion of large eddies. It is also more exact than the zero gradient boundary condition if applied to the boundaries in spanwise direction. Any other boundary condition would probably dampen that motion and introduce artificially high subgrid-turbulence levels at the boundaries. The boundary conditions at the outlet were actually of a free-gradient (zerostress) type.

The numerical schemes and SGS model used in the ship wake simulation are the same as in the flat plate wake (Shi, 2001; Smirnov et al., 2001a).

4.3.2 Results and Discussion

The streamwise vorticity contours at different planes are shown in Fig. 4.3 and the contours of the vertical component of vorticity are shown in Fig. 4.4. Fig. 4.3 shows that concentrated vorticity decreases with axial distance, and in the far wake vorticity is only concentrated near the free surface, while the size of the wake increases in axial direction of the flow. It is interesting to note the two distinctly concentrated vorticity streaks away from the center line of the wake (Fig. 4.4). These resemble the bilge vortexes (Reed et al 1990) generated by the ship-hull Fig. 4.1. The streamwise velocity contours at a plane near the free surface are shown in Fig. 4.5. It is interesting to see that the vorticity wake is slightly wider than that of the velocity wake.

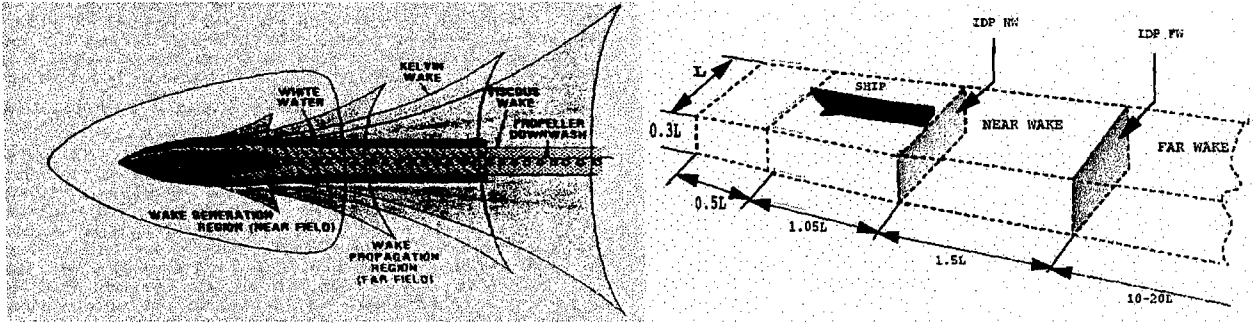


Figure 4.1: a) Hydrodynamic wake schematic showing major large-scale contributors to the wake (Reed et al. 1990), b) The schematic of the ship-wake

A comparison with experimental results reported by Reed et al. for the same ship model (1990) revealed a qualitative agreement. In particular the axial velocity contours at the cross-section of $x/L = 0.61$ shown in Fig. 4.6 have the same structure as the experimental flow-fields presented in that study (Figs. 36, 37). The same conclusion can be drawn for the velocity vectors at this cross-section (Fig. 4.7). The resolved component of turbulent intensity, which in our simulations is about 3.5%, as can be deduced from (Fig. 4.12), agrees closely with the measured total intensity at $X/L = 0.61$. A further observations that can be made on the results of the simulation is the rapid decay of the resolved turbulence with the increase in the width of the wake. In the far wake only larger turbulence structures can be seen. This behavior seems reasonable, since the small turbulence structures contain significantly less energy, hence they can only last for shorter time compared to the larger eddies.

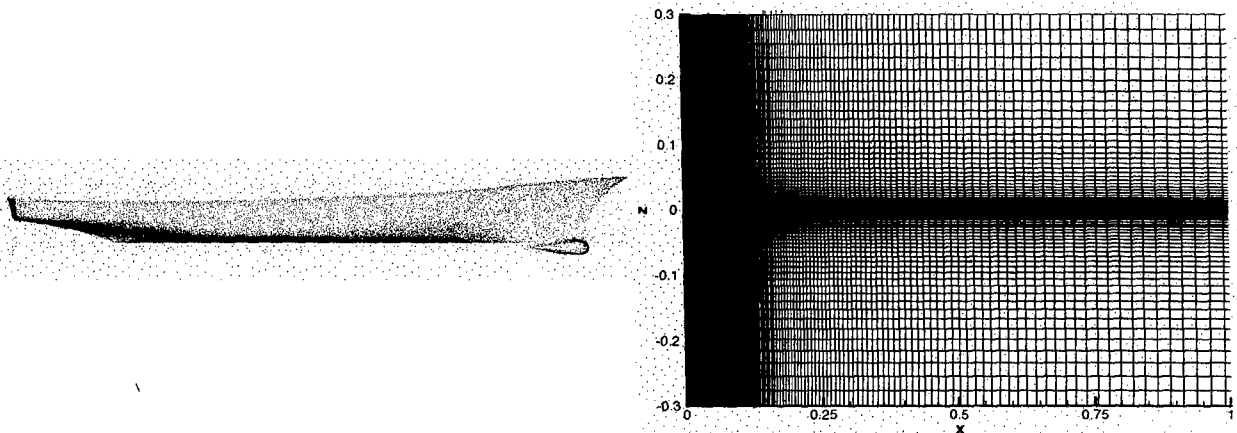


Figure 4.2: a) Geometry of DTMD 5415, b) Grid of the computational domain: 162x50x66.

The mean kinetic energy was calculated from the predicted velocity field. This was accomplished by calculating the mean velocity on several cross-sections in the flowfield via summation of the instantaneous velocity over 20000 timesteps. Then, these mean velocity fields were subtracted from the instantaneous velocity field on those cross-sections to calculate the root mean square velocity fluctuations and hence the turbulent kinetic energy field.

Figure 4.8 shows that noticeable changes are observed in the streamwise velocity profiles in both axial and vertical directions. The velocity has a peak below the free surface, which gets weaker in the axial direction. However, the location of peak axial velocity defect moves deeper into the wake indicating a plunging effect as the wake develops as seen in Figures 4.10(a)-4.10(c). The turbulent kinetic energy of the rms velocity fluctuations in Figure 4.9 shows decay and significant redistribution. Initially the turbulence is concentrated more near the free surface. This area plunges deeper with increasing axial distance as also observed in Figures 4.11(a)-4.11(c). This phenomena is investigated in more detail by Yavuz et al., 2004. Moreover, it can be concluded from these figures that the LES predictions clearly depict the two bilge vortices, whereas the RANS predictions are known to be incapable to do so.

The effects of different numerical schemes and SGS models were also investigated in this study. The resolved turbulence kinetic energy (TKE) for different schemes and different grid sizes is shown in Fig. 4.12. The RANS solution obtained by the CFD-SHIP code from IOWA is also shown in this picture for comparison. The resolved TKE from fine grid is higher than that of the coarse grid as expected. Central differencing discretization with Smagorinsky model gives better results than the other schemes in retrospect to the total TKE calculated from RANS. From this figure it can also be seen that there is no significant difference in the results when the QUICK scheme is used with or without SGS model. Moreover, the resolved TKE is lower than that of central differencing with Smagorinsky model. This means that the grid is relatively coarse and the QUICK scheme contains even higher numerical diffusion than the Smagorinsky model. For more detailed information about the comparisons of numerical schemes and subgrid-scale models the reader is referred to Shi et al. (2000b) and Shi (2001). One uncertainty in the computations is the presence of a sinusoidal-like distribution of TKE in the near wake. It may be because of the existing surface wave (not accounted directly here). When the wave descends towards the bottom of the domain, it creates a constriction with flow passing through a small

area. Thus both the velocity and TKE are higher at this region. A closer look at the wave profile of RANS calculation showed that the peak region of k-profile did indeed correspond to the descending wave region. It is interesting that our calculations also provide a similar trend although no surface wave profile was applied in our LES. This indicates that some wave information may be present implicitly in the inflow boundary data.

Figures 4.13 and 4.14 show the inlet flow-field as computed with RANS model and produced after the application of the RFG procedure, respectively. In figures 4.15-4.19 the velocity vectors on different vertical cross sectional planes are presented. Clearly, the large scale turbulent eddies (vortices) are captured. As can be seen from Fig. 4.17 the axial development of the flow shows the existence of unsteady vortices in the region around $X/L = 1$. These consist of two stable large bilge-type vortices, and an additional smaller vortices farther away from the axis. The axial development of the flow-field causes these vortices to weaken and drift in spanwise direction toward the outer region of the wake, where they eventually disappear (Fig. 4.19). Although there are no bilge vortexes at the inlet boundary, these structures are developed in the wake, which can be clearly seen in Figs. 4.15-4.19. This result gives more credit to our approach of inlet boundary specifications, which inherits most of the flow characteristics after the ship hull. The prediction of outward flow near free surface, and the streamwise evolution of the vortices, without largely being dissipated, are also very encouraging indications of the success of the present LES approach.

The vorticity contours on different vertical planes shown in Figs. 4.20 - 4.22 are indicative of the degree of resolution of the calculations. These structures are hard to see in Figures 4.15-4.19 due to relatively small magnitude of the velocity vectors. However, to demonstrate the small weak turbulence structures, like those in Fig. 4.18(a), we enlarged the velocity vectors in the areas containing turbulence structures corresponding to those in the vorticity contour plot and depicted them in Fig. 4.18(b). A corresponding area in the vorticity contour plot is also included in Fig. 4.22 for reference with the cross section taken at $x/L = 1.2$. Without interpolation, the weak vortices can not be seen in the velocity vector plot due to scale difference, whereas the interpolated contour plots do show small structures.

Figures 4.21 and 4.22 show again that much of the vorticity is concentrated near the free surface, and there are two large counter rotating vortexes on two sides of the wake in addition to several smaller ones which can play an important role in bubble dynamics.

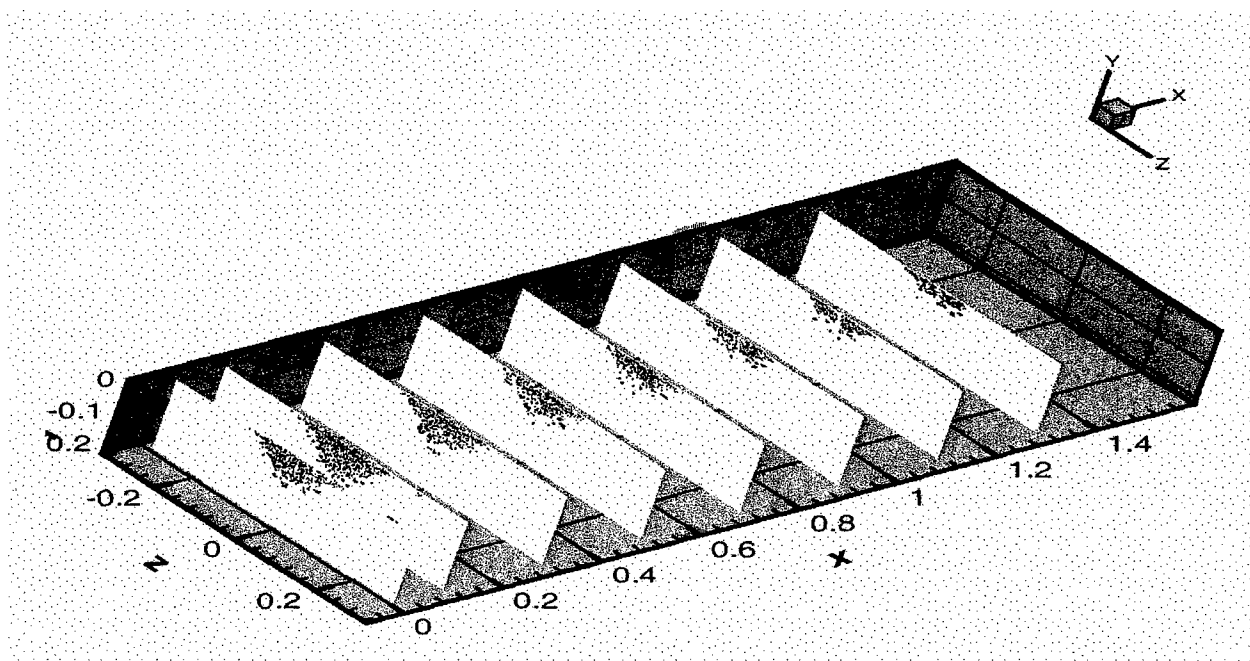


Figure 4.3: Typical instantaneous streamwise vorticity (ω_x) contours on different y-z planes in the wake of the ship model 5512

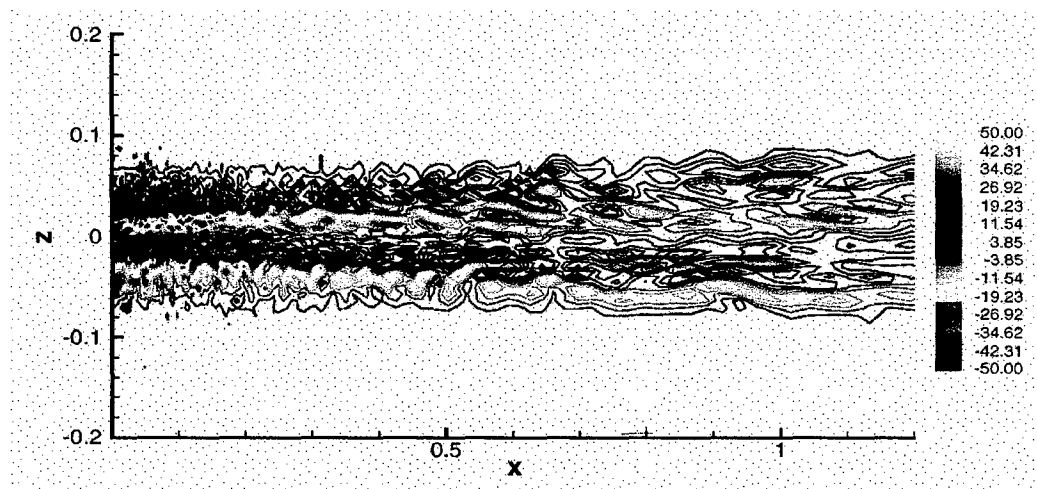


Figure 4.4: Typical instantaneous vorticity contours (ω_x) on a x-z plane parallel to free surface at $y/L = -0.01$ in the wake of the ship model 5512

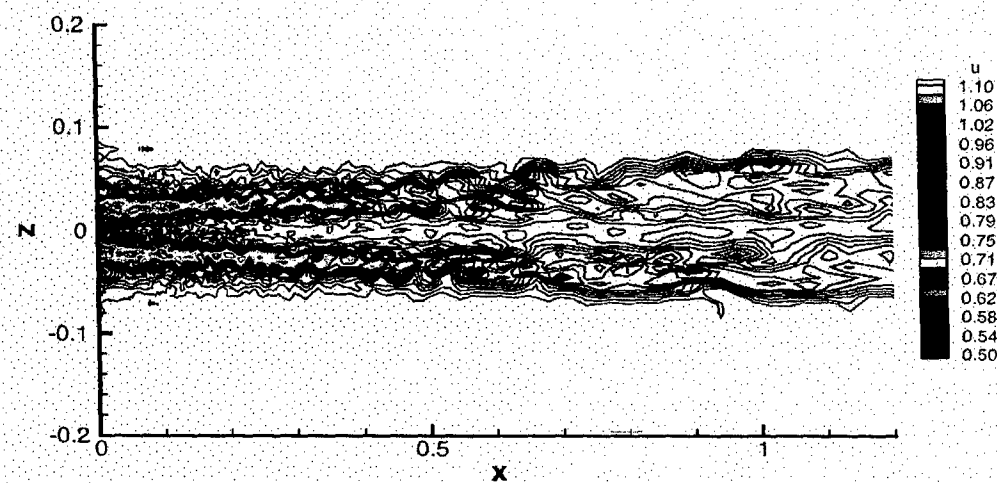


Figure 4.5: Typical instantaneous streamwise velocity contours on a x - z plane parallel to free surface at $y/L = -0.01$ in the wake of the ship model 5512

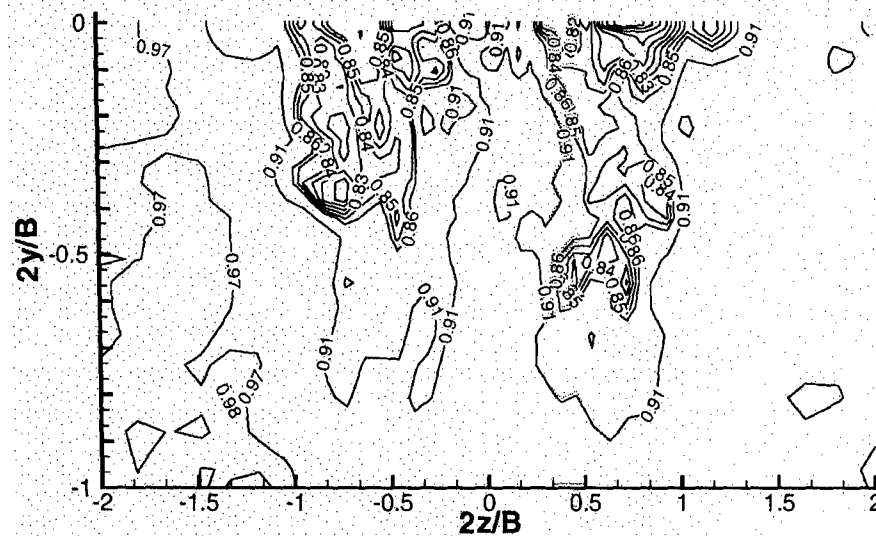


Figure 4.6: Axial velocity contours: $X/L = 0.61$.

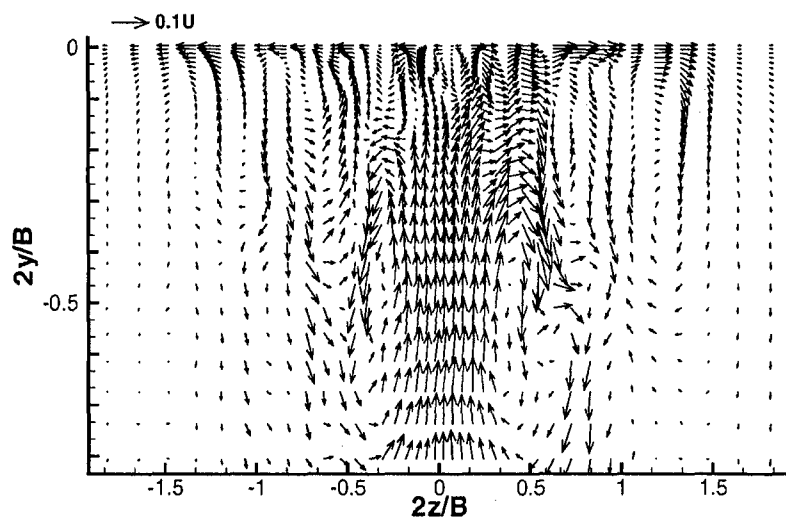


Figure 4.7: Velocity vectors: $X/L = 0.61$.

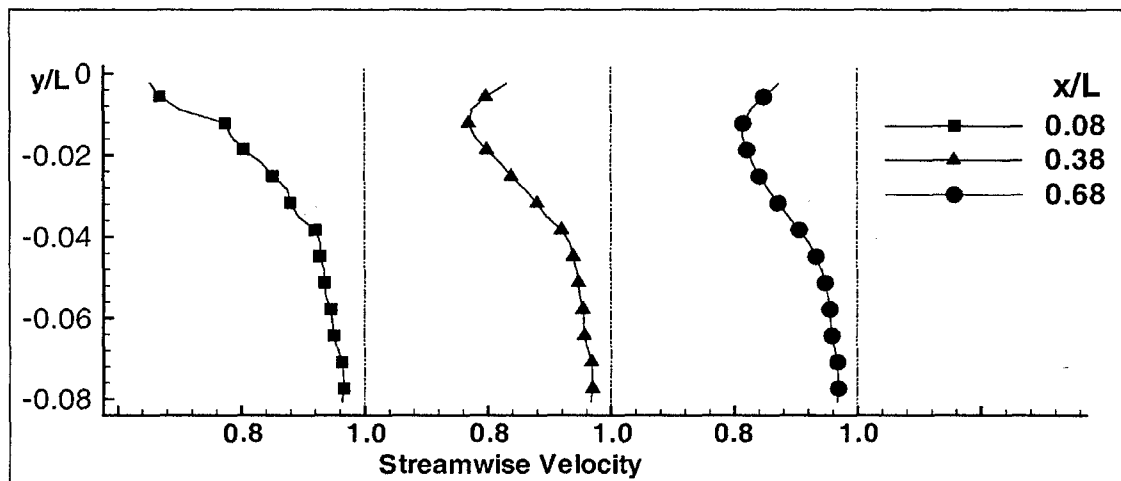


Figure 4.8: Streamwise mean velocity profiles in axial and vertical directions.

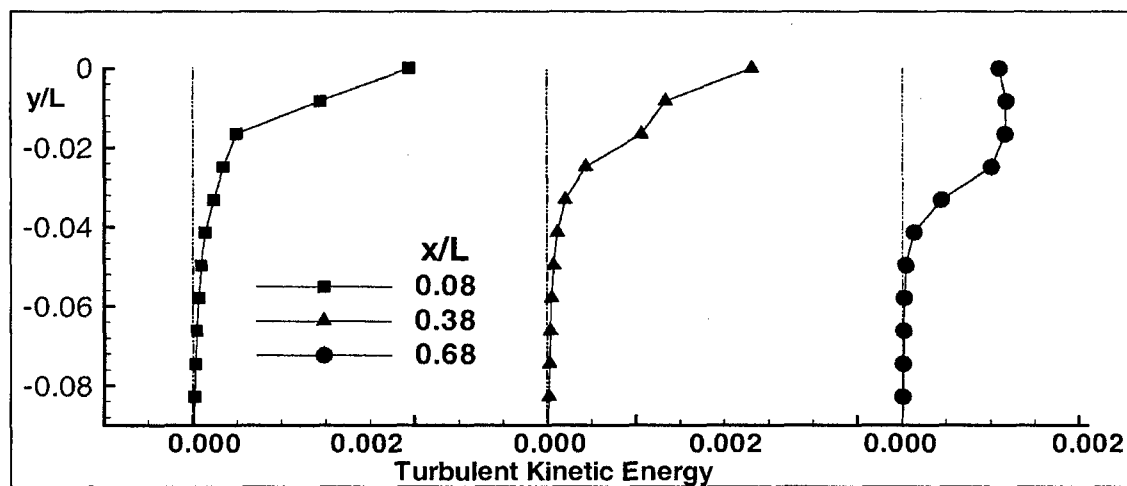


Figure 4.9: Turbulent kinetic energy variation in axial and vertical directions.

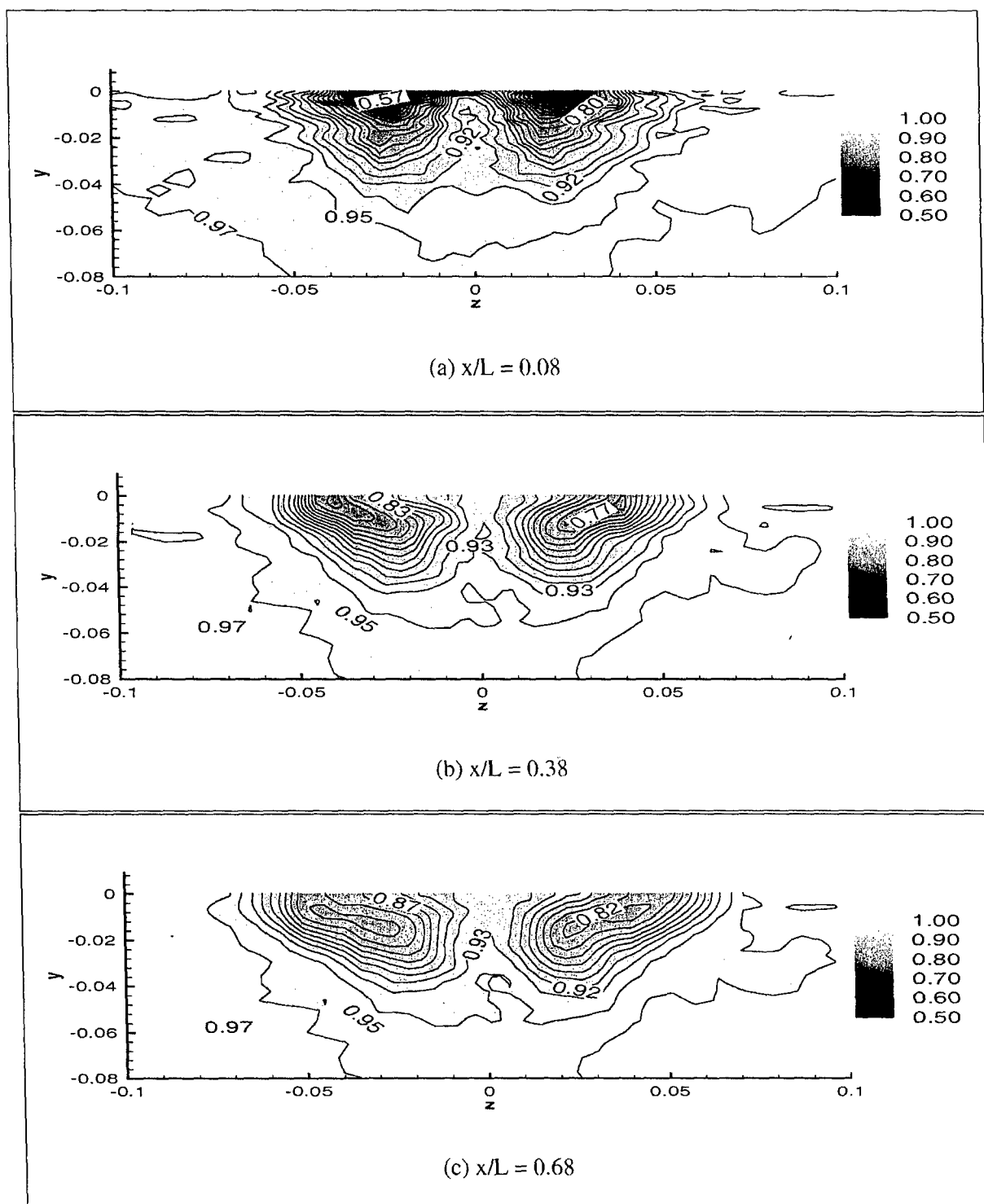


Figure 4.10: Axial mean velocity contours in the wake of the ship model 5512.

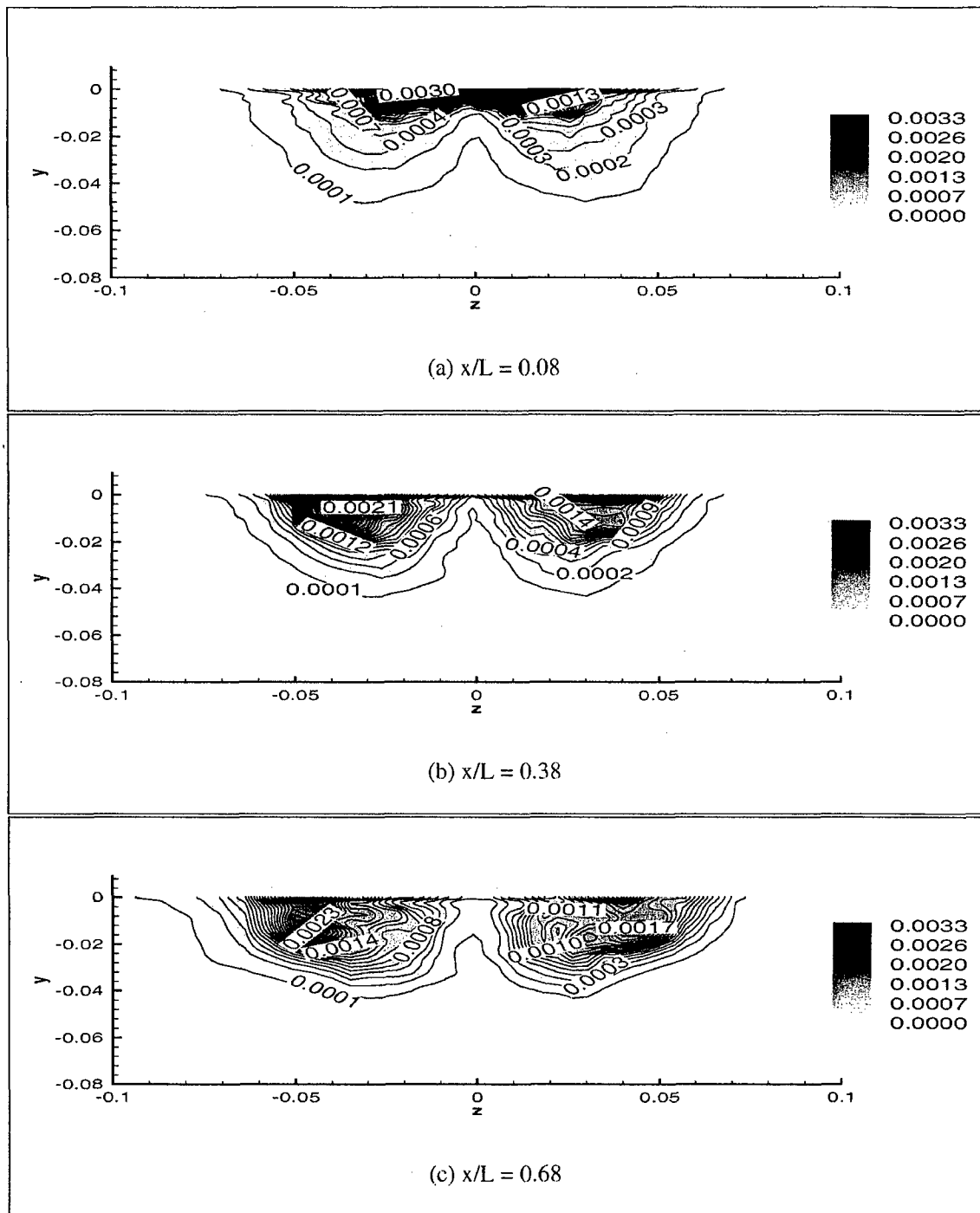


Figure 4.11: Turbulent kinetic energy contours in the wake of the ship model 5512

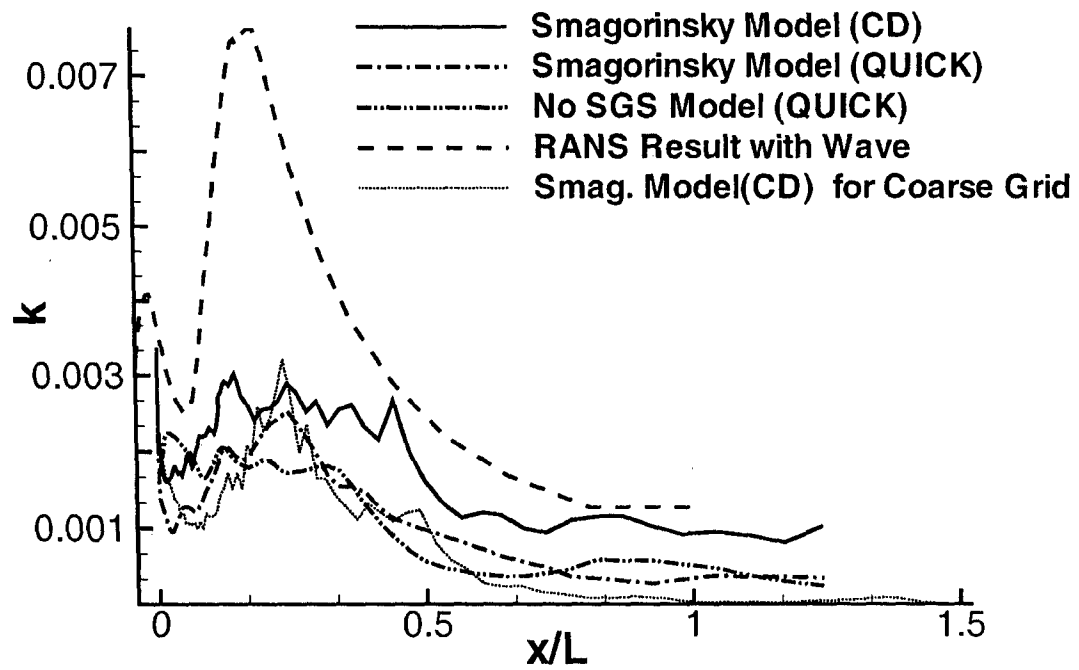


Figure 4.12: Comparison of resolved turbulence kinetic energy for different simulated cases; the wake of a ship model 5512

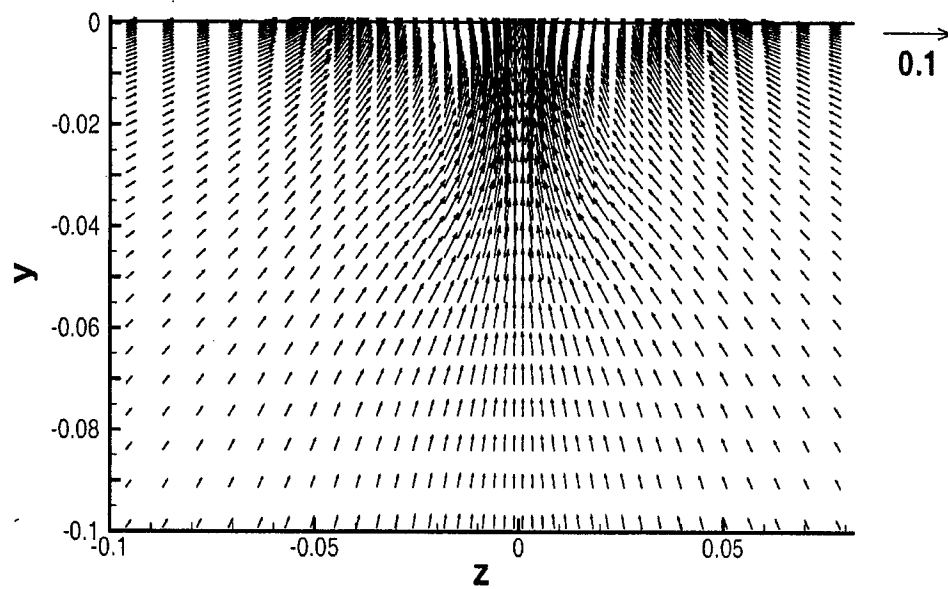


Figure 4.13: RANS solution at $x/L = 0.0$

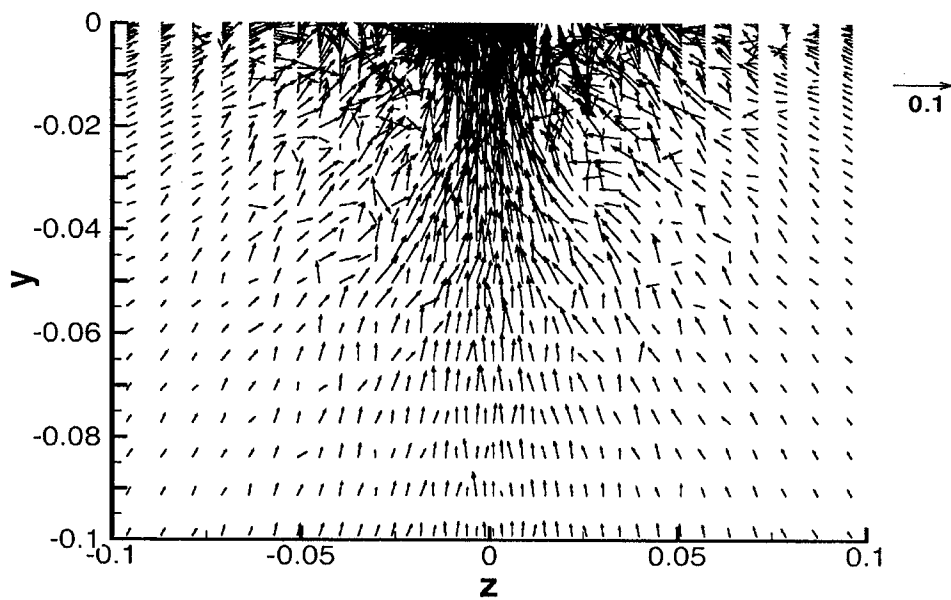


Figure 4.14: RANS+RFG solution at $x/L = 0.0$

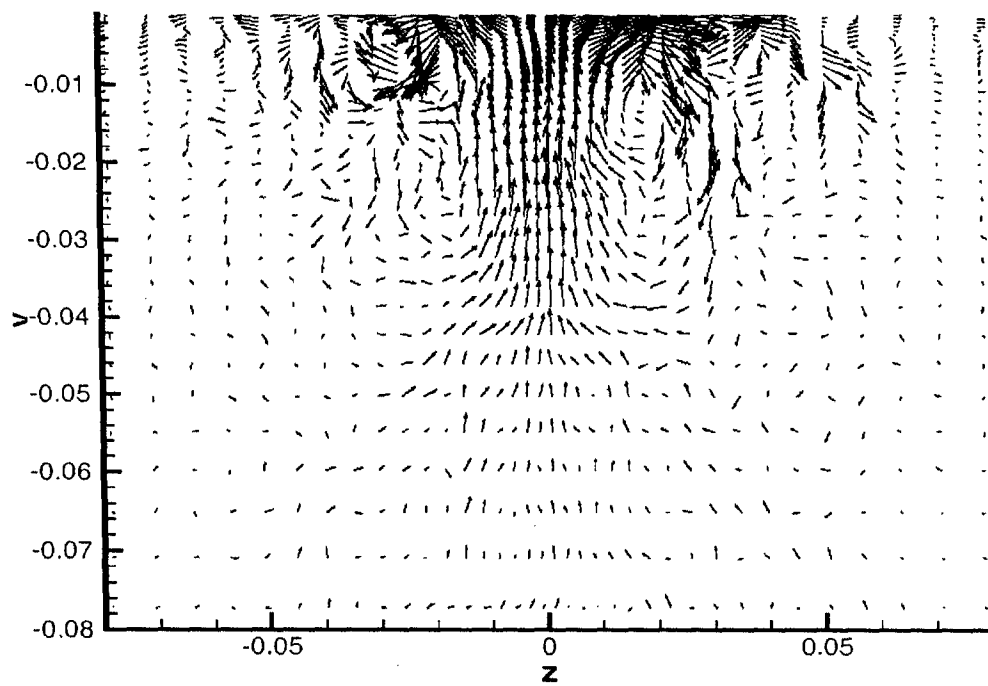


Figure 4.15: Typical instantaneous velocity vectors on y-z plane at $x/L = 0.2$ in the wake of the ship model 5512

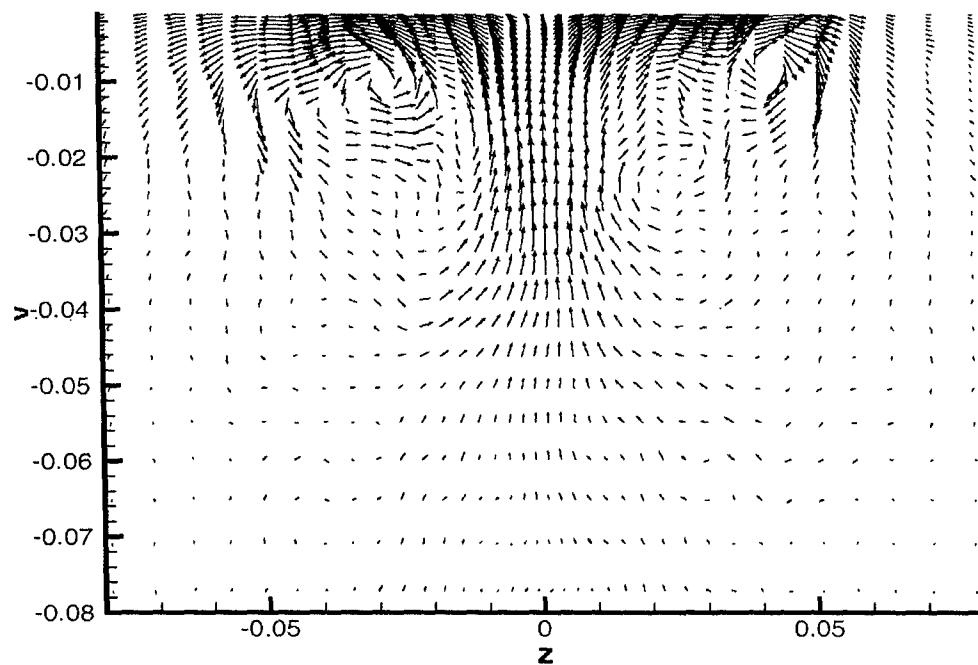


Figure 4.16: Typical instantaneous velocity vectors on y-z plane at $x/L = 0.6$ in the wake of the ship model 5512

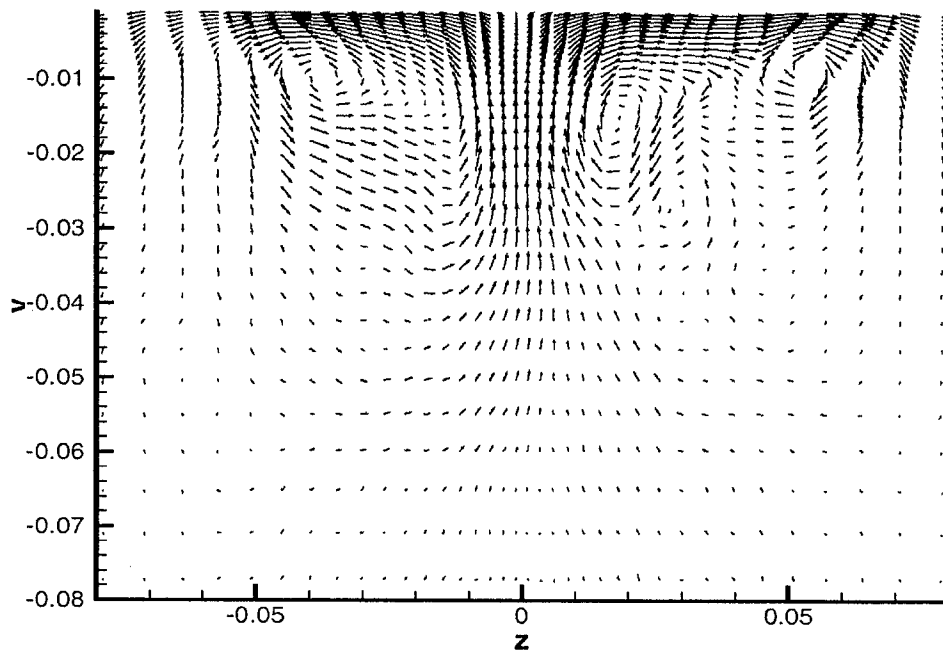


Figure 4.17: Typical instantaneous velocity vectors on y-z plane at $x/L = 1.0$ in the wake of the ship model 5512

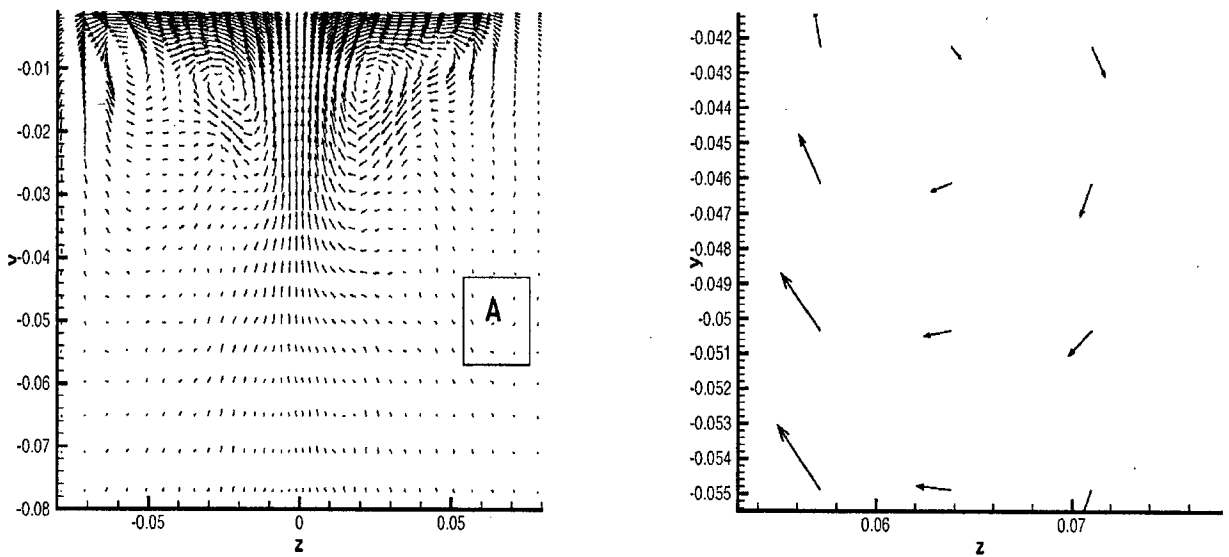


Figure 4.18: (a) Typical instantaneous velocity vectors on y-z plane at $x/L = 1.2$ in the wake of the ship model 5512 (b) The enlarged view of area A in Fig. 4.18(a)

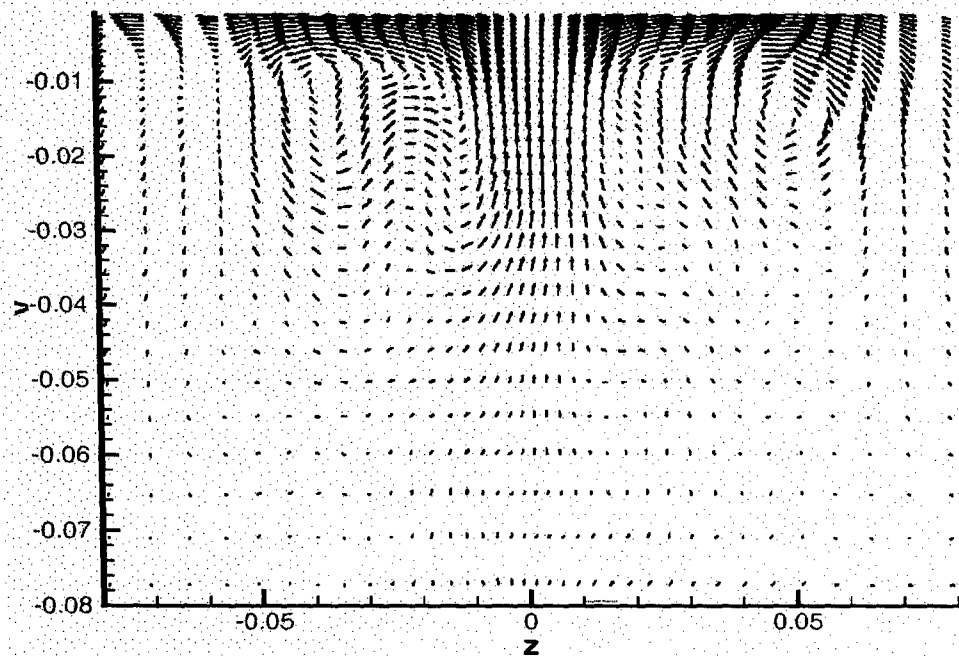


Figure 4.19: Typical instantaneous velocity vectors on y-z plane at $x/L = 1.4$ in the wake of the ship model 5512

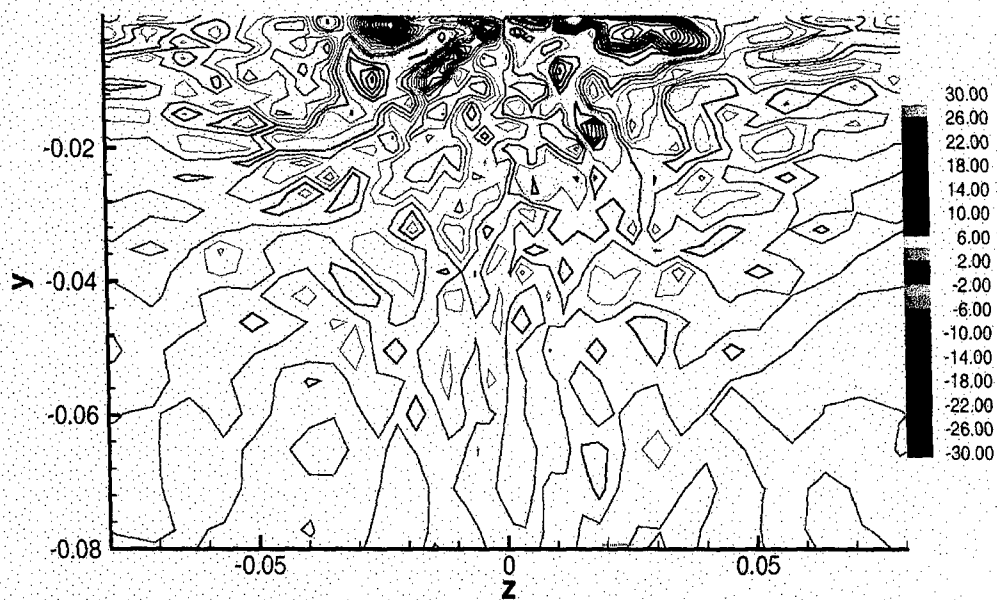


Figure 4.20: Typical instantaneous vorticity contours (ω_x) on y-z plane at $x/L = 0.2$ in the wake of the ship model 5512

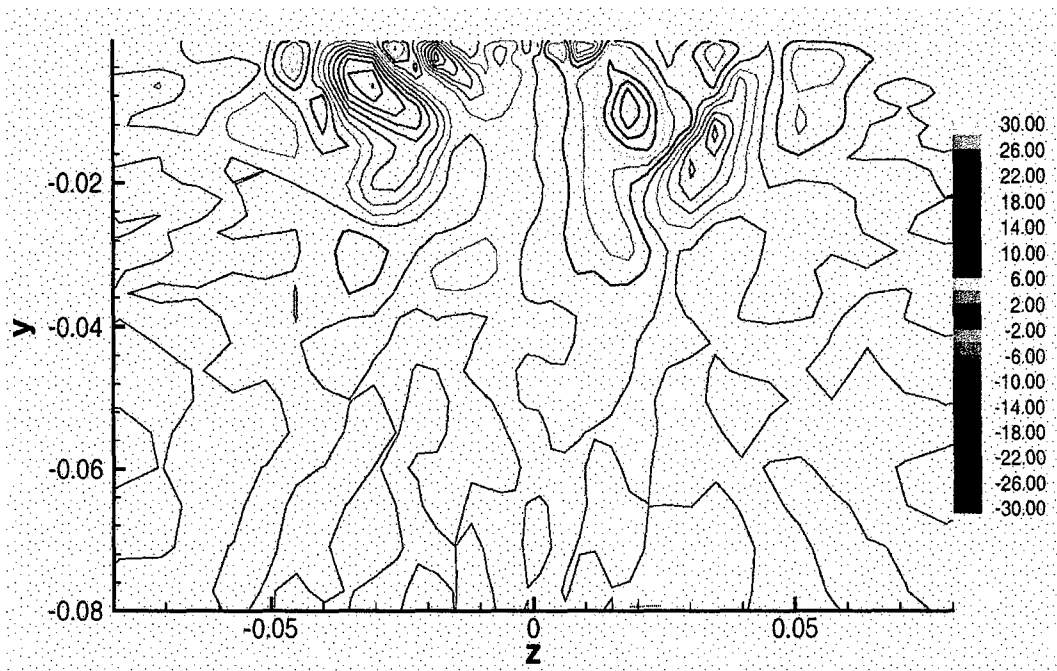


Figure 4.21: Typical instantaneous vorticity contours (ω_x) on y - z plane at $x/L = 0.6$ in the wake of the ship model 5512

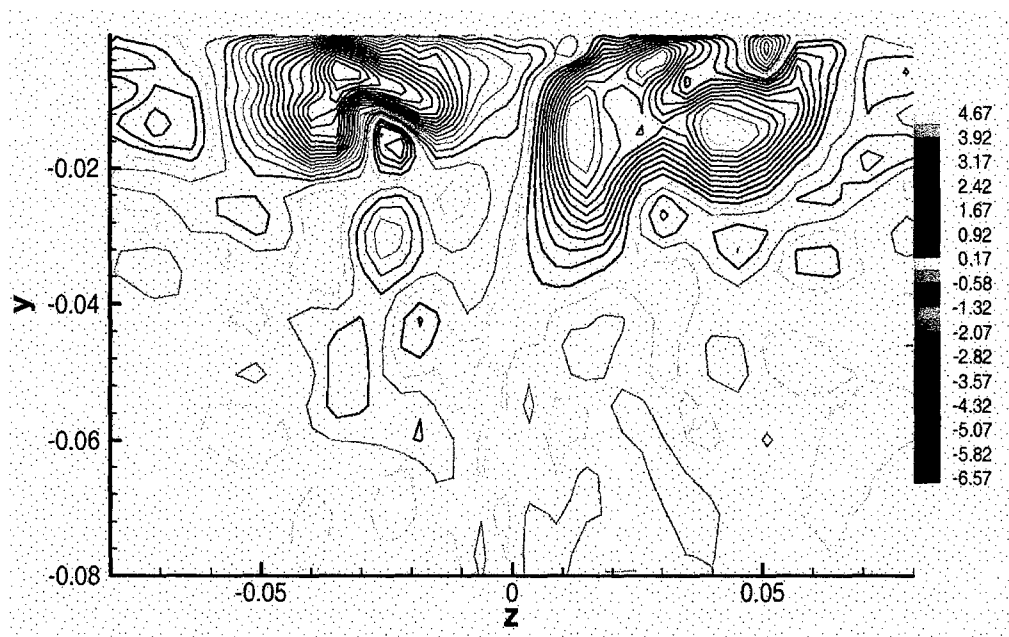


Figure 4.22: Typical instantaneous vorticity contours (ω_x) on y - z plane at $x/L = 1.2$ in the wake of the ship model 5512

4.4 Ship Wake Simulations on a Circular Track

As a first step for this study, a standard Smagorinsky model that forms the basis for the advanced models has been applied to investigate the influence of the Coriolis and centrifugal forces on turbulence generation on the ship wake flow field.

The focus of this study is the wake behind the Navy DDG51 surface ship, which is approximately 154 m long and 20 m wide, cruising on a circular track (see Figure 4.23). The average speed of the ship is assumed to be around 20 knots. The ship model data used for this simulation was taken from the data of DTMB 5415, a towing tank model representing a modern naval combatant, DDG51 (Stern et al., 2000). As stated in Shi (2001) and Yavuz et al. (2002), the ship hull is excluded from the LES calculations due to computational expenses and the computations were started from a plane aft of the ship. This is accomplished using the RFG technique, originally developed at West Virginia University, which calls for a time averaged flow field at the inlet data plane. Reynolds Averaged Navier Stokes (RANS) calculations (Hyman, 2001) (steady state RANS calculations around the ship hull) are used to provide the RFG procedure with the information needed on the inflow boundary (initial data plane) located 0.5L after the body in the wake. In other words, the pseudo random flow field generated by the RFG technique is added to the mean flow of the RANS simulations in order to provide the boundary condition at the inlet plane. The further development of the wake flow is calculated via LES (non steady LES of the wake). LES of high Reynolds number flows with complicated geometries are enabled by this combined approach (Smirnov et al., 2000). Therefore, the effect of the ship body on the flow field is embedded in the mean flow prescribed at the inflow plane. However, this technique, also known as the Initial Data Plane (IDP) approach (Hyman, 1998, Paterson et al., 1996) can introduce considerable errors (Hyman, 1998), as a matter of fact that the body generating the wake is not included in the non-steady LES simulations. It should be noted that it is possible to predict turbulence via LES technique by starting from a mean flow obtained from RANS. However, it takes a very long time for a turbulent flow to develop spatially and temporally without any initial perturbation. Also for some engineering applications, it may be too expensive in terms of computer resources and programming effort.

4.4.1 Conditions and Grids

As stated above, the ship model DTMB 5415 is a 5.72m long model of the Navy DDG51 surface ship (Stern et al., 2000). A computational domain of $1.75 \times 0.15 \times 1.0$ (given in non dimensional units in ship lengths and it starts from $x/L=1.50$, where $x/L=1$ is the end of the ship model) and a grid of $66 \times 33 \times 66$ (Coarse Grid) (Case-1) in x (axial), y (vertical), z (transverse) directions has been used to represent the near wake region. This grid configuration has been selected to quickly assess the effect of the Coriolis and centrifugal forces on the turbulence characteristics. It should be noted that a thorough study was not conducted as to whether the side boundary is far enough away from the wake. In the IDP plane, the RFG method is used in conjunction with the RANS calculations (Hyman, 2001) and the ship's stern is at $(0.5, 0, -3.0)$ in x -, y -, z - directions respectively. The core region of the numerical grid and the geometry of the ship model are illustrated in Figure 4.24 (a) & (c). The ship turns with a dimensionless angular velocity of $1/3$ (Figure 4.24 (b)) with a radius of curvature corresponding to three dimensionless ship lengths, which will result in a dimensionless ship velocity of 1. Only a 30° turn was investigated. Two Reynolds numbers have been used in the simulations. One is based on the real ship length, i.e. 1.5×10^9 stated as Case-1 and the other based on the model ship length, i.e. 1.0×10^7 stated as Case-2. Here, Reynolds number similarity is assumed, which is attained by changing the laminar viscosity of the fluid in the simulations.

The coordinate system used is with respect to an observer on the ship. The Smagorinsky constant used in the eddy viscosity relation is calculated to be 0.042 from scaling with the non-turning simulations (Shi, 2001). Moreover, a simulation with relatively fine grid in the axial direction has been conducted to investigate the grid sensitivity of the predictions. This grid consists of $130 \times 33 \times 66$ nodes (Medium Grid) for Case-1 in x , y , and z directions, respectively. Non-uniform grids were used in this study in both x and z directions with the expansion ratio not exceeding 1.03. The length scale and time scale used in RFG are calculated from $\tau = k/\epsilon$ and $l = 0.09k^{1.5}/\epsilon$, non dimensionalized by free stream velocity and ship length. A comparison of the results from using Smagorinsky constants, 0.065 (selected to be the constant for the non-turning ship simulation) and 0.042 has been presented for the relatively fine simulations. Then, the grid of $130 \times 50 \times 110$ (Fine Grid) and $190 \times 50 \times 110$ (Finest Grid) for Case-2 have been used to analyze the physics of the wake behind a turning ship. Finally, to investigate the effect of the free surface, another study has been conducted with fine grids for the model ship simulation. The

time step is 0.001 for all grid resolutions. On an Intel Pentium 4 3GHz machine, CPU-time and memory requirements were approximately 226 hours for one flow through time (time required for the flow to pass in the calculation domain, $x=1.75L$) and 491 MB respectively, for the fine grid simulations with the standard Smagorinsky model.

On the other hand, Shi (2001) and Shi et al. (2006) applied LES on the wake flow of the ship model DTMB 5512 (Longo et al., 1993, Gui et al., 1999, Stern and Wilson, 2000). A 3.048m long unpropelled model of a modern U.S. Navy fleet ship, Arleigh-Burke class destroyer, DDG51, with a Reynolds number of 4.65×10^6 cruising on a straight track has been investigated. The computational domain was $1.5 \times 0.3 \times 0.6$ (given in non dimensional units in ship length) in x -, y -, z -directions, respectively, with a grid size of $162 \times 50 \times 66$ and $322 \times 50 \times 66$. Non-uniform grid spacing with stretching smaller than 1.03 was used in both x and y directions.



Figure 4.23. Arleigh-Burke class destroyer (DDG51)

4.4.2 Boundary Conditions

For all simulations, the velocity components at inflow boundary plane are set equal to those calculated via RANS simulations by Hyman (2001) (see Figure 4.24. (b)) plus the fluctuating velocity component obtained from the RFG technique. The outflow boundary is assumed to be a free gradient boundary. At the top and bottom boundary surfaces a symmetry boundary condition is applied. At the free surface (i.e. the top boundary), a slip is allowed in x and z directions but the velocity component normal to the free surface is set to zero (as such the free surface is approximated as a moving flat plane; where the free surface is completely flat). The boundaries in the transverse direction are treated as stream surfaces, where the tangential velocities are specified using the turning ship velocity as a base and by accounting for the turning of the ship via a rigid body motion, such as,

$$\bar{u}_t = \Omega_s * \left(\frac{R^* - z^*}{L} \right) \quad (4.1)$$

Ω_s = the angular velocity of the system rotation due to the turning ship

R^* = the radius of the curvature, $R^* = 3.00L$

z^* = the distance measured from the centerline in the positive z direction

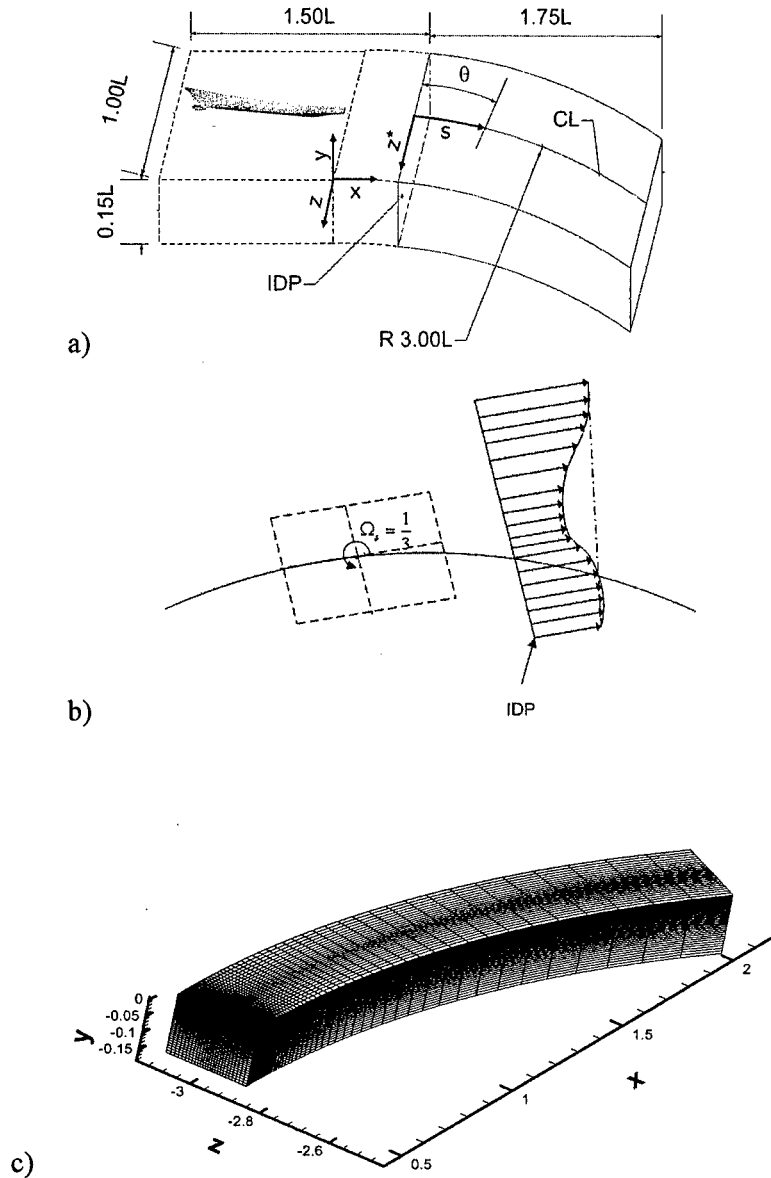


Figure 4.24. Turning ship wake: a) The geometry b) velocity profile specified at the IDP (top view) c) The coordinate space system and numerical grid (Only the core region is shown, distances are non-dimensionalized with ship length, L)

4.4.3 Results and Discussions

Figure 4.25 shows the instantaneous vertical velocity contours with Coriolis force (Case-1) at different y-z planes in the turning ship wake. This figure has been included to help the reader to visualize the cross sectional planes taken at different angles (5° , 10° , 15° , 20° , 25° , 30°). Figure 4.26 shows the radial velocity profiles at two different y-z planes (5° , 10°) for fine grid in order to check the boundary conditions specified in the transverse direction. The figure confirms that the LES code treats the boundaries in the transverse direction as stream surfaces. The unsteady velocity fluctuations are compared for cases with and without Coriolis force (Case-1) in Figures 4.27 to 4.28. The figures show the streamwise velocity components versus nondimensional time at an angle of 10 degrees measured from the inlet plane z. From approximate calculations, the resolved frequency of the velocity fluctuations is obtained to be around 4.7 Hz in all three directions with the Coriolis force and 3.5 Hz without the Coriolis force. This indicates that the Coriolis force tends to increase turbulence activity. In order to compare the results of the turning and non turning ship wake cases, a scaling has been done such that, $(C_s \Delta^2)_{\text{nonturn}} \cong (C_s \Delta^2)_{\text{turn}}$. From Shi's (2001) non turning ship wake calculations, C_s is set to be 0.065. Using the above scaling, C_s of 0.042 has been calculated and used for the medium grid simulations.

For fine and finest grid simulations, similar logic has been carried out in order to obtain C_s values in the Smagorinsky model. For the medium grid, the resolved frequency is around 9Hz for $C_s=0.042$ and 7 Hz for $C_s=0.065$. The frequencies are approximately calculated from the temporal history curves of all three directions, such that one over the difference of the two crest points divided by the time difference in those crest points gives the approximate frequency. If the Smagorinsky constant is smaller, the frequency obtained is higher, which implies that more energetic turbulent fluctuations are captured. This is an indication that higher frequencies and smaller turbulence scales are captured with the relatively fine grid for both values of the Smagorinsky constant. Hence, physical intuition and simulations give similar conclusions.

Figures 4.30-4.32 present the velocity vectors at vertical cross-sections at an angle of 5° with the z-axis. Note that R is taken to be minus to be consistent with the minus z- direction, that is calculated from $R = \sqrt{(x-0.5)^2 + y^2}$. The coarse grid case in Figure 4.30 with the Coriolis force shows better-defined turbulent structures or eddies than the case without the Coriolis force

in Figure 4.31, which seems to be more diffusive. Here, one could argue that the Coriolis force helps to maintain the turbulent structures of the flow. Moreover, the medium grid predictions with the Coriolis force presented in Figure 4.32 indicate even a lesser diffusion (or smearing) for both values of Smagorinsky constant. Here, it can be seen that the vortical structures are not penetrating as deeply as in the coarse grid case. Experimental observations of Matsubara and Alfredsson (1998) have shown that the Coriolis force may give rise to instabilities in the form of longitudinal vortices which supports the above assertions.

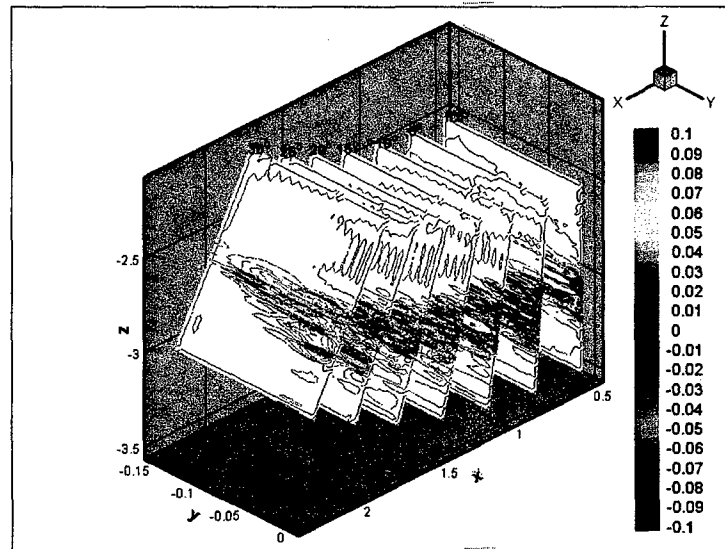


Figure 4.25. Typical instantaneous vertical velocity contours with Coriolis force on different y-z plane in the turning ship wake (coarse grid)

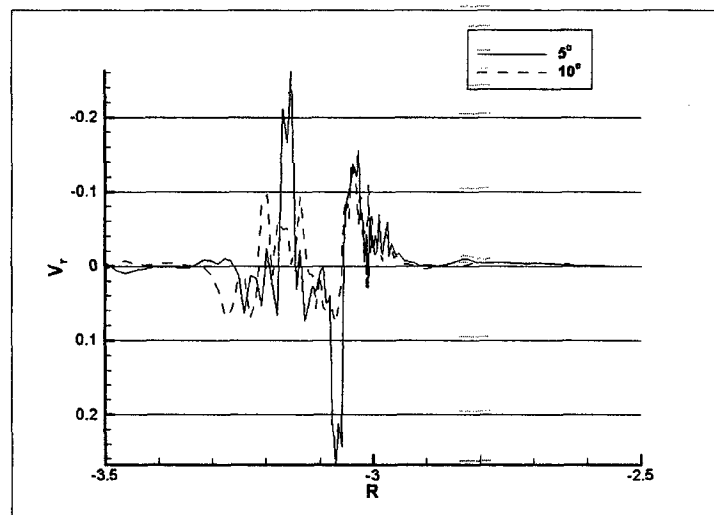


Figure 4.26. Radial velocity profiles on different y-z planes in the turning ship wake (fine grid)

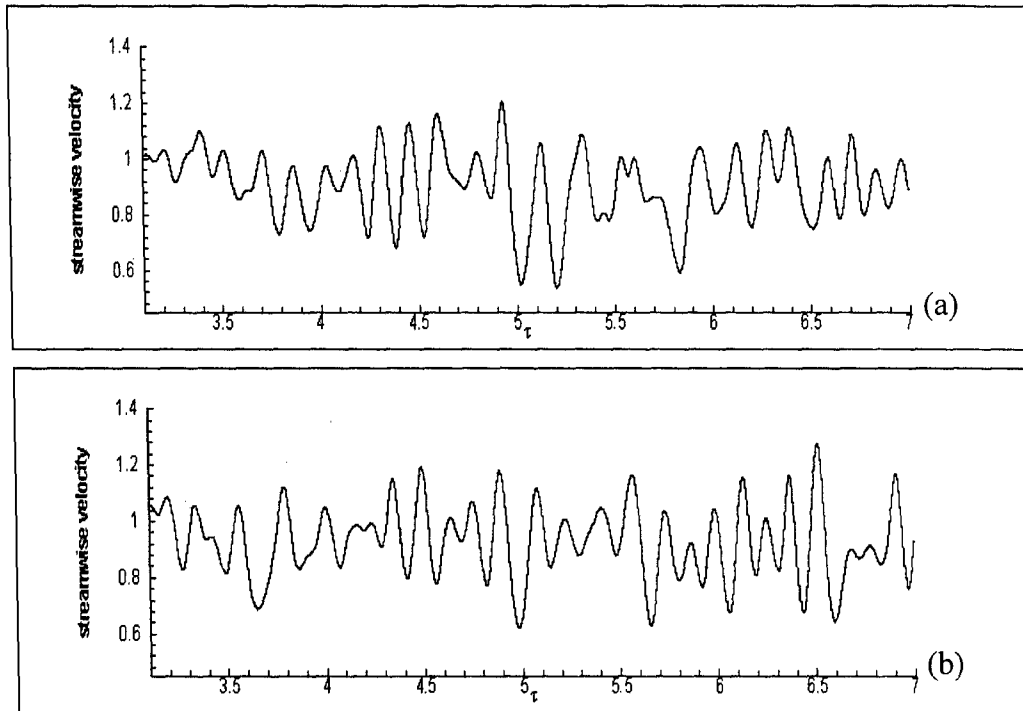


Figure 4.27. Temporal history of streamwise velocity components at 10° with the z axis, and $x=1.02$, $y=-0.002$ (coarse grid), a) w Coriolis force b) w/o Coriolis force

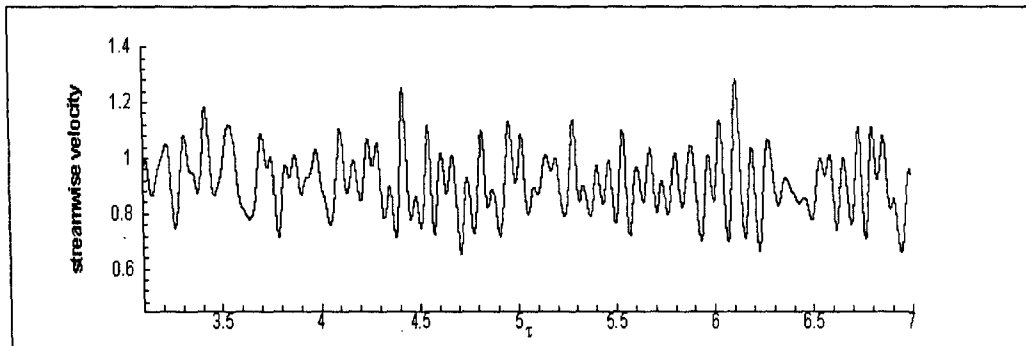


Figure 4.28. Temporal history of streamwise velocity components at 10° with the z axis, and $x=1.02$, $y=-0.002$ (medium grid), $C_s=0.042$

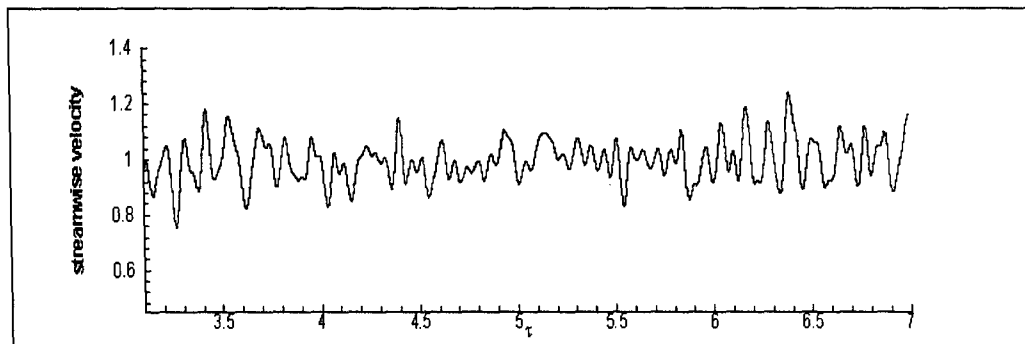


Figure 4.29. Temporal history of streamwise velocity components at 10° with the z axis, and $x=1.02$, $y=-0.002$ (medium grid), $C_s=0.065$

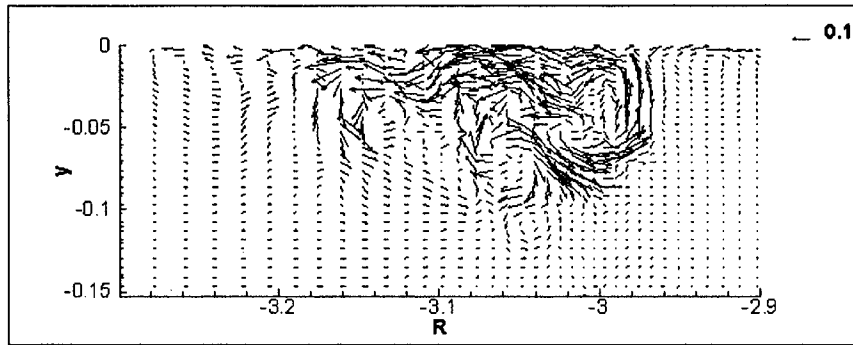


Figure 4.30. The velocity vectors on a vertical plane at an angle of 5° with the z-axis with Coriolis force (coarse grid)

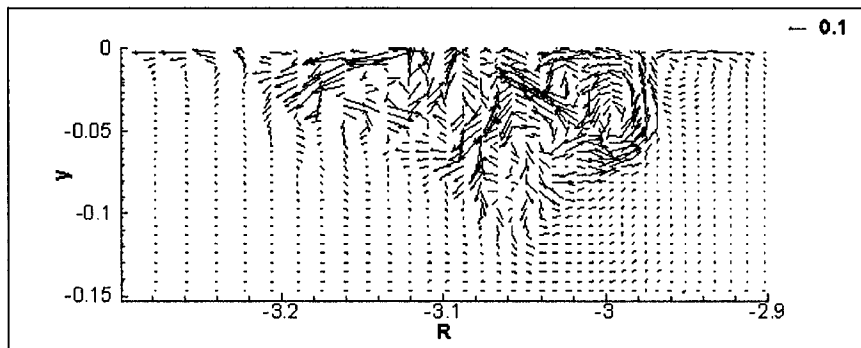


Figure 4.31. The velocity vectors on a vertical plane at an angle of 5° with the z-axis without Coriolis force (coarse grid)

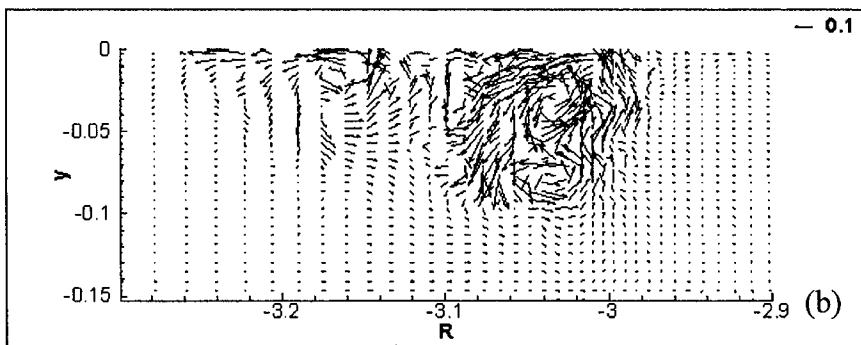
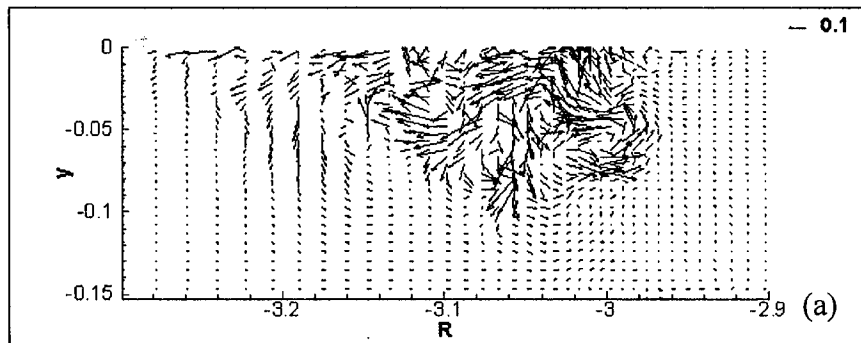


Figure 4.32. The velocity vectors on a vertical plane at an angle of 5° with the z-axis (medium grid) a) $C_s=0.042$ b) $C_s=0.065$

The velocity vectors on vertical cross-sections at an angle of 25° with the z-axis are shown in Figures 4.33-4.34. Although, similar structures in both near the inlet data plane and near the outlet are observed, the intensity of the velocity fluctuations diminish as the outflow plane is approached due to grid expansion. Moreover, it is seen that away from the wake centerline, the strength of the flow structures has already died in both cases. In the far downstream portion of the calculation domain, larger turbulent structures are seen to be merging with the smaller structures. Still, a significant level of vorticity can be captured in both cases. Overall, it is seen that one large vortex, presumably the one originating from the ship hull persists without significant dissipation.

A comparison of the resolved turbulence kinetic energy is shown in Figure 4.36. In calculating the kinetic energy values, the samples were taken to be 10000 time steps from 2 flow through times data (=35000 time steps). It is observed that due to the coarse grid towards the end of the calculation domain, vorticity (hence turbulence) decays rapidly, however the medium grid predictions have a very gradual decay of turbulent kinetic energy. For the coarse grid simulations, turbulence decays more rapidly due to the numerical dissipation. The kinetic energy values obtained from the case with Coriolis force is slightly higher than that of the case without Coriolis force, as expected. As seen from the figure, the adjustment of the Smagorinsky constant is necessary, as the kinetic energy values obtained with $C_s=0.042$ are almost on the same level as the ones obtained from the non-turning ship simulations(Shi, 2001). These observations allude to the fact that the Smagorinsky constant should be adjusted for streamline curvature effects. The turbulence intensity specified at the inlet was observed to decay rapidly, which was mainly due to the nature of the coarse grid used. For this reason a medium grid simulation has been performed. This improved the turbulent kinetic energy prediction and more detailed turbulence structures were captured.

Similar conclusions could also be drawn from the vorticity contours. Calculations showed that the highest and lowest vorticity magnitudes are more pronounced in the case with the Coriolis force, whereas the case without the Coriolis force shows a more diffused or smeared picture. The vorticity results again indicate that the Coriolis force keeps the vorticity concentrated in the flow-field.

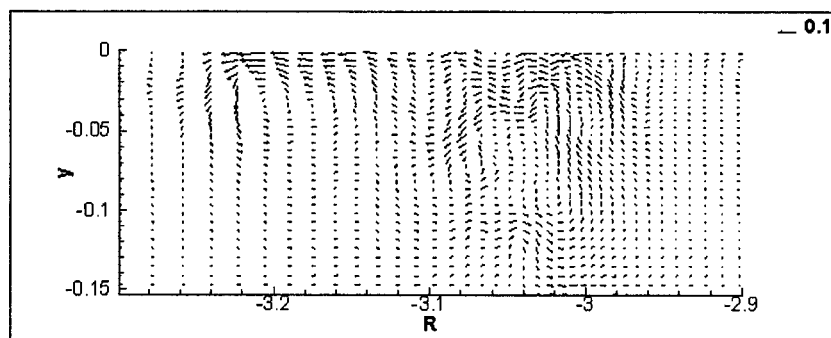


Figure 4.33. The velocity vectors on a vertical plane at an angle of 25° with the z-axis with Coriolis force (coarse grid)

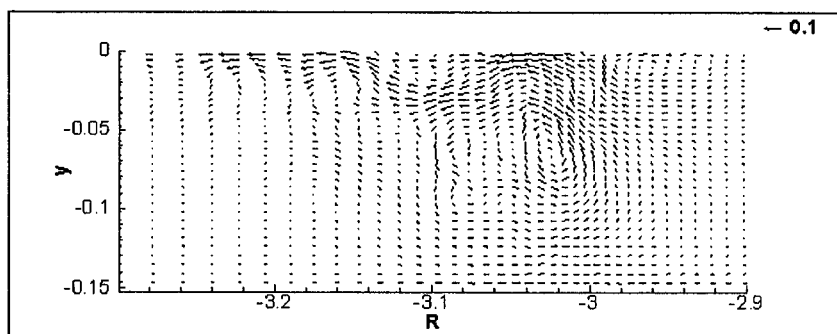


Figure 4.34. The velocity vectors on a vertical plane at an angle of 25° with the z-axis without Coriolis force (coarse grid)

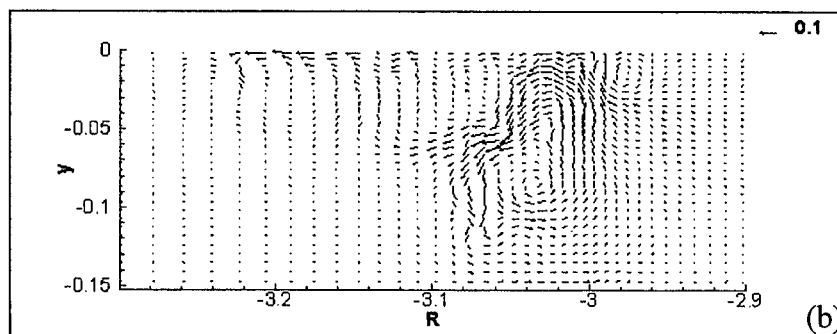
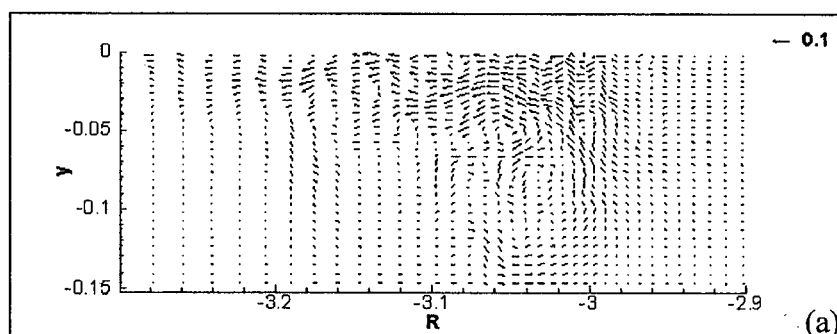


Figure 4.35. The velocity vectors on a vertical plane at an angle of 25° with the z-axis (medium grid) a) $C_s=0.042$ b) $C_s=0.065$

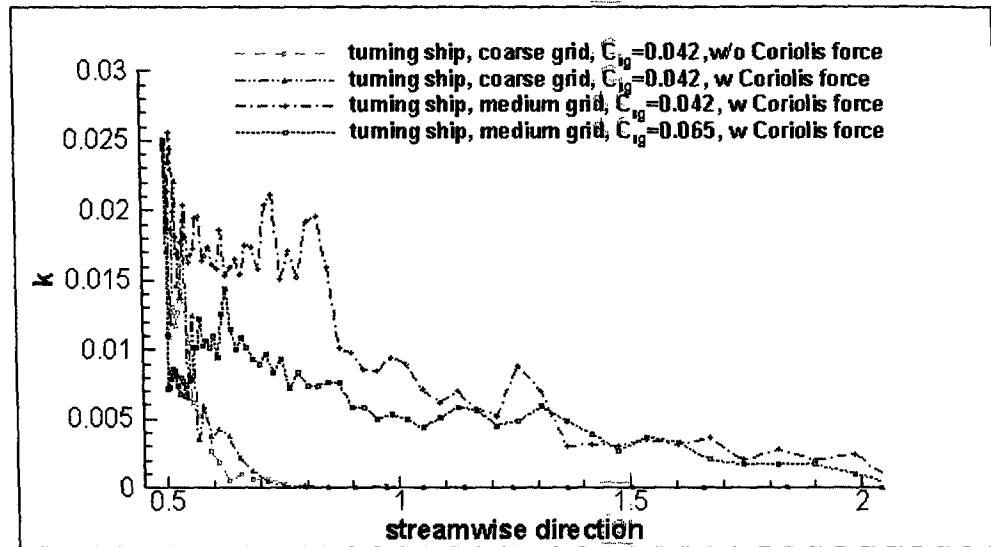


Figure 4.36. The comparison of the resolved turbulence kinetic energy for ship cruising on a circular track

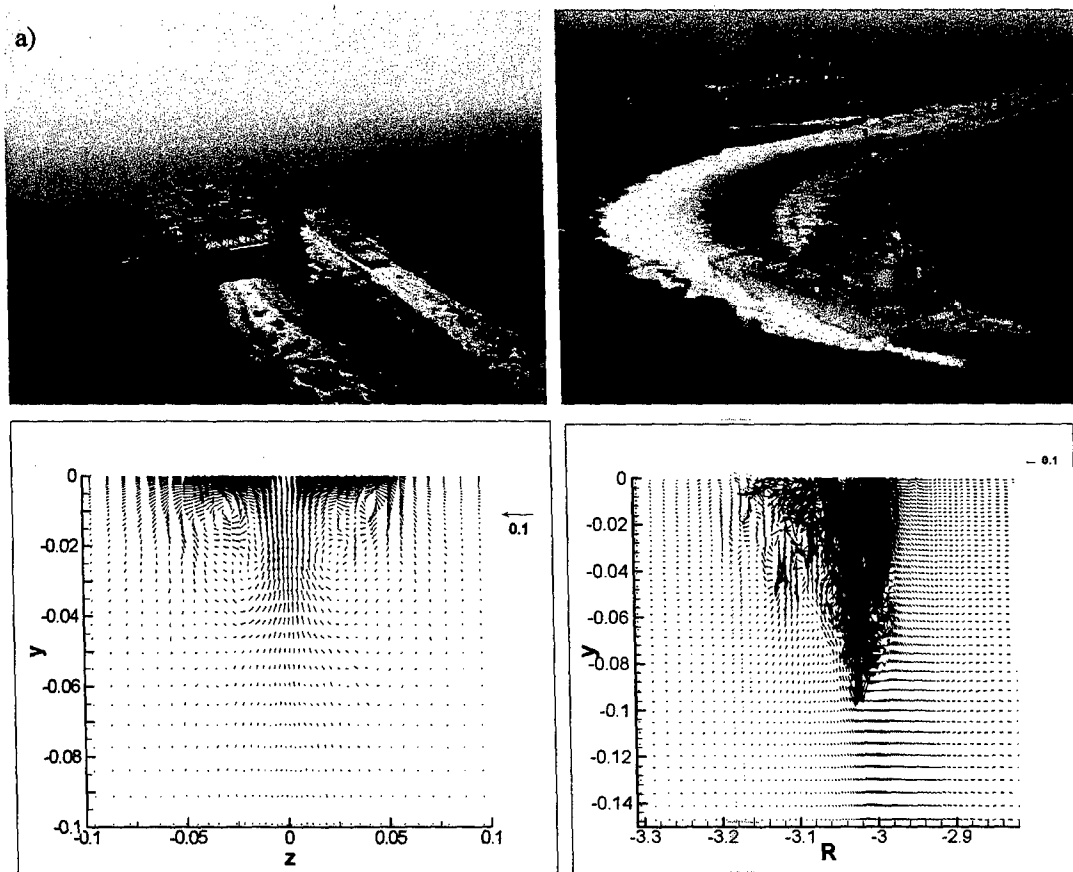


Figure 4.37. Velocity vectors at $x/L=0.2$: a) Non-turning ship (Shi et al. 2001) (fine grid) b) Turning ship (fine grid)

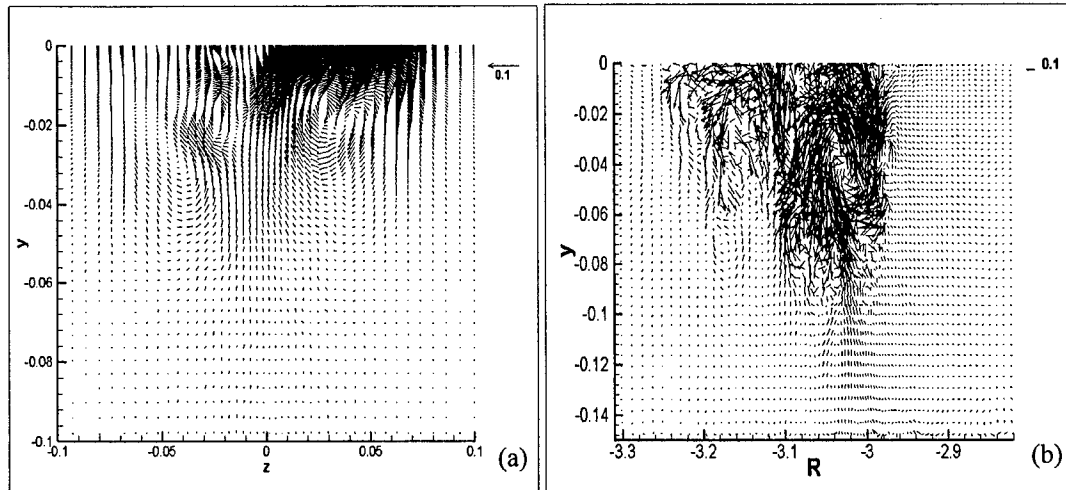


Figure 4.38. Velocity vectors at $x/L=0.65$ a) Non-turning ship (Shi et al. 2001) (finest grid) b) Turning ship (finest grid)

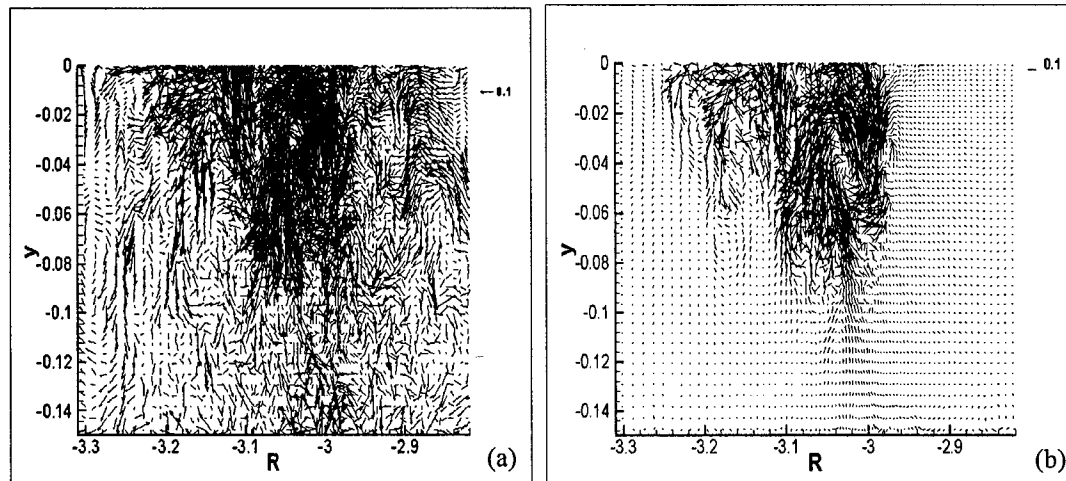


Figure 4.39. Velocity vectors at $x/L=0.65$ for turning ship wake a) Case-1; $Re=1.5 \times 10^9$: DDG51 (finest grid) b) Case-2; $Re=1.0 \times 10^7$: DTMB 5415 (finest grid)

The goal of this preliminary study was to assess the effects of the Coriolis and centrifugal forces on the vortical structures or turbulence characteristics of the flow in the wake of a turning ship using the large eddy simulation technique. The eddies resolved by LES have been observed to be more energetic and less diffusive when the Coriolis force was included. It seems as if this force supplies energy to the large turbulent structures and thus enhances anisotropy. The vorticity contours show a non-symmetric wake development with significant stretching in the radial direction away from the center of rotation. This is also seen from the velocity vectors comparison of non-turning and turning ship studies in Figures 4.37 & 4.38. As these figures show the non-

turning ship case has a symmetric wake with respect to the wake centerline, whereas in the turning ship case, there is a significant flow present in the radial direction that is believed to be caused in part by the centrifugal force, arising from turning of the ship. Here, the simulation of the model ship with grids of 130x50x110 and 190x50x110 has been studied to compare the results with the non-turning ship wake.

A study of the effect of Reynolds number for Case-2 and Case-1 using 190x50x110 grids is shown in Figure 4.39. This comparison can be done since all the values are nondimensionalized with respect to their ship velocities, either real ship or the ship model. The velocity vectors are at the same location, $x/L=0.65$ and standard Smagorinsky model has been used. When the Reynolds number is low, the turbulence structures are observed to be more visible, well defined and more diffusive. However for high Reynolds number flows, there are certain unorganized structures seen in the flow field and the flow structures seem to be less diffused. As the wake develops, the flow structures disappear rapidly for Case-1; however, for Case-2, the flow structures are observed to be still well defined. The unsteady velocity fluctuations are also compared for Case-1 and Case-2 in Figures 5.40. The resolved frequency of the velocity fluctuations is estimated to be around 40 Hz in all three directions for Case-1 and 30 Hz for Case-2. Here, 30 Hz and 40 Hz seem to correspond to large bilge vortex passage. If the Re is higher, the frequency obtained is higher, which is an indication that smaller turbulent structures are captured with high Reynolds number. The period (hence frequency) can also be approximated from the roughly eddy turnover, which is $T = \text{largest eddy size} / \text{ship velocity}$ where at 10° , the largest eddy size is approximately 0.04 from Figure 4.45 (b) and the ship velocity is 1, therefore $T = 0.04/1 = 0.04$, $f = 1/T = 25\text{Hz}$, which is close to 30Hz.

Although the classical Smagorinsky SGS model is not that suitable for complex flows as it uses a constant eddy viscosity coefficient for the entire domain, this study has shown that it can be used as a SGS to predict the flow dynamics of the wake behind a turning ship reasonably well.

4.4.4 Properties of Turbulent Ship Wakes

The mean inflow boundary data was obtained by slicing the RANS solution at $x/L=1.5$ plane for turning ship wake and $x/L=1.05$ for the non turning ship wake and then interpolated to the inlet plane of the computational domain. The mean axial velocities for both non turning and

turning ship wake after the interpolation are presented in Figure 4.41 (a) and (b). To see the effect of the LES wake calculation only, the axial velocity contours are adjusted due to rotation and the mean axial velocity adjusted for rotation at the IDP ($x/L=1.5$) for turning ship wake is given in Figure 4.41 (c). By using RFG and the mean flows on these planes, the turbulent inflow boundary for both ship simulations was reconstructed. Figure 4.42 presents the pseudo random flow field generated by the RFG on the IDP for turning ship wake. From the axial velocity contours in Figure 4.43(a), two stable large bilge type vortices are observed for the non-turning ship wake simulation using the standard Smagorinsky model ($Re=4.65 \times 10^6$) at $x/L=0.65$. Two small side vortex pairs are observed away from the center of the wake. These vortex pairs drift in the spanwise direction, get weaker and eventually disappear. From the axial velocity contours adjusted for rotation at $x'/L=0.65$ for the turning ship wake in Figure 4.43(b), one large bilge vortex, that moves downwards, is observed and is probably the result of merger of the two vortices (bilge vortices of opposite rotation) under the action of Coriolis and centrifugal forces for the turning ship wake simulation. There is a smaller circulation region (a side vortex) on the outer rim of the wake. The streamwise flow field causes the side vortex to weaken and the wake decays in the outer region of the near wake similar to non-turning ship. The Coriolis force seems to generate more energetic and less diffusive eddies, hence it seems to increase kinetic energy content of the wake (Yavuz et al., 2002).

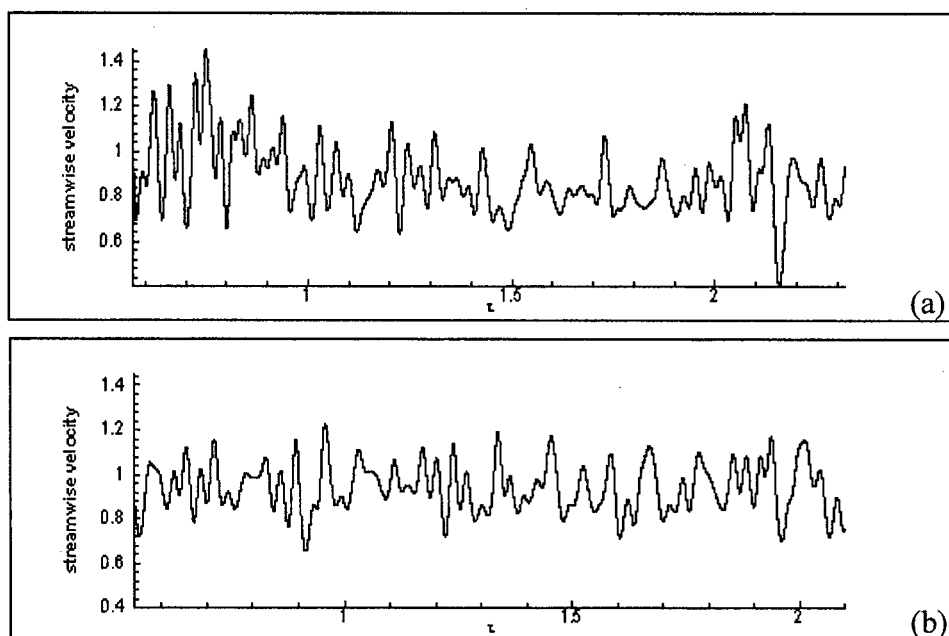


Figure 4.40. Temporal history of streamwise velocity components at 10° ($x=1.02$, $y=-0.001$ and $z=-3.18$) (finest grid) and $Cs=0.052$ a) Case-1 b) Case-2

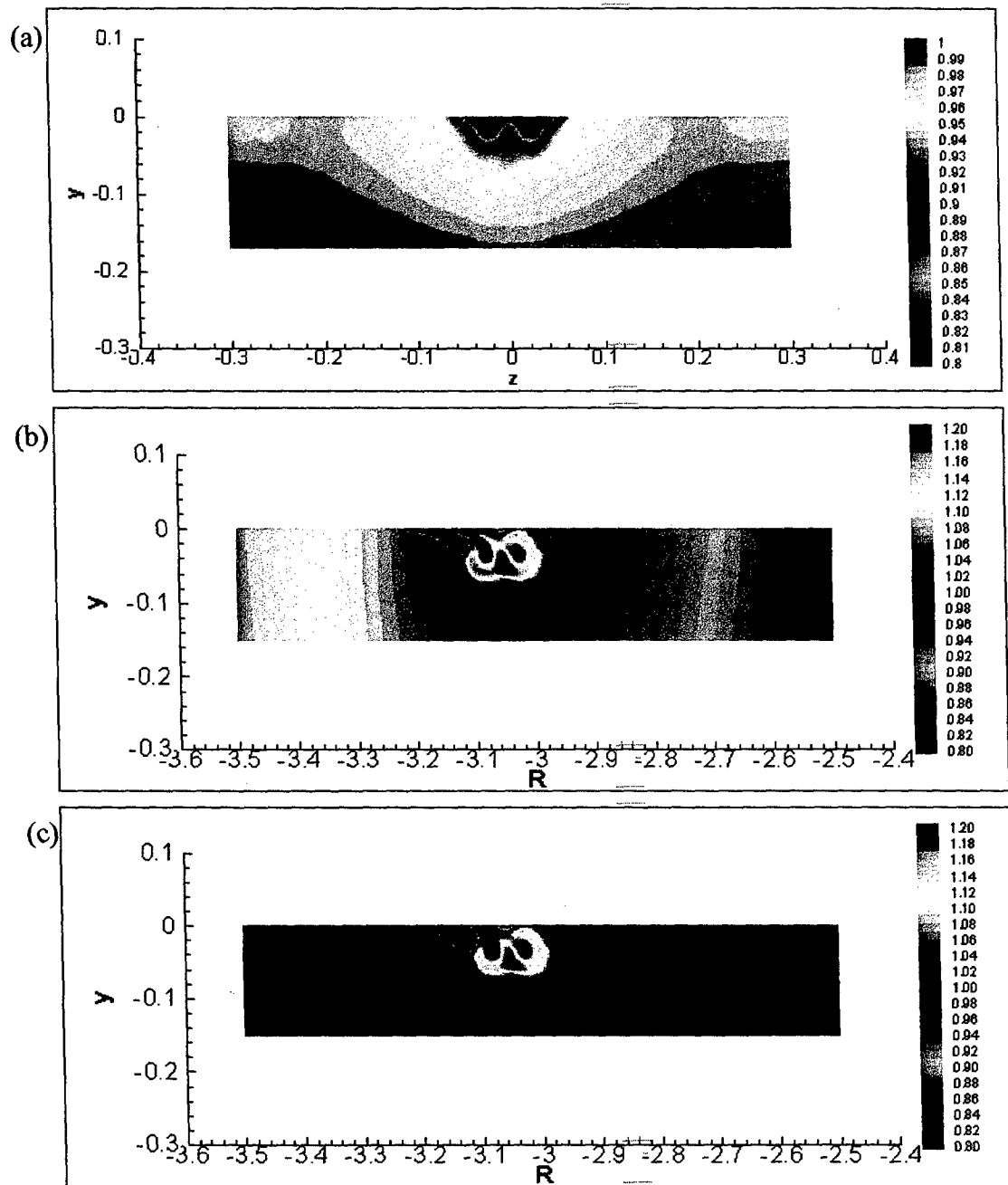


Figure 4.41 a) The mean axial velocity contour at the inlet data plane (IDP) for non-turning ship (Shi et al. 2001) (finest grid) b) The mean axial velocity contours at the IDP for turning ship wake (finest grid) c) The mean axial velocity contours after subtracting solid body rotation contribution at the IDP for turning ship wake (finest grid)

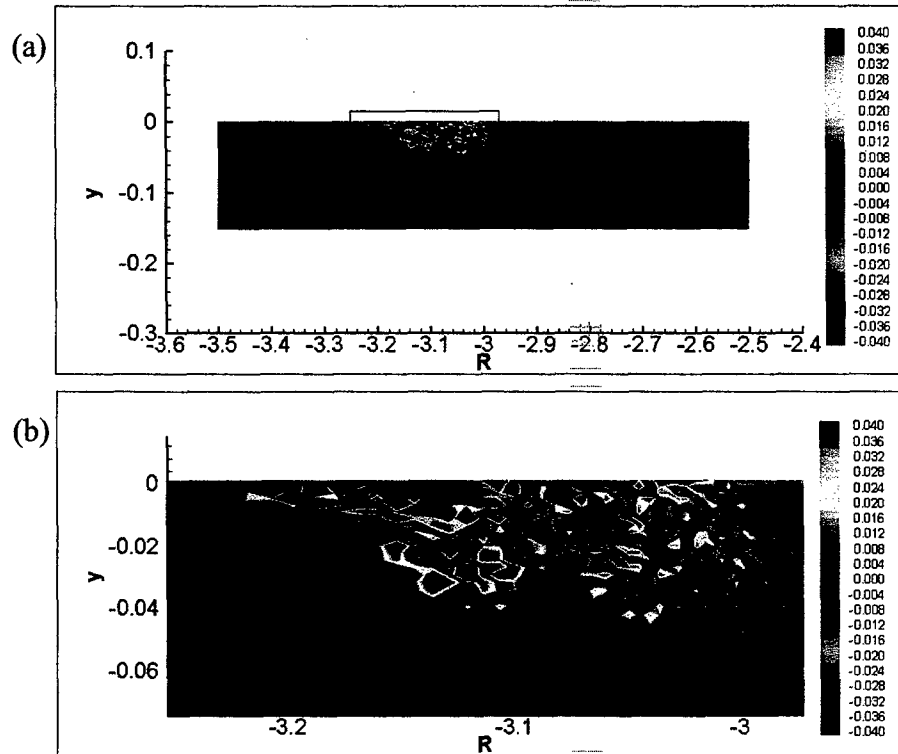


Figure 4.42. a) The axial flow field provided by RFG at the inlet plane (IDP) for turning ship wake b) Enlarged view of A (finest grid)

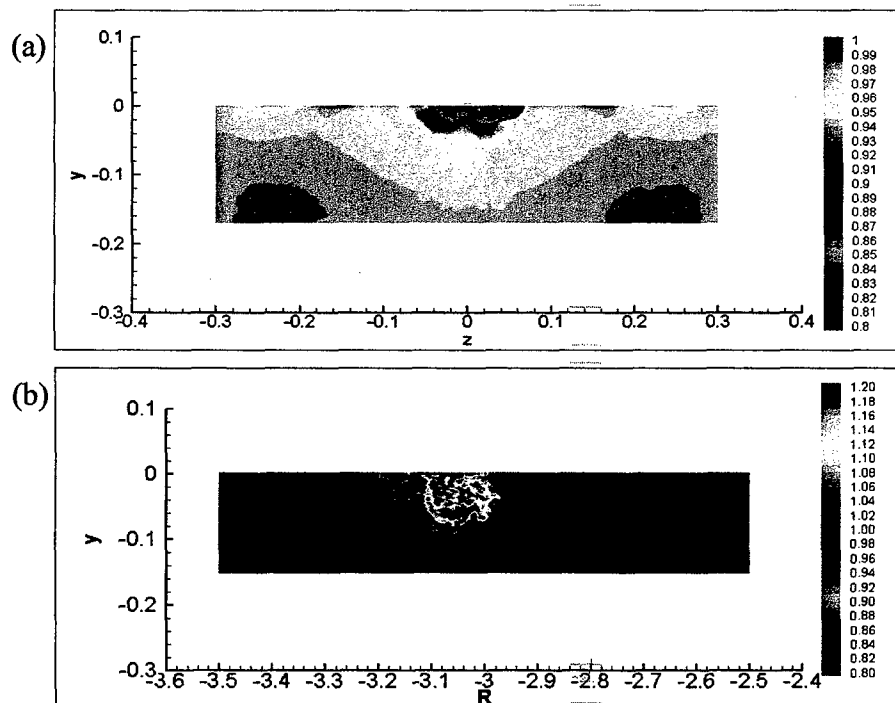


Figure 4.43. a) Axial velocity contour at $x/L=0.65$ for non-turning ship (Shi et al. 2001) (finest grid)
b) Axial velocity contours after subtracting solid body rotation contribution at $x'/L=0.65$ for turning ship wake (finest grid)

Figure 4.44 shows a comparison of the predicted velocity contours with the macro wake measurements at $x/L=1.20$ by Hoekstra & Ligtelijn (1991) for the ship model No. 5452 ($Re \sim 1 \times 10^7$) with the non-turning ship wake at the same location. In both studies, minimum axial velocity occurs near the free surface of the center of the wake, as seen in Figure 4.44. Both axial velocity contours resemble an upside down rimmed hat form. Two side lobes close to the free surface and a central lobe are observed. As stated by Hoekstra & Ligtelijn (1991), these contour forms are very much alike for all ship hulls. Figure 4.44 indicates that from the straight ship wake simulation, similar physics are obtained when compared with the macro wake measurements at the same location. Moreover, the extent of axial turbulence intensities is also in reasonably good agreement with measurements, as shown in Table 4.1. Figure 4.45 shows the axial development of the wake of a turning ship. The bulk movement of the large bilge vortex can be seen clearly through the wake as it moves under the action of the Coriolis and centrifugal forces. The comparison of the energy spectra of the velocity fluctuations for the two wakes is shown in Figure 4.46. It is seen that the turning ship wake has more energetic fluctuating eddies (the values are almost 10 times higher) as compared to the non-turning ship at the same location. This finding is expected as the initial value of the kinetic energy for the non-turning ship wake is almost 8 times smaller than the turning ship wake. For the turning ship wake, the smallest eddy turnover has been calculated to see whether it is correlated or not with the time step used in the simulation; $\Delta t = 1 \times 10^{-4}$. The smallest eddy turnover (numerical or discretization turbulence) can be defined as, the eddy size over the ship velocity, where the resolved eddy size is $2\sqrt{\Delta x_1 \Delta x_2 \Delta x_3}$ and the ship velocity is 1. At 10° , $\Delta x_1 = 4.523 \times 10^{-3}$, $\Delta x_2 = 2.779 \times 10^{-3}$, $\Delta x_3 = 4.07 \times 10^{-3}$, which yields an eddy turnover time of 4.52×10^{-4} , and a frequency, f , equal to 2520 Hz. Since this frequency is much larger than the estimated frequency of 30 Hz, there seems to be no correlation between them. It should also be noted that the shape of spectra for the turning ship case is quite different from the straight track case (Fig. 4.46). In addition to these, the wake spreading or wake width for the non-turning ship, which is obtained to be roughly $w \sim x^{1/4}$ is consistent with Buller & Tunaley (1989)'s measurements. Milgram et al. (1993) and Hoekstra & Ligtelijn (1991) found $w \sim x^{1/5}$. The spreading rate of the turning ship wake can't be easily observed like in the non-turning ship. This is also seen from the predicted vertical vorticity contours in Figure 4.25. It may be due to the grid coarsening towards the end of the calculation

domain. Moreover, the “inboard” side of wake has a much sharper edge while the “outboard” side is more diffusive. This might be due to instability in the “outboard” side.

for any ship hull - maximum value of root mean square fluctuations		
location	experimental	numerical
	(m/s)	(values obtained *U _s) (m/s)
x/L=0.25	0.106 ± 0.02	0.083
x/L=0.6	0.067 ± 0.01	0.069
x/L=1.0	0.047 ± 0.01	0.057

Table 4.1. Comparison of the maximum values of the root mean square fluctuations for some locations in units of (m/s) for non-turning ship

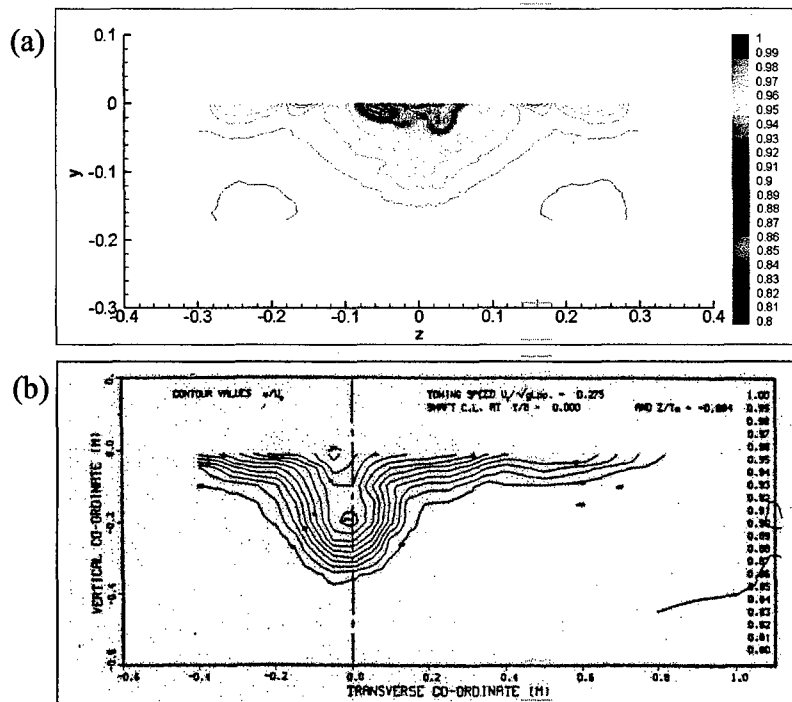


Figure 4.44. a) Predicted velocity contours at $x/L=1.20$ for non-turning ship-(Shi et al. 2001) (finest grid)
b) Macro wake measurements at $x/L=1.20$ by Hoekstra & Ligterijn (1991) for ship model No. 5452
(Re~1x10⁷)

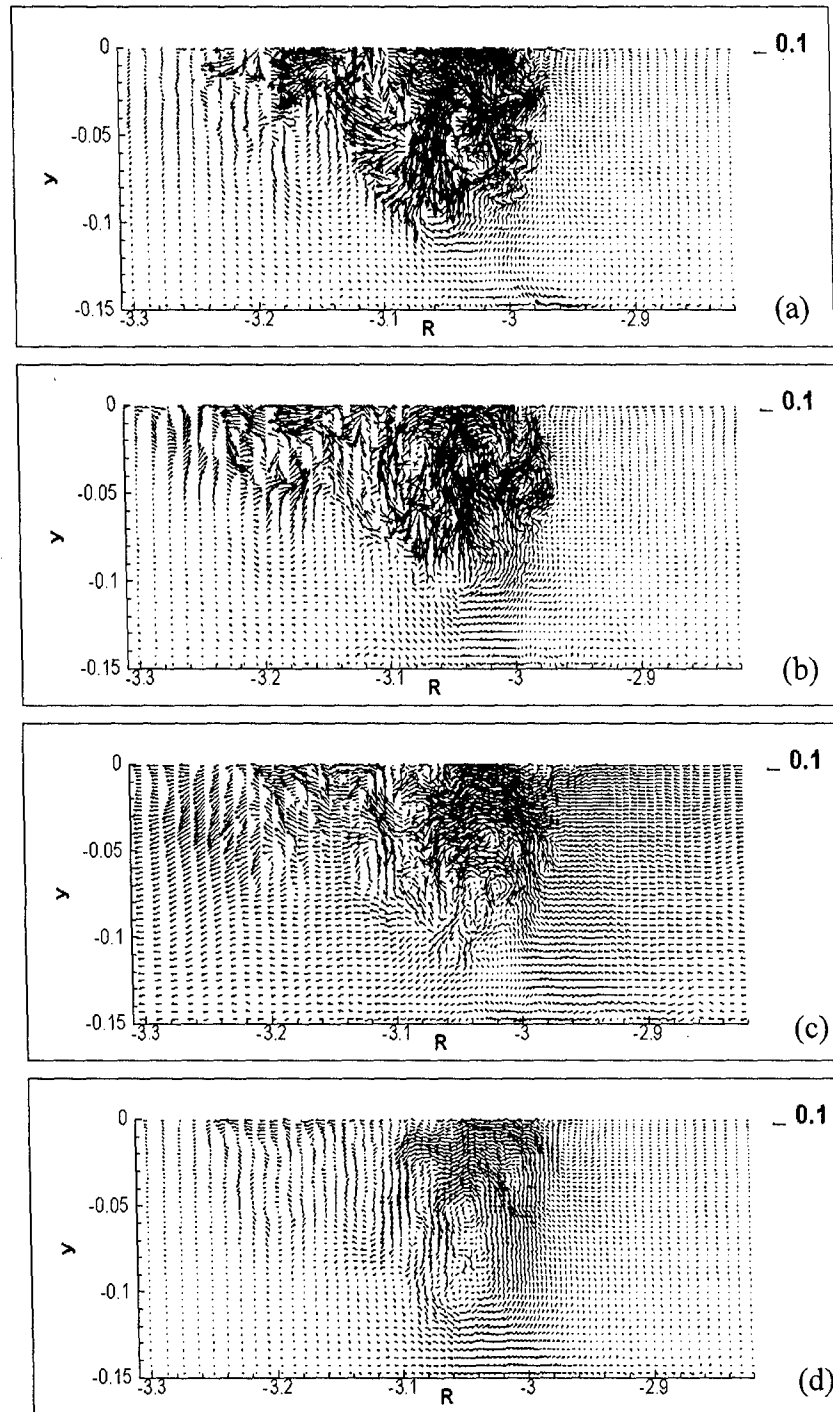


Figure 4.45. Velocity vectors for turning ship using standard Smagorinsky model (finest grid) on a vertical plane at an angle of a) 5° ($x'/L=0.8$) b) 10° ($x'/L=1.02$) c) 20° ($x'/L=1.55$) d) 30° ($x'/L=1.75$)

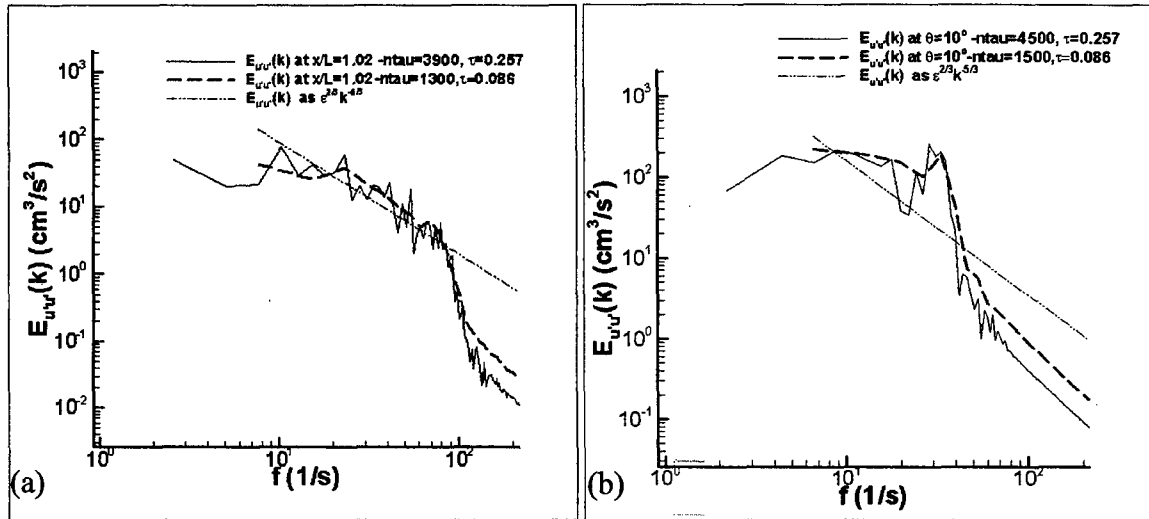


Figure 4.46. Energy spectra of the velocity fluctuations a) Non-turning ship (Shi et al. 2001) (finest grid) b) Turning ship (finest grid)

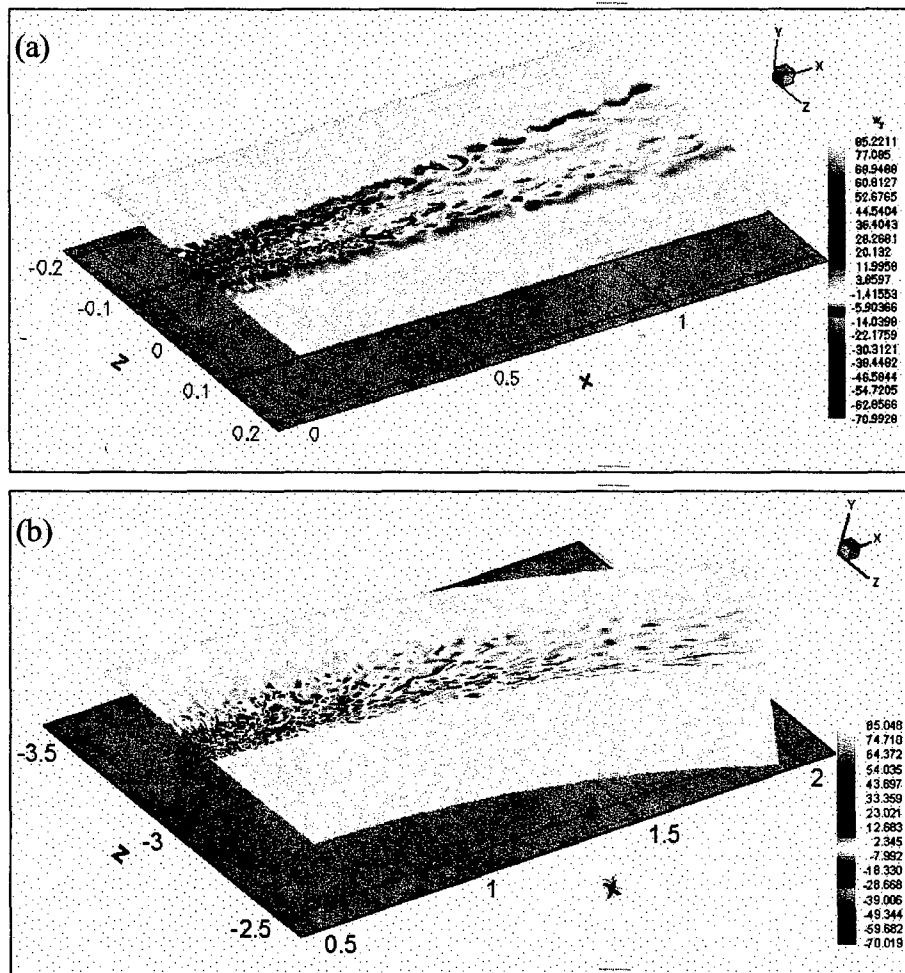


Figure 4.47. Predicted vertical vorticity (ω_y) for a) Non-turning ship (Shi et al. 2001) (finest grid), b) Turning ship wake (finest grid) (Case 2)

5 BUBBLE DYNAMICS

Prediction of bubble distribution in ship wakes is an important area of naval research primarily related to ship detectability from air-born platforms. Ship-wakes can be located by optical means using detection of light scattered from air bubbles entrained in the wake. On the other hand, experimental data on bubble distributions are usually obtained by acoustical methods. Thus, a complete analysis of this problem requires complex multi-physics modeling that would account for different physical processes. The perspective computational tools will have to be based on multi-phase fluid-dynamics solvers, capable of accurate turbulence predictions, and with potential for building composite models.

Considering relatively small volume fractions of bubble phase in the ship wakes, the method of Lagrangian particle dynamics (LPD) is most appropriate for computing bubble distributions. It has advantages over the Eulerian two-fluid methods in the cases of dilute suspensions or when large concentration variability of the discrete phase is present [Elghobashi; Crowe]. This situation is true for bubbly wake flows, such as those in ship-wakes, where bubbles may experience preferential concentration and clustering effects in the near wake region but are rather dilute in the far wake. The LPD method is also conceptually simple and methodologically robust providing a numerically stable statistical model for evaluating dispersed phase concentration and particle/bubble distribution functions. The algorithm for particle tracking and population dynamics developed earlier by the authors demonstrated the ability to efficiently simulate large populations of particles including coalescence effects with even modest computer resources [Shi et al. 2000a&b; Smirnov and Celik, 2000; Smirnov et al., 2000].

Simulations of bubbles in turbulent shear layers require accurate representation of the fluctuating flow-field that governs bubble dynamics. When conventional RANS (Reynolds Averaged Navier-Stokes) models are used this accuracy is often lost or comes at a cost of empirical physical sub-models for turbulence. On the other hand, direct numerical simulations (DNS) or LES require no, or a relatively simple subgrid-scale (SGS) model. LES has the advantage over DNS of being able to handle flows with higher Reynolds numbers and still accurately reproduce large-scale dynamics at a much reduced cost.

The majority of simulations of turbulent bubbly shear layers using Eulerian- Lagrangian approach is done using RANS methods for high Reynolds number flows [Joia, 1997; Murai, 2000] or DNS-type simulations for relatively low Reynolds number flows [Elghobashi and Lasheras, 1996; Ruetsch and Meiburg, 1994; Okawa et al., 2001; Murai et al., 2001]. Many commercial CFD codes now have LES algorithms with Lagrangian tracking techniques for turbulent flows. However, for the purpose of a complex multi-physics analysis of turbulent wakes, including the multi-phase and acoustical effects, the authors considered it important to use a research-grade LES code. This will enable us to build composite solvers including fluid, acoustic and bubble interactions. Thus, the LES-based approach pursued in this study provides the basis for multi-physics LES of large-Reynolds number flows.

One of perceived disadvantages of the Lagrangian approach is the requirement to simulate a relatively large number of particle trajectories to obtain the needed statistics. This study elaborates that this perception is exaggerated as long as the flow can be categorized as nominally dilute. Particularly, we made simple estimates (Sec. 5.4.2) to determine under what conditions the assumption of dilute two phase flow would be valid for calculations of turbulent bubbly flow, such as those in ship-wakes.

5.1 Formulation

The LPD algorithm for particle tracking and population dynamics developed by the authors demonstrated the ability to efficiently simulate large populations of particles including coalescence effects with even modest computer resources [Shi et al. 2000; Smirnov and Celik, 2000; Smirnov et al., 2000; Shi, 2000]. In this study the LPD algorithm was combined with the Large-Eddy simulation approach [Smirnov et al., 2001; Piomelli, 1999] to compute the distribution of bubbly phase in the near-wake flow of a ship-model. The LES technique [Piomelli, 1999] enhanced with the RFG procedure [Smirnov et al., 2001; Smirnov et al., 2000; Shi, et al., 2000] was implemented into the LES method to enable the appropriate representation of initial/inlet turbulence conditions and, as a subgrid scale for particle dynamics solver. It should be noted that the RFG approach is essentially a simplified spectral method, and as such it has a potential to be used as a part of an acoustic solver in the appropriate sub-model. This may be important for validation of the simulation results on the data produced in acoustical experiments [Trevorrow et al., 1994].

The combined LES/RFG method was validated on the cases of turbulent mixing layer, and used later to simulate the wake of a Navy ship model 5415⁴ [Smirnov et al., 2001]. The fluctuating velocities at the inflow boundary provided by RFG were generated from the data obtained in prior RANS calculations based on $k-\varepsilon$ turbulence model [Larreteguy, 1999].

To compute bubble motion the following equations were adapted from Sridhar and Katz [Sridhar and Katz, 1995]

$$\frac{d\mathbf{U}_b}{dt} = \mathbf{A}_a + \mathbf{A}_b + \mathbf{A}_d + \mathbf{A}_l \quad (5.1)$$

where the \mathbf{A} vectors on the right-hand side represent accelerations due to added mass (\mathbf{A}_a), buoyancy (\mathbf{A}_b), drag (\mathbf{A}_d) and lift (\mathbf{A}_l) given by the following expressions

$$\begin{aligned} \mathbf{A}_a &= C_a \left(\frac{\partial \mathbf{U}_f}{\partial t} + (\mathbf{U}_f \cdot \nabla) \mathbf{U}_f \right) \\ \mathbf{A}_b &= -C_b \mathbf{g} \\ \mathbf{A}_d &= \frac{3}{4r_b} C_d |\mathbf{U}_{rel}| \mathbf{U}_{rel} \\ \mathbf{A}_l &= \frac{3}{4r_b} C_l |\mathbf{U}_{rel}|^2 \frac{\mathbf{U}_{rel} \times \vec{\omega}}{|\mathbf{U}_{rel}| |\vec{\omega}|} \\ \vec{\omega} &= 0.5 * (\nabla \times \mathbf{U}_f) \end{aligned} \quad (5.2)$$

Relations (5.2) were obtained for spherical bubbles and by considering the limit of a small air-to-water density ratio $\rho_a/\rho_w \approx 0$. The coefficients of added mass (C_a) and buoyancy, (C_b) were found to be $C_a = 3.0$ and $C_b = 2.0$. The coefficients of drag (C_d) and lift (C_l) are themselves empirical functions of \mathbf{U}_{rel} and bubble diameter, which were obtained from experimental measurements of bubbles dynamics in turbulent vortexes. The Bassett term involving the history integral was neglected in this case, following the conclusions of Sridhar and Katz [Sridhar and Katz, 1995] on small contribution of this term compared to the buoyancy term for a typical wake flow turbulence. The typical bubble sizes used in the experiments were

⁴<http://www50.dt.navy.mil/5415>

500–800 μm , and the Reynolds numbers, based on relative velocity between 20 and 80, and vorticity between 2 and 20 s^{-1} .

The set of equations (5.1), (5.2) was selected, because they were obtained from the experimental data on bubble dynamics in vortex flows, similar to those of turbulent bubbly wake flows. Since the parameters of a single bubble dynamics in simple vortexes were directly measured, these data represent the features of pure bubble dynamics not affected by the random effects of turbulence, as may be the case with some experimental data collected from stochastic bubble ensembles. It should be noted that there are other alternatives to the approach selected here. For example, the classical analytical formulation of Auton, [Auton, 1987; Auton et al., 1988] and its extension to the viscous flow [Auton et al., 1988] is likewise "non-polluted" by stochastic effects of turbulence, and this form of the lift force has been successfully used to predict a variety of bubbly flows. Generally, the question of which expression is optimal for a given bubbly flow is still an open research issue. The authors used the results of Sridhar and Katz, because they appeared to be most appropriate for representing bubble dynamics in a vortex and a suitable choice for LES. However, it is possible that similar results could be obtained using another set of equations.

Equation (5.1) was discretized using a second-order Runge-Kutta time stepping scheme. In the mixing-layer case (Sec.5.3) bubble tracking throughout the computational domain was simplified by using a uniform Cartesian grid, so that the index of the cell containing the bubble could easily be obtained using a simple division by modulus operation. In the case of a ship wake (Sec.5.4) this restriction was lifted and a more general grid-independent tracking algorithm (Sec.5.2) was used. Fluid velocities were interpolated to the location of a bubble using tri-linear interpolation formula.

In a joint LES/LPD/RFG approach the flow solver and the particle solver can use different time-stepping schemes with independent selection of time-steps. This was necessary due to the difference in turbulence time-scales and bubbles relaxation times. Usually sub-cycling of bubble iterations inside the flow iterations is required to reach a stable solution.

To estimate the dissolution of bubbles of different diameters at different depths we used the bubble dissolution equation as formulated in [Rightley and Lasheras, 2000] and corrected in [Hyman 1994; Carrica et al., 1998].

$$\frac{dm}{dt} = 6(C_\infty - C_0)D_{aw}^{2/3} |u|^{1/3} r^{4/3} \quad (5.3)$$

where r is the bubble radius, $|u|$ is the relative air-bubble velocity and D_{aw} is the diffusivity of air in water. Constants C_∞, C_0 represent the concentrations of dissolved gas at a distant point and at the bubble surface respectively and are computed as in [Carrica et al., 1998].

$$C_\infty = HP_{atm} \quad (5.4)$$

$$C_0 = H(P_{atm} + \rho g h + 2\sigma/r) \quad (5.5)$$

where H is Henry's constant, P_{atm} is the atmospheric pressure, g is the gravity acceleration constant, and σ is a surface tension coefficient.

The current model does not include bubble breakup. This can be justified for the mixing layer and ship-wake cases, considered below, on the grounds of rather small turbulence energies and bubble sizes. Indeed, if we use the conditional breakup probability for a bubble hit by an eddy [Luo and Svendsen 1996 (Eqn. 26)]:

$$P = \exp\left(-\frac{12c_f\sigma}{\beta\rho_c\varepsilon^{2/3}d^{5/3}\xi^{11/3}}\right)$$

We can get an estimate for largest bubbles of sizes around $1mm^5$. The breakup probability in this case is around 10^{-5} , and falls rapidly for smaller bubble diameters, d , as $d^{-5/3}$, which justifies neglecting their breakup effects.

5.2 Implementation

There were two tasks to be solved for an efficient implementation of an LPD procedure: (1) particle tracking and (2) particle population dynamics. The first task is related to the problem of identifying the grid-cell where the particle is located, and interpolating the relevant grid-based variables to the particle location. The second task is related to the problem of creating and destroying particles as the need arises due to the processes of particle injection, disappearance through the free surface and crossing the boundaries of the computational domain. Since both

⁵We used: $c_f = 0.26$, $\sigma = 0.0741 \text{ kg/s}^2$, $\beta = 2.0$, $\rho_c = 1000 \text{ kg/m}^3$, $\varepsilon = 1.0 \text{ m}^2/\text{s}^3$, $\xi = 1$

particle tracking and population control are frequently occurring operations, it would be highly desirable to solve each task in a manner that would avoid expensive loops through the particles or grid-node arrays.

Particle tracking

When the particle tracking is done on structured grids, the location of the grid-cell containing the particle is a straightforward task reduced to a division-by-modulus, multiplication and addition operations. When non-uniform or unstructured grids are used the procedure is not as simple. In this case there should be a way to identify if the current location of the particle is inside the same cell it was inhabiting in the previous iteration or whether the particle has moved into a neighboring cell.

The present LPD procedure accomplished this task by solving the inclusion problem in a polyhedron. This is a standard algorithm in the area of computational geometry [O'Rourke, 1998], where the given point is tested against each face of a polyhedron and it is decided if the point is on the inside or the outside of the face relative to the center of the polyhedron. In the end the point is either found to be inside the polyhedron or the search is repeated in the neighboring polyhedron lying across the first face, which failed the test. Identification of the neighboring cells is a simple matter on structured grids, whereas on unstructured ones cell-neighbor connectivity information should be used⁶.

Population Dynamics.

For an efficient implementation of particle population control algorithm, it would be desirable to avoid both looping through the particles and dynamic memory allocations/deallocations in cases when new particles are created or destroyed. It can be achieved by using linked lists. In the present scheme an array of the size equal to the maximum number of particles is initially allocated. Then the pointer system is setup to link all the particles together in a ring fashion, separating them into active and dead sublists (Fig.5.1(a)). Whenever a particle is

⁶In parallel implementation the neighbor connectivity should cross domain boundaries

created or destroyed it takes only six pointer assignment operations to move it between the active and dead sublists. Figure 5.1(b) shows an example of destruction of particle B by the appropriate reassignment of pointers between the old neighbor-particles A,C and the new ones: D,E.

Even though the limitation on the maximum number of particles in the domain may seem restrictive, it is a compromise, allowing to avoid dynamic allocation/ deallocation of memory space for each newly created or destroyed particle. Since the latter operations can be rather frequent this procedure seems reasonable from efficiency standpoint.

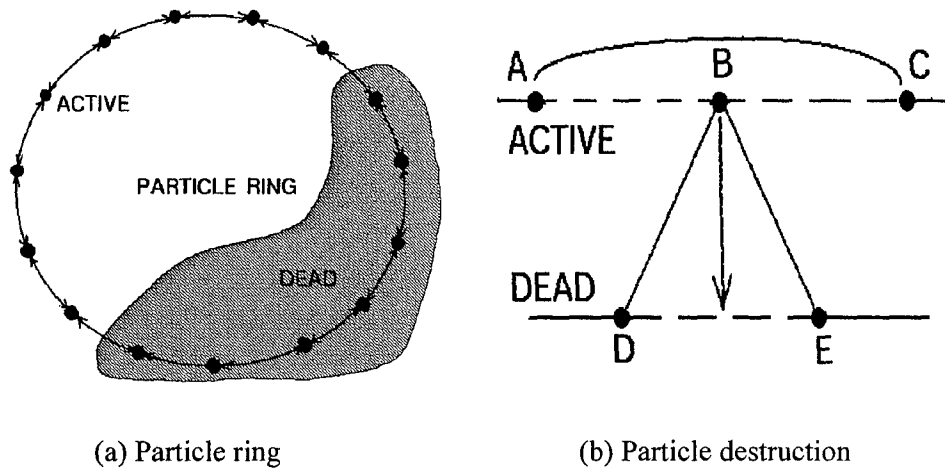


Figure 5.1 Dynamic memory allocation of particle storage

5.3 Validation on a Turbulent Mixing Layer

The validation of the LES/LPD approach was done on experimental data of a mixing layer [Rightley and Lasheras, 2000] (Fig. 5.2). A detailed description of the validation study including the results for the flow-field distribution is presented in [Smirnov et al., 2001]. Here we present additional data on the influence of the effect that the RFG sub-grid model had on the results.

In the experiments the mixing layer was generated by two separate parallel flows with different incoming velocities. A thin flat plate of $0.15m$ length, $0.003m$ height, and $0.2m$ width (the whole span-wise extent), was mounted in the middle of the inlet plane. The average velocity of the lower half flow was $0.28m/s$, while the upper half value was $0.07m/s$. Bubbles of $40\mu m$ in diameter were carried in from the lower half of the channel. For further details of the

experimental installation and computational setup we refer to the relevant sources [Rightley and Lasheras, 2000,15; Smirnov et al., 2001].

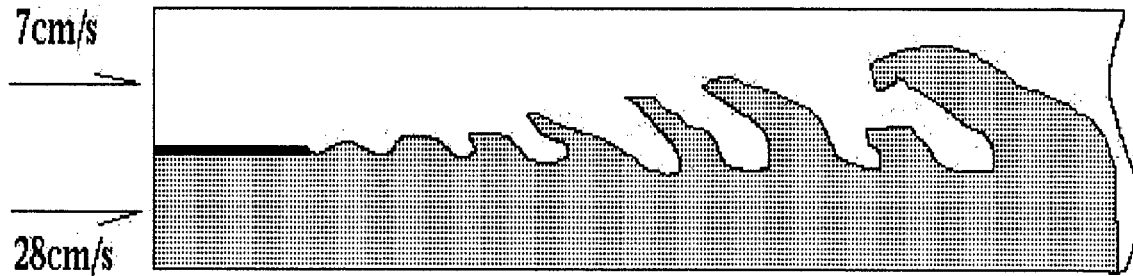


Figure 5.2 Mixing layer experimental setup

In bubble simulations two runs were conducted: with and without the RFG subgrid-scale model. In both cases a column of 100 bubbles was injected at the inlet of the domain with time interval of 27 milliseconds for the duration of 12.7 seconds, resulting in 47,000 bubbles that entered the domain during the course of the run. Figure 5.3 shows a typical bubble distribution computed by LES/LPD algorithm compared with those observed in experiments. The bubble cloud can be seen to be entrained by the fluid entering the mixing region from the high speed side into the cores of the coherent vortex structures present in the mixing region. The pictures represent an instantaneous distribution, which is different for any given time, but shows common statistics and similar dynamical features.

Spatial histograms of bubble distributions were obtained by counting all bubbles passing the cells of the 3D-histogram and accumulating the statistics. Normalizing the histogram data by the total number of bubbles injected, gave bubble probability density functions and concentrations. The statistical error, σ , in the number of bubble counts, n , for each slot of the histogram can be estimated from binomial distribution as $\sigma = [n(1 - n/N)]^{1/2}$, where N is the maximum number of bubbles injected during the simulation. This will add to the uncertainty in the layer thickness calculations for larger X , and smaller bubble concentrations.

Figure 5.4 shows the surface of the histogram and the contour plot of the constant concentration levels. Figure 5.5 shows the growth of the mixing layer thickness in the stream-wise direction (X) with and without the RFG model. Over-prediction of layer thickness at small X is due to the finite resolution of the histogram. The inclusion of the RFG model improves the predictions at greater X .

Figure 5.5 also shows predicted and measured development of the mixing layer thickness. The overall agreement is good except at large axial distances where a smaller rate of growth of the mixing layer in the stream-wise direction is observed when no subgrid scale model was applied. Although the inclusion of the RFG model [Smirnov et al., 2001] improved the predictions of the boundary layer growth at higher axial asymptotics, it also increased the uncertainty in the boundary layer thickness because of the higher dispersion in bubble distribution.

Figure 5.6 provides comparison of predicted bubble concentrations against experimental data. The agreement is reasonably good especially at the beginning of the boundary layer. Some irregularity of computed data further downstream is most probably due to statistical uncertainty of the sample as bubble concentration becomes more dilute.

It should be noted that, being statistical in nature, the LPD method enables the refinement of the histogram and improvement of the accuracy by subsequent accumulation of bubble statistics. Since the statistical error is proportional to $1/n^{1/2}$, where n is the number of bubbles in a histogram box, it would require four times as many bubbles for a two-dimensional histogram to double the resolution along each axis, or to reduce the statistical error by half with the same resolution. The choice of histogram size is a trade-off between the spatial resolution and statistical error.

It should be noted that the statistical nature of the Lagrangian approach can be of an especial benefit when using distributed memory computer platforms to compute multiphase flows. By simply running the same simulation on several processing nodes with a different initial conditions one can increase the sample size and improve the statistics. A particularly attractive feature of this approach is that no domain decomposition will be necessary for these computations and therefore a strictly linear scalability can be achieved. This is the case of what is sometimes referred to as an *embarrassingly parallel* computation.

5.4 Ship-wake Simulations

5.4.1 LES Results

Ship-wake simulations were setup to correspond to the un-propelled Navy 5415 model [Smirnov et al., 2001]. The Reynolds number based on the ship width is on the order of $2 \cdot 10^5$.

Computational grid with dimensions $164 \times 98 \times 92$ was used to represent the near-wake region (Fig. 5.7) of one ship-length, L , in the axial direction, $0.3L$ in depth and $0.6L$ in the span-wise direction. The simulations were performed on a 1GB 1GHz DEC Alpha computer, with an average computing time of one month for a single flow-through time.

Only the wake flow was simulated, with the inlet plane conditions provided by prior RANS results carried out at the university of Iowa [Ramaprian, 1981]. A distribution of turbulent kinetic energy in the inlet plane is shown in Fig. 5.8. The turbulent kinetic energy data were used to set the amplitudes of unsteady subgrid-velocity field by means of RFG procedure [Smirnov et al., 2001]. At this stage RFG was not used for stochastic tracking of the bubbles inside the domain as was done in the mixing layer simulations. The free surface was assumed to be flat, invoking the low Froude number approximation.

Bubble motion was governed by the model of Sridhar and Katz (1). Bubbles of $100\mu m$ in size were randomly injected at the inlet plane with the probability distribution proportional to the turbulent kinetic energy level (Fig. 5.8). At the free surface the life-time of the bubbles was set to zero for the absence of more exact empirical data. The integration of (Eqn. 5.1), via a second-order Runge-Kutta scheme provides the new velocity, $v_i(t)$, in the x_i direction for each particle as a function of time.

It should be noted that the range of bubble sizes used to calibrate Eqn. 5.1, $500 - 700\mu m$, is larger than the bubble size used in simulations. Although our validation on the case of mixing layer may indicate that approximation (Eqn. 5.1) may still be valid for smaller bubble sizes, a more through investigation of the influence of bubble size may be appropriate.

Figure 5.9 shows an instantaneous picture of all the bubbles in the wake as observed from the rear-bottom corner of the computational domain (ship stern is not shown). It can be seen that the bubbles tend to cluster in preferential concentration regions corresponding to high vorticity. These regions are dictated by the dynamics of the flow in the near wake. Figure 5.10 provides a cross-sectional view of an instantaneous velocity and bubble distributions in the wake, which is rather typical. Two symmetrical vortex structures in the velocity distribution coincide with the bubble agglomeration regions. With the higher vortex intensities, which will take place at a higher Reynolds number, bubble distribution in the wake will be increasingly affected by these vortices. This is especially true for smaller bubbles.

Figure 5.11 shows typical cross-sectional distributions of bubbles in the wake. These distributions are not instantaneous, but represent total counts of bubbles accumulated over the simulation run.

Figure 5.12 shows the contours of probability density functions of bubble occurrence in the wake. These probabilities were computed from bubble distribution histograms obtained in the similar way as for the mixing layer validation case described above. The profiles shown in Fig. 12 indicate a rapid bubble population decay and gradual spreading of the bubble cloud at the distance of one ship-length. Although the classified nature of bubble measurement data in the wakes of Navy ships prevents us from making a direct comparison, we found that the predicted bubble distributions are similar to those observed in typical ship wakes [Hyman, 1998; Hyman, 2000].

Table 5.1 shows the total bubble counts in different planes $C_{i=1,4}$ and the corresponding normalized ratios: $R_i = C_i/C_1$. These distributions indicate a strong depletion of bubbles over the half ship-length distance, shown in Fig. 5.13. The depletion of bubbles is due to the buoyancy driven migration to the surface and the dissolution effects. Buoyancy forces affect mainly large bubbles, whereas the dissolution affects primarily small ones. Therefore, even the small bubbles entrained by the vortexes will eventually disappear from the domain.

PLANE	COUNT	RATIO
1	46998	0.01
2	9803	0.21
3	3326	0.07
4	1119	0.02

Table 5.1 Cumulative bubble distributions in different planes

5.4.2 Bubble Clustering Effects

Bubbles motion in a turbulent vortex may lead to clustering in the vortex center. This, in turn, may cause bubble coalescence and influence the flow itself. In order to analyze the conditions under which such clustering takes place we considered the case of a realistic vortex

flow obtained from experimental data [Larsson et al., 1998]. An equation of bubble motion, including all the important terms [Sridhar and Katz, 1995] was used to predict bubble behavior. The results were analyzed to determine the limiting values of non-dimensional parameters under which bubble clustering and coalescence effects may become important.

The objective of the computations was to capture the regime where the bubble would converge to the center of the vortex rapidly enough to make the coalescence events more likely. Then, using two non-dimensional parameters, α , representing the vortex strength (Stokes number) and β , representing the ratio of bubble-size to bubble-separation, general conditions for bubble clustering can be obtained.

Given two bubbles separated by a distance d in a vortex centered at the middle point between the bubbles, the necessary condition for bubble coalescence is

$$C_R \geq \beta^{-1} \quad (5.6)$$

where C_R is a convergence rate, defined as

$$C_R = \frac{r_0}{r_1} \quad (5.7)$$

with r_0 is the initial distance of the bubble from the axis and r_1 its distance from the axis after one revolution in a vortex. Condition (Eqn. 5.6) means that the bubbles should come into contact with each other after one revolution in the vortex⁷.

Coalescence criterion (Eqn. 5.6) may be rather strong. In reality bubble-bubble interaction effects may become important long before the criterion (Eqn. 5.6) is satisfied. Consequently, we introduce the criterion of bubble clustering

$$C_R \geq 0.5 \beta^{-1} \quad (5.8)$$

which identifies the bubbles that approach each-other to the distance of one bubble-diameter or less.

To compute bubble motion in the turbulent vortex equation (5.1) was used to describe the bubble motion and the flow-field was constructed using a curve-fit to the experimental data [Larsson et al., 1998] (Fig. 5.14). The following function was used to approximate the data

$$U_z = a(1 - B_z \exp(-(r/R_z)^2)) \quad (5.9)$$

⁷Usually turbulent eddies do not last for more than one revolution

$$U_\theta = a r \exp(-(r/R_\theta)^\gamma) \quad (5.10)$$

where

$$a = 1.0$$

$$B_z = 0.08$$

$$R_z = 0.7$$

$$R_\theta = 0.22$$

$$\gamma = 0.58 \quad (5.11)$$

The advantage of using the analytical formula is that all the velocity derivatives required in the bubble-equation of motion can be computed analytically, thereby minimizing the discretization errors. So, the spatial derivatives needed for calculating the vorticity, $\vec{\omega}$ in (5.1), can be easily computed from the expressions (5.9), (5.10), which gives only two non-zero derivatives

$$\begin{aligned} \frac{\partial U_z}{\partial r} &= \frac{2B_z a r}{R_z^2} e^{-(r/R_z)^2} \\ \frac{\partial U_\theta}{\partial r} &= a(1-\gamma)(R_\theta)^{-\gamma} r^\gamma e^{-(r/R_\theta)^\gamma} \end{aligned}$$

An important measure of the strength of the vortex is its turnover time. For the whole core region this time is almost the same, since the core region can be approximated by the solid body rotation

$$U_\theta = a \cdot r \quad (5.12)$$

where a is the strength of the vortex, which is related to the turnover time of the core as $\tau_e = 2\pi a^{-1}$. Since data in Fig. 14 are non-dimensional, we used a as a parameter to define the vortex strength. The vortex size parameters R_θ, R_z were kept constant, which corresponds to the vortex core size of $d_e \approx 0.5m$. We did not scale down the vortex size since the results of Fig. 5.14 were obtained for a large vortex produced in the stern of the ship and it is not clear if they can be scaled-down to small eddy sizes. All computations were applied to the case of $d \leq d_e$ and $d_b \ll d_e$, i.e. the bubbles were considered to be inside of the vortex core and bubble size much smaller than the typical eddy size. For a given bubble separation d the results would apply to all the eddy sizes greater than d , and having the same vortex strength a . The neglect of eddy sizes

smaller than the separation length, i.e. $d_e \leq d$, may lead to some overestimate of clustering effects for highly turbulent flows.

Figure 5.15 shows a typical convergent trajectory of a bubble. In this case a bubble of $r_b = 700 \mu m$ and $\tau_b = 1.03 \cdot 10^{-4} s$ was injected into a core of a vortex with $a = 10 s^{-1}$ at $r_e = 1 cm$ from the axis. The convergence factor was close to $C_R = 2$. The corresponding non-dimensional parameters for this case are: $\alpha = 1.64 \cdot 10^{-4}$ and $\beta = 0.07$, which lies outside of coalescence limits defined by (Eqns. 5.6 and 5.8).

To visualize the results the computed particle trajectories were plotted in a coordinate system moving along the vortex axis with the velocity equal to the center-line axial velocity of the flow: $U_z(r=0)$. In Fig. 5.15 gravity acceleration vector \mathbf{g} is directed along the axis. The main contribution to the bubble dynamics in this flow came from the added mass force \mathbf{F}_a , responsible for bubbles attraction toward the the vortex axis, and the gravity force, \mathbf{F}_b , which caused them to accelerate along the axis. As can be seen in the figure, the displacement along the axial direction is smaller than the drift toward the center, which approximately relates to the ratio of buoyancy to added-mass forces characteristic for this particular bubble size and vortex strength. In only about 1/3 of all cases the vortex axis can be considered as approximately aligned with the gravity force, whereas in the other 2/3 of the cases the corresponding axes are misaligned, and bubbles convergence toward the center is slower. So, for the bubble with $C_R = 2$ and axis aligned with the gravity the convergence rate went down to approximately 1.5 when the axis was turned at the right angle to \mathbf{g} . Considering this, a more accurate convergence criterion can be formulated as

$$\overline{C_R} \geq \beta^{-1} \quad (5.13)$$

where

$$\overline{C_R} = 1/3 C_{R\parallel} + 2/3 C_{R\perp} \quad (5.14)$$

with $C_{R\parallel}$ being the convergence rate for the parallel and $C_{R\perp}$ for the normal alignment of the gravity and vortex axis. As can be seen, large enough bubbles, experiencing strong gravity, can be completely drifted away from the vortex in the normal alignment. It should be noted that the coalescence criteria (Eqn. 5.6), (Eqn. 5.8), (Eqn. 5.13) are rather approximate, and should only be used for order of magnitude estimates.

Our calculations of bubbles with $d_b = 1\text{mm}$ ($\tau_b = 5.26 \cdot 10^{-5}$) show (Fig. 5.16) that for $\beta = 0.25$ the coalescence criterion (Eqn 5.6) is approximately satisfied for the vortex strength of $a = 40\text{s}^{-1}$ and clustering criterion (Eqn 5.8) - for $a = 20\text{s}^{-1}$. This corresponds to the Stokes numbers of $\alpha \geq 3.34 \cdot 10^{-4}$ and $\alpha \geq 1.67 \cdot 10^{-4}$ respectively.

In our LES computations of a wake behind a Navy ship model⁸ the vorticity varies between 0 and 100. Using the relation $|\vec{\omega}| \approx a$, valid in the vortex core region, we can get an estimate of the range of Stokes numbers that may be encountered in simulations. For a bubble of $d_b = 1\text{mm}$ it is $0 \leq \alpha \leq 8.33 \cdot 10^{-4}$. For bubbles of smaller sizes the lower bound on α will be lower. Hence, if we restrict our analysis to the bubbles of sizes less than 1mm in size, we may infer that the maximum Stokes number that we can currently reproduce in computations is $\alpha \approx 8.33 \cdot 10^{-4}$. Considering our clustering bound for bubble coalescence of $\alpha \geq 1.67 \cdot 10^{-4}$, we may conclude that in our current LES computations we may consider bubble clustering and coalescence effects in the range of $(1.67 \leq \alpha \leq 8.33) \cdot 10^{-4}$.

The important spatial measure is the distance of the bubble from the vortex axis rather than the size of the eddy, which can be much bigger. Considering this, the bubble/eddy size ratio, β , would greatly depend on bubble size distribution and concentration. The value $\beta = 0.25$, which was used in the previous calculations, requires bubble separation from the axis to be of 4mm or less for all bubble sizes under 1mm. Consequently, for the clustering of the bubbles to occur their concentration should be high enough to allow at least two bubbles at distances shorter than 4mm from each other, which gives the lower bound on bubble number density as $N_b > 2/(4 \cdot 10^{-3})^3 = 3.13 \cdot 10^7 \text{ m}^{-3}$. Combining with our previous estimate of α , we conclude that for bubble number densities above $3.13 \cdot 10^7 \text{ m}^{-3}$ bubble coalescence effects can be present for $\alpha > 1.67 \cdot 10^{-4}$.

On the other hand, considering the maximum vorticity in the wake $a_{\max} = 100\text{s}^{-1}$, we may give an estimate of lower bubble concentration limit when the coalescence effects become important. The computations showed that the coalescence criterion (Eqn 5.6) for a bubble of

⁸<http://www50.dt.navy.mil/5415/>

$d_b = 1\text{mm}$ ($\tau_b = 5.26 \cdot 10^{-5}$) in a vortex core of $a = 100\text{s}^{-1}$ gives $\beta = 8.33 \cdot 10^{-2}$, which provides the following coalescence conditions on bubble number density, N_b , and void fraction, F_b :

$$\begin{aligned} N_b^{co} &\geq \frac{2}{(d_b/\beta)^3} = 1.15 \cdot 10^6 \text{ m}^{-3} \\ F_b^{co} &\geq N_b^{co} \frac{4\pi}{3} r_b^3 = 6.02 \cdot 10^{-4} \end{aligned} \quad (5.15)$$

Bubble clustering criterion (Eqn 5.8) results in $\beta = 4.17 \cdot 10^{-2}$, and the corresponding relations for the number density and the void fraction are

$$\begin{aligned} N_b^{cl} &= 1/2 N_b^{co} \geq \frac{1}{(d_b/\beta)^3} = 5.75 \cdot 10^5 \text{ m}^{-3} \\ F_b^{cl} &= 1/2 F_b^{co} \geq 3.01 \cdot 10^{-4} \end{aligned} \quad (5.16)$$

With the higher resolution of LES than we are currently using, and which we shall be able to attain on distributed memory platforms, higher levels of vorticity can be reached. This is usually a result of smaller eddies generating higher vorticities than parent-eddies. It may bring the estimates (Eqn. 5.15), (Eqn. 5.16) further down in number densities and void fractions.

The cases above relate to the situation of mono-dispersed bubbles (single-size). In the poly-dispersed case the coalescence criteria can be formulated by redefining β as

$$\beta = (d_{b1} + d_{b2}) / (2d_e) \quad (5.17)$$

where d_{b1}, d_{b2} are diameters of bubbles of two different sizes in the vortex, separated by d_e . This expression for β should now be used in (Eqn 5.6) and (Eqn. 5.8). To obtain an estimate of bubble collision/coalescence frequency a double integration over all the bubble sizes d_{b1}, d_{b2} weighted by the bubble-size distribution would be required. A rough estimate can still be made by single integration of the results for the mono-dispersed case, considering that the obtained void fraction limits will represent an over-estimation of the real case.

Since estimates (Eqns. 5.15 & 5.16) were based on LES computations of a ship model with a relatively small length of 5.72m we can expect the upper bounds on vorticity to further increase in the case of a real ship where the Reynolds number and vorticity are much higher. Consequently, the estimates of N_b and F_b in (Eqns. 5.15 & 5.16) can be lower.

We should also note that clustering/coalescence effects considered here were attributed to a single revolution of the vortex. In reality an accumulated effect of many revolutions in one or many subsequent eddies may significantly amplify the effect of a single revolution. Consequently it will lead to lower values of N_b, F_b than estimated in (Eqns. 5.15 & 5.16). On the other hand the estimates were made for the case of two bubbles aligned on the opposite side of the vortex axis, which will be true for only a fraction of all possible bubble alignments. The account of this will increase the values of N_b, F_b .

Considering all these factors, the actual values of void-fraction limits for clustering/coalescence can be close to the maximum values observed in real-size experiments, which is about 10^{-4} , and lie within the range of values that can be expected in the stern region [Hyman, 2000]. The numerical studies of Carrica et al. (1998) provide the estimates of maximum void fractions of 10^{-3} , which occur mainly near the free surface in the stern region.

Therefore, we can conclude that in realistic ship-wake situations bubble clustering and coalescence effects may be important, especially in the near-wake region of 1-3 ship lengths.

5.5 Discussions

The results of this study show the viability of joint LES/LPD/RFG method for computing turbulent bubbly wakes, which can be applied to high Reynolds-number ship-wake flows. Bubble distributions for mixing layers and wakes were obtained.

The effect of bubble influence on the flow field was not considered in this study. Nevertheless, the work by others [Elghobashi and Truesdell, 1993; Truesdell, and Elghobashi, 1994] indicates that when there is a large density ratio between the phases, as considered in this study, the influence of bubbles on the carrier phase may become important even though the void fraction remains small. Works on this topic are continuing under the current project.

To further improve the accuracy of predictions for the flat-plate wake a more realistic no-slip wall boundary condition may be used together with the grid refinement at the wall so as to resolve the turbulent boundary layer.

Stochastic bubble tracking with RFG for the ship-wake case will have to be introduced and compared to the current approach and experimental data to build a more thorough ship-wake validation case.

Performed estimates of bubble clustering effects show that they can be important in certain regions of the near wake. In the first approximation the account of these effects can be done by introducing a two way coupling (bubble-flow influence) scheme. In the second level of approximation it can be done by including bubble coalescence effects, which can be accomplished within an implicit probabilistic interaction scheme proposed earlier by the authors [Smirnov and Celik, 2000].

Given long execution times on a single work station, it would be appropriate to consider an "embarrassingly parallel" run on a computer cluster (Beowulf), where each work station would run essentially the same simulation with the initial conditions taken from independent statistical samples. This way a linear speedup can be achieved in collecting the statistics and improving the accuracy of the computations. This assertion has been investigated and encouraging results have been obtained for shipwake simulations (see Appendix A).

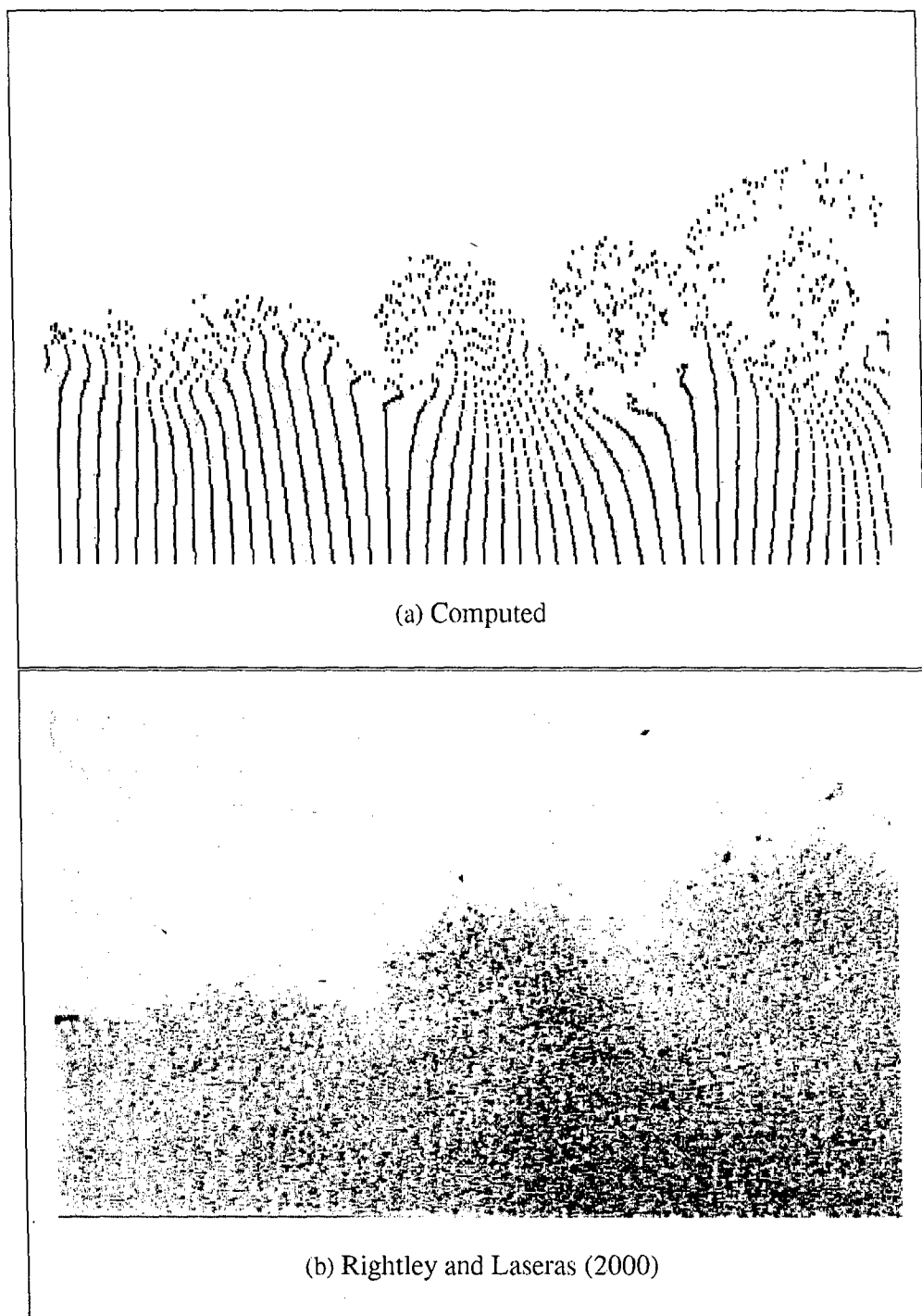


Figure 5.3 Instantaneous bubble distribution

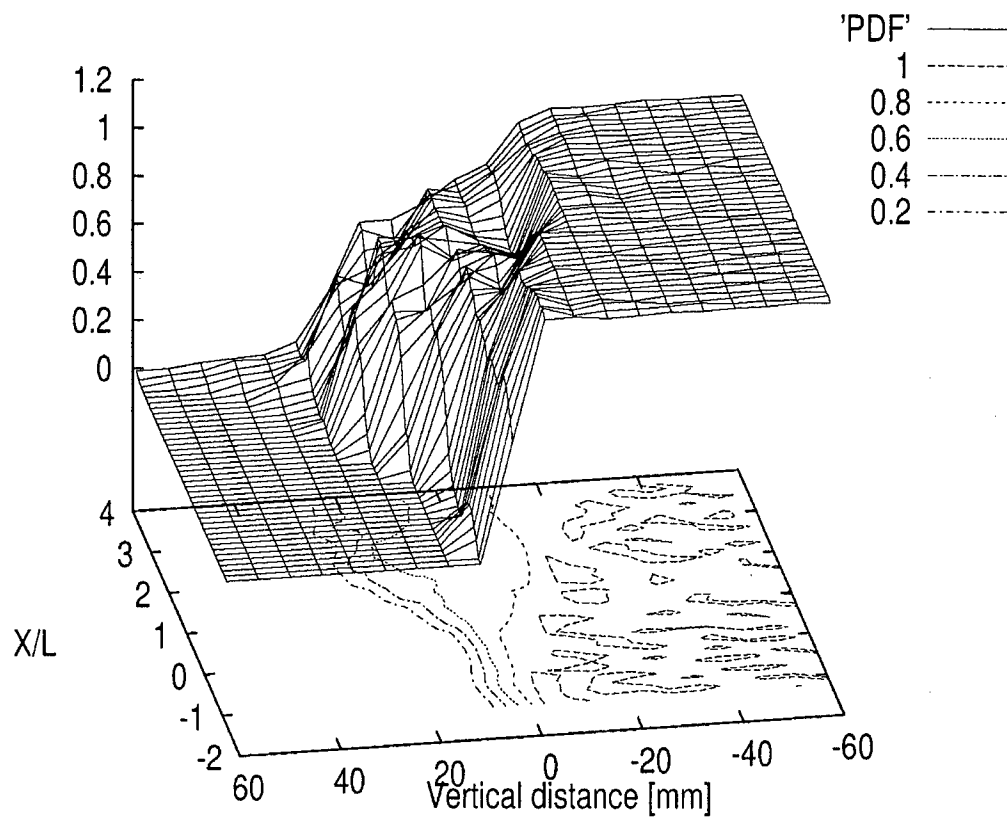


Figure 5.4. Normalized histogram of probability density function of bubble distributions.

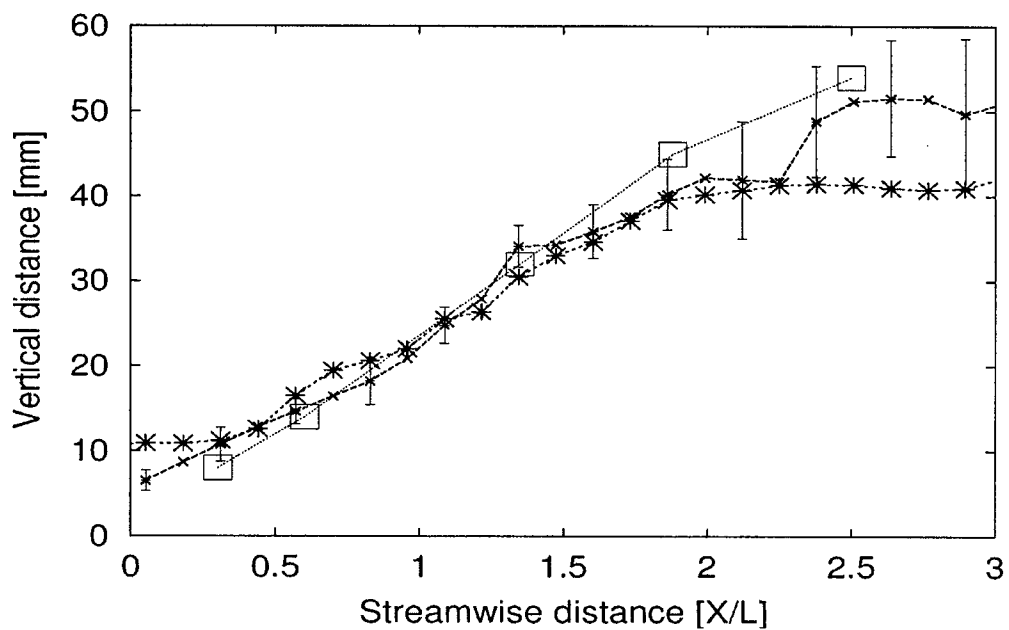
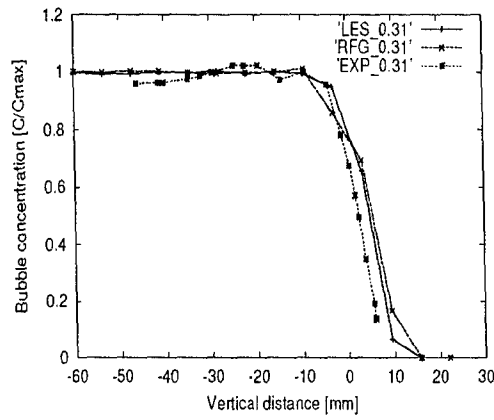
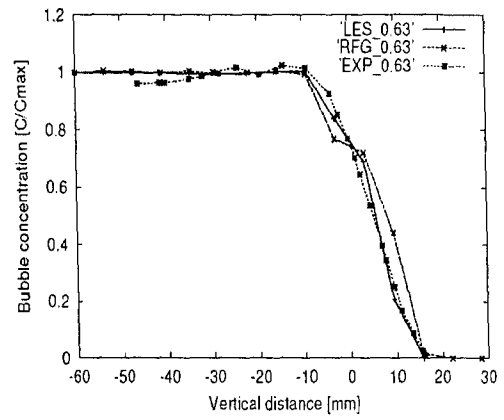


Figure 5.5 Mixing layer thickness.

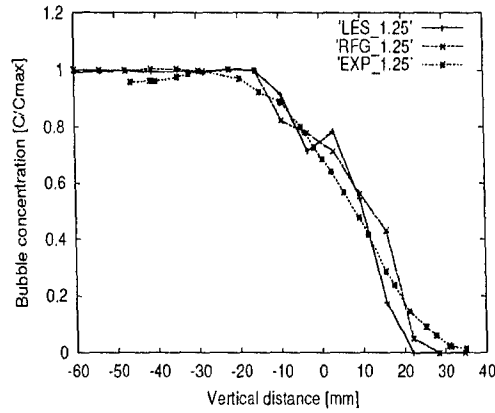
· measured, *- computed without RFG, × - computed with RFG



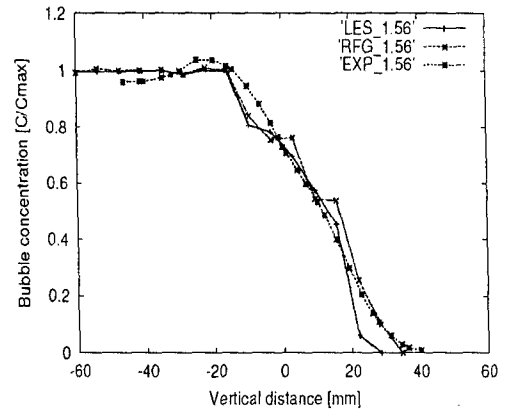
(a) $x/\lambda=0.31$



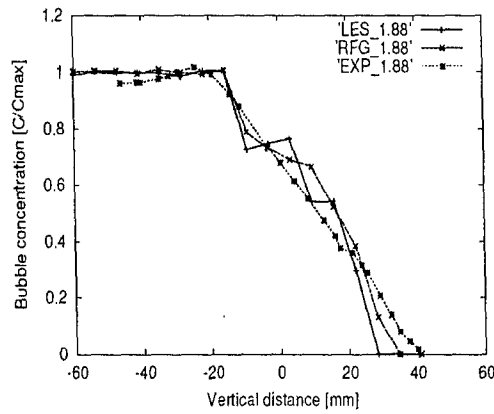
(b) $x/\lambda=0.63$



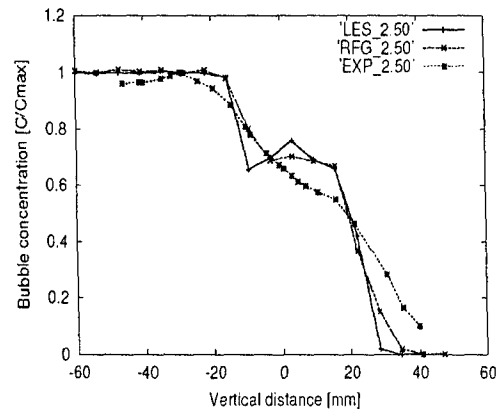
(c) $x/\lambda=1.25$



(d) $x/\lambda=1.56$

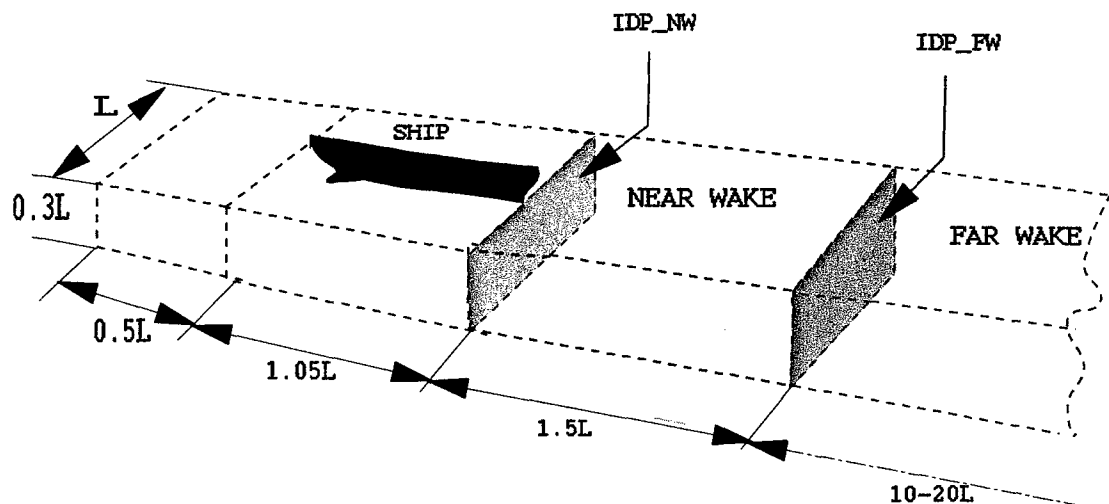


(e) $x/\lambda=1.88$



(f) $x/\lambda=2.50$

Figure 5.6 Bubble concentrations ($\lambda=0.079365$ m).



THE SKETCH OF FLOW PAST SHIP HULL
(L is the ship length)

Figure 5.7 Near and far ship wake regions.

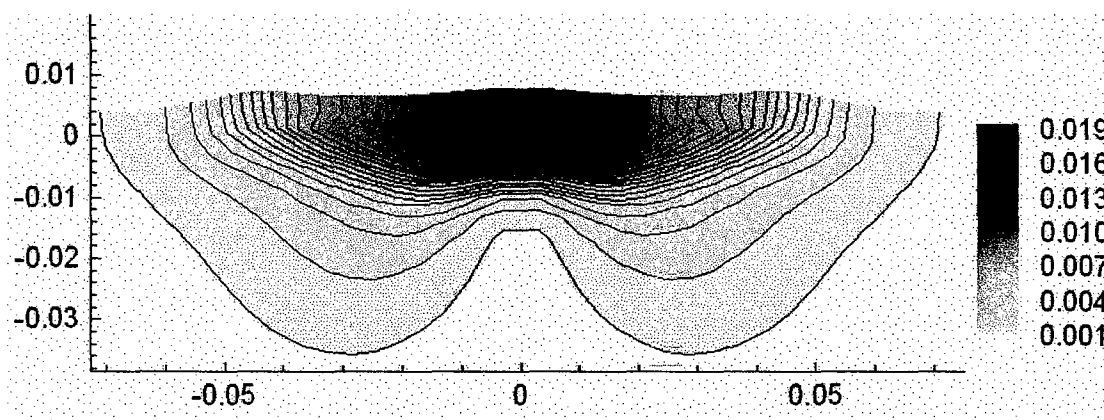


Figure 5.8 Turbulent kinetic energy in the computational inlet plane (m^2/s^2).

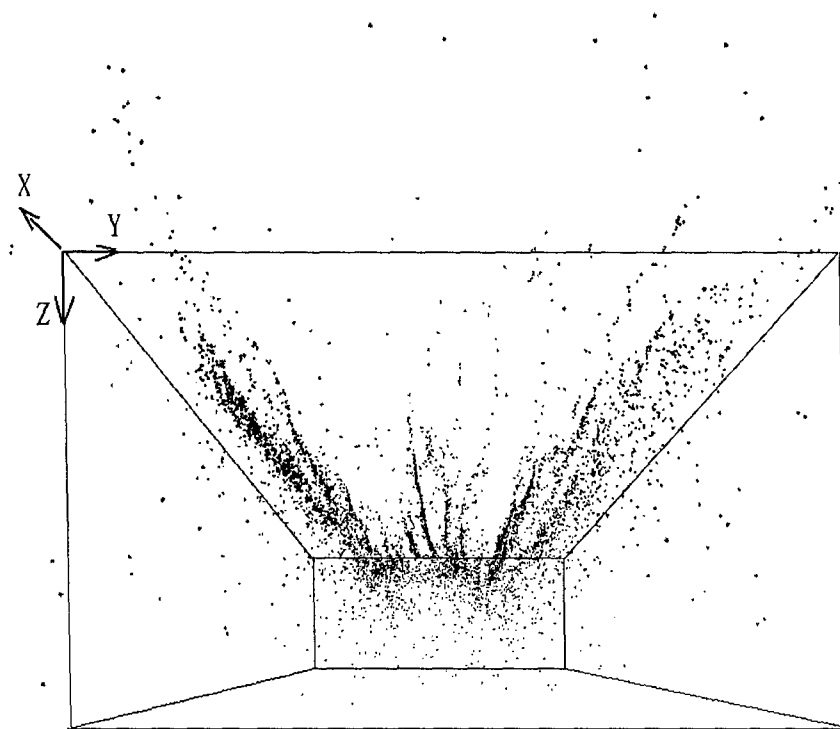
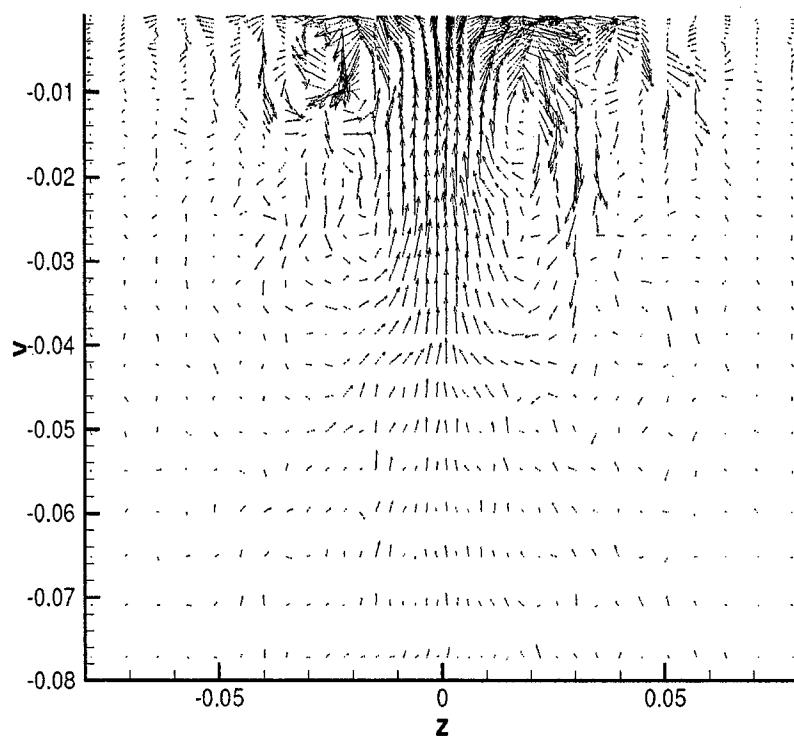
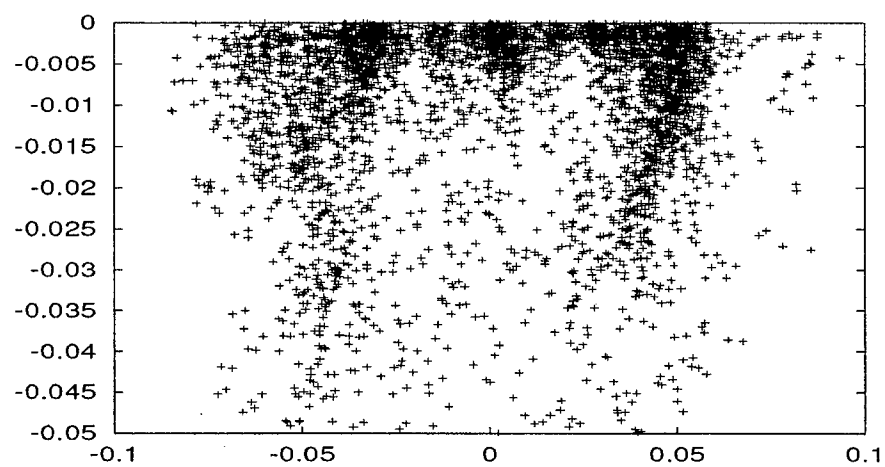


Figure 5.9 Bubbles in a ship-wake. Rear bottom view. The upper surface of the box represents the free surface. The middle rectangle represents the inlet plane. More detailed cross-sectional distributions are shown in Figure 11.

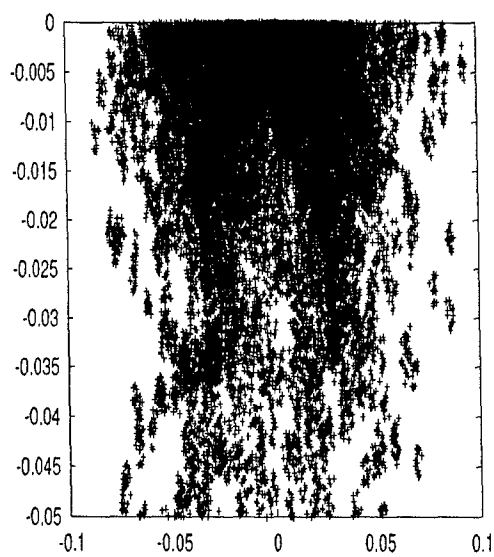


(a) Velocity vectors

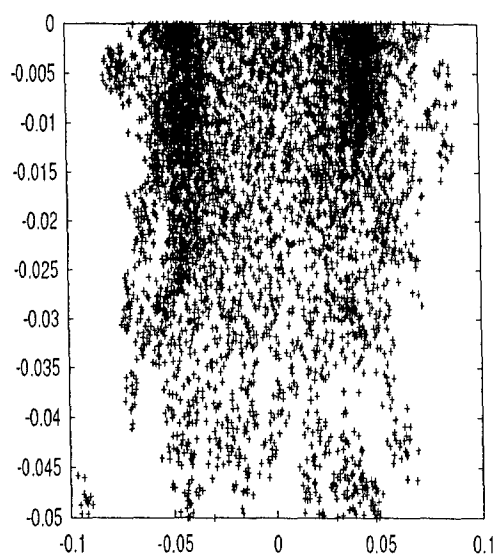


(b) Bubble distribution

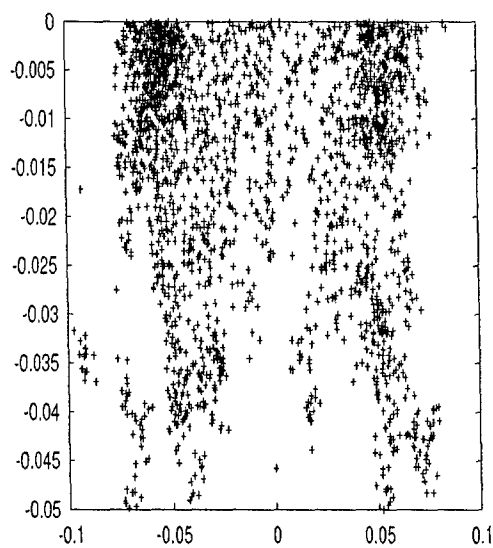
Figure 5.10 Velocity vectors and bubble distribution at $X/L = 0.2$.



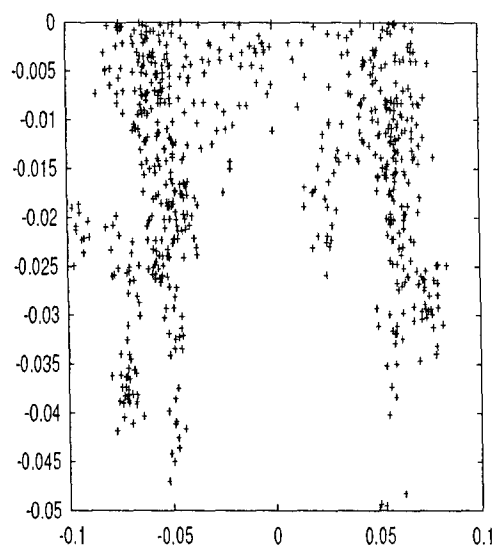
(a) $X/L = 0.01$



(b) $X/L = 0.25$

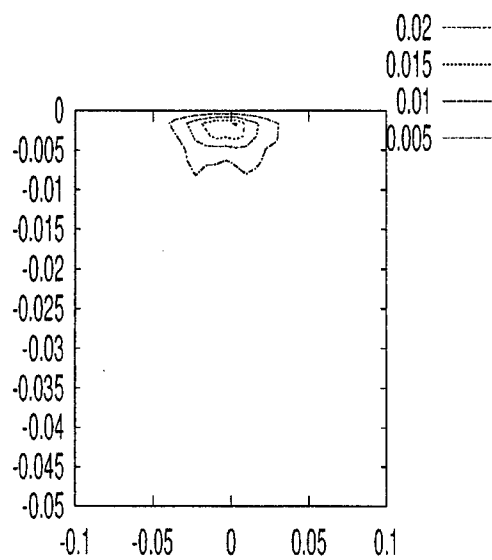


(c) $X/L = 0.50$

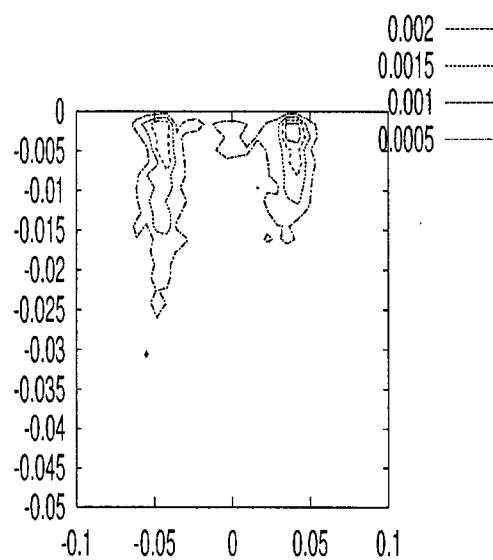


(d) $X/L = 0.75$

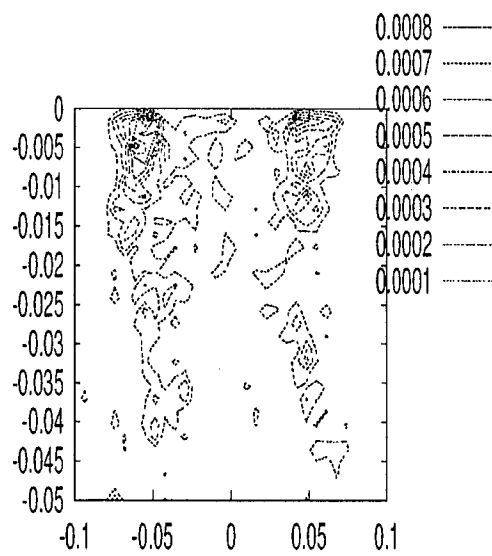
Figure 5.11 Bubble distributions at different cross-sections



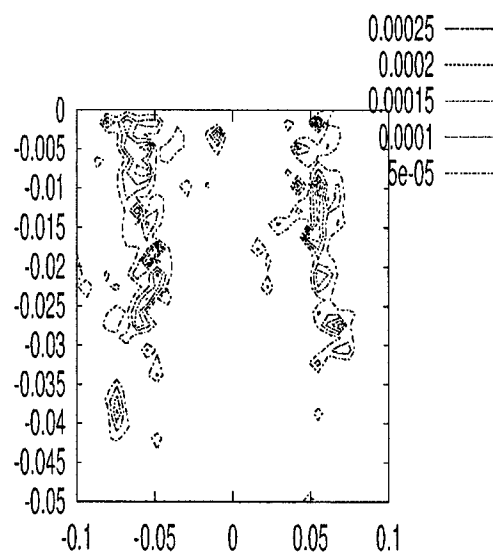
(a) $X/L = 0.01$



(b) $X/L = 0.25$



(c) $X/L = 0.50$



(d) $X/L = 0.75$

Figure 5.12 Bubble probability density functions at different cross-sections

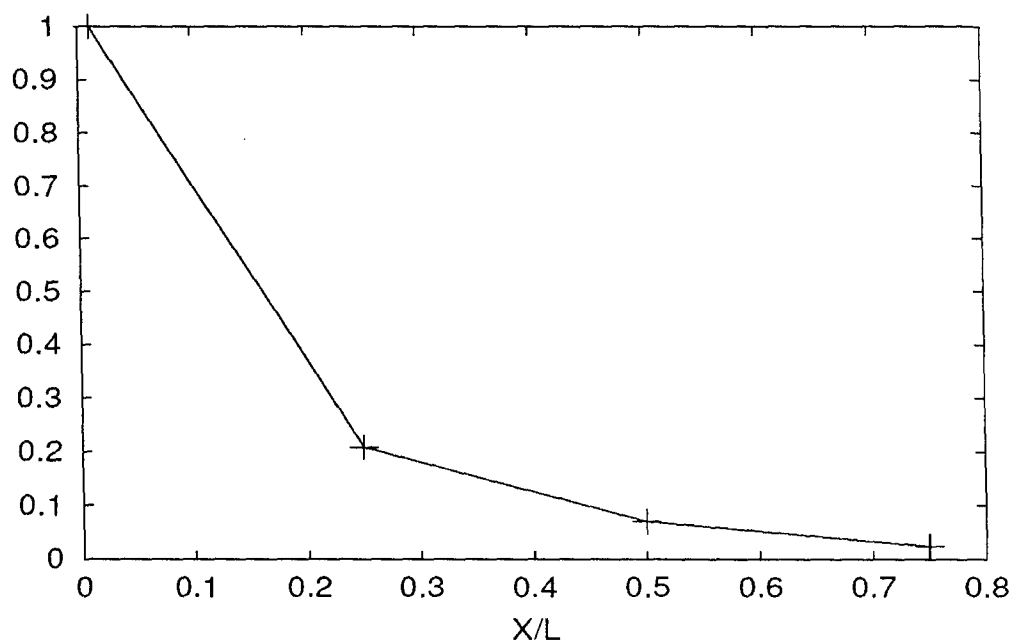
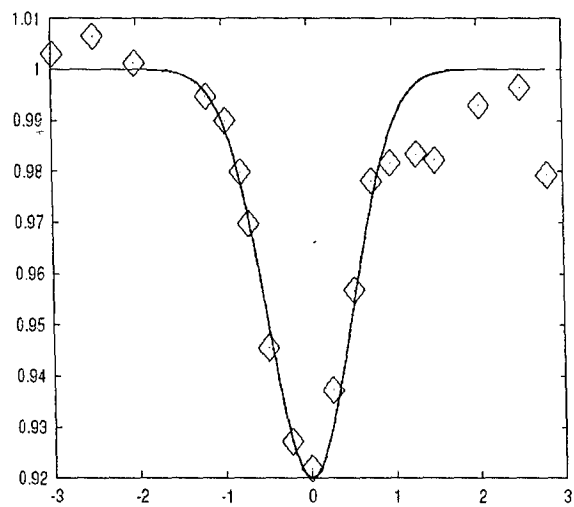
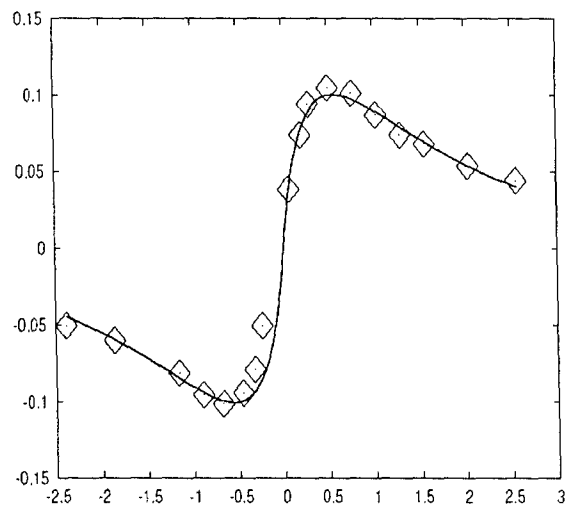


Figure 5.13 Bubble depletion in the wake (LES).



(a) Axial



(b) Tangential

Figure 5.14 Velocity in a vortex

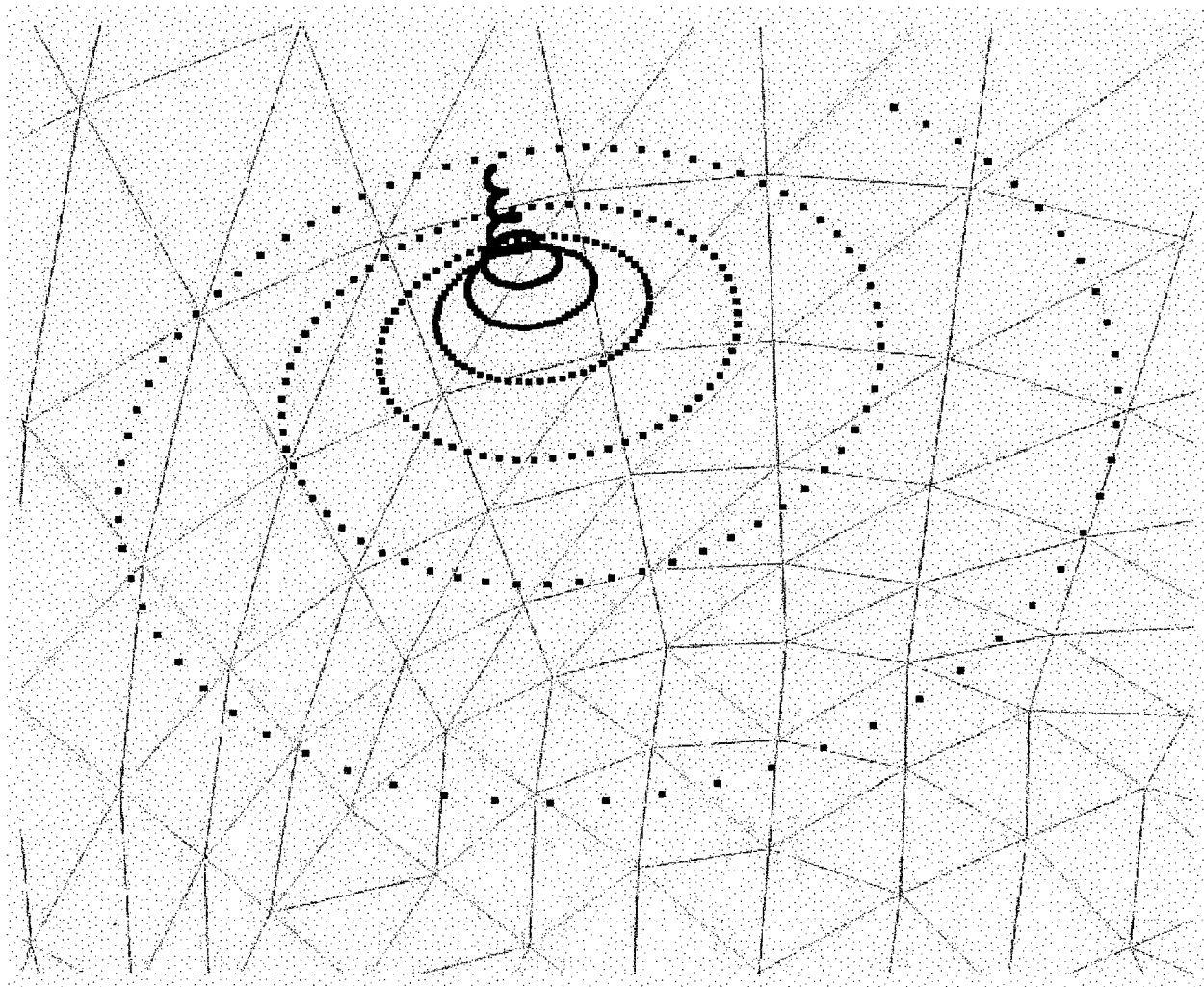


Figure 5.15 Trajectory of a bubble in a turbulent vortex ($R=700\mu\text{m}$).

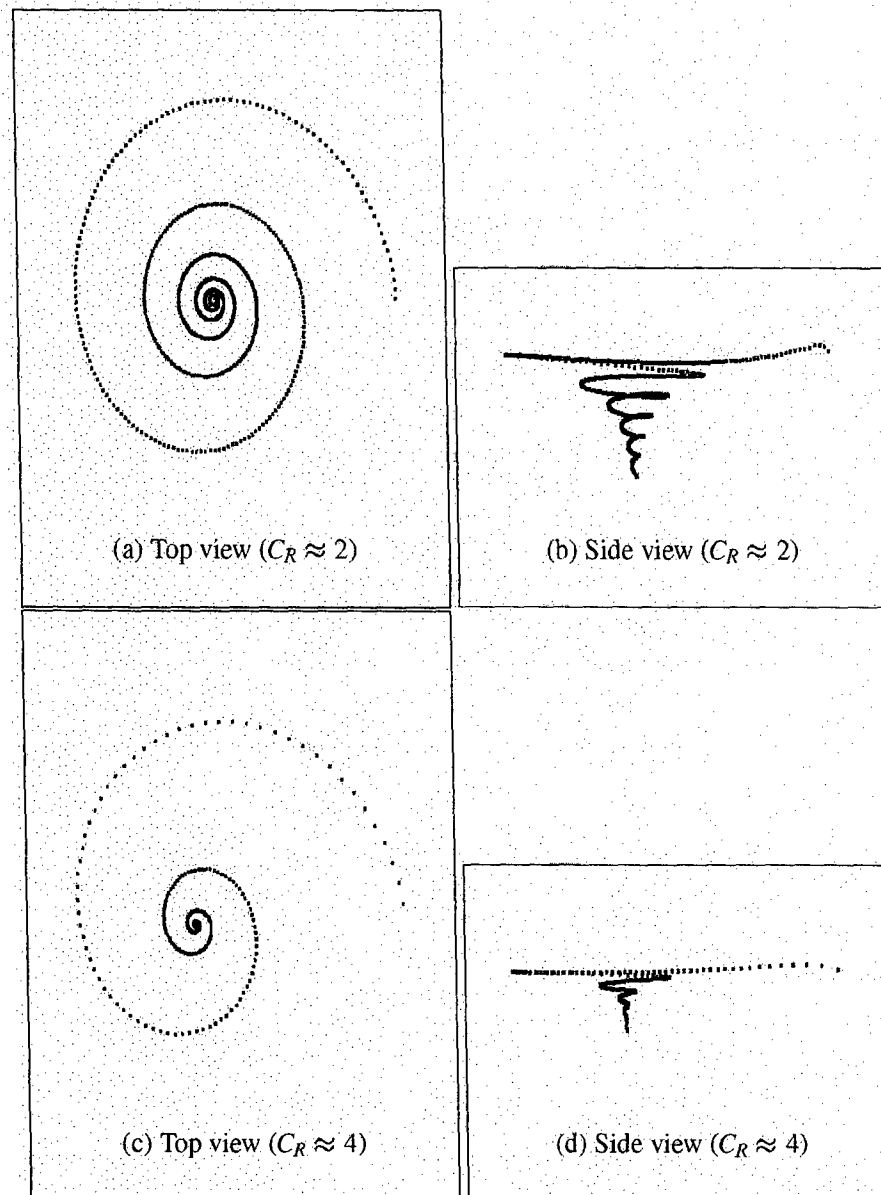


Figure 5.16 Convergent bubbles (Bubble motion shown is relative to an observer moving with the axial velocity of the vortex.)

6 PARALLELIZATION OF THE LES CODE FOR SHIP WAKES

Fast computers have stimulated the rapid growth of a new way of doing science. The two broad branches of theoretical science and experimental science have been joined by computational science. Computational scientists simulate on supercomputers phenomena too complex to be reliably predicted by theory and too dangerous or expensive to be reproduced in the laboratory. There is always a demand for greater computational speed. Areas requiring great computational speed include numerical modeling and simulation of scientific and engineering problems. The cost of an advanced single processor computers increases more rapidly than their power, which made parallel processing evolve.

In this part of the study we present the parallel implementation of large eddy simulations (LES) of a ship wake using the domain decomposition technique. We present the results of the implementation executed on a cluster of workstations at West Virginia University and Pittsburgh Supercomputing Center. Also, we will show how the implementation scales up with the number of workstations and that it is possible to obtain better accuracy by increasing the number of workstations in the cluster system.

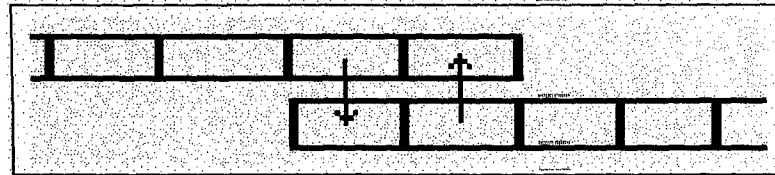
Algorithmic improvements and faster machines, particularly parallel machines, provide the opportunity for effectively using large-eddy simulations for the problems of practical importance. The main objective in this study is to predict the development of turbulence in a ship wake flow using cluster computing.

This requires analysis of the ship wake flow, development of an efficient and accurate simulation of turbulence in the ship wakes by refining the large eddy simulation methodology, setting up the computational domain, analysis of the computer resources, and analysis of the results.

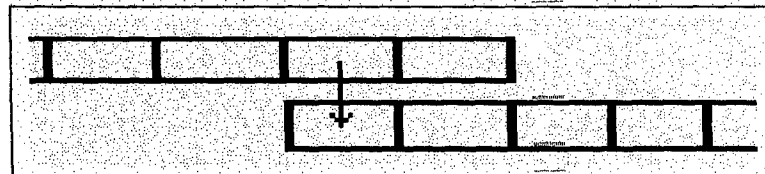
6.1 Methodology

The conventional domain decomposition technique for elliptic problems is realized through a two-way exchange of data at the boundaries of the domains (Simon, 1992; Dihn et al., 1984) as illustrated in Fig. 6.1(a). This guarantees the convergence to the corresponding single

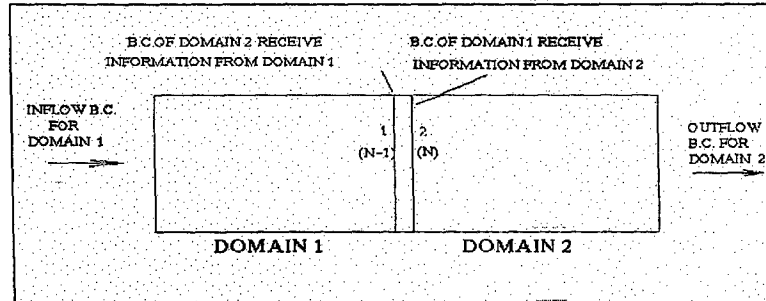
domain case. However, this strategy may carry an excessive communication overhead for three dimensional CFD simulations. If the problem is parabolic in one of the spatial directions one can employ a parabolic communication approach (Fig. 6.1(b)). This may reduce communication overhead by half. To test the validity of this approach a parallel version of the LES code has been implemented using a one-way data exchange (Osman et al., 2000).



(a) Elliptic decomposition



(b) Parabolic decomposition



(c) Boundary conditions

Figure 6.1 Domain decomposition strategy.

The drawback of the parabolic exchange scheme is the necessity to provide additional outlet boundary conditions for each domain, which can alter the character of the flow close to the domain outlet. To avoid the influence of this distortion on the flow-field the communication plane should be set at some distance from the outlet plane. Thus some of the memory space and the processing time is inevitably lost. Moreover, only by using elliptic message transfer can one apply domain decomposition technique in non-parabolic directions which is necessary for geometrically complex flows.

For a linear solver a two-node overlap communication strategy (Fig. 6.1a) would be enough. For a high-order accurate solver, however, a wider overlap in communication planes will be appropriate. Since the LES solver is usually at least second order accurate, we employed four and six-node overlaps in our communication schemes. For second order accurate diffusion terms in momentum equations a four-point overlap is enough, whereas for pressure solver decomposition a six point overlap would be more appropriate.

6.2 Applications

The parallelizing methodology described above was implemented on a Beowulf cluster at WVU and at Pittsburgh supercomputer center (www.psc.edu). Both clusters run Linux operating system with the interprocessor communications based on MPI.

6.2.1 One Way Communication Simulations

In order to test the viability of the implemented decomposition scheme several test simulations were performed. The communicated data were velocities and contravariant velocities and pressure. It should be noted that since the pressure solver is usually sub-cycled to the flow solver sending the pressure information carries most of the communication overhead. In practice, it appears that excluding pressure communication does not lead to a significant degradation of the solution for non-pressure driven flows, like wake flows. This conclusion was also confirmed in our simulations. A flat plate wake flow was used as the first case. The geometry and numerical scheme can be found in (Smirnov et al. 2001). For the sake of a higher accuracy the simulations were continued with two-way communications as required in elliptic solutions.

6.2.2 Two Way Communication Simulations

Several medium scale simulations were performed. First a laminar channel flow case was computed on 2, 4 and 8 processors. Figure 6.2 shows the axial velocity contours obtained from the 8-processor run. Although pressure communication was blocked in this simulation the contour lines show no irregularities at the inter-processor boundaries. These results confirm the correctness of the decomposition scheme, and support our assumption that pressure coupling is rather weak between the processors. For the case of a wake flow the effect of pressure will be even smaller, thus justifying the velocity-only decomposition strategy. Despite this finding, for

the sake of universality the pressure communications were also invoked in the simulations from this point on.

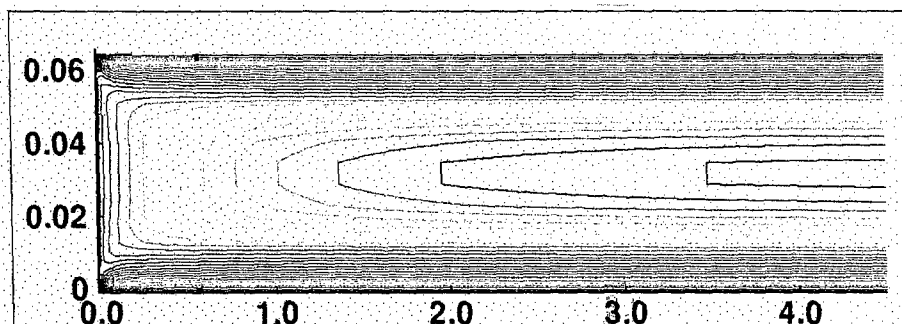


Figure 6.2: Laminar channel flow. Results of 8-processor run. Axes dimensions are given in meters.

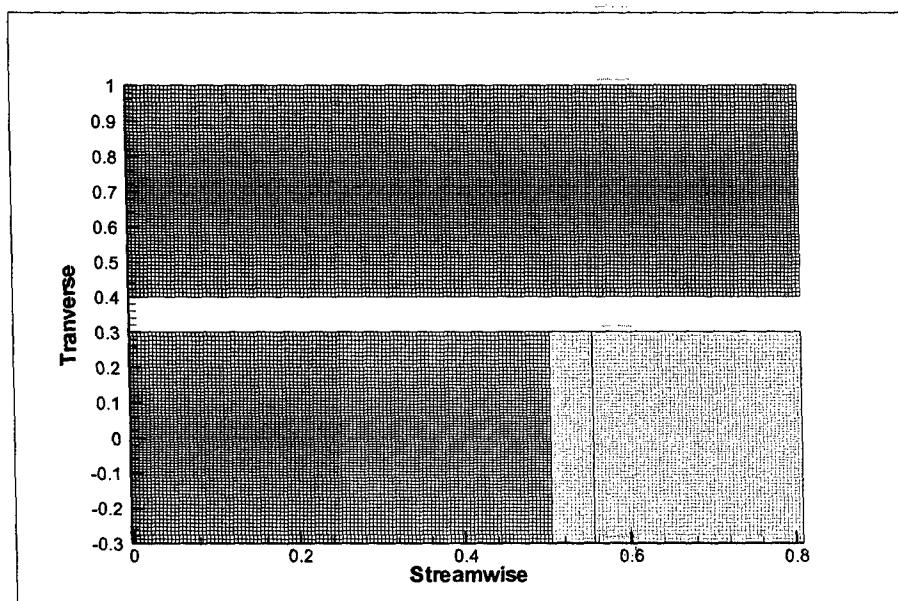


Figure 6.3 Comparison of numerical meshes used in single and 3-processor simulation (black lines indicate inter-processor boundaries.)

The flat-plate shear layer was investigated for verification. The mesh created for this task is shown in Figure 6.3. Keeping the domain size and effective number of grid points (570K nodes) constant, the same simulation was performed on a single processor and on 3 processors. The comparison of the predictions as shown in the streamwise contours in Figure 6.4 and profile along the x-axis in Figure 6.5 has shown that both simulations are in perfect agreement. This has ensured us with confidence in the predictions of parallel simulations of this type of flows. The processor time was also recorded for this case on the local DecAlpha Cluster (570K grid nodes). Here, the single processor execution took 7.15 seconds per pits (pits = Pressure Iteration * Time

Step) and the 3 processor execution took 2.78 sec/pits per CPU, which indicated a scale up of 2.57 or 85% efficiency.

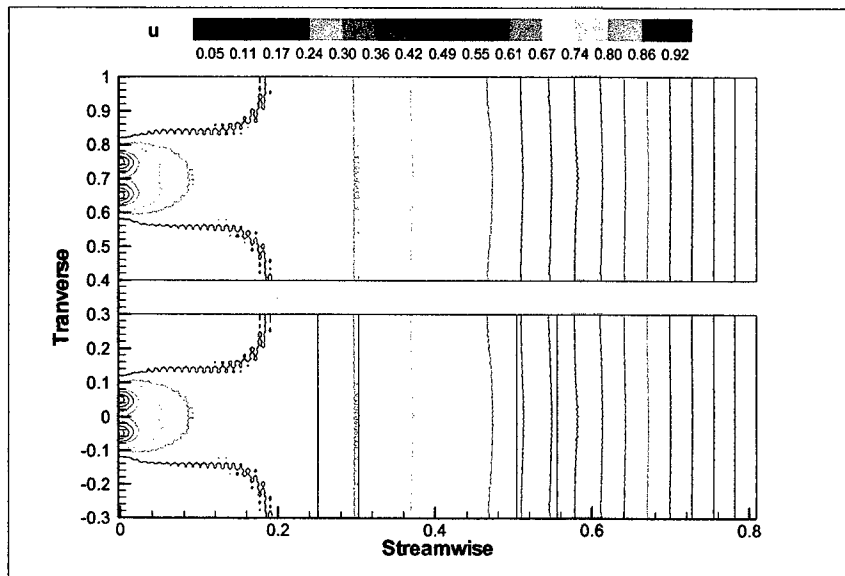


Figure 6.4 Comparison of predicted streamwise velocity contour in single and 3-processor simulations (black lines indicate inter-processor boundaries.)

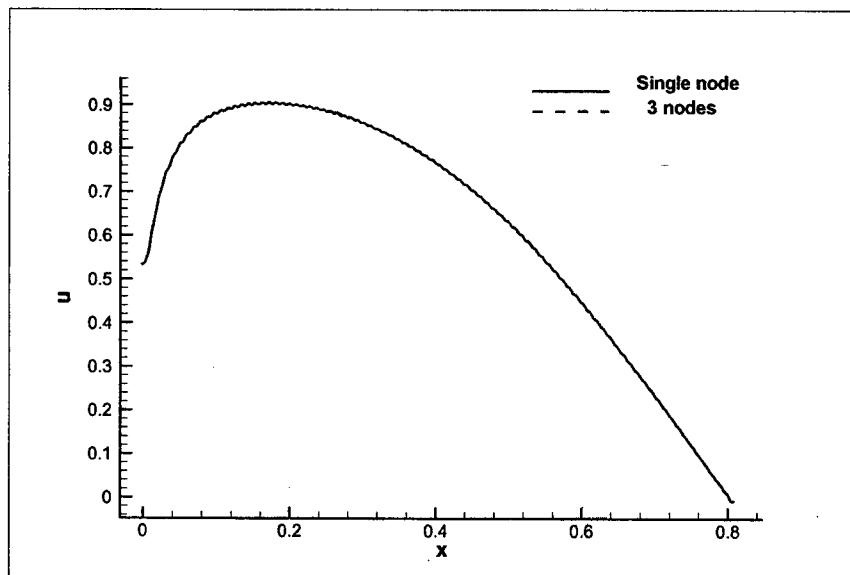
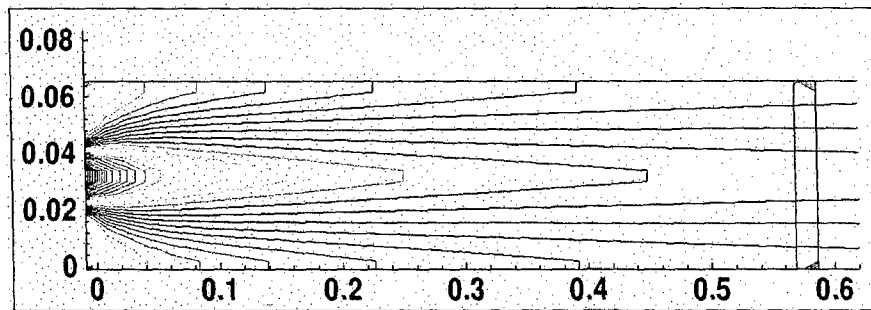


Figure 6.5 Comparison of predicted streamwise velocity at one point in single and 3-processor simulations

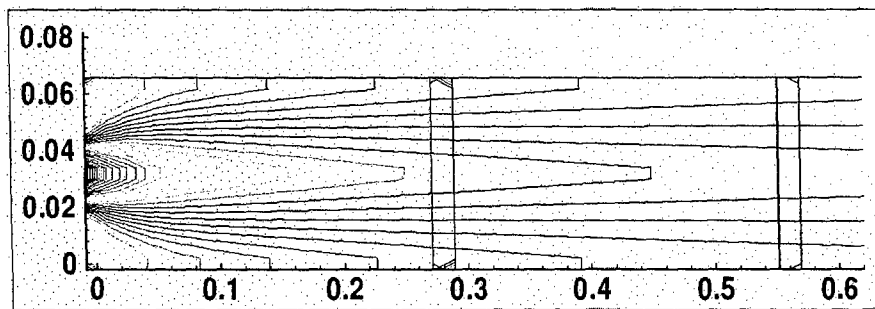
Next, two flat-plate wake simulations on 4 and 8 processors were done for the wake flow of Reynolds number $1.2 \cdot 10^6$. In both simulations the total number of grid nodes was equal to $224 \times 18 \times 10$, with $28 \times 18 \times 10$ nodes per processor in 8-processor run and $56 \times 18 \times 10$ nodes per processor in a 4-processor run. The results were compared to look for any possible discrepancy

introduced by the inter-processor communications. Figure 6.6 shows a perfect agreement between these two cases on the computed flow-field. The virtual absence of turbulent unsteadiness in the figures is the result of high numerical diffusion related to relative coarseness of the grid. Another simulation of a shear layer flow was performed on 8 processors with the grid size of 250K nodes on each processor. The maximum Reynolds number, based on shear layer thickness was 375. As can be seen in Fig. 6.7 the development of shear-layer was not affected by inter-processor communications. The speed of execution of the large-scale run was considerably slower with one iteration computed in approximately 1.5 sec on a DEC-Alpha cluster consisting of 533MHz, 512MB nodes.

The scalability analysis performed for different domain decompositions (Osman et al., 2000) indicted that the speedup is almost linearly proportional to the number of processors (domains) being used.



(a) 28x18x10-node 4-processor run



(b) 56x18x10-node 8-processor run

Figure 6.6: Comparison of wake simulations on different number of processors.

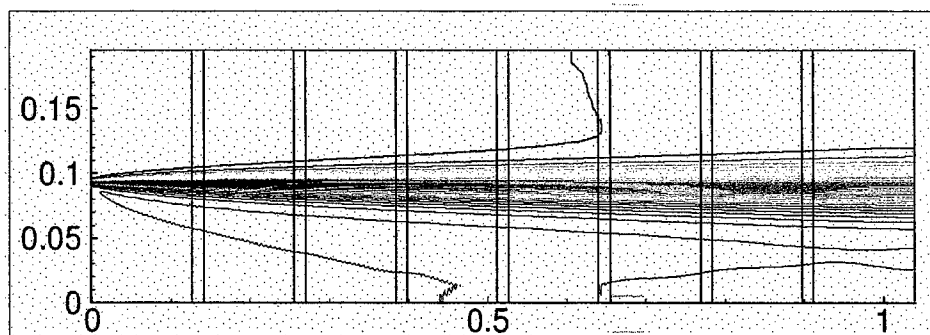


Figure 6.7: Large-scale 8-processor simulation (250K nodes on each processor).

6.2.3 Parallel LES Simulations of a Ship Wake on a Straight Track

The case presented in section 4.3 is considered for the parallel simulations in this part of the study. In order to avoid solving for the flow around the ship model, the computational domain starts from the inflow boundary (or initial data plane) located immediately after the body in the wake, where there is no flow-reversal. The pseudo-random flow field generated by the RFG method is added to the mean flow of RANS simulations to establish the unsteady boundary conditions at the inlet plane. The whole ship flow including the ship wake can be sketched as in Fig. 4.1(b). The computational domain starts from $x/L = 1.05$ (where x starts from the front of the ship model). At this plane the RFG method is used in conjunction with the RANS calculations (Stern and Wilson, 2000).

At the inflow boundary all components of the velocity are specified as a function of time and space. At the outflow boundary Neumann (free gradient) boundary conditions are applied. Symmetry conditions have been used in y direction and periodic boundary conditions have been used in the spanwise (z) direction. At the free surface a slip condition is allowed in x and z directions, but the velocity component normal to the free surface is set to zero. As such the free surface is approximated as a moving flat plane, i.e. low Froude number approximation is involved.

The computational domain size is $3.0 \times 0.3 \times 0.5$ (given in non-dimensional units in ship length) in x , y and z -directions (axial, vertical and transverse directions), respectively. The grid size is $108 \times 50 \times 66$ per processor multiplied by 10 processors, which sums up to ~ 3 million grid nodes. Non-uniform grid spacing, stretching smaller than $1:03$, is used in both z - and y -directions. The length scale and time scale used in RFG were selected as constant in this case. The length scale was 0.02 of the ship length, and the time scale was 0.001, non-dimensionalized

by free stream velocity and ship length. Those numbers were selected because the turbulence length scale is estimated to be about 15% of the ship width. The Smagorinsky SGS model, and second order central differencing scheme were used unless otherwise stated.

The unsteady streamwise velocity variation is presented in Figure 6.8, where τ is the flow trough time. This point was selected inside the wake, as seen from the velocity defect. Figures 6.9 and 6.10 show the vertical variations of the mean velocities and the root mean square velocities, respectively, where the time averaging was made over 3τ . Figure 6.9 shows that the spanwise velocity at the center does not change much in the axial direction, but same velocity components off centerline become more uniform as the wake develops. The vertical velocity at the centerline has a peak below the free surface, which gets weaker in the axial direction. Significant changes are observed in the streamwise velocity profiles in both axial and vertical direction. The location of peak axial velocity moves deeper into the wake indicating a plunging effect as the wake develops in the streamwise direction. This peak is stronger off the centerline indicating the strength of one of the bilge vorticities seen in Fig. 6.11. The intensity of the rms velocity fluctuations show very little decay but significant redistribution and become more isotropic as the wake develops. Initially the turbulence is concentrated more near the free surface. This area plunges deeper with increasing axial distance.

The development of the wake in the axial direction is presented in Figures 6.11 and 6.12. The two large bilge vortices seem to first move away from each other, then further downstream they gradually merge together as they loose strength. However, the resolved turbulent kinetic energy seems to increase in certain regions as seen in Figures 6.11b and 6.12b, even towards the end of the domain (see also Fig. 6.15). This indicates that the domain should be longer than the selected 3 ship lengths. Also, one has to account for the wake spreading and a deeper and wider cross-section is necessary to accommodate the whole wake further downstream than 3 Ship lengths.

In addition to these, the wake spreading or wake width, which is obtained from the parallel run to be roughly $w \sim x^{1/4}$ is also consistent with Buller and Tunaley (1989)'s measurements. Milgram et al. (1993) and Hoekstra & Ligterijn (1991) found $w \sim x^{1/5}$. And the spreading rate of the ship wake on a straight track is observed to be significantly higher than that of a ship wake on a circular track. This is well observed from the parallel simulation predictions of the time averaged streamwise velocity magnitude contours in Figure 6.11 for a straight track

ship wake using 3 million grid nodes on 10 processors (Intel Pentium4) on a domain of 3 ship lengths. These parallel computations were also expanded to a 6 million nodes simulation on 6 processors (3rd generation DecAlpha), and more detailed structures were captured. However, the turn around time for these simulations has significantly increased. The predicted extra detail is especially pronounced in the vorticity contours presented in Figure 6.13. The 6 million nodes simulation was still in the early stages, therefore one should not fall into the wrong conclusion, that the wake spreading is much more pronounced. In fact, it will tighten as the simulations continue.

The resolved turbulence kinetic energies of the wake simulations (on a single processor) of a ship cruising on a straight and circular track are presented in Figure 6.14, where a significant decay of kinetic energy in the streamwise direction can be observed. The locations for both studies are taken to be at the highest kinetic energy value obtained from the IDP (along the centerline for the non turning ship and at $y = -0.001$ and $z = -3.18$ for the turning ship wake simulation). Comparing to the predictions of a non-turning ship wake, the turning ship case indicates less kinetic energy values. However, it should be noted that, this may be due to the coarser grid resolution in the far wake. Overall the trends are similar, but there is a sinusoidal-like distribution of the TKE prediction in the near wake for the straight ship case. It may be because of the existing surface wave from the RANS calculations (Stern and Wilson, 2000). This indicates that some wave information may be present implicitly in the inflow boundary. However, this sinusoidal-like distribution of TKE is not seen in the simulations of a ship on a circular track, which may imply that there is not any wave information present in the RANS simulations (Hyman, 2001).

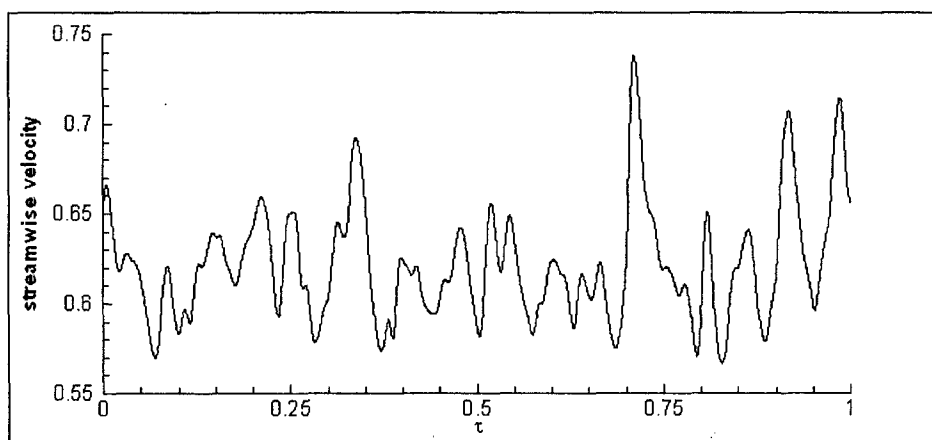


Figure 6.8. Temporal history of streamwise velocity components at $x = 0.6$, $y = -0.012$, $z = -0.06$

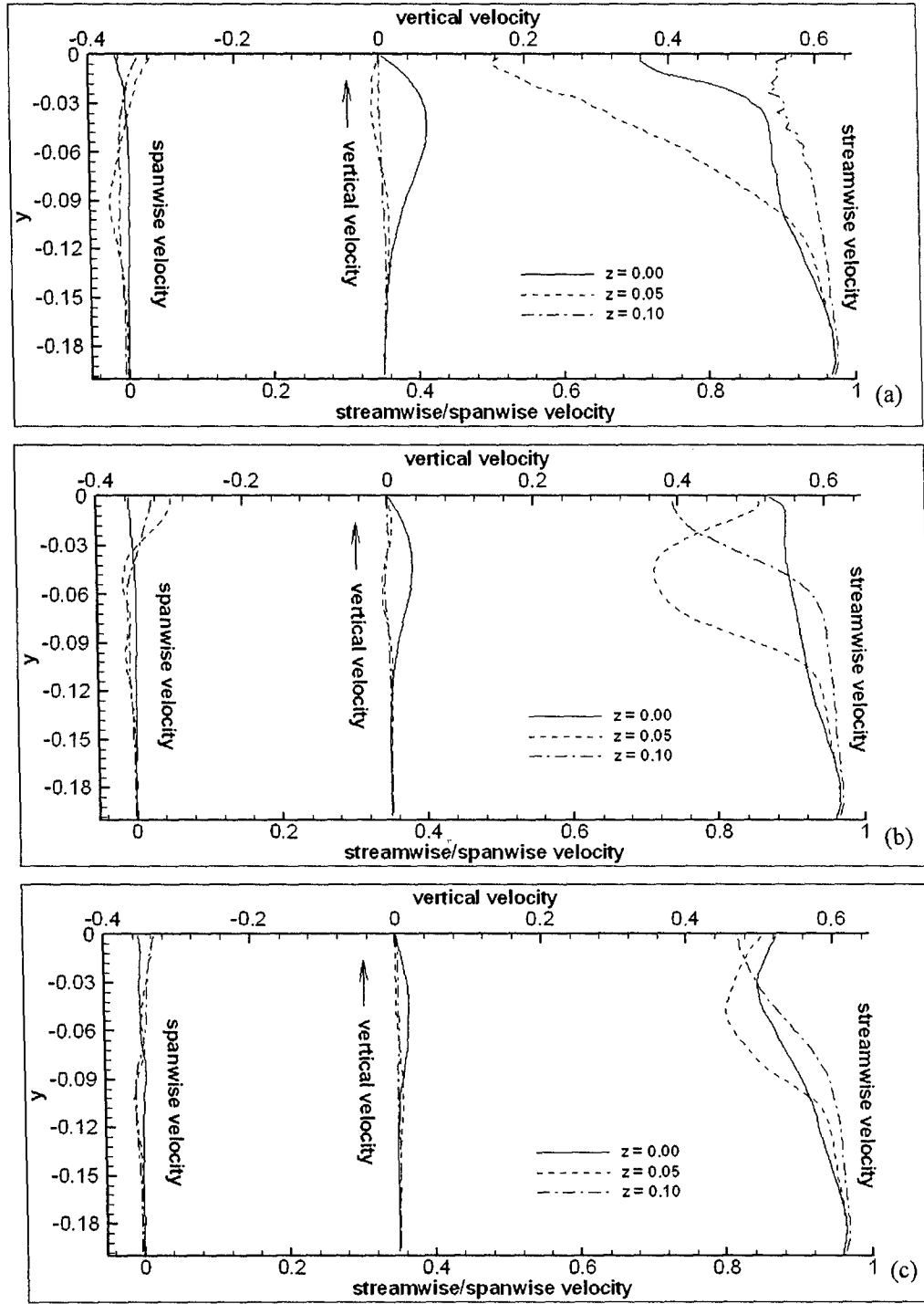


Figure 6.9. The root mean square velocity profiles at 3 spanwise locations at a) $x'/L=0.09$, b) $x'/L=1.60$, c) $x'/L=2.80$ (parallel)

(a)

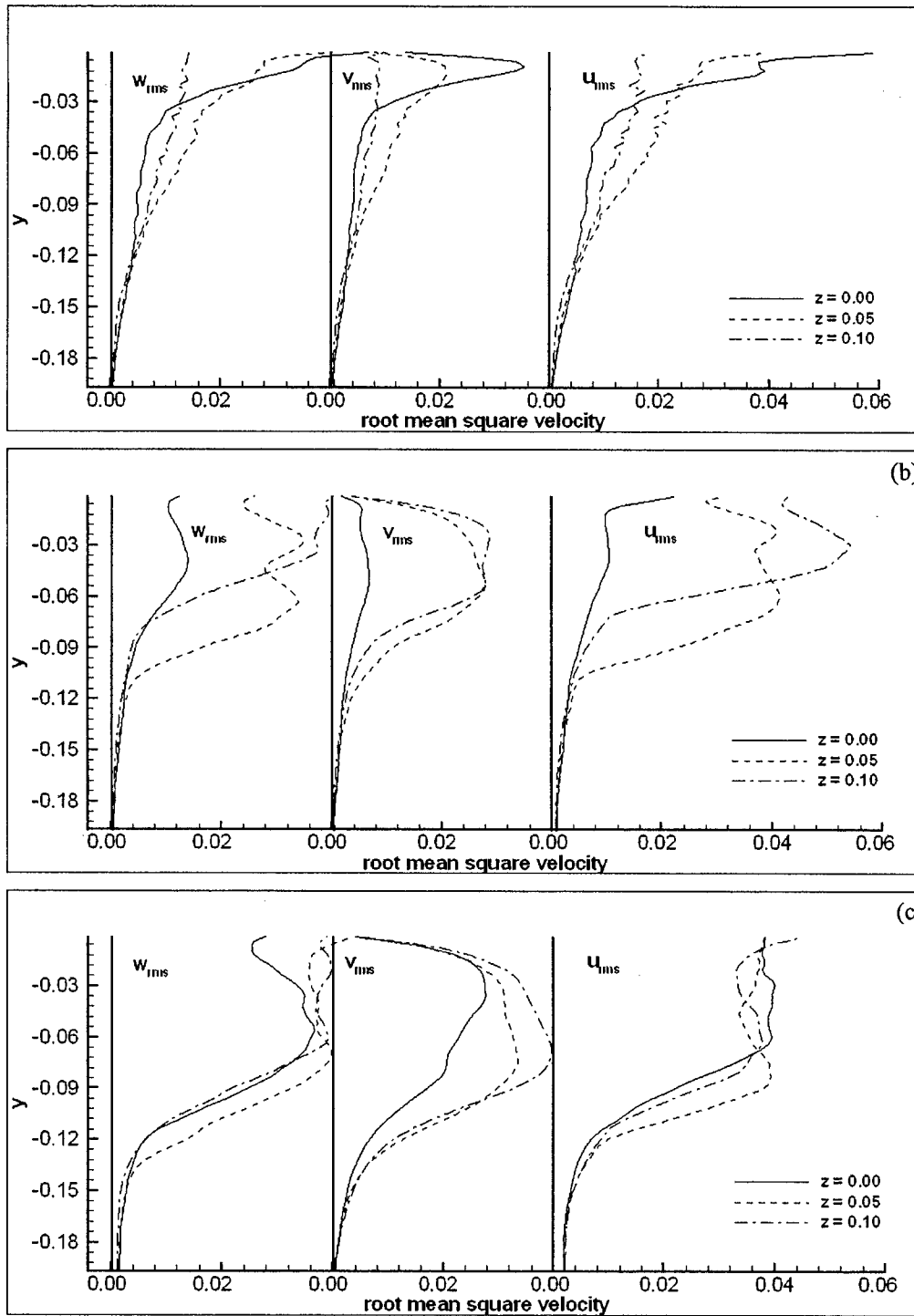


Figure 6.10. The root mean square velocity profiles at 3 spanwise locations at a) $x'/L=0.09$, b) $x'/L=1.60$, c) $x'/L=2.80$ (parallel)

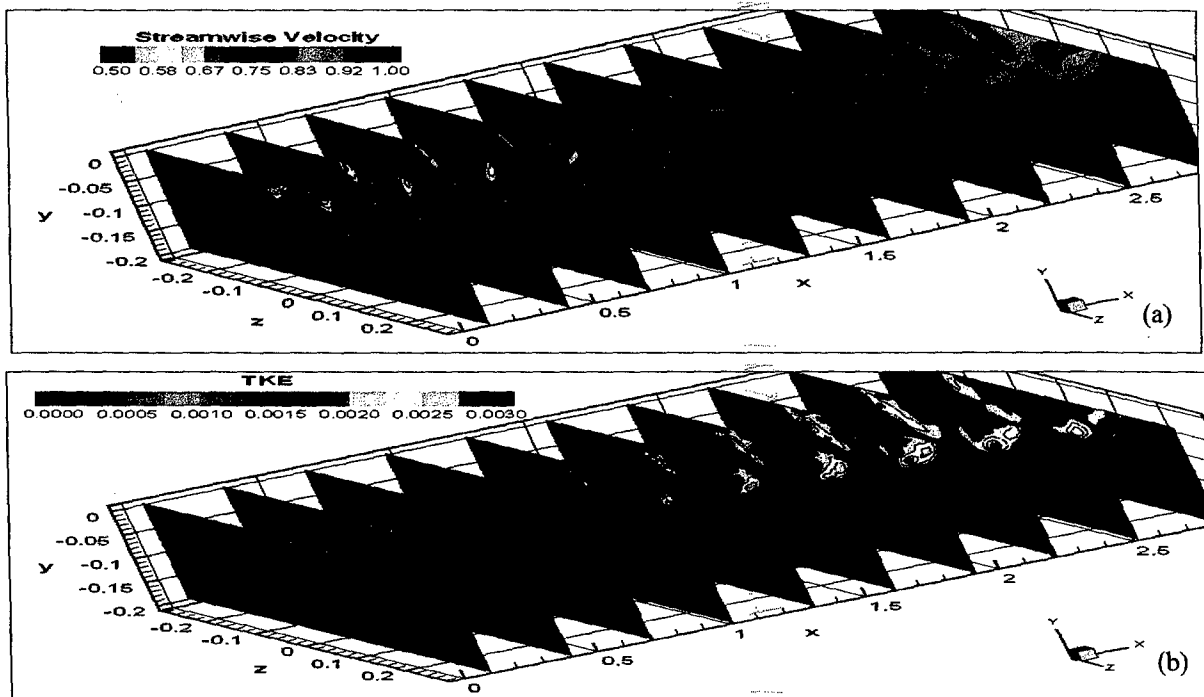


Figure 6.11 Contours on vertical x-planes of time averaged a) streamwise velocity b) turbulent kinetic energy (parallel simulations, 108x50x66 nodes per processor)

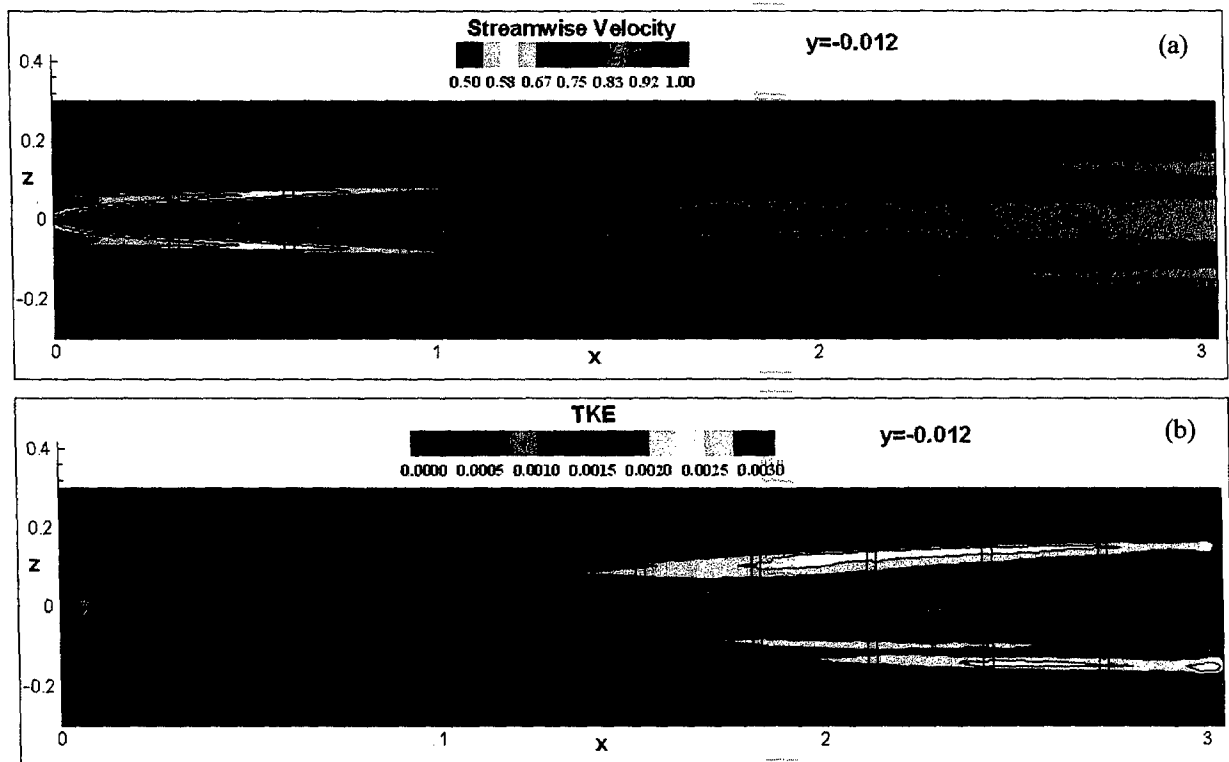


Figure 6.12 Contours on horizontal y-planes of time averaged a) streamwise velocity b) turbulent kinetic energy (parallel simulations, 108x50x66 nodes per processor)

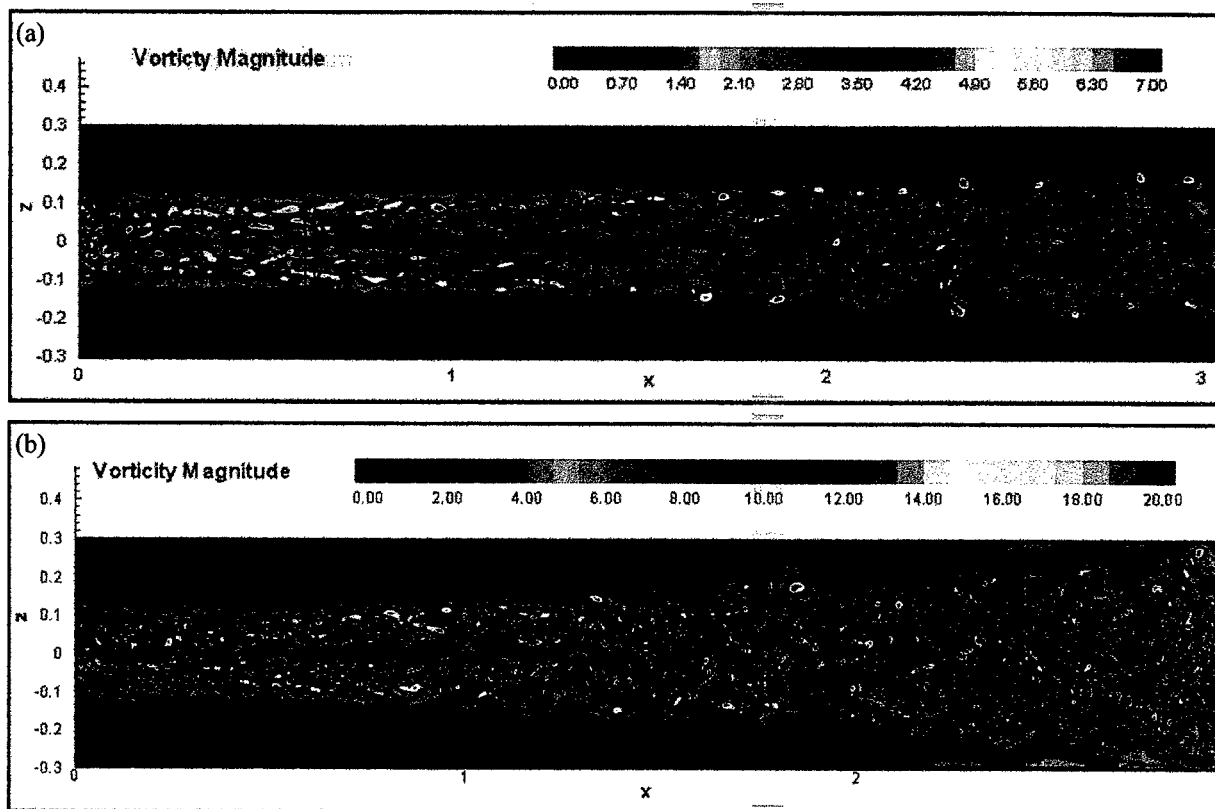


Figure 6.13 a) Vorticity magnitude contours obtained for the wake behind a ship on a straight track using parallel computations with 3 Million grid nodes, b) Preliminary vorticity magnitude contours obtained for the wake behind a ship on a straight track using parallel computations with 6 Million grid nodes (black lines show processor boundaries, overlap/communication regions)

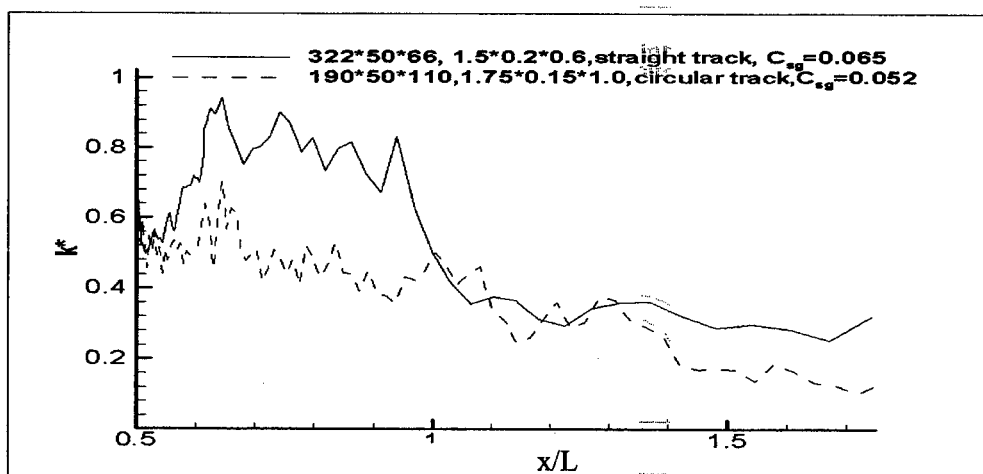


Figure 6.14 Resolved turbulence kinetic energy of the wake simulation of a ship cruising on a straight and circular track normalized w.r.t. its inlet value (single node computation)

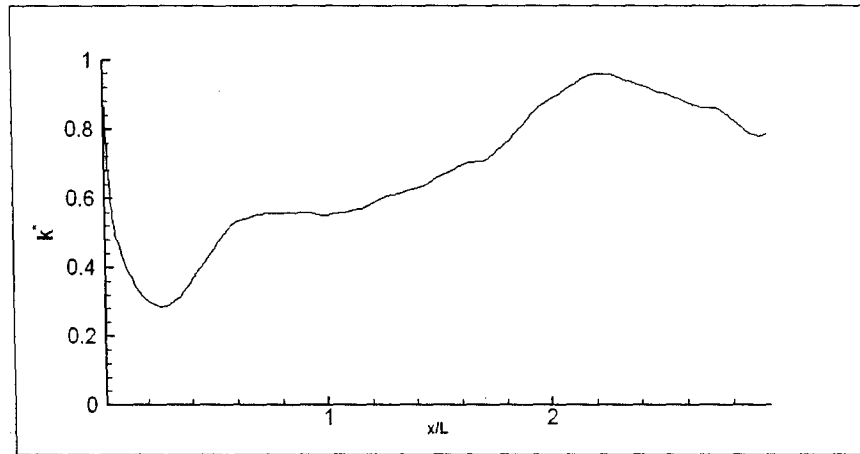


Figure 6.15 Resolved turbulence kinetic energy of the wake simulation of a ship cruising on a straight track normalized w.r.t. its inlet value along a line of center $z = 0.055$, $y = -0.012$ (Parallel computations)

The same dip seen in Figure 6.14 is also present in the 3 million nodes simulation predictions. However, the kinetic energy presented in Figure 6.15 also indicates that the kinetic energy is increasing in the downstream direction. However, the increase in TKE towards the end of the wake is an art effect of taking a line, along which TKE is computed, that is not aligned with the main streamwise direction. To have a better perspective, Figures 6.11b and 6.12b should be investigated. Here, the bilge vortices separate and later merge closer as they become larger, which is probably the cause for the turbulent kinetic energy rise. Moreover, if the ship turns on a circular track, the wake generated by the ship may not follow a circular track. Hence, a line that is not aligned with the center of a bilge vortex would give a false idea of the TKE variation. It should be mentioned that some of the initial decay in k could be the out effect of the application of RFG at IDP. This issue is currently under investigation.

6.3 Discussions

Detailed LES calculations have been performed for the developing wake of a surface ship cruising on a straight track with 3 million nodes (108x50x66 nodes per domain, $\Delta x \sim 0.46\text{m}$; $\Delta y \sim 0.5\text{m}$; $\Delta z \sim 1.2\text{m}$ in the wake region) and 6 million nodes (330x50x66 nodes per domain, $\Delta x \sim 0.23\text{m}$; $\Delta y \sim 0.5\text{m}$; $\Delta z \sim 1.2\text{m}$ in the wake region).

The results are analyzed and turbulence statistics have been presented for further comparison with RANS and/or experiments as they become available. Qualitative comparison

with experimental observations indicate that the LES results are credible, but rigorous validation is necessary to make definite conclusions.

Relatively under-resolved LES of the wake of a ship turning on a circular track has also been performed and the results are compared to those of a ship cruising on straight track.

It seems that the wake of the turning ship is much narrower and has more concentrated vorticity due to the merger of the two bilge vortices. There is little similarity between these two wakes. The wake of the turning ship exhibits more dynamic features. A thorough comparison of the two cases will only be possible when the grid resolution of the turning ship wake is increased by employing parallel runs.

7 CONCLUSION

Large eddy simulation of complex turbulent flows and bubble dynamics in the wake of cruising ships has been studied in detail. To reduce cost and simulation time the calculations were started using an inflow plane in the wake of the ship itself. This requires a robust approach for providing an instantaneous velocity field in conjunction with the prescribed mean flow field. A new technique was developed for this purpose, namely the RFG technique. RANS calculations which were including the ship hull were used to provide the RFG procedure with the information needed on the inflow boundary. The further development of the wake flow was calculated via LES using the domain decomposition technique on parallel machines. Furthermore, the flow was injected with bubbles to compute bubble statistics

Detailed LES calculations have been performed for the developing wake of a surface ship cruising on a straight track with 3 million nodes (108x50x66 nodes per domain, $\Delta x \sim 0.46\text{m}$; $\Delta y \sim 0.5\text{m}$; $\Delta z \sim 1.2\text{m}$ in the wake region) and 6 million nodes (330x50x66 nodes per domain, $\Delta x \sim 0.23\text{m}$; $\Delta y \sim 0.5\text{m}$; $\Delta z \sim 1.2\text{m}$ in the wake region).

The results are analyzed and turbulence statistics have been presented for further comparison with RANS and/or experiments as they become available. Qualitative comparison with experimental observations indicate that the LES results are credible, but rigorous validation is necessary to make definite conclusions.

The Random Flow Generation (RFG) technique, that has been developed can be used to initialize the turbulent flow field and also to prescribe realistic turbulent inflow boundary conditions for LES. By using this technique, the turbulent flow field can be reproduced with good accuracy, even when limited information is available on the mean flow. This information can include the turbulent kinetic energy, its dissipation rate, or shear stresses.

The wake simulations for the ship model DTMB 5512 moving on a straight track has been compared with the macro wake measurements by Hoekstra & Ligtelijn (1991). The prominent flow structures such as the bilge vortices are captured by LES. In measurements and simulations, the minimum axial velocity occurs near the free surface of the center of the wake. Moreover, the extent of axial turbulence intensities is in good agreement with measurements. Additional smaller side vortex pairs are observed away from the center of the wake. As the wake

widens, the strength of these vortex pairs weaken. The vorticity becomes more concentrated near the free surface. Moreover, the wake spreading or wake width, which is obtained to be roughly $w \sim x^{1/4}$ is consistent with Tunaley & Buller (1989)'s measurements.

It seems that the wake of the turning ship is much narrower and has more concentrated vorticity due to the merger of the two bilge vortices. There is little similarity between these two wakes. The wake of the turning ship exhibits more dynamic features. A thorough comparison of the two cases will be possible when the grid resolution of the turning ship wake is increased by employing parallel runs. This is the topic of an upcoming publication which will be an addendum to this report.

The classical SGS model, namely the standard Smagorinsky model, is not totally suitable for complex flows as it uses a constant eddy viscosity coefficient for the entire domain. It was observed that the resolved eddies and the kinetic energy are sensitive to the eddy viscosity coefficient. To remedy this, the Smagorinsky model was modified to account directly for the effect of the free surface on turbulence generation, and the performance of a nonlinear one-equation SGS model was assessed.

It has been clearly demonstrated that if there are wall boundaries, there should be wall modifications. The results indicated that very reasonable turbulence statistics were predicted with the mentioned modifications and it could be used as a SGS model in the simulation of ship wakes. These models were applied to the wake behind a circular track and have been compared with the standard Smagorinsky model.

The results of this study show the viability of a joint parallel LES/LPD/RFG method for computing the developing turbulent bubbly wakes generated by surface ships, at high Reynolds-numbers. This is well documented in our publications (see References) by Celik, Smirnov, Yavuz, Shi, Cehreli and Hu.

8 REFERENCES

- Akselvoll, K. and Moin, P., (1995), Technical Report TF-63, Stanford University
- Anderson, T.B. and Jackson, R.G., (1967) "A Fluid Mechanical Description of Fluidized Beds", Industrial & Engng. Chemistry Fundamentals, Vol.6, pp. 527-539
- Auton, T.R., (1987) "The Lift Force on a Spherical Body in a Rotational Flow," Journal of Fluid Mechanics, 183:199-218
- Auton, T.R., Hunt, J.C.R., and Prudhomme, M. (1988) "Force Exerted on a Body in Inviscid Unsteady Non-uniform Rotational Flow," Journal of Fluid Mechanics, 197:241-257
- Balzer, G., Bagis J., Simonin O., and Koniuta A. (1997) "Modeling of a Cold Circulating Fluidized Bed Focusing on the Effect of the Turbulence Modification by the Particles," Gas-Solid Flow Symposium, ASME Fluids Engineering Div. (FED) Conference, Vancouver, BC, Canada, June 22-26
- Bechara, W., Bailly, C., and Lafon, P., (1994), "Stochastic Approach to Noise Modeling for Free Turbulent Flows," AIAA Journal 32(3)
- Benilov, A., Bang, G., Safray, A., and Tkachenko, I. (2000), "Ship Wake Detectability in the Ocean Turbulent Environment," in Twenty-Third Symposium on Naval Hydrodynamics, Val de Reuil, France
- Berlemont, A., Desjonqueres, P., and Gouesbet, G. (1993) "Particle Tracking in Turbulent Flows," Proc. of Symp. on Gas-Solid Flows, ASME Fluids Conf., Washington, D.C., June 20-24, pp. 121-129
- Bertodano, M.L. et al., (1990), "The Prediction of Two-Phase Turbulence and Phase Distribution Phenomena Using Reynolds Stress Model" J. of Fluids Engineering, Vol. 112, pp. 107-113
- Brandt, A., (1977), "Multi-level Adaptive Solutions to Boundary-value Problems," *Math. Comput.* 31, 333
- Buller, E.H. and Tunaley, J.K.E. (1989), "The Effect of the Ships Screws on the Ship Wake and its Implication for the Radar Image of the Wake," Proc. IGARSS 89, 362-365

- Carrica, P.M., Bonetto, F.J., Drew, D.A., and Lathey, Jr., (1998) "The Interaction of Background Ocean Air Bubbles with a Surface Ship," *Int. J. Numer. Meth. Fluids*, 28:571-600
- Cehreli, Z.N., (2003) "Investigation of Ship Wakes Using Les with Various SGS Models", Dissertation, West Virginia University, Morgantown, WV
- Cehreli, Z. N., Yavuz, I., Celik, I. B., (2004), "Modeling of Free Surface Effects in LES of Ship Wakes," ASME 2004 Heat Transfer/Fluids Engineering Summer Conference, Charlotte, NC, on July 11-15, 20
- Celik, I. (1988) "Isothermal Prediction of Particle and Gas Flow in a Coal Fired Reactor," *Journal of Particulate Science and Technology*, Vol. 6, No. 1, pp. 53-68
- Celik, I. and Gel, A. (1997) "Modeling of Two-Phase Turbulence in Fully Developed Bubbly Flow Regime," ASME FED, Summer Meeting, Vancouver, B.C., FEDSM'97, June 22-26
- Celik, I., Smirnov, A., and Smith, J. (1999) "Appropriate Initial and Boundary Conditions for LES of a Ship Wake," *Proc. of 3rd ASME/JFE Joint Fluids Engineering Conference*, Vol. FEDSM99-7851, San Francisco, California
- Chen, P.P. and Crowe, C.T., (1984), "On the Monte-Carlo Method for Modeling Particle Dispersion in Turbulence", *Proceedings of Sympo. on "Gas-Solid Flows"*, ASME Publ. No. FED-Vol. 10, Editor: J.T. Jurewicz, Energy Source Tech. Conference, New Orleans, LA, Feb. 12-16, pp. 37-41
- Chen, X.-Q. and Pereira, J.C.F., (1995) "Eulerian-Eulerian Predictions of Dilute Turbulent Gas-Particle Flows," In *Gas-Particle Flows*, Editor Stock et al., ASME Publication FED-Vol. 228, pp.265-272
- Crowe, C.T., (1998) "An Assessment of Multiphase Flow Models for Industrial Applications," In *Proceeding of FEDSM'98*, volume FEDSM-5093, Washington,DC,USA
- Crowe, C., Sommerfeld, M., and Tsuji, Y., (1998), "Multiphase Flows with Droplets and Particles," CRC Press Elghobashi, S., (1994), "On Predicting Particle-laden Turbulent Flow," *Applied Scientific Research* 52, 309
- Dasgupta, S., Jackson, R., and Sundaresan, S. (1994) "Turbulent Gas-Particle Flow in Vertical Risers," *AIChE J.*, Vol. 40, No. 2, pp. 215-228
- Deardoff, J.W., (1970), "A Numerical Study of Three-dimensional Turbulent Channel Flow at Large Reynolds Numbers," *Journal of Fluid Mechanics* 41 (2), 453-480

- Dihn, Q.V., Glowinski, R. and Periaux, J., (1984) "Solving Elliptic Problems by Domain Decomposition Methods with Applications," In G. Birkhoff and A. Schoenstadt, editor, Elliptic Problem Solvers II. Academic Press, New York
- Dommermuth, D. and Novikov, E., (1993), "Direct Numerical and Large-eddy Simulations of Turbulent Free-surface Flows," in Proceeding of the Sixth International Conference on Numerical Ship Hydrodynamics, pp 239-270, Iowa City, IOWA
- Dommermuth, D., Gharib, M., Huang, H., Innis, G., Maheo, P., Novikov, E., Talcott, J., and Wyatt, D., (1996), "Turbulent Free-Surface Flows: A Comparison Between Numerical Simulations and Experimental Measurements," 21st Symposium of Naval Hydrodynamics, 200-215, Trondheim, Norway.
- Drew, D. (1992) "Analytical Modeling of Multiphase Flows," Boiling Heat Transfer / R.T. Lahey, Jr. (editor) Elsevier Science Publishers B. V., pp. 31-84
- Dukowicz, J.T. (1980) "A Particle-Fluid Numerical Model for Liquid Spray," J. Comp. Physics, Vol. 35, pp. 229-253
- Durst, F., Milojevic, and Schonung, B., (1984), "Eulerian and Lagrangian Prediction of Particulate Two-Phase Flows: A numerical study", Appl. Math Modeling, Vol. 8, pp. 101-11
- Ebert, F. and Dehning, C. (1992) "Large Eddy Simulation of Turbulent Chaneel Flow of Dilute Suspensions," Proc. of 6th workshop on Two-Phase Flow Predictions: Erlangen, March 30-April 2, Editor: M. Sommerfeld, pp. 230-249
- Elghobashi, S., (1994) "On Predicting Particle-laden Turbulent Flows," Applied Scientific Research, 52:309-329
- Elghobashi, S. (1996) "Direct Numerical Simulation of Dispersed Dilute Two_phase Turbulent Flows – Part 1: Decaying Turbulence and Part 2:Homogenous Shear," In collection of von Karman Institute Lecture Series on Combustion and Turbulence in Two-Phase Flows, Jan 29-Feb 2, Lect. Series 1996-02, Editors M. Manna and D. Vandromme
- Elghobashi, S., and Lasheras, J., (1996) "Effects of Gravity on Sheared Turbulence Laden with Bubbles or Droplets. In 3-rd Microgravity Fluid Physics Conference, pages 443-448, Cleveland, OH

- Elghobashi, S., and Truesdell, G.C., (1993) "On the Two-way Interaction Between Homogeneous Turbulence and Dispersed Solid Particles. i: Turbulence Modification," *Physics of Fluids A*, 5:1790-1801
- Ferziger, J., (1983), "Higher-level Simulations of Turbulent Flows," in J. Essers (ed.), *Computational Methods for Turbulent Transonic and Viscous Flows*, pp 93-183, Hemisphere Publishing Co., Springer Verlag
- Ferziger, J. and Peric, M., 1997, *Computational Methods for Fluid Dynamics*, Springer, Mercedesdruck, Berlin
- Fung, J., Hunt, J., Malik, N., and Perkins, R., (1992), "Kinematic Simulation of Homogeneous Turbulence by Unsteady Random Fourier Modes," *J. Fluid Mech.* 236, 281 *Flows* Cambridge University Press, New York, 1993
- Galperin, B. and Orszag, S.A., "Large Eddy Simulation of Complex Engineering and Geophysical"
- Gouesbet, G. (1992) "Eulerian and Lagrangian Approaches for Predicting the Behaviour of Discrete Particles in Turbulent Flows," 2nd ERCOFTAC Summer School on Advanced Flow Simulation, 10th-21st September, 1990, Oxford, Proceedings, Cambridge Univ.Press
- Gui, L., Longo, L., and Stern, F., (1999), "Towing Tank PIV Measurements System and Data and Uncertainty Assessment for DTMB Model 5512," 3rd International Workshop on PIV, Santa Barbara, CA, 16-18 September.
- Hallmann, M., Scheurlen, M., and Witting, S. (1995) "Computation of Turbulent Evaporating Sprays: Eulerian Versus Lagrangian Approach," *ASME J. of Fluids Engineering*, 117:112-119
- Hayasa, T., (1999), "Monotonic Convergence Property of Turbulent Flow Solution with Central Difference and Quick Schemes," *Journal of Fluids Engineering* 121, 351
- Hinze, J., (1975), "Turbulence", 2nd edition, McGraw-Hill, New York
- Hoekstra, M. and Ligtelijn, J. (1991), "Macro Wake Features of a Range of Ships," MARIN Report No. 410461-1-PV, Netherlands.
- Hoekstra, M., (1991), "Macro Wake Features of a Range of Ships," Technical Report Report No. 410461-1-PV, Maritime Research Institute Netherlands

- Hyman, M., (1994) "Modeling Ship Microbubble Wakes," Technical Report CSS/TR-94/39, Naval Surface Warfare Center. Dahlgren Division
- Hyman, M.: 1995, "Calculation of Initial Data Planes for Shipwake Simulations," Technical Report CSS/TR-96/07, Coastal Research and Technology Department
- Hyman, M., (1998) "Computation of Ship Wake Flows with Free-surface/turbulence Interaction," In 22nd Symposium on Naval Hydrodynamics, pages 11-32, Washington, D.C.
- Hyman, M., (2000) "Bubble Concentrations Near a Ship Surface," Private communication
- Hyman, M., (2001), "Ship-Wake simulations," Private communication
- Ishii, M. (1975) Thermo-Fluid Dynamics of Two-Phase Flow. Eyrolles, France.
- Joia, I.A. , Ushima, T., and Perking, R.J., (1997) "Numerical Study of Bubble and Particle Motion in a Turbulent Boundary Layer Using Proper Orthogonal Decomposition," *Applied Scientific Research*, 57:263-277
- Jordan, S., 1999, "A Large-eddy Simulation Methodology in Generalized Curvilinear Coordinates," *Journal of Computational Physics* 148, 322
- Joseph, D. D. and Lundgen, T. S. (1990) "Ensemble Averaged and Mixture Theory Equations of Incompressible Fluid-particle Suspensions," *Int. J. Multiphase Flow*, 16:35
- Karniadakis, G. E., Orszag, S. A., and Yakhot, V., (1990) "Large-Eddy/RNG Simulation of Flow Over a Backward-Facing Step," *Engineering Turbulence Models and Experiments*, Editors: Rodi and Ganic, Elsevier Sci. Publ. Co., Inc., New York
- Kim, J. and Moin, P., (1985), "Application of a Fractional Step Method to Incompressible Navier-Stokes Equations," *Journal of Computational Physics* 59, 308
- Klebanoff, P., (1954), NACA Tech. Notes 3133
- Kraichnan, R., (1970), "Diffusion by a random velocity field," *Phys. Fluid* 11, 43
- Larreteguy, A., (1999), "Ship-Wake simulations," Private communication
- Lapin, A. and Lubbert, A. (1994) "Numerical Simulation of the Dynamics of Two-phase Gas-liquid Flows in Bubble Columns" *Chemical Engineering Sci.*, 49(21):366-374
- Larreteguy, A., (1999) "Ship-wake Simulations" Private communication
- Larsson, L., Rengnstrom, B., Broberg, L., Li, D.Q., and Janson, C.E., (1998) "Failures, Fantasies, and Feats in the Theoretical/numerical Prediction of Ship Performance," In 22nd Symposium on Naval Hydrodynamics, Washington, DC

- Lavieville, J., Deutsch, E. and Simonin, O., (1995) "Large Eddy Simulation of Interactions between Colliding Particles and a Homogeneous Isotropic Turbulence Field," In Gas-Particle Flows, Editors Stock et al., ASME Publication FED-Vol. 228, pp. 347-357
- Lee, S., Lel , S., and Moin, P., (1992), "Simulation of Spatially Evolving Turbulence and the Applicability of Taylor's Hypothesis in Compressible Flow," *Physics of Fluids* 4, 1521
- Leonard, A. (1974), "Energy Cascade in Large Eddy Simulations of Turbulent Fluid Flows," *Adv. Geophys.*, 18A, 237-248
- Leonard, B., (1988), "Simple High Accuracy Resolution Program for Convective Modeling of Discontinuities," *International Journal for Numerical Methods in Fluids* 8, 1291
- Lesieur, M. and Metais, O. (1996) "New Trends in Large-Eddy Simulation of Turbulence," *Ann. Rev. Fluid Mech.*, 28:45-82.
- Li, A., Ahmadi, G., Bayer, R., and Gaynes, M., (1994), "Aerosol Particle Deposition in an Obstructed Turbulent Duct Flow," *J. Aerosol Sci.* 25(1), 91
- Longo, J., Stern, F., and Toda, Y., (1993), "Mean-Flow Measurements in the Boundary Layer and Wake and Wave Field of a Series 60 CB=0.6 Ship Model - Part 2: Scale Effects on Near-Field Wave Patterns and Comparisons with Inviscid Theory," *J. Ship Research*, 37 (1), 16-24.
- Lund, T., (1998), "Generation of Turbulent Inflow Data for Spatially-developing Boundary Layer Simulations," *Journal of Computational Physics* 140, 233
- Lund, T.S., Wu, X., and Squires K.D. (1998) "Generation of Turbulent Inflow data for Spatially Developing Boundary Layer Simulations," *J. of Computational Physics*, 140, 233-258
- Luo, H., and Svendsen, H.F., (1996) "A Theoretical Model for Drop or Bubble Breakup in Turbulent Dispersions," *AIChE*, 42(5):1225-1233
- Matsubara, M. and Alfredsson, P.H., (1998), "Secondary Instability in Rotating Channel Flow," *J. Fluid Mech.* 368, 27-50.
- Maxey, M., (1987), "The Gravitational Settling of Aerosol Particles in Homogeneous Turbulence and Random Flow Fields," *J. Fluid Mech.* 174, 441
- Maxey, M.R. and Riley, J. J. (1983) "Equation of Motion for a Small Rigid Sphere in a Nonuniform Flow" *Phys. Fluids*, 26:883-889
- McLaughlin, J.B., (1994) "Numerical Computation of Particle-Turbulence Interaction," *Int. J. Multiphase Flow*, 20:211-232

- Milgram, J.H., Peltzer, R.D. and Griffin, O. M., (1993), "Suppression of Short Sea Waves in Ship Wakes: Measurements and Observations," J. Geophysics Res. 98, No. C4, 7103-7114
- Morel, C. and Bestion, D., (1997), "Study about Turbulence Modeling in Steam Water Two-Phase Flows," ASME Fluids Engineering Division Summer Meeting, FEDSM'97-3684, Vancouver, B.C
- Mostafa, A.A. and Mongia, H.C., (1987), "On the Modeling of Turbulent Evaporating Sprays: Eulerian versus Lagrangian approach," Int. J. Heat and Mass Transfer, 30, pp. 2583-2593
- Mostafa, A.A. and Mongia, H.C., (1989), "Evolution of Particle-Laden Jet Flows: A Theoretical and Experimental Study," AIAA Journal, Vol. 27, No. 2, pp. 167-183
- Murai, Y., (2000), "Numerical Study of the Three-dimensional Structure of a Bubble Plume," Transactions of ASME, 122:754-760
- Murai, Y., Ohno, Y., Bae, D.S., Abdulmouti, H., Ishikawa, M., and Yamamoto, F., (2001), "Bubble Generated Convection in Immiscible Two-phase Stratified Liquids," In ASME FEDSM-01, New Orleans, LA
- Naudascher, E., (1965), "Flow in the Wake of Self-propelled Bodies and Related Sources of Turbulence," J.Fluid Mech. 22, 625
- Nakayama, A. and Liu, B., (1990), "The Turbulent Near Wake of a Flat Plate at Low Reynolds Number," J.Fluid Mech. 217, 93
- Okawa, T., Nakazumi, M., Yoshida, K., Matsumoto, T., and Kataoka, I., (2001), "Interfacial Forces Acting on a Bubble in Vertical Upflow," In ASME FEDSM-01, New Orleans, LA
- O'Rourke, J., (1998) "Computational Geometry in C," Cambridge Univ. Press
- Osman, A., Ammar, H., Smirnov, A., Shi, S. and Celik, I., (2000), "Parallel Analysis and Implementation of Large Eddy Simulations of Ship Wakes". In IEEE International Conference on Cluster Computing CLUSTER 2000 Chemnitz Technical University, Saxony, Germany, 2000
- Ounis, H., and Ahmadi, G., (1990), "Analysis of Dispersion of Small Spherical Particles in a Random Velocity Field," J. Fluids Engineering, Vol. 112, pp. 114-120
- Patankar, S.V., 1980, Numerical Heat Transfer and Fluid Flow, Hemisphere Publishing Corporation, New York, N.Y

- Paterson, E., 2003, Private Communications
- Paterson, E., Hyman, M., Stern, F., Carrica, P., Bonetto, F., Drew, D., and Lahey, Jr. R., (1996), "Near-and Far-Field CFD for a Naval Combatant Including Thermal-Stratification and Two-Fluid Modeling," 21st Symp. On Naval Hyrdodynamics, Trondheim, Norway, June. pp. 102-117
- Pedinotti, S., Mariotti, G. and Banerjee, S., (1993), "Direct Numerical Simulation of Particle Behaviour in the Wall Region of Turbulent Flows in Horizontal Channels," Int. J. Multiphase Flow, 18:927-941
- Piomelli, U., (1999), "Large-eddy Simulation: Achievements and Challenges," Progress in Aerospace Sciences, 35:335-62
- Piomelli, U., Ferziger, J. H., and Moin, P., (1988), "Models for Large Eddy Simulation of Turbulent Channel Flows Including Transpiration," Dept. of Mech. Engng, Rept. TF-32, Stanford Univ., CA
- Rai, M. and Moin, P., 1991, "Direct Simulation of Turbulent Flows Using Finite-difference Schemes," Journal of computational physics 109 (2), 169
- Ramaprian, B., Patel, V., and Sastry, M., (1981), "Turbulent Wake Development Behind Streamlined Bodies," Technical Report IIHR Report No.231, Iowa Institute of Hydraulic Research, The University of IOWA
- Ravikanth, V. and Pletcher, R.: 2000, AIAA Paper (2000-0542)
- Ratcliffe, T., (1998), "Validation of Free Surface Reynolds Averaged Navier Stokes and Potential Flow Codes," in 22nd Symposium on Naval Hydrodynamics, pp 964-980, Washington, D.C.
- Reed, A., Beck, R., Griffin, O., and Peltzer, R., (1990), "Hydrodynamics of Remotely Sensed Surface Ship Wakes," SNAME Transactions 98, 319
- Reynolds, W.C. (1989) "The Potential and Limitations of Direct and Large Eddy Simulations," in Whither Turbulence, Turbulence at Crossroads, Edt.: J.L. Lumley, Springer-Verlag, N.Y., pp.313-342.
- Rhie, C.M. and Chow, W.L., (1983), "Numerical Study of the Turbulent Flow Past an Airfoil with Trailing Edge Separation," *AIAA* 21 (11), 1525-1532
- Rightley, P.M., and Lasheras, J.C., (2000), "Bubble Dispersion and Interphase Coupling in a Free-shear Flow," Journal of Fluid Mechanics, 412:21-59

- Rouson, D. and Eaton, J., (1994), "Direct Numerical Simulation of Turbulent Channel Flow with Imersed Particles," ASME Publication FED-Vol. 185, pp. 47-57
- Ruetsch, G.R., and Meiburg, E., (1994), "Two-way Coupling in Shear Layers with Dilute Bubble Concentrations," *Physics of Fluids*, 6(8):2656-2670
- Saif A.A. and Bertondano, M.A.L., (1996), "Modified k- ϵ Model for Two-Phase Turbulent Jets," Proc. 31st National Heat Transfer Conference, Houston, TX, Aug 3-6
- Sato, Y., Hishida, K. and Maeda, M., (1996), "Effect of Dispersed Phase on Modification of Turbulent Flow in a Wall Jet" *J. Fluids Engineering*, Vol. 188, pp. 307-315
- Shi, S., (2001), "Towards Large Eddy Simulation of Ship Wakes", Ph.D. Thesis, West Virginia University.
- Shi, S., Smirnov, A., and Celik, I., (2000), "Large Eddy Simulations of Particle-laden Turbulent Wakes Using a Random Flow Generation Technique," In ONR 2000 Free Surface Turbulence and Bubbly Flows Workshop, pages 13.1-13.7, California Institute of Technology, Pasadena, CA
- Shi, S., Smirnov, A., and Celik, I., (2000), "Large-Eddy Simulations of Turbulent Wake Flows," In Twenty-Third Symposium on Naval Hydrodynamics, pages 203-209, Val de Reuil, France
- Shi, S., Celik, I., Smirnov, A. and Yavuz, I., (2006), "LES of a Spatially Developing Turbulent Wake Flows," to appear in *Journal of Ship Research*, January 2006
- Shimizu, A. and Yokomine, T., (1993), "Modeling of Turbulent Energy Equation of Gas Phase in the Gas-Solid Suspension Flow," ASME Publication, FED-Vol. 166, Gas-Solid Flows, pp. 85-91
- Simon, H.D., (1992), editor. "Parallel Computational Fluid Dynamics: Implementations and Results Using Parallel Computers," MIT Press, Cambridge
- Simonin, O., Deutsche E., and Boivin, M., (1995), "Large Eddy Simulation and Second-Moment Closure Model of Particle Fluctuating Motion in Two-Phase Turbulent Shear Flows," To be published, *Proceedings of Ninth Symposium on Turbulent Shear Flows*, Editor: F. Durst et al., Springer Verlag
- Smagorinsky, J., (1963), "General Circulation Experiments with the Primitive Equations; I. The Basic Equations," *Mon. Weather Rev* 91, 99-164

- Smirnov, A., and Celik, I., (2000), "A Lagrangian Particle Dynamics Model with an Implicit Four-way Coupling Scheme," In The 2000 ASME International Mechanical Engineering Congress and Exposition. Fluids Engineering Division, volume FED-253, pp. 93-100, Orlando, FL
- Smirnov, A., Shi, S., and Celik, I., (2000), "Random Flow Simulations with a Bubble Dynamics Model," In ASME Fluids Engineering Division Summer Meeting, number 11215 in FEDSM2000, Boston, MA
- Smirnov, A., Shi, S., and Celik, I., (2001), "LES of a Bubbly Shipwake Flow," In Symposium on CFD Applications in Aerospace, 2001 ASME Fluids Engineering Division Summer Meeting, number 18013 in FEDSM-2001, New Orleans
- Smirnov, A., Shi, S., and Celik, I., (2001), "Random Flow Generation Technique for Large Eddy Simulations and Particle-dynamics Modeling," Trans. ASME. Journal of Fluids Engineering, 123:359-371
- Smirnov, A.V., Celik, I., Shi, S. (2005) "LES of Bubble Dynamics in Wake Flows" Journal: Journal of Computers and Fluids, Vol: 34, Number: 3, pp: 351-373
- Smirnov, A.V., Hu, G. and Celik, I. (2005) "Embarrassingly Parallel Computations of Bubbly Wakes", Conference: International Conference on Parallel Computational Fluid Dynamics, College Park, Maryland, USA, May 24-27
- Sotiropoulos, F. and Patel, V., (1995), "Application of Reynolds-stress Transport Models of Stern and Wake Flows," Journal of Ship Research 39, 263
- Spalart, P.R., (1988), "Direct Simulation of a Turbulent Boundary Layer up to $Re_\theta = 1410$," J. Fluid Mechanics, 187, 61
- Spain, B., (1965), "Tensor Calculus," Oliver and Boyd
- Speziale, C., (1998), "Turbulence Modeling for Time-dependent RANS and VLES: A Review," AIAA Journal 36(2), 173
- Sridhar, G., and Katz, J., (1995), "Drag and Lift Forces on Microscopic Bubbles Entrained by a Vortex", Physics of Fluids, 7(2):389-399
- Stern, F., Longo, J., Oliveieri, A., and Coleman, H., (2000), "International Collaboration on Benchmark CFD Validation Data for Surface Combatant dtmb model 5415," in Twenty-Third Symposium on Naval Hydrodynamics, Val de Reuil, France

- Stern, F. and Wilson, R., (2000), "RANS solution of Ship Wake," University of IOWA, Private communication
- Trevorrow, M., Vagle, S., and Farmer D.M., (1994) "Acoustical Measurements of Microbubbles within Ship Wakes," *Journal of Acoustical Society of America*, 95(4)
- Truesdell, G.C., and Elghobashi, S., (1994) "On the Two-way Interaction Between Homogeneous Turbulence and Dispersed Solid Particles. ii: Particle Dispersion," *Physics of Fluids*, 6:1405-1407
- Voke, P. and Potamitis, S., (1994), "Numerical Simulation of a Low-reynolds-number Turbulent Wake Behind a Flat Plate," *International Journal for Numerical Methods in Fluids* 19, 377
- Wang, Q. and Squires, K., (1995) "On the Prediction of Particle Deposition in Turbulent Channel Flow using Large Eddy Simulation," In *Gas-Particle Flows*, Editors Stock et al., ASME Publication , FED-Vol. 228, pp. 33-38
- Wang, M. and Moin, P. (2000) "Computation of trailing-edge flow and noise using large-eddy simulation," *AIAA Journal*, 38(12) 2201-2209
- Yakhot, V. and Orszag, S. A. (1986) "Renormalization Group Analysis of Turbulence," *J. Sci. Comput.* 1(1), 3
- Yavuz, I., Cehreli, Z., Celik, I., (2004), "Comparison of Detailed Simulations of a Turbulent Ship Wake on a Straight and Circular Track," 25th Symposium on Naval Hydrodynamics, St. John's, Newfoundland and Labrador, Canada on Aug. 8-12, 2004
- Yavuz, I., Cehreli, Z. N., Celik, I. B. (2002) "Large Eddy Simulation of the Wake Behind a Turning Ship", 2002 Fluids Engineering Division Summer Meeting, July 14-18, 2002, Montreal, Quebec, Canada
- Zang, Y., (1993) "On the development of tools for the simulation of geophysical flows", Ph.D. Thesis, Stanford University.
- Zang, Y., Street, R. L. and Koseff, J. R., 1993, "A Dynamic Mixed Subgrid-scale Model and its Application to Turbulent Recirculating Flows," *Phys. Fluids* 5 (12), 3186
- Zang, Y., Street, R. L. and Koseff, J. R., 1994, "A Non-staggered Grid, Fractional Step Method for Time-Dependent Incompressible Navier-Stokes Equations in Curvilinear Coordinates," *J. Comp. Phys.* 114, 18-33

- Zhou, O. and Leschziner, M., (1991), "A Time-correlated Stochastic Model for Particle Dispersion in Anisotropic Turbulence," in 8-th Turbulent Shear Flows Symp., Munich
- Zhou, Q. and Leschziner, M., (1996), "Modelling Particle Dispersion in Turbulent Recirculating Flow with an Anisotropy- Resolving Scheme," Technical Report TFD/96/07, UMIST

9 APPENDIX A

Smirnov, A.V., Hu, G. and Celik, I. (2005) “Embarrassingly Parallel Computations of Bubbly Wakes”, Conference: International Conference on Parallel Computational Fluid Dynamics, College Park, Maryland, USA, May 24-27

Embarrassingly Parallel Computations of Bubbly Wakes

A.V.Smirnov, G.Hu, I.Celik

West Virginia University

Morgantown, WV 26506, U.S.A.

Email: asmirnov@wvu.edu

Keywords: CFD; domain decomposition; multiphase flows; LES; wake flows; Lagrangian particle dynamics;

A major drawback in the Lagrangian particle simulation in dispersed two-phase flows, in terms of the computational cost and machine capacity, is the limitation on the number of particles, or particle clouds whose trajectories are to be tracked parallel to the solution of the continuous flow field. Insufficient number of particles being tracked commonly leads to inaccurate statistics.

Earlier work of the authors on parallelization of a LES solver by means of domain decomposition [1, 2] provided the possibility to simulate large scale turbulent structures of typical ship-wakes on computer clusters. The next logical step is to extend the pure turbulence model with important multi-phase features of the wake such as bubble dynamics. The algorithm for particle tracking and population dynamics developed earlier by the authors demonstrated the ability to efficiently simulate large populations of particles including coalescence effects with even modest computer resources [3, 4, 5, 6]. However, parallel implementation of a discrete particle dynamics algorithm and LES flow solver by means of domain decomposition technique commonly leads to large communication overheads and load balancing problems. In this study we pursued a simple embarrassingly parallel strategy, which enabled us to avoid these two problems. The basic idea is to perform the simulation of statistically independent realizations of the flow-field and particle ensembles, with each realization assigned to one cluster node. This strategy completely excludes any communication between the computing nodes, at the same time achieving the perfect load balance. However, the technique calls for a new compromise between the required accuracy in the resolution of flow features and the desired quality of particle

statistics. With the whole computational domain residing on one node, the accuracy of flow solution is restricted by the single node memory size.

Despite its seeming simplicity this parallelization strategy should take care of ensuring statistical independence of ensembles generated on different computing nodes. This is achieved by imposing independent random generation of three important flow and particle conditions: (1) initial conditions on the flow-field, (2) inlet flow conditions, (3) particle injection distribution. All three conditions are subjected to randomized time-dependent change, which nevertheless follows a predefined statistical distribution.

It should be noted, that while generating independent ensemble of particle injection coordinates/velocities with a given distribution is a simple matter of Monte-Carlo sampling, the generation of randomized inflow and initial conditions for the flow field should be subjected to certain restrictions imposed by continuum dynamics laws. For example, the continuity relation will generally not be satisfied for any random distribution of flow velocity vectors, even if this distribution obeys Gaussian or other valid statistics. This problem of adequately representing time varying random fluid velocity field was solved earlier by the authors in the development of RFG method [7], and was applied successfully in this case to generate statistically independent and divergencefree flow-field ensembles.

Iterations of the discrete bubble solver were sub-cycled inside flow iterations following Lagrangian particle dynamics (LPD) in a dilute dispersed two-phase flow with one way coupling, i.e. where the particles motion is determined by the continuous phase flow, but the continuous flow is not influenced by the particles. The number of particles tracked in each simulation can vary, depending on the machine capacity and optimal computational expense. The realizations from different runs on different nodes were collected and analyzed to produce histograms of bubble distribution. The global particle statistics was obtained by averaging over all the ensembles.

The combined LES/LPD solver was set up to run on a Beowulf cluster, with 1GHz 1GB computing nodes. A set of simulations of a turbulent bubbly ship wake flow was performed, in which a total of about 254000 particles were tracked on nine different computing nodes. The combined statistics is compared to the statistics from a single run, indicating qualitatively equivalent, but much better results.

Figure 1 shows a snapshot of a particle ensemble representing bubbles in a ship wake. The cumulative cross-sectional distribution of bubbles in the inlet plane is shown in Fig.2. Only the near-wake region was modeled in this simulation, which was dictated by available computer memory restrictions. The post-processed bubble distribution at various cross-section are presented as histograms in Fig.3. The total bubble decay computed on the basis of the simulations (Fig.4) is consistent with the experimental data [8].

In conclusion we would like to mention that along with the relative simplicity of implementation, and parallel efficiency of the approach, this embarrassingly parallel strategy is especially suitable for the newly emerging grid computing infrastructure, which is still not well adapted for the tightly coupled problem, as those relying on domain decomposition methods.

Acknowledgments

This work has been performed under a DOD EPSCoR project sponsored by the Office of Naval Research (ONR), Grant No.N00014-98-1-0611, monitored by Dr. Edwin P. Rood and later by Patrick L. Purtell.

References

- [1] A. Smirnov, I. Yavuz, C. Ersahin, I. Celik, Parallel computations of turbulent wakes, in: Parallel CFD 2003, Russian Academy of Sciences, Moscow, Russia, 2003.
- [2] A. Smirnov, Domain coupling with the DOVE scheme, in: B. Chetverushkin (Ed.), Parallel Computational Fluid Dynamics: Advanced numerical methods, software and applications, Elsevier, North-Holland, Amsterdam, 2004, pp. 119-127.
- [3] A. Smirnov, I. Celik, S. Shi, Les of bubble dynamics in wake flows, Journal of Computers and Fluids 34 (3) (2005) 351-373.
- [4] S. Shi, A. Smirnov, I. Celik, Large eddy simulations of particle-laden turbulent wakes using a random flow generation technique, in: ONR 2000 Free Surface Turbulence and Bubbly Flows Workshop, California Institute of Technology, Pasadena, CA, 2000, pp. 13.1-13.7.
- [5] A. Smirnov, S. Shi, I. Celik, Random Flow Simulations with a Bubble Dynamics Model, in: ASME Fluids Engineering Division Summer Meeting, no. 11215 in FEDSM2000, Boston, MA, 2000.

- [6] A. Smirnov, I. Celik, A Lagrangian particle dynamics model with an implicit fourway coupling scheme, in: The 2000 ASME International Mechanical Engineering Congress and Exposition. Fluids Engineering Division, Vol. FED-253, Orlando, FL, 2000, pp. 93-100.
- [7] A. Smirnov, S. Shi, I. Celik, Random flow generation technique for large eddy simulations and particle-dynamics modeling, Trans. ASME. Journal of Fluids Engineering 123 (2001) 359-371.
- [8] M. Hyman, Modeling ship microbubble wakes, Tech. Rep. CSS/TR-94/39, Naval Surface Warfare Center. Dahlgren Division. (1994).

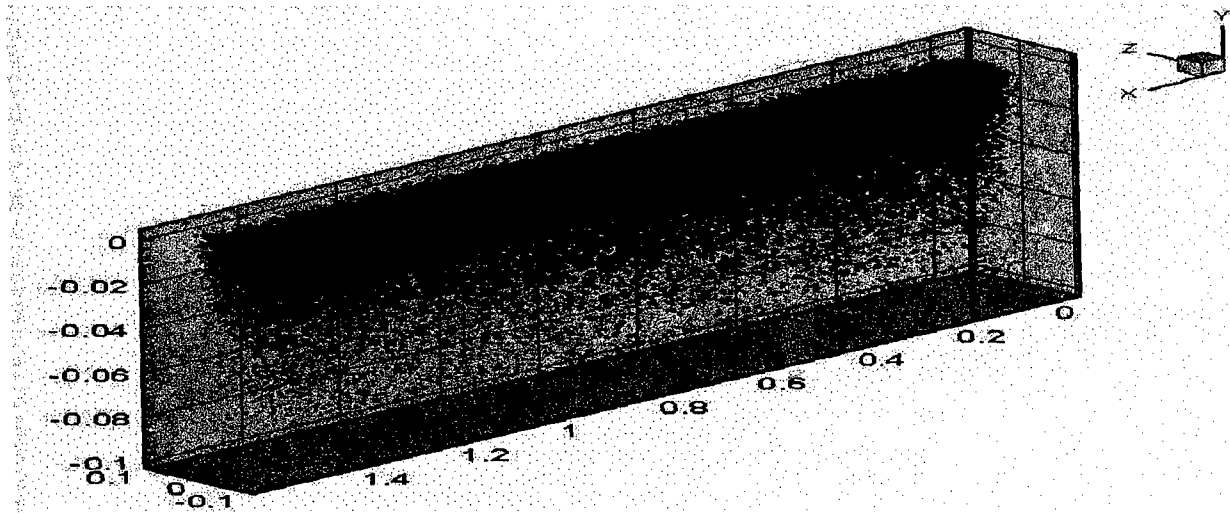


Figure 1: Particle ensemble

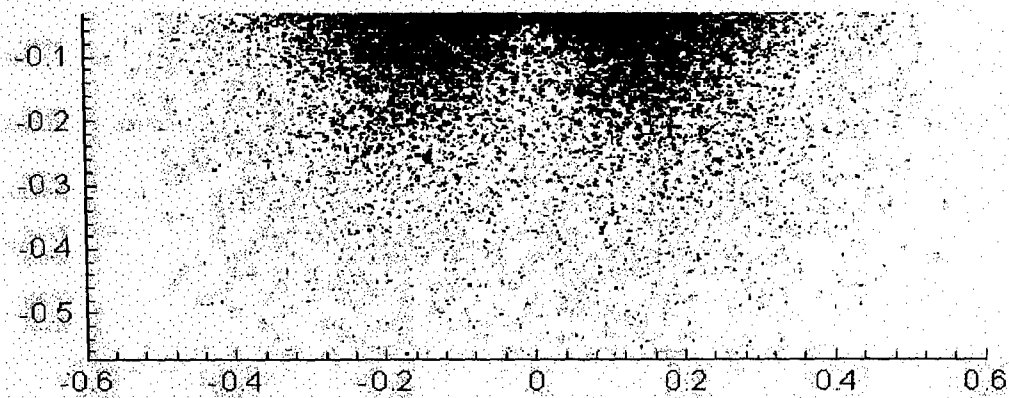
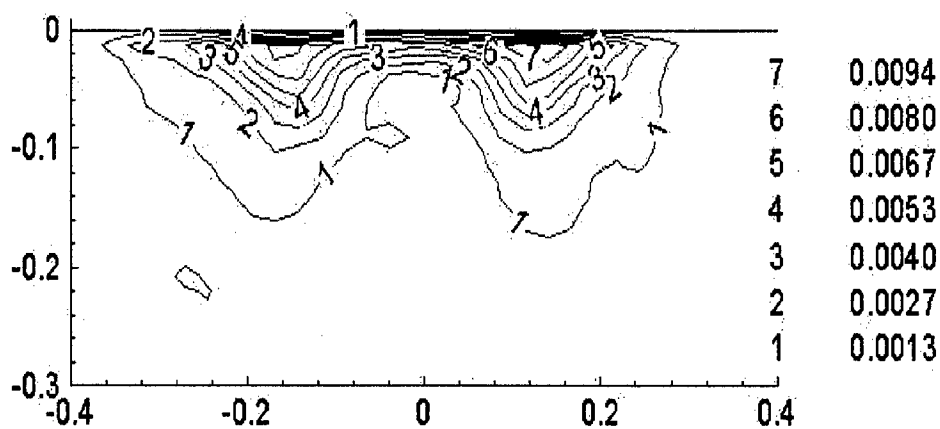
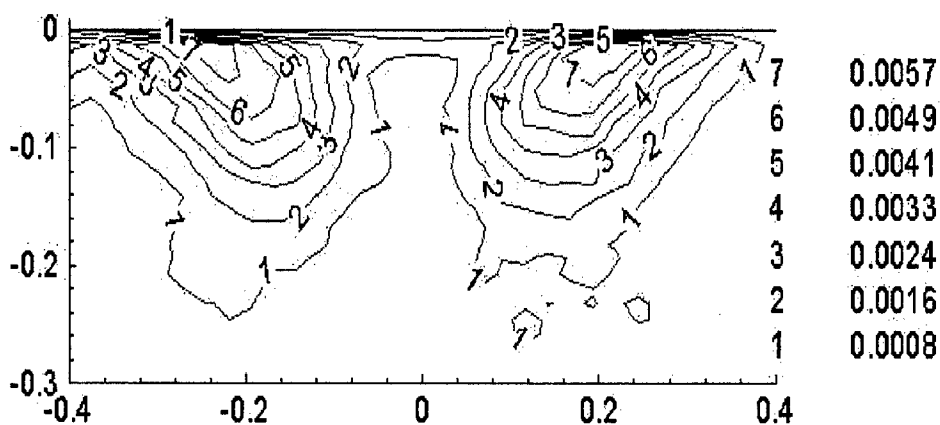


Figure 2: Particle distribution in the inlet plane



(a) $X/L=0.25$



(b) $X/L=0.75$

Figure 3: Particle distribution histograms in cross-sectional planes

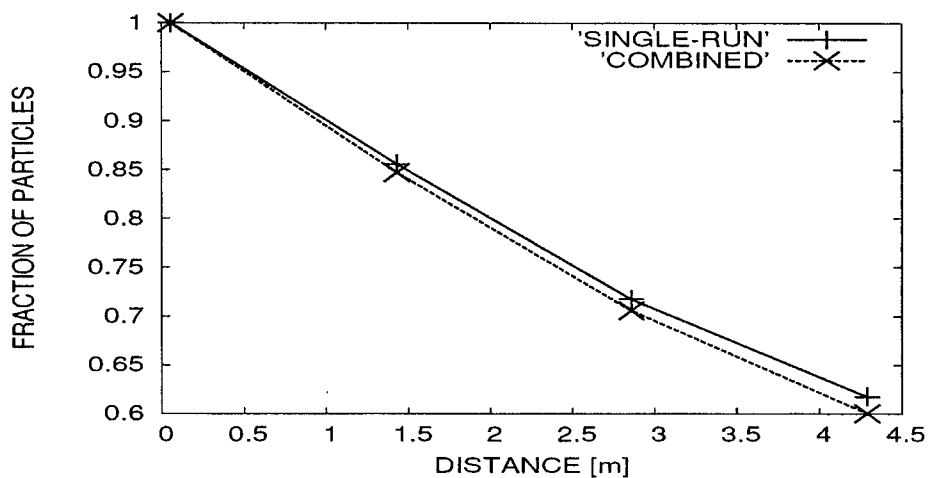


Figure 4: Bubble decay